

STRESS STRAIN BEHAVIOR AND DYNAMIC PROPERTIES OF CABO ROJO CALCAREOUS SANDS

by

Joanna Cataño Arango

A thesis submitted in partial fulfillment of the requirements for the degree of

MASTER OF SCIENCE
in
CIVIL ENGINEERING

UNIVERSITY OF PUERTO RICO
MAYAGÜEZ CAMPUS
May 2006

Approved by:

Miguel A. Pando, Ph.D.
President, Graduate Committee

Date

Americo Fernández, Ph.D.
Member, Graduate Committee

Date

Hiram González, MSCE, P.E.
Member, Graduate Committee

Date

Ricardo Ramos, Ph.D., P.E.
Member, Graduate Committee

Date

Wilson Ramírez, Ph.D.
Representative of Graduate Studies

Date

Ismael Pagán Trinidad, MSCE
Chairperson of the Department

Date

ABSTRACT

This thesis involved studying the stress-strain behavior and dynamic properties of uncemented calcareous sands from southwest Puerto Rico (Cabo Rojo sand). A silica sand (South Bend sand) with similar grain sizes was included for comparison purposes. The research involved a comprehensive experimental program of both sands, which included: Index testing, XRD mineralogy, SEM imaging, Direct shear tests, 1-D compression tests, ICU triaxials, and Resonant column tests.

The calcareous sand consisted of skeletal remains of marine organisms with unique particle shapes and intraparticle porosity. Results indicated that in general this sand was more ductile, more crushable, more contractive, and less stiff than the silica sand. However, the effective friction angles of the calcareous sand were higher than the silica sand, mainly due to differences in their pore pressure generation tendencies.

This research highlighted important differences in geotechnical behavior between the two sands, which may warrant special design considerations. Further research on these sands is recommended.

RESUMEN

Esta tesis comprende el estudio del comportamiento esfuerzo-deformación y las propiedades dinámicas de las arenas calcáreas no-cementadas del suroeste de Puerto Rico (arena Cabo Rojo). Para fines comparativos se incluyó además una arena sílice con similar distribución de tamaños (arena South Bend). Esta investigación presenta un exhaustivo programa experimental para ambas arenas que incluye: Ensayos de Propiedades índice, Mineralogía por refracción de rayos X, Imágenes en microscopio electrónico (SEM), pruebas de Corte directo, Compresión uniaxial, ensayos Triaxiales y de Columna resonante.

La arena calcárea presentó un contenido importante de fósiles de organismos marinos, que ocasionan partículas de formas peculiares y alta porosidad intra-granular. Los resultados indicaron que, en general, esta arena fue más dúctil, triturable y contractiva, así como menos rígida que la arena sílice de comparación. Sin embargo, los ángulos de fricción efectivos de la arena calcárea fueron más altos que los de la arena sílice, debido principalmente a las diferentes tendencias en la generación de la presión de poros.

Esta investigación mostró diferencias importantes en el comportamiento geotécnico de las dos arenas de estudio, que sugieren la necesidad de consideraciones especiales de diseño para las arenas calcáreas de Cabo Rojo. Se recomienda por lo tanto, continuar esta investigación.

To my family ...

ACKNOWLEDGMENTS

First I would like to thank God for giving me the strength and patience to be able to finish this work. Thanks to Dr. Miguel A. Pando, my advisor and president of my Graduate Committee, for his guidance and friendship throughout the course of my graduate studies at the University of Puerto Rico – Mayagüez (UPRM). His support and expertise were fundamental to the conclusion of this work. Thanks also for always being concerned about my academic and professional improvement.

Thanks are also extended to the other members of my Graduate Committee, Dr. Américo Fernández, Prof. Hiram González, Dr. Wilson Ramírez and Dr. Ricardo Ramos. They greatly contributed to the improvement of this thesis with their advice and ideas. The great task made by Prof. Hiram González reviewing this document is specially acknowledged.

I gratefully acknowledge the supervision and support of Dr. Lynn Salvati during the experimental work carried out at the University of Notre Dame. My thanks for giving me the opportunity to work in her lab. It was a rewarding experience, both professionally and personally.

I specially acknowledge the help and advice given by Dr. Juan Bernal and Dr. Luís Suárez. Thanks also to Mr. Jaime Ramírez, the lab technician of the Geotechnical Laboratory at UPRM, for his help during the experimental phase of this work.

This research was supported by the Civil Engineering Department at UPRM. Special thanks to Dr. Jose A. Martínez from the Strong Motion Program; his financial support is gratefully acknowledged.

Very special thanks to Delio A. Ramírez for his help, patience and support throughout the course of this work. Your love and encouragement were essential to keep going every day!

Thanks also to my friends and family in Puerto Rico, Colombia and Florida; Cataños, Alzates, Zuñigas, Domínguez, Boteros, Quinteros, Briceños, Iván, Tere, Rafael, Gloria, Víctor, Mauricio, Alonso, Orlando, Omayra, Mónica, Andrés, Néstor, Adriana, Carlos Andrés, Luz Adriana, Eimar, John, Guillermo, Paul, Hebenly, María Fernanda, Hector, Amelia, Aidcer, Luís, Edgardo, Rolando, Jorge, Daniel, Samuel and Liz. Thanks for your good thoughts and encouraging words; they were very meaningful for me.

Finally, I really want to thank my parents Eduardo and Amparo, and my brother and sister, Carlos Eduardo and Claudia. I am so grateful to have you in my life... this work is dedicated to you.

TABLE OF CONTENTS

<i>LIST OF FIGURES</i>	<i>x</i>
<i>LIST OF TABLES</i>	<i>xiv</i>
<i>SYMBOLS AND ABBREVIATIONS</i>	<i>xv</i>
1 INTRODUCTION	1
1.1 Introduction	1
1.2 Motivation	2
1.3 Objectives	2
1.4 Organization	4
2 BACKGROUND AND LITERATURE REVIEW	6
2.1 Introduction	6
2.2 Critical State Soil Mechanics Definitions	6
2.2.1 <i>Steady state of sands</i>	6
2.2.2 <i>State of phase of transformation</i>	9
2.3 Background	10
2.3.1 <i>Calcareous soils</i>	10
2.3.2 <i>Marine carbonate sediments in Puerto Rico</i>	12
2.4 Literature Review	15
2.4.1 <i>Index properties of calcareous sands</i>	15
2.4.2 <i>Crushing of calcareous sands</i>	18
2.4.3 <i>Stress-strain behavior of calcareous sands</i>	18
2.4.4 <i>Dynamic properties of calcareous sands</i>	23
2.5 Summary	25
3 LABORATORY TESTING PROGRAM	27
3.1 Introduction	27
3.2 Soils Tested	27
3.2.1 <i>General description of the test sand</i>	29
3.2.2 <i>Grain characterization using SEM microscopy</i>	32

3.2.3	<i>Mineralogy</i>	35
3.2.4	<i>Shear strength</i>	38
3.2.5	<i>Crushability analyses</i>	46
3.3	1-D Compression Test	48
3.4	Monotonic Triaxial Testing Program	49
3.4.1	<i>Triaxial specimen preparation</i>	50
3.4.2	<i>Triaxial specimen setup and saturation</i>	53
3.4.3	<i>Triaxial test setup</i>	54
3.4.4	<i>Final specimen void ratio calculations</i>	57
3.4.5	<i>Calibration of sensors used in the triaxial testing</i>	59
3.5	Resonant Column Testing Program	60
3.5.1	<i>Resonant column background</i>	60
3.5.2	<i>RC test set-up</i>	66
3.5.3	<i>Specimen preparation</i>	67
3.5.4	<i>RC equipment calibrations</i>	70
4	STRESS-STRAIN BEHAVIOR OF THE CABO ROJO SAND	71
4.1	Introduction	71
4.2	Stress-Strain Behavior of Cabo Rojo Sand	71
4.2.1	<i>Initial Young's modulus for Cabo Rojo calcareous sand</i>	76
4.2.2	<i>Internal friction angles for Cabo Rojo calcareous sand</i>	79
4.3	Steady State Behavior for Cabo Rojo Calcareous Sand	85
4.4	Stress-Strain Behavior Comparison between the Two Tests Sands	88
4.5	Summary and Discussion	98
5	DYNAMIC PROPERTIES OF THE CABO ROJO SANDS	101
5.1	Introduction	101
5.2	Dynamic Properties of Cabo Rojo Sands at Small Shear Strains	101
5.2.1	<i>Maximum shear modulus of the Cabo Rojo sand</i>	102
5.2.2	<i>Minimum damping ratio of the Cabo Rojo sand</i>	113
5.3	Variation of Dynamic Properties of Cabo Rojo Sand with Medium to Large Shear Strain	115
5.3.1	<i>Shear modulus (G)</i>	115
5.3.2	<i>Damping ratio (D)</i>	118
5.4	RC Test Results Comparison for the Cabo Rojo and South Bend Sands	120
5.5	Summary and Discussion	128

6	SUMMARY AND CONCLUSIONS.....	131
6.1	Introduction.....	131
6.2	Summary.....	131
6.3	Conclusions.....	135
6.4	Recommendations for Future Work.....	141
	REFERENCES.....	143
	APPENDIX 1. SEM Micrographs.....	149
	APPENDIX 2. Non-standardized Tests for Sands Characterization.....	159
	APPENDIX 3. Direct Shear Test (DST). Other results.....	170
	APPENDIX 4. Isotropic Consolidated Undrained (ICU) Triaxial Test. Other results.....	183
	APPENDIX 5. Resonant Column (Rc) Test. Theoretical Background and other Results.....	190
	APPENDIX 6. Equipment and Sensors Calibration.....	224

LIST OF FIGURES

<i>Figure 2.1. Diagram of the steady-state line.</i>	7
<i>Figure 2.2. Steady-state line for non-calcareous sands (After Poulos et al., 1985).</i>	8
<i>Figure 2.3. Diagram of the state of phase transformation.</i>	9
<i>Figure 2.4. Geological map of the Puerto Real quadrangle (Volckmann, 1984).</i>	13
<i>Figure 2.5. Surficial sediments of the insular shelf of Puerto Rico (Scanlon et al., 1998).</i>	14
<i>Figure 3.1. General location of the calcareous sand samples source (Metrodata Inc., 2002).</i>	28
<i>Figure 3.2. Photo of the source site for the tested calcareous sands.</i>	29
<i>Figure 3.3. Grain size distribution curves for calcareous sand and silica sand.</i>	31
<i>Figure 3.4. Microscopy view of the sands used for the experimental program. a) Cabo Rojo calcareous sand, b) South Bend silica sand.</i>	33
<i>Figure 3.5. Comparison of grain surface texture for a) Cabo Rojo sand, b) South Bend sand.</i>	34
<i>Figure 3.6. Biogenic grains found in the Cabo Rojo sand: a) Millipora sp. (aragonitic hydrozoan) b) calcite-aragonite gastropod, c) Urchine spine (high-magnesian calcite).</i>	34
<i>Figure 3.7. Diffractogram for the Cabo Rojo calcareous sand.</i>	36
<i>Figure 3.8. Diffractogram for the South Bend silica sand.</i>	37
<i>Figure 3.9. Direct shear test device at the University of Puerto Rico at Mayagüez.</i>	39
<i>Figure 3.10. Direct shear test results for Cabo Rojo sand, medium relative density.</i>	42
<i>Figure 3.11. Direct shear test results for Cabo Rojo sand, maximum relative density.</i>	43
<i>Figure 3.12. Direct shear test results for South Bend sand, medium relative density.</i>	44
<i>Figure 3.13. Particle breakage factor measured for the two test sands for different tests.</i>	47
<i>Figure 3.14. Specimen compression versus consolidation pressure, consolidation test.</i>	49
<i>Figure 3.15. Split mold, latex membrane and vacuum pump.</i>	51
<i>Figure 3.16. Deposition of calcareous sand using the water pluviation method.</i>	51
<i>Figure 3.17. Moist tamping method: a) placement of moist sand, b) tamping of sand layer.</i>	52
<i>Figure 3.18. Installation diagram for LoadTrac-II/FlowTrac-II system for triaxial testing. (Geocomp, 2006).</i>	55
<i>Figure 3.19. LoadTrac-II/FlowTrac-II Triaxial system, University of Puerto Rico at Mayagüez.</i>	56
<i>Figure 3.20. Dynamic response curve obtained by CATS© program.</i>	61
<i>Figure 3.21. Free-vibration decay – CATS© software.</i>	64
<i>Figure 3.22. Damping determination from free-vibration decay – CATS© program.</i>	65
<i>Figure 3.23. Alignment between the proximator and the magnet.</i>	67
<i>Figure 3.24. Diagram of the GCTS resonant column system.</i>	68
<i>Figure 3.25. GCTS resonant column apparatus, University of Notre Dame.</i>	70

Figure 4.1. ICU test results for Cabo Rojo sand with average $D_{r_ini} = 44\%$	72
Figure 4.2. ICU test results for Cabo Rojo sand with average $D_{r_ini} = 69\%$	73
Figure 4.3. ICU test results for Cabo Rojo sand with average $D_{r_ini} = 87\%$	74
Figure 4.4. Initial portion of the deviator stress curves vs. axial strain curves.....	77
Figure 4.5. Initial portion of the deviator stress curves vs. axial strain curves.....	78
Figure 4.6. Initial portion of the deviator stress curves vs. axial strain curves.....	78
Figure 4.7. Variation of initial undrained Young's modulus with effective confining pressure on Cabo Rojo calcareous sand.	80
Figure 4.8. Effective stress paths for Cabo Rojo sand at minimum density.	83
Figure 4.9. Effective stress paths for Cabo Rojo sand at medium density.....	84
Figure 4.10. Effective stress paths for Cabo Rojo sand at maximum density.	85
Figure 4.11. Steady state line for Cabo Rojo sand.....	87
Figure 4.12. Excess pore pressure vs. axial strain curves for "steady-state" specimens of Cabo Rojo sand.	88
Figure 4.13. Comparison of ICU results for medium relative density.	89
Figure 4.14. Comparison of ICU results for maximum relative density.....	90
Figure 4.15. Comparison of the initial undrained Young's modulus.	92
Figure 4.16. Effective stress paths for Cabo Rojo and South Bend sands at medium density.	96
Figure 4.17. Effective stress paths for Cabo Rojo and South Bend sands at maximum density. ...	96
Figure 4.18. Comparison between steady state lines (SSL) for non-calcareous sands and Cabo Rojo sand.	97
Figure 5.1. Variation of maximum shear modulus with effective confining pressure on Cabo Rojo calcareous sand.....	103
Figure 5.2. Coefficients α and β for Cabo Rojo calcareous sand (After Fernandez, 2000).....	106
Figure 5.3. Linear regression to obtain the parameters of the G_{max} expression for the Cabo Rojo calcareous sand.....	110
Figure 5.4. Comparison between equation (5.15) for G_{max} and actual test data.	111
Figure 5.5. Comparison between equation (5.17) for G_{max} and actual test data.	113
Figure 5.6. Variation of minimum damping ratio (D_{min}) with effective confining pressure on Cabo Rojo sand.	114
Figure 5.7. Variation in shear modulus with shearing strain on Cabo Rojo sand.....	116
Figure 5.8. Variation in shear modulus with shearing strain on Cabo Rojo sand.....	116
Figure 5.9. Variation in shear modulus with shearing strain on Cabo Rojo sand. Maximum density ($D_r = 91\%$).	117
Figure 5.10. Variation of normalized shear modulus with shear strain on Cabo Rojo sand. Minimum density ($D_r = 21\%$).	117
Figure 5.11. Variation of normalized shear modulus with shear strain on Cabo Rojo sand.....	118

Figure 5.12. Variation of material damping ratio with shear strain on Cabo Rojo sand.	119
Figure 5.13. Variation of material damping ratio with shear strain on Cabo Rojo sand.	120
Figure 5.14. Comparison of a) shear wave velocity, and b) maximum shear modulus for Cabo Rojo and South Bend sands at minimum density.....	121
Figure 5.15. Comparison of a) shear wave velocity, and b) maximum shear modulus for Cabo Rojo and South Bend sands at maximum density.	122
Figure 5.16. Variation in shear modulus with shear strain on Cabo Rojo and South Bend sands at minimum density.....	124
Figure 5.17. Variation in shear modulus with shear strain on Cabo Rojo and South Bend sands at maximum density.	124
Figure 5.18. Variation in damping ratio with shear strain on Cabo Rojo and South Bend sands at minimum density.....	125
Figure 5.19. Variation in damping ratio with shear strain on Cabo Rojo and South Bend sands at maximum density.	125
Figure A.1.1. General view of the Cabo Rojo sand particles, scale = 1000 μm	149
Figure A.1.2. Particle features, Cabo Rojo sand, a) scale = 1000 μm , b) scale = 100 μm	150
Figure A.1.3. Detail of the surface texture for a Cabo Rojo sand particle,.....	151
Figure A.1.4. Biogenic grain, Cabo Rojo sand. (Halimeda, aragonite alga),.....	152
Figure A.1.5. Biogenic grain, Cabo Rojo sand. (calcite-aragonite gastropod),.....	153
Figure A.1.6. General view of the South Bend sand particles, scale = 100 μm	154
Figure A.1.7. Shape particle features, South Bend sand,	155
Figure A.1.8. Detail of the surface texture for a South Bend sand particle,.....	156
Figure A.1.9. Induced cementation on Cabo Rojo sand. Cementing material in the form of a coating, a) scale = 100 μm , b) scale = 20 μm	157
Figure A.1.10. Induced cementation on Cabo Rojo sand. Cementing material in the form of a needle-like, a) scale = 100 μm , b) scale = 20 μm	158
Figure A.2.1. Initial results for maximum density test, ASTM D4253-93.....	160
Figure A.2.2. Alternative method for maximum density test.....	160
Figure A.2.3 Micromeritics–AccuPyc 1330 gas pycnometer.....	162
Figure A.2.4 Fundamental of the operation of gas pycnometer.....	163
Figure A.2.5 NETZSCH TG 209 device, University of Notre Dame.	164
Figure A.2.6 Procedure to determine calcium carbonate content from TGA results.....	165
Figure A.2.7 Mass changes with temperature obtained from the TGA tests.....	169
Figure A.3.1. DST results for Cabo Rojo sand sample, Normal stress = 50 kPa, Dr = 57%.....	172
Figure A.3.2. DST results for Cabo Rojo sand sample, Normal stress = 200 kPa, Dr = 54%....	173
Figure A.3.3. DST results for Cabo Rojo sand sample, Normal stress = 300 kPa, Dr = 60%....	174
Figure A.3.4. DST results for Cabo Rojo sand sample, Normal stress = 500 kPa, Dr = 68%....	175
Figure A.3.5. DST results for Cabo Rojo sand sample, Normal stress = 50 kPa, Dr = 89%.....	176

Figure A.3.6. DST results for Cabo Rojo sand sample, Normal stress = 100 kPa, Dr = 103%.	177
Figure A.3.7. DST results for Cabo Rojo sand sample, Normal stress = 300 kPa, Dr = 104%.	178
Figure A.3.8. DST results for Cabo Rojo sand sample, Normal stress = 500 kPa, Dr = 90%.	179
Figure A.3.9. DST results for South Bend sand sample, Normal stress = 50 kPa, Dr = 53%.	180
Figure A.3.10. DST results for South Bend sand sample, Normal stress = 300 kPa,	181
Figure A.3.11. DST results for South Bend sand sample, Normal stress = 500 kPa, Dr = 58%.	182
Figure A.4.1. a) Deviator stress curves vs. axial strain and b) excess pore pressure curves vs. axial strain for South Bend sand. (Average Dr = 81%).	186
Figure A.4.2. a) Deviator stress curves vs. axial strain and b) excess pore pressure curves vs. axial strain for South Bend sand. (Average Dr = 103%).	187
Figure A.4.3. Initial portion of the deviator stress curves vs. axial strain curves for South Bend sand, (Average Dr = 81%).	188
Figure A.4.4. Initial portion of the deviator stress curves vs. axial strain curves for South Bend sand, (Average Dr = 103%).	188
Figure A.4.5. Effective Stress Paths for South Bend sand at minimum density.	189
Figure A.4.6. Effective Stress Paths for South Bend sand at maximum density.	189
Figure A.5.1. Kelvin-Voigt model used to represent the soil column.	191
Figure A.5.2. Idealization of the fixed-free RC specimen.	192
Figure A.5.3. Response curve of the system obtained by CATS© program.	196
Figure A.5.4. Shearing strain, γ , for solid soil column.	197
Figure A.5.5. Free-vibration decay – CATS© software.	199
Figure A.5.6. Damping determination from Free-vibration decay – CATS© program.	200
Figure A.5.7. Dynamic response curve obtained by CATS© program. (From GCTS, 2004)	201
Figure A.6.1. Configuration used for the calibration of the system load cell.	225
Figure A.6.2. Calibration line for the system load cell.	225
Figure A.6.3. Configuration used for the calibration of the sample pressure transducer. From Geocomp (2006).	227
Figure A.6.4. Calibration line for the cell pressure transducers.	227
Figure A.6.5. Calibration line for the sample pressure transducers.	228
Figure A.6.6. Response curve for calibration test. Aluminum bar without the added mass.	230
Figure A.6.7. Response curve for calibration test. Aluminum bar with the added mass.	231
Figure A.6.8. Damping ratio calculation. Calibration test, aluminum bar.	232
Figure A.6.9. Configuration used for the calibration of the RC displacement sensors.	233
Figure A.6.10. Calibration line for the proximator # 1.	233
Figure A.6.11. Calibration line for the proximator # 2.	234

LIST OF TABLES

<i>Table 2.1. Typical index properties of some calcareous sands.....</i>	<i>17</i>
<i>Table 2.2. Summary of literature review on stress-strain behavior of calcareous sands.....</i>	<i>19</i>
<i>Table 2.3. Empirical formulations for Gmax prediction of calcareous sands.....</i>	<i>25</i>
<i>Table 3.1. Index properties of sands used in this study.....</i>	<i>31</i>
<i>Table 3.2. Calcium carbonate content of the test sands from TGA analysis.....</i>	<i>38</i>
<i>Table 3.3. Summary of direct shear test results on Cabo Rojo calcareous sand.....</i>	<i>40</i>
<i>Table 3.4. Summary of direct shear test results on South Bend silica sand.....</i>	<i>40</i>
<i>Table 3.5. Summary of shear strength parameters for ICU triaxial tests.....</i>	<i>46</i>
<i>Table 4.1 Summary of ICU triaxial test results on Cabo Rojo calcareous sand.....</i>	<i>77</i>
<i>Table 4.2. Power law parameters for Cabo Rojo calcareous sand.....</i>	<i>80</i>
<i>Table 4.3. Friction angles for Cabo Rojo calcareous sand - Peak strength failure criterion.....</i>	<i>81</i>
<i>Table 4.4. Friction angles for Cabo Rojo calcareous sand – Maximum σ_u failure criterion.....</i>	<i>81</i>
<i>Table 4.5. Friction angles for Cabo Rojo calcareous sand – 10% axial strain failure criterion.....</i>	<i>82</i>
<i>Table 4.6. Initial undrained Young’s modulus for Cabo Rojo and South Bend sands.....</i>	<i>91</i>
<i>Table 4.7. Characteristic stress-strain values for Cabo Rojo and South Bend sands.....</i>	<i>95</i>
<i>Table 5.1. Power law parameters for Cabo Rojo calcareous sand.....</i>	<i>104</i>
<i>Table 5.2. Typical parameters of Gmax of quartz sand (After Kokusho, 1987).....</i>	<i>108</i>
<i>Table 5.3. Values of X and Y in equation (5.12).....</i>	<i>110</i>
<i>Table A.4. 1. Initial state of CIU-TX Cabo Rojo sand samples.....</i>	<i>183</i>
<i>Table A.4. 2. Initial state of CIU-TX South Bend sand samples.....</i>	<i>183</i>
<i>Table A.4. 3. After consolidation state. CIU-TX Cabo Rojo sand samples.....</i>	<i>184</i>
<i>Table A.4. 4. After consolidation state. CIU-TX South Bend sand samples.....</i>	<i>184</i>
<i>Table A.4. 5. After shearing state. CIU-TX South Bend sand samples.....</i>	<i>185</i>

SYMBOLS AND ABBREVIATIONS

- α : Velocity of the medium subjected to an effective isotropic confining stress of 1 kPa.
- A: Constant related to soil shear stiffness.
- A_0 : G_{\max} corresponding to an effective isotropic confining stress of 1 kPa.
- A_c : Corrected area of specimens.
- A_o : Initial area of specimens.
- β : Exponent for V_s formulation.
- B: Skempton's pore pressure parameter.
- B_{10} : Particle breakage factor.
- C_c : Coefficient of concavity.
- C_n : Coordination number.
- C_u : Coefficient of uniformity.
- δ : Logarithmic decrement.
- $\Delta\phi$: Reduction in peak secant friction angle.
- Δu_f : Excess pore pressure at failure.
- Δu_{\max} : Maximum excess pore pressure.
- ΔV_{cons} : Volume change during consolidation.
- ΔV_{ini} : Specimen volume change during initial saturation with CO₂ flushing.
- $\Delta V_{\text{membrane}}$: Specimen volume change due to membrane penetration.
- ΔV_{piston} : Volume change of the cell water due to the penetration of the piston rod.
- ΔV_{sat} : Specimen volume change during back pressure saturation.
- ΔV_{shear} : Specimen volume changes during the shearing stage.
- $\Delta V_{\text{tx.cell}}$: Total volume change of the water in the triaxial cell.
- D: Damping ratio.
- D_{10} : Grain diameter corresponding to 10% of the material being smaller by weight.
- D_{10i} : Initial grain diameter corresponding to 10% of the material being smaller by weight.
- D_{10f} : Final grain diameter corresponding to 10% of the material being smaller by weight.
- D_{30} : Grain diameter corresponding to 30% of the material being smaller by weight.
- D_{50} : Grain diameter corresponding to 50% of the material being smaller by weight.
- D_{60} : Grain diameter corresponding to 60% of the material being smaller by weight.
- d_{cv} : Horizontal displacement at residual shear stress.
- D_{eq} : Equipment-generated damping.

D_{\min} : Minimum damping ratio.
 d_p : Horizontal displacement at peak shear stress.
 D_r : Relative density.
 D_{r_cons} : Relative density after specimen consolidation.
 D_{r_ini} : Initial relative density, after specimen preparation.
 ϵ_a : Axial strain.
 $\epsilon_{axial \Delta u_{max}}$: Axial strain at maximum excess pore pressure.
 $\epsilon_{axial peak}$: Axial strain at peak deviator stress.
 ϵ_v : Volumetric strain.
 e : Void ratio.
 e_{max} : Maximum void ratio.
 e_{min} : Minimum void ratio.
 $E_{u\ ini}$: Initial undrained Young's modulus.
 ϕ_o : Peak secant friction angle.
 $\phi'_{10\% \text{ axial strain}}$: Internal friction angle at 10% axial strain failure criterion.
 ϕ'_{cv} : Residual (nearly constant volume) friction angle.
 $\phi'_{\Delta u_{max}}$: Internal friction angle at maximum excess pore pressure.
 ϕ'_{peak} : Peak friction angle.
 $\phi'_{q_{peak}}$: Internal friction angle at peak deviator stress.
 f_1, f_2 : Half-power frequencies.
 $F(e)$: Homogenization function related to the soil void ratio.
 f_r : Resonant frequency.
 γ : Shear strain.
 γ_{dry} : Dry unit weight.
 γ_{eq} : Equivalent shear strain.
 γ_{max} : Maximum dry unit weight.
 γ_{min} : Minimum dry unit weight.
 γ_{th} : Threshold strain.
 G : Shear modulus.
 G/G_{max} : Normalized shear modulus.
 G_{max} : Small-strain shear modulus.
 G_s : Specific gravity.
 H, h : Height of the soil specimen.
 I : Mass moment of inertia of the soil column.

I_0 : Mass moment of inertia of the driving system.
 ICU: Isotropically consolidated undrained triaxial test.
 ICD: Isotropically consolidated drained triaxial test.
 K: Modulus number.
 M_s : Mass of solids.
 ν : Poisson's ratio.
 n: Modulus exponent.
 n: Exponent for G_{\max} empirical formulation.
 OCR: Overconsolidation ratio.
 P_{atm} : Atmospheric pressure (101 kPa).
 p' : Mean effective principal stress.
 θ_{\max} : Maximum angle of twist at the top of the soil column.
 q: Deviator stress.
 $q_{10\% \epsilon_{\text{axial}}}$: Deviator stress at 10% axial strain.
 q_{peak} : Peak deviator stress.
 ρ_w : Density of water.
 ρ : Soil mass density.
 r_0 : Radius of solid soil specimen.
 R^2 : Correlation coefficient.
 RC: Resonant column test.
 r_{sensor} : Radius to the position of the sensor displacement.
 σ_a : Total axial stress.
 σ_n : Total normal pressure.
 σ_{yield} : Yield pressure.
 σ'_0 : Effective isotropic confining stress.
 σ'_1 : Major effective principal stress.
 σ'_{1f} : Principal major effective stress at failure.
 σ'_3 : Minor effective principal stress.
 σ'_{3f} : Principal minor effective stress at failure.
 σ'_c : Effective isotropic confining stress.
 σ'_n : Effective and total normal pressure.
 $\sigma'_{n_{\text{ini}}}$: Effective normal pressure at the beginning of direct shear tests.
 SSL: Steady-state line.
 τ_{cv} : Constant volume shear stress.

τ_p : Peak shear stress.

u_b : Back pressure.

V_0 : Initial specimen volume.

V_{final} : Final specimen volume.

V_s : Shear wave velocity.

x : Sensor displacement.

1 INTRODUCTION

1.1 Introduction

This research was undertaken to investigate the geotechnical behavior of uncemented calcareous sands from Cabo Rojo, located in the southwest of Puerto Rico. Calcareous sands refer to sands consisting of skeletal remains of marine organisms and that typically have a high carbonate content. Calcareous sands have unique features that distinguish them from silica sands (e.g., quartzitic sands). These sands have a wide variety of particle types which differ in nature, shape, and form, and exist in both cemented and uncemented states. Due to their carbonate mineralogy and unique particle characteristics such as presence of intraparticle voids, calcareous sands tend to be considerably more susceptible to crushing under stress than terrigenous non-carbonate sands.

Over the past 30 years, off-shore platform installations and construction of coastal facilities in tropical and sub-tropical regions of the world (e.g., Australia, Brazil, USA-Florida, India, Israel) have highlighted the important differences in geotechnical behavior of calcareous sands with respect to terrigenous noncarbonated sands (Datta et al. 1982, Allman and Poulos 1988).

The most remarkable reported differences are their lower strength and more ductile response compared to others types of sands (Golightly and Hyde, 1988, and Hull et al.,

1988). This is believed to be associated to their higher susceptibility to exhibit particle crushing when subjected to stress. Other factors which have been found to contribute to their unusual behavior are the unique characteristics of their particles including form, intraparticle voids, structure, texture and variations in size. Fabric and cementation are other important characteristics, but are not included in this research, which is focused on uncemented calcareous sands.

1.2 Motivation

A significant part of the coast line of the island of Puerto Rico is overlain by deposits of calcareous sands. The warm marine environment of the insular shelf of Puerto Rico results in biogenic and biochemical processes that produce calcareous sand deposits with a unique internal structure. This internal structure is mainly characterized by the presence of skeletal remains of rich-carbonate marine organisms with particles of peculiar shapes, high intraparticle porosity, and high susceptibility to crushing. The large extent of these deposits coupled with the recent increase construction of port facilities and coastal developments in Puerto Rico motivated this research. The high seismicity of the island motivated the study of the dynamic properties of these calcareous sand deposits.

1.3 Objectives

The main objective of this research project is to study the stress-strain behavior and dynamic properties of uncemented calcareous sands from Cabo Rojo, Puerto Rico. More specific objectives are:

1. Perform a geotechnical characterization of a calcareous sand and comparable silica sand. Geotechnical characterization includes determination of index properties, uniaxial compressive behavior, and shear strength.
2. Conduct mineralogical analyses and particle characterization for calcareous and silica test sands. This involves mineralogical composition, calcium carbonate content, and evaluation of the sand particle size and shape.
3. Evaluate the grain crushing potential of the calcareous and silica sands used in this study. The evaluation will be performed for the following types of loading: 1-D compression, direct shear, triaxial monotonic and torsional harmonic.
4. Evaluate the stress-strain response of the Cabo Rojo calcareous sands, including response at large deformations. This objective will include the determination of the steady state line (SSL) for the Cabo Rojo calcareous sand. Comparisons with the silica test sand will also be performed.
5. Determine the dynamic properties of the Cabo Rojo calcareous sands. This includes definitions of the small strain shear modulus (G_{\max}), damping and variation of the shear modulus values and damping ratios with shear strain levels. Comparisons with the silica test sand will also be performed.

1.4 Organization

This thesis is organized into six chapters and six appendices. Chapter 2 presents some definitions that are useful in the description of the geotechnical behavior of sands, followed by background information about calcareous soils and their distribution in the insular shelf of Puerto Rico. A literature review on the stress-strain behavior and dynamic properties of uncemented calcareous sands is also included.

Chapter 3 presents a description of the studied soil materials, test procedures employed, and other details of the laboratory testing program performed for this research.

Chapter 4 presents the results of the experimental study on shear-strain behavior of the Cabo Rojo calcareous sand. A summary of the monotonic undrained triaxial test results is given for three relative densities and three isotropic confining stresses. Triaxial test results for the silica sand are also presented in this chapter for comparison purposes.

Chapter 5 presents the resonant column test results for the determination of the dynamic properties of the Cabo Rojo calcareous sand and the comparison with the dynamic properties obtained for the silica test sand. The results are presented in terms of shear modulus, damping ratio, and their variation with shear strain.

Chapter 6 presents a summary of the main findings of the research project, the main conclusions, and recommendations for future work.

The results of the SEM analyses are presented in Appendix 1. A description of some non-standardized tests used in this research as part of the characterization of test sands is presented in Appendix 2. Appendix 3 presents additional results obtained for the direct shear tests. Additional results obtained for the monotonic undrained triaxial tests, are presented in Appendix 4. Appendix 5 presents theoretical background of the resonant column test as well as additional resonant column test results not included in Chapter 5. The procedures followed for calibration of transducers and measuring devices of the equipments used in this research, and the results of the calibration procedures are included in Appendix 6.

2 BACKGROUND AND LITERATURE REVIEW

2.1 Introduction

This chapter provides a brief review of concepts related to critical state soil mechanics, along with background information on marine calcareous sediments and their distribution in the insular shelf of Puerto Rico. A literature review focused on the stress-strain behavior and dynamic properties of calcareous sands is also presented.

2.2 Critical State Soil Mechanics Definitions

This section presents a brief review of concepts related to critical state soil mechanics (CSM). The experimental results of this thesis are presented in terms of the initial state of the sand with respect to the steady-state line. Therefore steady state of sands is briefly reviewed. The phase transformation state is also discussed. The reader may choose to skip this section if already familiar with critical state soil mechanics concepts.

2.2.1 *Steady state of sands*

The steady state of sands is the state in which the soil continually deforms at constant void ratio, constant effective minor principal stress (σ'_3), and constant shear stress (Castro and Poulos, 1977). The steady state has traditionally been measured using

undrained tests on loose sand samples (Been et al., 1991). For undrained conditions, the state of stress of sand at a steady state deformation is determined uniquely by the void ratio (Ishihara, 1996), and by the final effective confining pressure, which is inherent to the void ratio. Thus it becomes possible to plot the confining stress at the steady state versus the void ratio of sand and to draw a line, which is generally referred to as steady-state line, SSL (Ishihara, 1996). The steady-state line (SSL) represents the locus of steady state points in the void ratio/stress space, as shown in Figure 2.1. Poulos et al. (1985) observed that the slope of the steady-state line (SSL) on a semilog plot is affected chiefly by the shape of the grains, while the vertical position of SSL is affected by even small differences in grain size distribution. Everything else being equal, a more angular sand will have a steeper SSL, as shown in Figure 2.2.

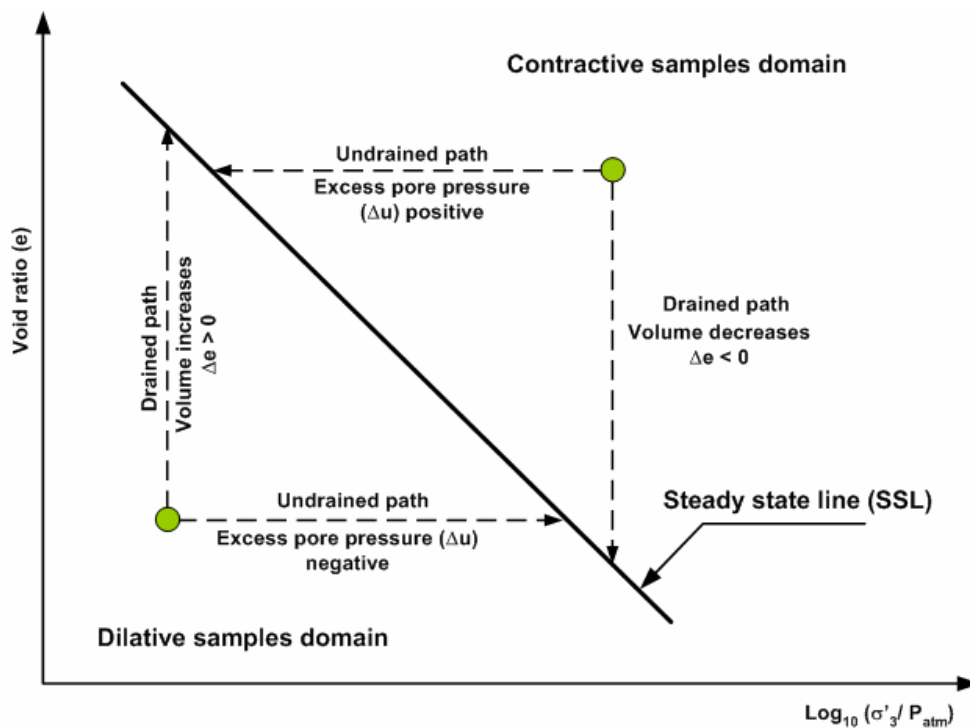


Figure 2.1. Diagram of the steady-state line.

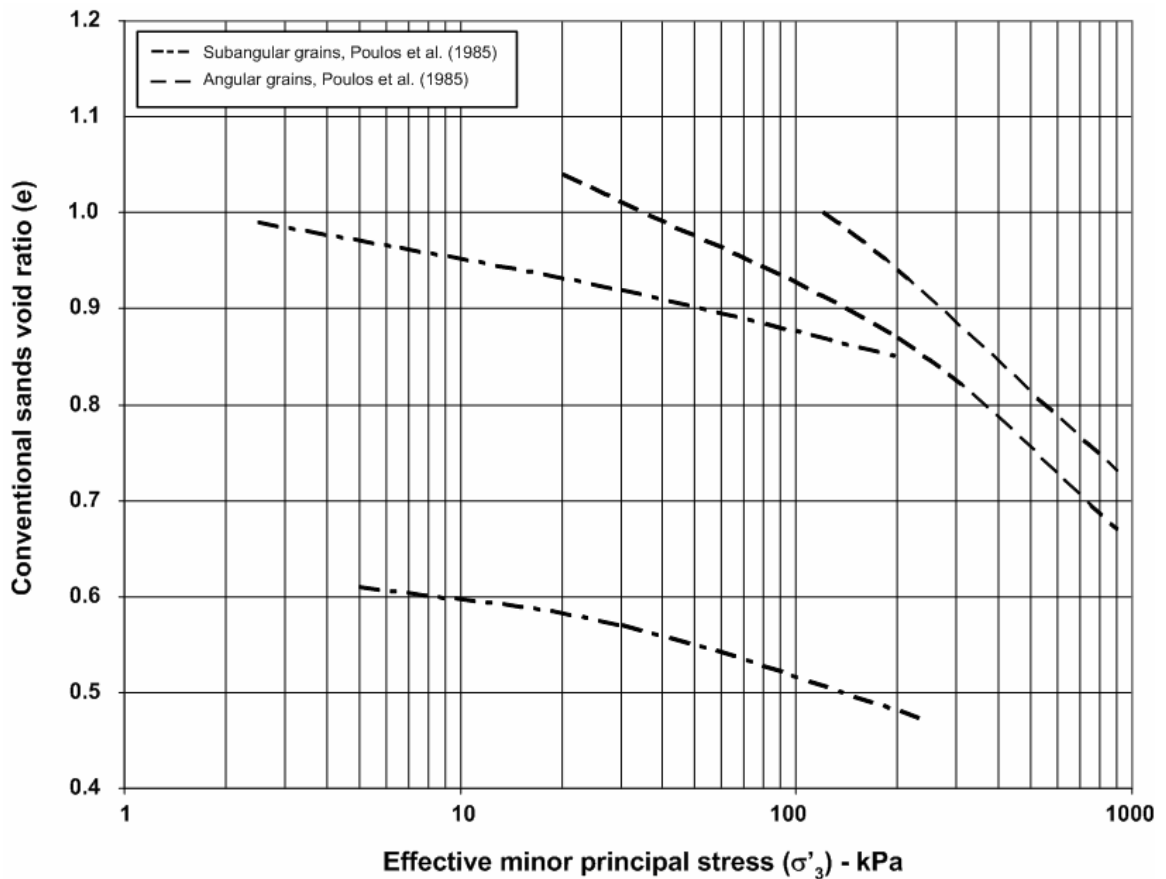


Figure 2.2. Steady-state line for non-calcareous sands (After Poulos et al., 1985).

Sand samples with an initial state above the SSL are referred to as *contractive* sands. Sands above the SSL will move towards this line by the generation of positive pore pressures during undrained shearing or decrease void ratio during drained shearing. Sand samples with an initial state below the SSL are referred to as *dilative* sands. During undrained loading sands will move towards the SSL by generation of negative pore pressures. During drained shearing they will dilate or increase void ratio. Poulos et al. (1985) affirmed that only contractive soils can suffer the necessary loss of shear strength to result in liquefaction.

From the above brief discussion, it is evident that determination of the state of sand samples with respect to the steady-state line (SSL) of the sand is important to define its behavior, especially for geotechnical problems involving dynamic loading and liquefaction.

2.2.2 State of phase of tranformation

The state of phase transformation is important when studying undrained behavior of sands. It refers to the transient state of a sand at which the behavior changes from contractive to dilative (Ishihara, 1996). In other words, at this point the pore pressures begin to decrease as the deviator stress increases. This is illustrated in the stress path diagram shown in Figure 2.3. The state of phase transformation is used to complement the steady-state line when characterizing the stress-strain behavior of sands.

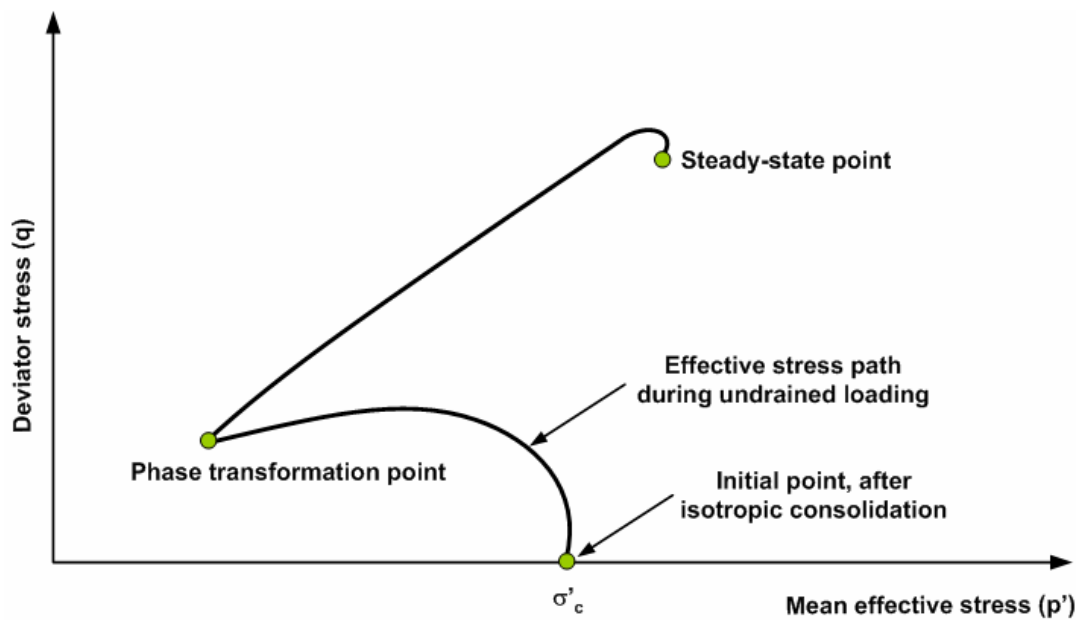


Figure 2.3. Diagram of the state of phase transformation.

2.3 Background

2.3.1 *Calcareous soils*

Calcareous soils may be grouped in two major categories based on their depositional environment: sedimentary and nonsedimentary (Chaney et al., 1982). Sedimentary calcareous soils are formed in marine environments from the skeletal remains of corals, shells of mollusks, and algae. These biogenic fragments cover a wide area of sea floor and coastal plains of tropical and subtropical regions of the world. They may also exist in continental ancient marine environments like the Alabama black-belt soils and Pierre shale North Dakota (Demars and Chaney, 1982).

Nonsedimentary calcareous soils are derived from a parent or source material rich in carbonates. This may be through weathering or from an influx of carbonate-rich aeolian dust or carbonates dissolved in rainwater (Demars and Chaney, 1982). Nonsedimentary calcareous soils are found throughout the arid and semi-arid parts of the world. Nonsedimentary calcareous particle sizes typically vary from silt-size powder to massive rocks, including cement nodules (Demars and Chaney, 1982).

Mineralogy: Mineralogy is the primary factor controlling the size, shape, physical and chemical properties of soil particles (Mitchell, 1993). Mineralogy of marine carbonate soils has been studied by many, e.g., Chaney et al. (1982), Morse and Mackenzie (1994), and Morelock and Ramirez (2004). According to Chaney et al. (1982), the distribution of carbonate materials in marine environments is highly variable.

The factors controlling the source, mineralogy and diagenesis of carbonates are different for shallow marine environments and for deep water environments (Morse and Mackenzie, 1994).

In shallow water environments, carbonate-rich sediments are generally dominated by aragonite (CaCO_3), followed by calcites rich in magnesium (CaCO_3). In deep water environments, according to Morse and Mackenzie (1994), the vast majority of the calcareous sediments are composed of calcite low in magnesium (i.e., $\text{CaCO}_3 >99\%$). Deep water sediments are primarily derived from skeletal organisms like coccolithophores and foraminifera.

Grain types: Marine carbonate grains can be broadly divided into two types: skeletal grains and non-skeletal grains (Morelock and Ramirez, 2004). Skeletal grains have a biochemical origin, and are formed as internal or external skeletal units of marine plants or animals. They are also referred to as biogenic grains. Non-skeletal grains are formed by a variety of physical and chemical processes such as biochemical precipitation, inorganic physio-chemical precipitation, erosion of pre-existing rocks and comminution through bioerosion.

Biogenic particles are the principal source of calcium carbonate (CaCO_3) content in marine deposits of carbonate sediments (Chaney et al. 1982). The most common skeletal grains are: crustose corallines, articulate corallines, molluscs as whole shells or fragments, forams, gastropods, algae, and echinoid fragments. Some non-skeletal grains found in

marine environments are: ooids, peloids, composite grains, and mud. A detailed description of skeletal and non-skeletal grains present in calcareous sands can be found in Morelock and Ramirez (2004).

Calcareous sands are composed of several types of grains. These grains may have unique features and characteristics in terms of shape, surface texture, intra-porosity, among others. These unique grain characteristics play an important role defining grain crushability and material compressibility (Golightly and Hyde, 1988).

Calcium carbonate content: The content of calcium carbonate (CaCO_3) in the calcareous sands will greatly depend on the mineralogy of the sand. For skeletal grains it will be determined by the marine organism from which the grains are derived (Morelock and Ramirez, 2004). Other factors such as surface water temperatures, presence of nutrients and water pressure at the depth of the sand deposit will also influence the content of calcium carbonate of sands (Chaney et al., 1982). Typical CaCO_3 contents ranging from 70% and 98% have been reported in the literature of calcareous soils.

2.3.2 Marine carbonate sediments in Puerto Rico

The geologic map sampling area is shown in Figure 2.4. This map includes geological information for the Puerto Real quadrangle, located at southwest Puerto Rico. According to this map, the sampling site area falls within beach deposits (Q_b) that belong to the Holocene age. Volckmann (1984) describes these beach deposits as typically

composed of sands and minor quantities of gravel, with rounded shell debris, volcanic rock, chert and locally quartz

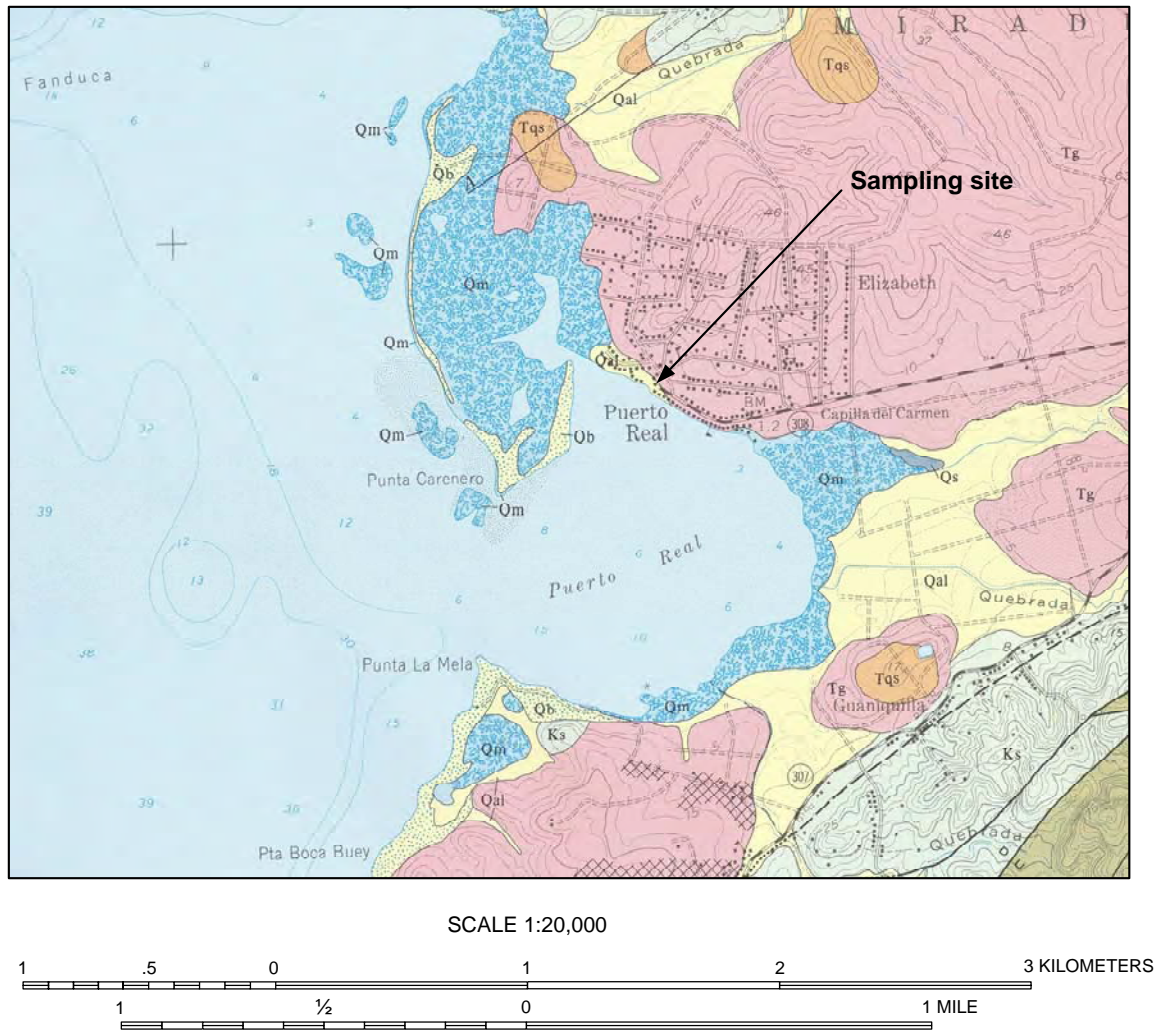


Figure 2.4. Geological map of the Puerto Real quadrangle (Volckmann, 1984).

Regarding the insular shelf of Puerto Rico, Scanlon et al. (1998) prepared a map of surficial sediments for Puerto Rico (Figure 2.5). Based on more than 2500 samples, the authors classified the sediments of the insular shelf of Puerto Rico into three major types: carbonate sediments with high calcium carbonates (more than 75% of CaCO_3);

terrigenous sediments with low calcium carbonate content (less than 25%); and mixed sediments with calcium carbonate content between 25% and 75%. This map shows the location where these three sediments types are located.

Scanlon et al. (1998) found that terrigenous sediment deposits are primarily found near the mouths of major rivers. Mixed sediments generally lie between areas of dominantly terrigenous and dominantly carbonate sediments. Carbonate sediments were found to be concentrated in areas where the shelf is sufficiently wide to extend beyond the direct influence of sediment input from rivers.

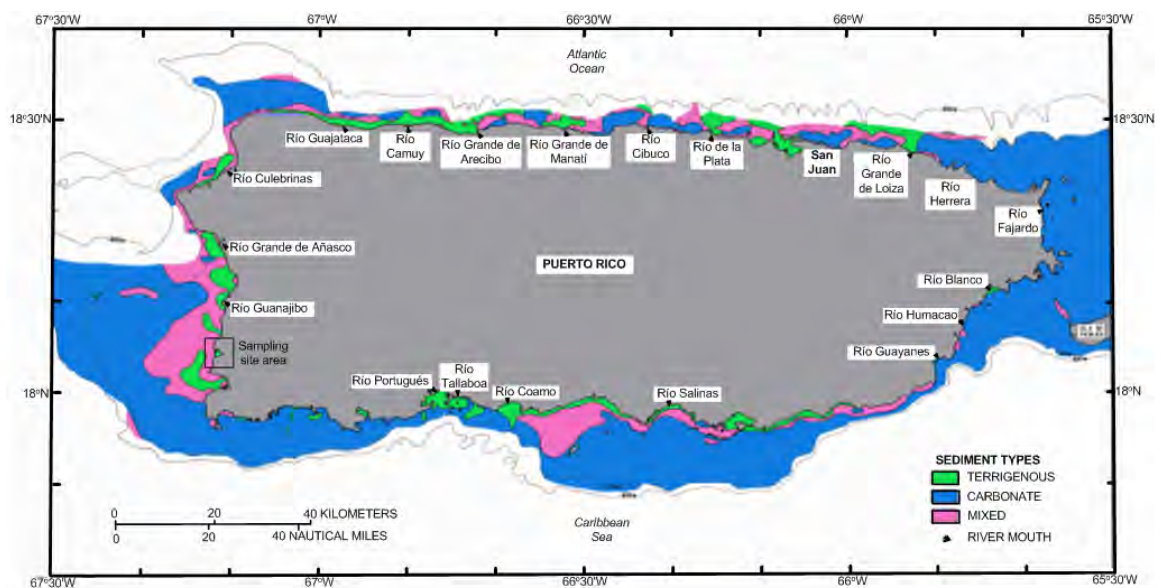


Figure 2.5. Surficial sediments of the insular shelf of Puerto Rico (Scanlon et al., 1998).

Although Figure 2.5 shows deposits of mixed and terrigenous sediments in the area where the sands of this study were obtained, the sampling site actually exhibited a high-

carbonate marine environment. The carbonate nature of the Cabo Rojo sands used in this study was confirmed in the mineralogical characterization described in Chapter 3.

2.4 Literature Review

The geotechnical research of calcareous soils has increased over the last few years due to the increased offshore activity in areas of the world consisting of carbonate sediments. Published research on calcareous soils generally recognizes that these soils warrant special consideration due to their unique characteristics (Allman and Poulos, 1988). The literature review that follows deals with the main findings published on the geotechnical behavior of calcareous sands on a non-cemented state, which are the subject of this research. The review will be presented in terms of the following topics:

- Index properties
- Particle crushing
- Static stress-strain behavior
- Dynamic properties

2.4.1 *Index properties of calcareous sands*

Calcareous sands present higher specific gravities and void ratios than quartz silica sand (Morioka, 1999). The higher specific gravity values are due to their mineralogy composition which usually includes minerals such as calcite (specific gravity, G_s of 2.75) and aragonite ($G_s = 2.95$) (Hurlbut, 1971). Siliceous minerals, on the other hand, are less

heavy, since they typically include quartz which is a mineral with a specific gravity value of 2.65.

Another important difference between calcareous sands and silica sands is related to their void ratio values. The void ratio (e) of a soil mass is defined as the volume of its voids at a given density or compaction state, divided by the volume of its solids; i.e., volume occupied by the minerals of the soil grains. Void ratios in sands typically range between 0.43 and 0.85 (Terzaghi et al., 1996). For calcareous sands the volume of voids can include an additional component related to their intra-particle porosity. This component can be large and is mainly related to calcareous sands with grains of biogenic nature. Therefore, void ratios of calcareous sands with large amounts of biogenic grains can be much higher than those of silica sands with similar skeletal arrangements.

Engineering properties of sands are often associated to the void ratio related to the voids of the skeleton structure of the sand. Since void ratio values of calcareous sands are the sum of two components (the regular void ratio related to the skeleton structure and the void ratio related to the grain voids), engineering behavior may be difficult to infer from total void ratio values. A more useful parameter may be relative density (D_r). Relative density relates the density of the soil structure to the “loosest” and “densest” states obtained using standardized procedures. Equation (2.1) is used to determine the relative density of soils (Terzaghi et al., 1996):

$$D_r = \frac{e_{\max} - e}{e_{\max} - e_{\min}} \times 100 \quad (2.1)$$

where e is the total void ratio of the soil; e_{\max} is the maximum void ratio of the soil at the “loosest” state; and e_{\min} is the minimum void ratio of soil at the “densest” state.

A listing of typical specific gravity and void ratio values for selected calcareous sands is presented in Table 2.1.

Table 2.1. Typical index properties of some calcareous sands.

Location	Country	CaCO ₃ (%)	G _s ⁽¹⁾	e _{max} ^(2,4)	e _{min} ^(3,4)	Reference
Kingfish B.	Australia	84	2.75	1.12	1.48	Morioka (1999)
Bass Strait	Australia	62-88	2.73	1.13	0.54	Hull et al., (1988)
North Ranking	Australia	91	2.77	1.87	1.15	Hull et al., (1988)
Bombay Mix	India	70-80	2.80	0.75	1.07	Golightly and Hyde (1988)
West Coast	India	>85	2.79 to 2.81	0.77	1.39	Morioka (1999)
Lakshdweep Island	India	>85	2.78	0.8	1.2	Morioka (1999)
Florida	USA	92	2.84	1.06	1.44	Morioka (1999)
Dry Tortugas, Florida	USA	93	2.71 to 2.86	1.0	1.6	Pizzimenti (1996)
Dogs Bay	Eire	85-95	2.75	0.98	1.83	Golightly and Hyde (1988)
Ballyconeely	Eire	90-95	2.72	1.62	1.98	Golightly and Hyde (1988)
Guam Island	Guam	90	2.8	1.12	1.36	Morioka (1999)
Waikiki Beach	Hawaii	>90	2.79	1.12	1.69	Morioka (1999)
Ewa Plains	Hawaii	98	2.72	0.66	1.30	Morioka (1999)

Notes: (1) G_s: Specific gravity,
 (2) e_{max}: Maximum void ratio
 (3) e_{min}: Minimum void ratio..
 (4) No mention was made whether void ratio values include both interparticle and intraparticle voids or only interparticle voids.

2.4.2 Crushing of calcareous sands

Susceptibility to crushing is a very important consideration for calcareous sands since it highly influences their shear strength and geotechnical behavior. For example, Datta et al. (1982) found that crushing significantly reduces the drained angle of shearing resistance. Crushability in calcareous sands may mask or inhibit any tendency to dilate during shearing of these soils, which leads to lower lateral stresses in the ground, and consequently result in a less stiff response (Hull et al., 1988). Sweet (1988) studied the bearing capacity of piles installed in calcareous sands, and determined that crushing can reduce the material stiffness by an order of magnitude, thus resulting in significantly reduced ultimate end bearing capacities.

Datta et al. (1982) found that the susceptibility to crushing is primarily related to the nature of the grains of calcareous sands. They determined that susceptibility to crushing increases with an increase in: (1) the amount of grains having large intraparticle voids; (2) the amount of thin-walled shell fragments; (3) the angularity of grains; (4) the coarseness of grains; and (5) the uniformity of its gradation.

2.4.3 Stress-strain behavior of calcareous sands

A summary of the most relevant studies involving stress-strain behavior of calcareous sands in an uncemented state is shown in Table 2.2.

Table 2.2. Summary of literature review on stress-strain behavior of calcareous sands.

Reference	Sand description Name, (location).	Mineralogy	Tests performed	Summary of findings
Golightly and Hyde, (1988)	▪ Leighton Buzzard	▪ Quartzitic sand. (0% CaCO ₃)	▪ Strain controlled drained (ICD) and undrained (ICU) compression triaxial tests. (Confining pressures: 5 to 1000 kPa).	<ul style="list-style-type: none"> ▪ Carbonate sands are much less stiff than the siliceous sand. ▪ Carbonate sands contract when sheared at relatively low confining pressures in (ICD). ▪ Dilatancy angles for the carbonate sands are much lower than for silica sands. ▪ Carbonate sands present early generation of high positive pore pressures in (ICU). ▪ Contractive behavior of carbonate sands would cause reduction in effective stress magnitudes around driven piles.
	▪ Dogs Bay (west coast of Eire)	▪ Molluscan carbonate sand. (85-95% CaCO ₃)		
	▪ Ballyconeely (west coast of Eire)	▪ Coralline algae carbonate sand. (90-95% CaCO ₃)		
	▪ Bombay Mix (west continental shelf of India)	▪ Marine siliceous carbonate sand. (70-80% CaCO ₃)		
Hull, Poulos and Alehossein, (1988)	▪ North Ranking (west coast of Australia)	▪ Calcareous sand. (91-94% CaCO ₃)	▪ Undrained (ICU) compression triaxial tests. (Confining pressures: 50 to 400 kPa).	<ul style="list-style-type: none"> ▪ Silica sand does not possess high friction angles but does have a reliable tendency to dilate, which helps to ensure high mean stress levels during failure and thus maintain stiffness and strength at large stress levels ▪ Naturally occurring calcareous sediments possess high peak friction angles but tend to suffer crushing of particles. This produces unreliable generation of lateral stresses in the ground and a less stiff response. ▪ Processed sands presented no dilation and significant particle crushing that ensures the mobilization of full strength at unacceptable large strains.
	▪ Barry's beach	▪ Calcareous sand. (89% CaCO ₃)		
	▪ Bass Strait	▪ Calcareous sand. (88% CaCO ₃)		
	▪ Sydney	▪ Silica sand.		
	▪ Processed sands (CSIRO)			
Hyodo, Hyde and Aramaki, (1998)	▪ Masado (Ube, Japan)	▪ Granite soil.	▪ Undrained monotonic compression and extension triaxial tests.	<p><i>Monotonic stress-strain behavior of Dogs Bay sand (Confining pressures: 100 to 500 kPa):</i></p> <ul style="list-style-type: none"> ▪ Very stiff response up to the phase transformation points, which occurred at low strains. ▪ Universal hardening behavior was observed up to strains in excess of 20% after the phase transformation points. ▪ The stress paths after phase transformation showed lessening of the degree of dilatant behavior.
	▪ Masado (Hiroshima, Japan)	▪ Granite soil.		
	▪ Shirasu (Kyushu, Japan)	▪ Volcanic soil.	▪ Cyclic undrained triaxial tests.	
	▪ Dogs Bay (west coast of Eire).	▪ Skeletal carbonate sand.		
	▪ Toyoura sand (Japan)	▪ Standard silica sand		

Table 2.2. (Continued).

Reference	Sand description Name, (location).	Mineralogy	Tests performed	Summary of findings
Morioka, (1999)	<ul style="list-style-type: none"> ▪ Ewa Plains sand (Oahu island, Hawaii). 	<ul style="list-style-type: none"> ▪ Carbonate sand (98% CaCO₃) 	<ul style="list-style-type: none"> ▪ Cone penetrometer testing on a calibration chamber. ▪ Static triaxial tests. ▪ Cyclic triaxial tests. 	<p><i>Uncemented calcareous sands:</i></p> <ul style="list-style-type: none"> ▪ Ewa Plain specimens generally showed significantly higher static strengths than Monterey Silica specimens. ▪ Ewa Plain samples required approximately 1.5 to 2 times axial deformation to achieve peak strength. ▪ Calcareous sand exhibited distinct fluctuations in the differential vertical stress as the specimens are loaded and typically strain in contraction at failure. ▪ Silica sands typically demonstrated less or no fluctuation and tend to dilate at failure. <p><i>Aged specimens:</i></p> <ul style="list-style-type: none"> ▪ Results do not indicate any static strength gain due to aging.
	<ul style="list-style-type: none"> ▪ Monterey Silica sand (California) <p>Artificial cementation of Ewa Plains sand was studied using 2% to 6% cement.</p>	<ul style="list-style-type: none"> ▪ Terrigenous silica sand 		
Allman and Poulos, (1988)	<ul style="list-style-type: none"> ▪ North Ranking (west coast of Australia). Non-cemented and cemented samples. <p>Cementation with Portland cement at 2%, 4% and 8%.</p>	<ul style="list-style-type: none"> ▪ Carbonate sand, predominantly of bioclastic and pelletal origin) 	<ul style="list-style-type: none"> ▪ Drained, isotropically consolidated (ICD) triaxial. (Low confining pressures: 100 to 500 kPa; High confining pressures: 100 to 6400 kPa). 	<p><i>Uncemented calcareous sands:</i></p> <ul style="list-style-type: none"> ▪ The monotonic response reflects a non-dilative nature. ▪ Compressive volumetric strains recorded, even at low confining pressure. ▪ Stress-axial strain response is non-linear and ductile, exhibiting a peak at very large axial strain. ▪

From this review it is possible to conclude that calcareous and silica sands behave differently when subjected to mechanical deformation. For instance, calcareous sands typically present a higher friction angle than silica sands with similar relative densities, however, they tend to exhibit a much less stiff response than silica sand, primarily due to particle crushing (Hull et al., 1988).

Three factors were reported in the literature as being the main causes for anomalous behavior of calcareous sands are: (1) the susceptibility of calcareous grains to crushing when stressed; (2) particle characteristics such as the variation in size and shape, and the presence of intraparticle voids; and (3) the cementation and fabric related to its carbonate materials.

Data presented by Golightly and Hyde (1988) and Hull et al. (1988) indicates that calcareous sands in general exhibit a contractive behavior during monotonic triaxial loading for confining pressures ranging between 5 kPa and 1000 kPa. For the same levels of confining pressures, the authors found that silica sand exhibits dilative behavior. Contractive behavior of calcareous sands results in lower mean stress levels, thus decreasing stiffness (Hull et al., 1988). The contractive behavior exhibited by calcareous sand was revealed in the compressive volumetric strains obtained during drained triaxial tests and in the early generation of high positive pore pressures in undrained triaxial tests. However, Hyodo et al. (1998) found that for low confining pressures (100 kPa to 500 kPa), calcareous sands can present an initial dilative behavior. For increased confining

pressures, the initial dilative behavior was less pronounced. The contractive behavior exhibited by uncemented calcareous sands during monotonic loading resulted in a ductile stress-strain response with peak strengths achieved at large axial strains.

Hull et al. (1988) found that grain size distribution affects the stress-strain response of calcareous sands, mainly due to the higher susceptibility to crushing of sands with uniform gradations. For a constant confining pressure, the stress-strain response of a uniform sample presented a markedly more ductile response, with mobilization of full strength at very large strains (30%). This was not the case for a well-graded calcareous sand (Bass Strait sand), which exhibited a more brittle response, with a peak deviator stress at about 8% of axial strain, and with strain softening after peaking.

Another important factor that greatly influences the stress-strain behavior of calcareous sands is the occurrence of inter-particle cementation. Allman and Poulos (1988), and Airey (1993), determined that cementation in calcareous sands changes their stress-strain response from ductile (uncemented) to brittle, with initial near-linear stress-strain behavior followed by a peak and then strain softening to a residual strength. Saxena and Lastrico (1978), and Allman and Poulos (1988), reported a near-linear response up to axial strains near 1%. At these low strain levels, the cohesion caused by particle bonding is the major strength contributor (Saxena and Lastrico, 1978). For greater strain levels they found that the cementation bond is destroyed and the strength of calcareous sands becomes predominantly frictional in nature.

2.4.4 Dynamic properties of calcareous sands

Lo Presti et al. (1993) studied the monotonic and cyclic loading behavior at small strains of Quiou calcareous sands and Ticino silica sand. Their testing program included resonant column tests, torsional shear tests, and static monotonic loading torsional tests. The influence of confining pressure, shear strain levels and type of loading on the shear modulus were analyzed. They found that at the same confining stress, the Ticino silica sand exhibited small-strain shear modulus values (G_{\max}) higher than those for the Quiou calcareous sand. For instance, at 100 kPa of confining pressure, G_{\max} values for Ticino silica sand ranged between 81 and 118 MPa, while Quiou calcareous sand exhibited G_{\max} values ranged between 47 and 85 MPa. The elastic threshold shearing strains for both sands were less than about 0.001%. The volumetric threshold shearing strain for Quiou calcareous sand ranged between 0.08% and 0.016%. The shear moduli obtained from the cyclic tests were 20% greater than those from the static monotonic loading tests, for Quiou calcareous sands. They concluded that this difference is due to the sand crushability caused by the load repetition in cyclic tests. This behavior was not observed for Ticino silica sand.

Fioravante et al. (1994) studied the mechanical behavior of uncemented carbonate Quiou sand. The testing program included resonant column tests, torsional shear tests, and triaxial compression tests. They reported two main findings for the dynamic properties of calcareous Quiou sand: (a) experimental data showed the influence of stress

history (i.e., overconsolidation ratio, OCR) on the shear deformational behavior of Quiou sand at very small strains; and (b) the number of interparticle contacts affects the stiffness of calcareous sands. The increase of interparticle contacts was caused by the crushing of particles and their re-arrangement.

Valle et al. (2003) made a comparative study of the influence of cementation in the dynamic properties of the Hickory silica sand and the dynamic properties of the Campeche Bay non-cemented calcareous sand, using the resonant column test. They reported greater small-strain shear moduli for uncemented silica sand than for uncemented calcareous sands at comparable confining pressures. As cementation increased, cemented silica sands presented greater elastic threshold shearing strains (about 0.001%) than uncemented sands (between 0.001% and 0.002%).

Fioravante et. al. (1994) and Valle et el. (2003) provided empirical correlations for estimating the small strain shear modulus (G_{\max}) for calcareous sands. These correlations are shown in Table 2.3. Examination of these empirical relationships indicates that G_{\max} is primarily controlled by confining pressure and density of the sample. The density state of the samples is included in the function $F(e)$.

Table 2.3. Empirical formulations for G_{\max} prediction of calcareous sands.

Type of sand (location)	Empirical relationship for G_{\max}	Constant	Exponent
Quiou calcareous sand: Fioravante et al. (1994)	$G_{\max} = C_g F(e) p_r^{(1-n)} p_r^{(n)} OCR^{(k)}$ $F(e) = \frac{(b-e)^2}{(1+e)}, \text{ where } b = 3.6$	C_g : 116 (non- dimensional)	n: 0.592 k: 0.29
Campeche Bay (México) Valle et al. (2003)	$G_{\max} = \frac{A_G}{F(e)} \left(\frac{\sigma'_0}{P_a} \right)^{n_G}$ $F(e) = 0.3 + 0.7e^2$	Calcareous uncemented sand: A_G : 64-70 kPa	Calcareous uncemented sand: n_G : 0.49-0.50

Notes: C_g : Non-dimensional material constant; e : Void ratio; p_r : Reference pressure = 1 MPa; p_r' : Confining pressure (kPa); n , k : Interpolation constant; OCR: Overconsolidation ratio. A_G : Shear modulus at 100 kPa; σ'_0 : Effective confining pressure; P_a : Atmospheric pressure, in the same units of the effective confining pressure; n_G : Dimensionless exponent.

2.5 Summary

Research on the stress-strain behavior and dynamic properties of calcareous sands indicated that the most relevant factors influencing the behavior of uncemented calcareous sands are:

- Mineralogy
- Particle crushing susceptibility
- Grain characteristics (shape, intraparticle voids, texture, among others)

Therefore, characterization of these factors will be necessary to adequately study the geotechnical behavior of the Cabo Rojo calcareous sand, which is the subject of this work.

Another finding from the literature review is that few studies included steady state considerations when defining the state of their sands. Definitions of the steady-state line

for the Cabo Rojo calcareous sand will help define the state of the sand samples and distinguish from contractive or dilative response.

3 LABORATORY TESTING PROGRAM

3.1 Introduction

This chapter presents a description and details of the laboratory testing program performed for this research. First the soils tested are described, including a summary of their index and strength properties. Next, a description of the Isotropic Consolidated Undrained (ICU) monotonic triaxial testing equipment used for determination of the stress-strain behavior and steady state parameters is presented. And finally, the chapter presents a description of the resonant column testing device used for determination of the soil dynamic properties. These descriptions include details pertaining to test methodology and specimen preparation. The procedures followed for the calibration of transducers and measuring devices of the equipments used are included in Appendix 6.

3.2 Soils Tested

The main focus of this research was to study the soil behavior of a calcareous sand from southwest Puerto Rico. The experimental program also included tests on a quartz silica sand with a grain size distribution similar to the one of the calcareous test sand. The silica sand was included in several phases of the test program in an attempt to compare the influence of grain characteristics such as particle shape, texture and mineralogy in the observed behavior of sands. Both sands have notable differences in

particle shape, texture, and mineralogy, but the influence of grain size distribution was minimized by ensuring similar gradations.

The tested calcareous sand was obtained right from Puerto Real beach, in Cabo Rojo, Puerto Rico. Figure 3.1 shows the general location of the sampling site. The geographic coordinates of this sampling location recorded with a portable GPS were $18^{\circ}05'34''\text{N}$, $67^{\circ}11'45''\text{W}$.

This sampling site was selected because it exhibits a high-carbonate marine environment. The sand samples were retrieved from the near surface using a shovel. The sand collected at this site was in an uncemented state as shown in Figure 3.2.

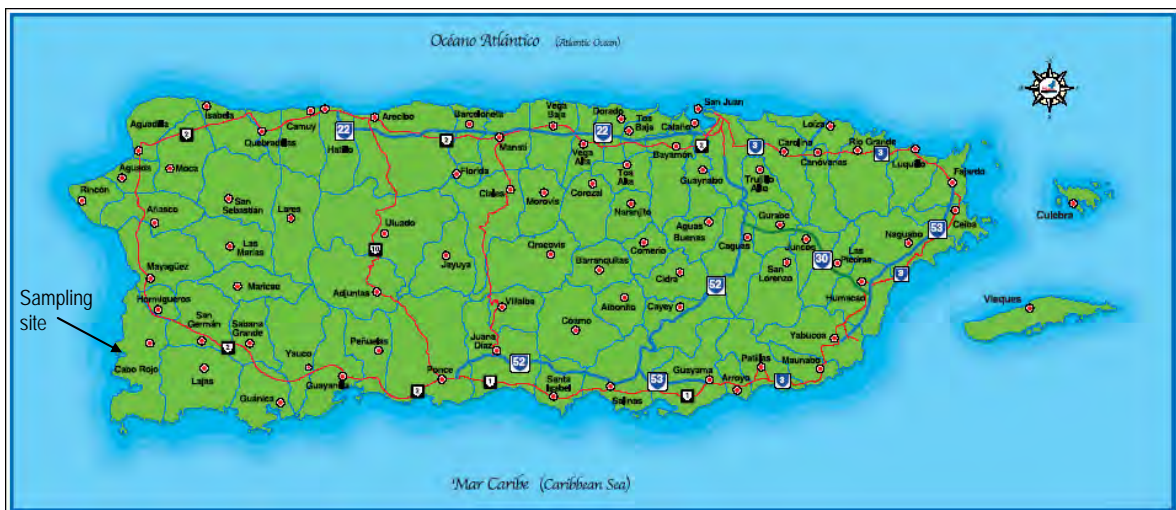


Figure 3.1. General location of the calcareous sand samples source (Metrodata Inc., 2002).



Figure 3.2. Photo of the source site for the tested calcareous sands.

The silica sand chosen for comparison purposes was a regular silica sand obtained from the Transit-Mix plant in South Bend, Indiana. This sand was selected for convenience since the resonant column component of the testing program was carried out at the University of Notre Dame in South Bend, IN.

Information for both test sands regarding soil description, mineralogy, shear strength and crushability are presented in the following subsections.

3.2.1 General description of the test sand

As previously mentioned, two different sands were used in the experimental program of this work:

1. Cabo Rojo calcareous sand: Fine to medium calcareous sand, poorly graded, with subangular to angular grains and light tan to yellow color.

2. South Bend silica sand: Fine to medium silica sand, poorly graded, with subrounded to subangular grains and light brown color.

The main index properties of these two sand types are listed in Table 3.1. Their grain size distribution is presented in Figure 3.3.

Samples for the Cabo Rojo calcareous sand were retrieved on three different dates throughout this research. Gradations results for the different dates showed small variations. To ensure repeatability and uniformity, all calcareous sand samples were adjusted to have the grain size distribution shown in Figure 3.3.

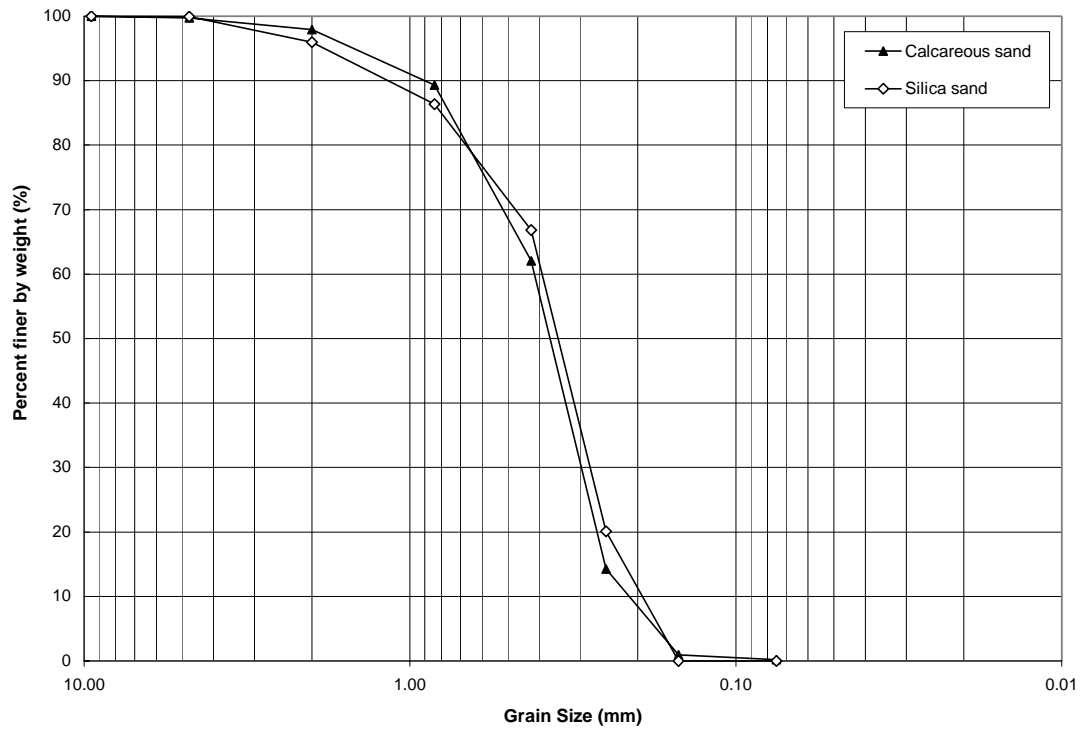
These small gradation variations are expected from a natural beach deposit. Therefore the property values reported in Table 3.1 are average values resulting from the chosen sand gradation shown in Figure 3.3.

The gradation curves of Figure 3.3 confirm that both sands present a fairly uniform gradation, with grain sizes ranging from 0.2 mm to 2 mm, and with no fines; i.e. no sizes less than 0.075 mm. Both soils classified as poorly graded sand (SP) according to the Unified Soil Classification System (ASTM D2488-00).

Table 3.1. Index properties of sands used in this study.

Parameter	Calcareous sand	Silica sand	Standard
D ₁₀ (mm)	0.20	0.20	ASTM D422-63 (2002)
D ₃₀ (mm)	0.30	0.29	
D ₅₀ (mm)	0.38	0.36	
D ₆₀ (mm)	0.42	0.40	
C _u	1.05	1.03	
C _c	2.08	2.00	
G _s	2.86	2.70	ASTM D5550-00
e _{max}	1.71 ⁽²⁾	0.74	ASTM D4254-00
γ _{min} (kN/m ³)	10.5 ⁽²⁾	15.2	
e _{min}	1.34 ⁽²⁾	0.50	Alternative method ¹
γ _{max} (kN/m ³)	12.1 ⁽²⁾	17.6	

Note: (1) Description described in Appendix 2.
(2) Average value.

**Figure 3.3. Grain size distribution curves for calcareous sand and silica sand.**

3.2.2 Grain characterization using SEM microscopy

To further evaluate the test sands, a series of micrographs were taken using a Scanning Electron Microscope (SEM). SEM pictures were initially taken at the Environmental Molecular Science Institute of the University of Notre Dame. A second set of micrographs was taken at the Microscopy Center of the University of Puerto Rico at Mayagüez, using a gold coating in order to reduce charging. The magnification factor used ranged from $15\times$ to $1500\times$. The scanning electron microscope used at the University of Notre Dame was a LEO EVO-50XVP scanning electron microscope with variable pressure/high humidity. At the University of Puerto Rico at Mayagüez the SEM device used was a GEOL JSM-5410-LV.

SEM sample preparation consisted of carefully mounting a small amount of sand that was carefully adhered to a double side carbon tape, which was attached to an aluminum sample stub. A compressed air gun was used to remove those particles that were not securely adhered to the tape. No epoxy or glue was used to adhere the sand grains to the stub. For tests carried out at University of Puerto Rico at Mayagüez specimens were sputter coated with gold.

Examination of the Cabo Rojo calcareous sand images from scanning electron microscope revealed that its grains are subangular to angular (ASTM D2488-00), with length to width ratios ranging from 1.29 to 2.20, as shown in Figure 3.4a. The South

Bend silica sand was found to have predominantly subangular grains with length to width ratios ranging from 1.06 to 1.81, as shown in Figure 3.4b.

Figures 3.5 and 3.6 illustrate in more detail the grain characteristics of both sands. A non-skeletal calcareous sand grain is shown in Figure 3.5a, where the rough texture and intraparticle porosity can be appreciated. Figure 3.5b shows a silica sand grain that exhibits predominantly even surfaces with occasional textural changes. Some biogenic particles commonly found in this calcareous sand are shown in Figure 3.6. It is expected that these unique grain features are likely to make the calcareous sand more susceptible to particle crushing and compressibility as compared to a quartz silica sand. More details regarding grain characterization are provided in Appendix 1.

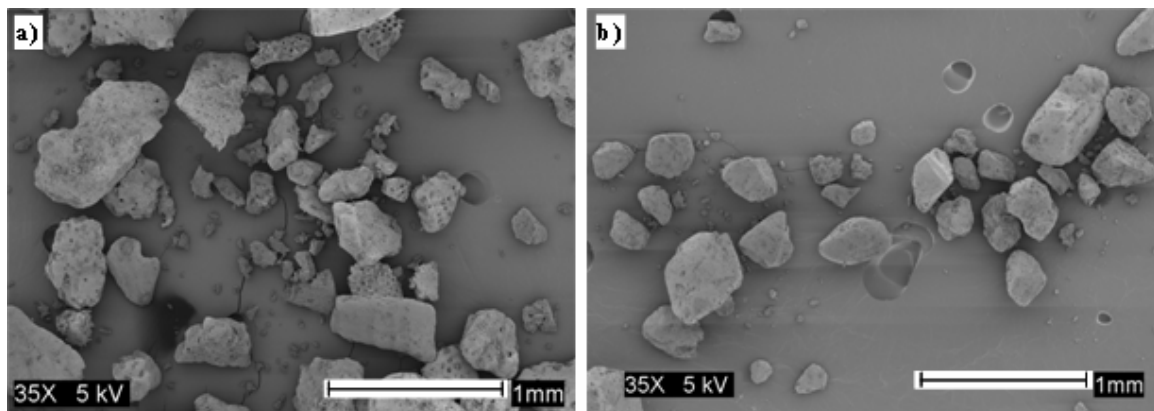


Figure 3.4. Microscopy view of the sands used for the experimental program. a) Cabo Rojo calcareous sand, b) South Bend silica sand.

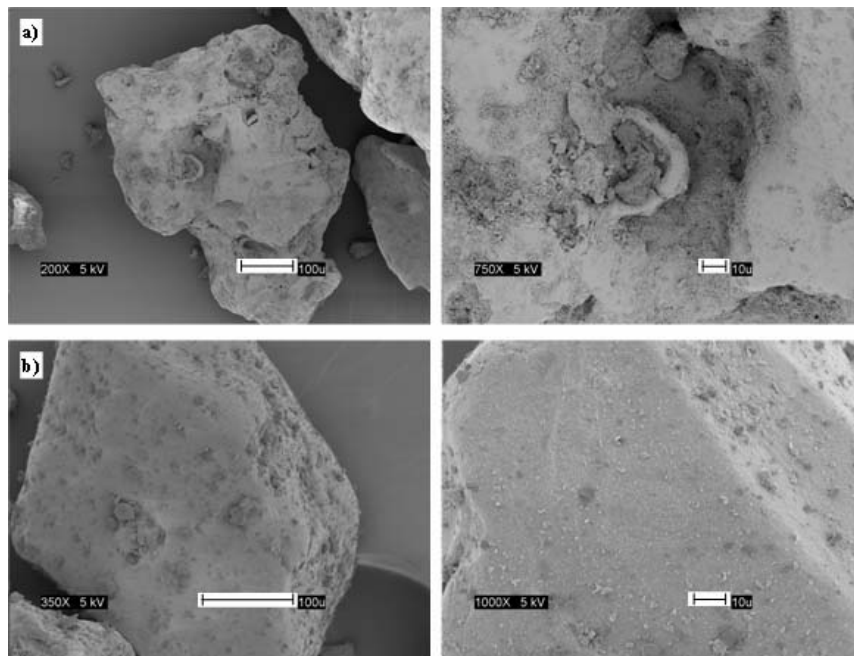


Figure 3.5. Comparison of grain surface texture for a) Cabo Rojo sand, b) South Bend sand.

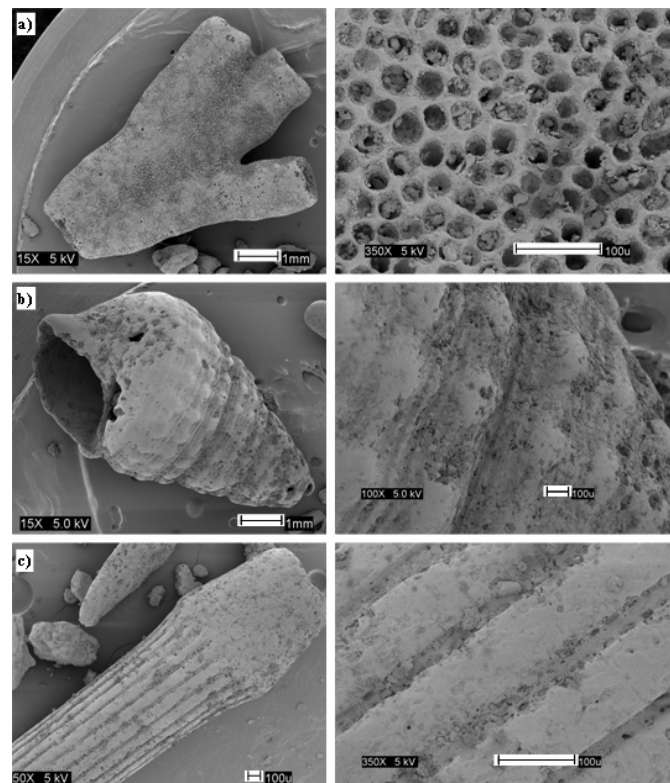


Figure 3.6. Biogenic grains found in the Cabo Rojo sand: a) *Millipora* sp. (aragonitic hydrozoan), b) calcite-aragonite gastropod, c) Urchine spine (high-magnesian calcite).

3.2.3 Mineralogy

The mineralogy of the test sands was evaluated using two different methods: x-ray diffraction and thermogravimetric analyses.

X-ray diffraction analyses: A qualitative mineralogical characterization of both test sands was done using X-ray diffraction (XRD) analyses. The analyses were carried out using an x-ray diffractometer model SIEMENS D5000, belonging to the Earth X-ray Analysis Center (EXACt) of the Geology department of the University of Puerto Rico at Mayagüez. The analyses were carried out in accordance with the test procedure given in ASTM Standard D934-80 (2003).

The XRD diffractogram obtained for the Cabo Rojo sand is shown in Figure 3.7. As expected, this diffractogram revealed a predominance of carbonate minerals. The two main carbonate minerals encountered were aragonite and magnesian calcite. A small amount of quartz was also detected.

The diffractogram obtained for the South Bend sand is shown in Figure 3.8. This diffractogram clearly showed that quartz (SiO_2) is the predominant mineral for this sand, which belongs to the silicates mineral class.

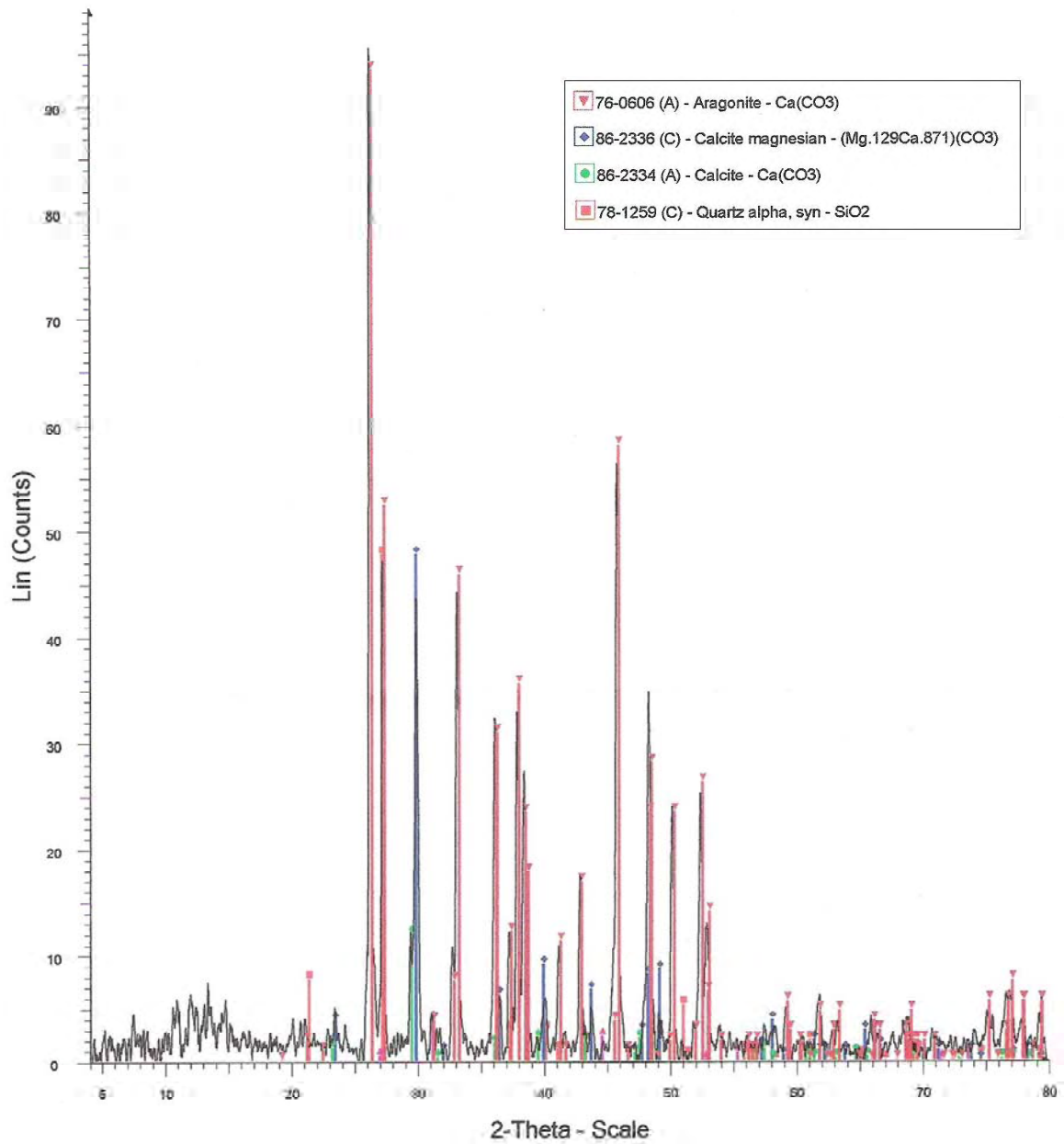


Figure 3.7. Diffractogram for the Cabo Rojo calcareous sand.

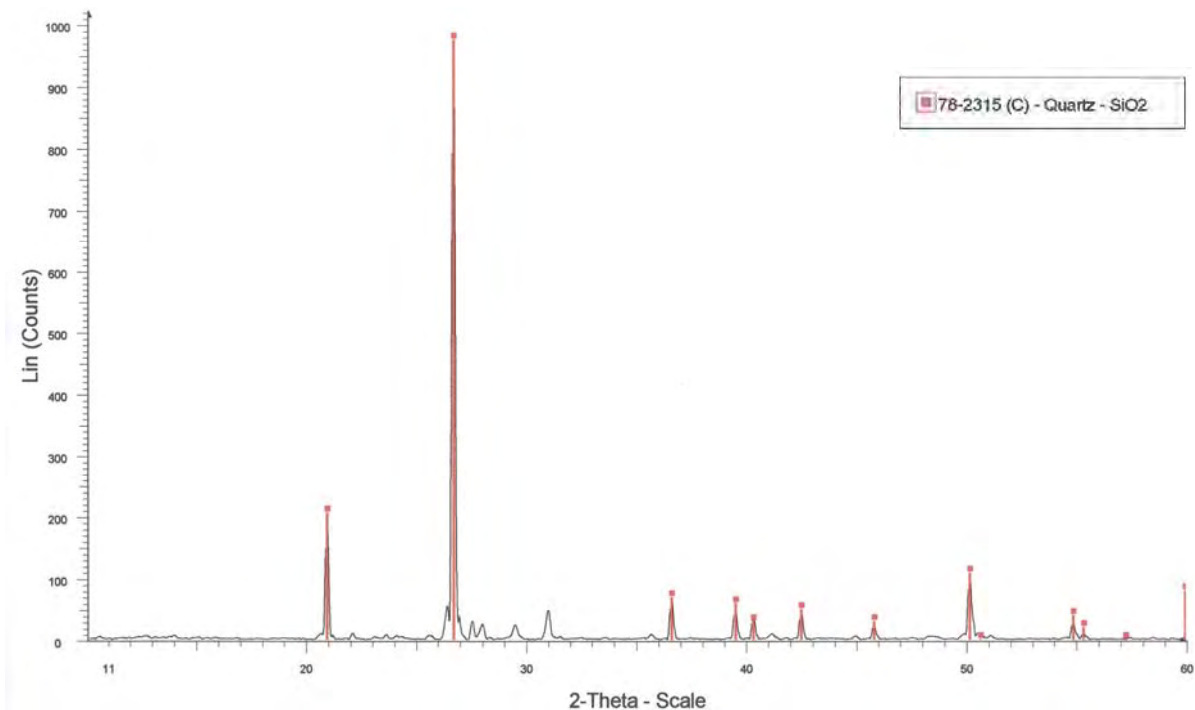


Figure 3.8. Diffractogram for the South Bend silica sand.

Thermogravimetric analyses: Thermogravimetric analyses (TGA) were carried out to quantitatively determine the amount of calcium carbonate (CaCO_3) present in both test sands. The determination is based on the loss of mass that is expected to occur in a soil sample with calcium carbonate content when subjected to temperatures up to around 950°C . Todor (1976) indicates that calcium carbonate (CaCO_3) loses carbon dioxide (CO_2) at about 675°C and reaches complete outgassing at about 950°C . This can be represented in the following chemical reaction that occurs in calcium carbonate when heated to these temperatures:



Based on this observation, the amount of calcium carbonate present in the sand specimens can be determined using a thermal analyzer system, which gradually heats the sand from ambient temperature to 950°C. During this process the mass of the specimen is continuously tracked. TGA analyses were carried out using the thermal analyzer system model NETZSCH TG209 of the Characterization Laboratory of the University of Notre Dame. TGA results are summarized in Table 3.2. TGA analyses confirmed the predominance of the calcareous minerals in the Cabo Rojo test sand, with calcium carbonate contents ranging between 91% and 97%. In contrast, only 11% of calcium carbonate was measured for the South Bend silica sand. More details regarding the TGA analyses are provided in Appendix 2.

Table 3.2. Calcium carbonate content of the test sands from TGA analysis.

SAND	Specimen	Initial mass [mg]	Mass loss [mg]	CaCO ₃ content
Cabo Rojo Sand	CR-001	79.15	31.78	91.3%
	CR-002	246.72	33.90	97.3%
	CR-003	76.52	30.64	91.1%
	CR-004	88.45	35.56	91.4%
South Bend	SB-001	94.13	4.37	10.6%

3.2.4 Shear strength

Estimation of the shear strength parameters (internal friction angle) for both test sands were made using conventional direct shear tests and isotropically consolidated undrained triaxial (ICU) tests. Internal friction angles were determined for a range of relative

densities. A summary of the main results is presented below. Additional detailed results are presented in Appendixes 3 and 4, for the direct shear and ICU tests, respectively.

Direct shear test results: Direct shear tests were performed to determine the internal friction angles for the Cabo Rojo (calcareous) and South Bend (silica) sands. Displacement controlled direct shear tests with a 63.5 mm square shear box were performed. All tests were carried out at a horizontal displacement rate of 2 mm/min and in accordance with ASTM standard D3080-03. Specimens were prepared using air pluviation of dry sand which was carefully poured through a funnel. Higher densities were achieved by means of a small tamping device. The direct shear device used is shown in Figure 3.9.



Figure 3.9. Direct shear test device at the University of Puerto Rico at Mayagüez.

The results of direct shear tests are summarized in Tables 3.3 and 3.4. As indicated in these tables, direct shear tests were carried out with normal stresses ranging from 50 to 500 kPa. The shearing area of the soil specimens decreases during direct shearing testing. Therefore, normal stresses experienced small variations throughout the test.

Table 3.3. Summary of direct shear test results on Cabo Rojo calcareous sand.

D_{r_cons}	σ'_{n_ini} kPa	τ_p kPa	d_p mm	τ_{cv} kPa	d_{cv} mm	ϕ'_p deg.	ϕ'_{cv} deg.
57%	50	33.79	2.64	31.93	7.68	37.0	35.3
54%	200	156.50	3.68	140.60	7.40		
60%	300	243.04	5.61	238.70	7.41		
68%	500	427.42	6.90	415.84	8.19		
89%	50	48.22	1.45	36.64	8.96	41.3	36.7
103%	100	97.34	1.60	63.91	7.29		
104%	300	277.36	3.65	248.57	7.54		
90%	500	481.30	5.54	442.77	9.01		

Notes: D_{r_cons} : Relative density after consolidation, σ'_{n_ini} : Normal pressure at the beginning of test, τ_p : Peak shear stress, d_p : Horizontal displacement at peak, τ_{cv} : Constant volume shear stress, d_{cv} : Horizontal displacement at residual, ϕ'_{peak} : Peak friction angle, ϕ'_{cv} : Residual (nearly constant volume) friction angle.

Table 3.4. Summary of direct shear test results on South Bend silica sand.

D_{r_cons}	σ'_{n_ini} kPa	τ_p kPa	d_p mm	τ_{cv} kPa	d_{cv} mm	ϕ'_p deg.	ϕ'_{cv} deg.
53%	50	34.01	1.98	30.08	5.24	32.2	30.4
53%	300	191.29	3.11	186.76	4.55		
58%	500	340.46	3.99	331.21	7.01		

Notes: D_{r_cons} : Relative density after consolidation, σ'_{n_ini} : Normal pressure at the beginning of test, τ_p : Peak shear stress, d_p : Horizontal displacement at peak, τ_{cv} : Constant volume shear stress, d_{cv} : Horizontal displacement at residual, ϕ'_{peak} : Peak friction angle, ϕ'_{cv} : Residual (nearly constant volume) friction angle.

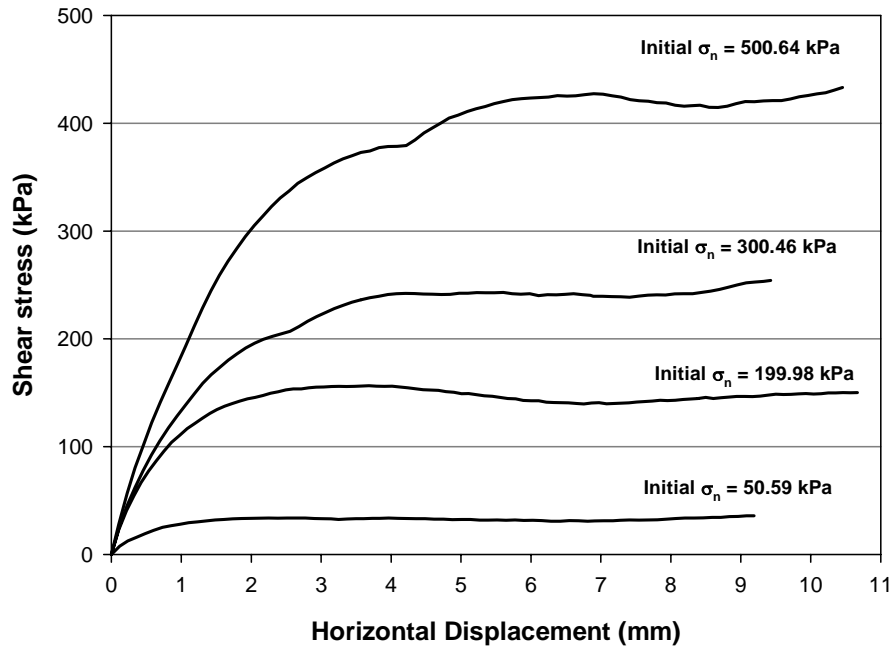
Relative densities (D_{r_cons}) in Tables 3.3 and 3.4 refer to the relative densities of the specimen after consolidation. This parameter was found useful for comparing the behavior of the two test sands, given the large differences of void ratios that were achieved while preparing the specimens (see Table 3.1). The large difference in void

ratios is primarily due to the intraparticle voids present in the calcareous sand grains. Hence, the void ratios for calcareous sands are actually the sum of the void ratio of the skeleton structure (conventional void ratio) and the void ratio corresponding to the void spaces inside the grains. The differences in void ratios due to the intraparticle void spaces can be significant. The use of relative density allows the comparison of “skeletal” void ratios, or densities, between two different soils given its relationship to the two extreme grain packing arrangements; i.e. the densest state or e_{\min} , and the loosest state or e_{\max} . The specimen relative densities were calculated as follows (Terzaghi et al., 1996):

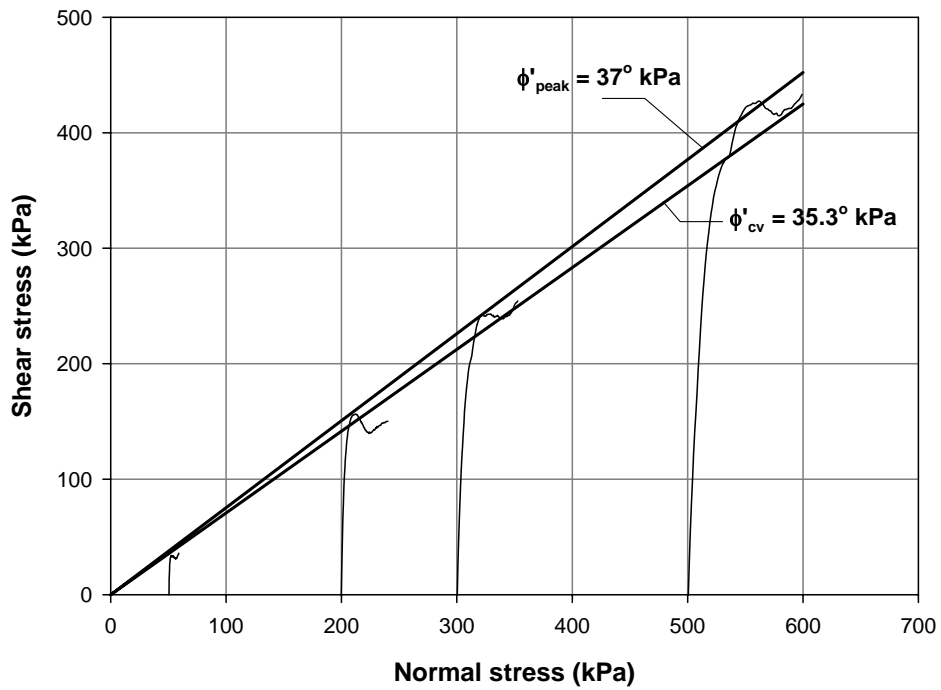
$$D_r = \frac{e_{\max} - e}{e_{\max} - e_{\min}} \times 100 \quad (3.2)$$

where e is the total void ratio of the specimen in the direct shear tests, and e_{\max} and e_{\min} are the maximum and minimum void ratio for each test sand (values given in Table 3.1). Relative densities vary throughout the direct shear test due to compression and dilation process that occur during shearing.

Direct shear test results, in terms of shear stress versus horizontal displacement curves, and in terms of peak shear strength envelopes are presented in Figures 3.10 through 3.12 for the medium dense calcareous sand, the dense calcareous sand, and the silica sand respectively. Additional details of the direct shear tests performed during this investigation are presented in Appendix 3.

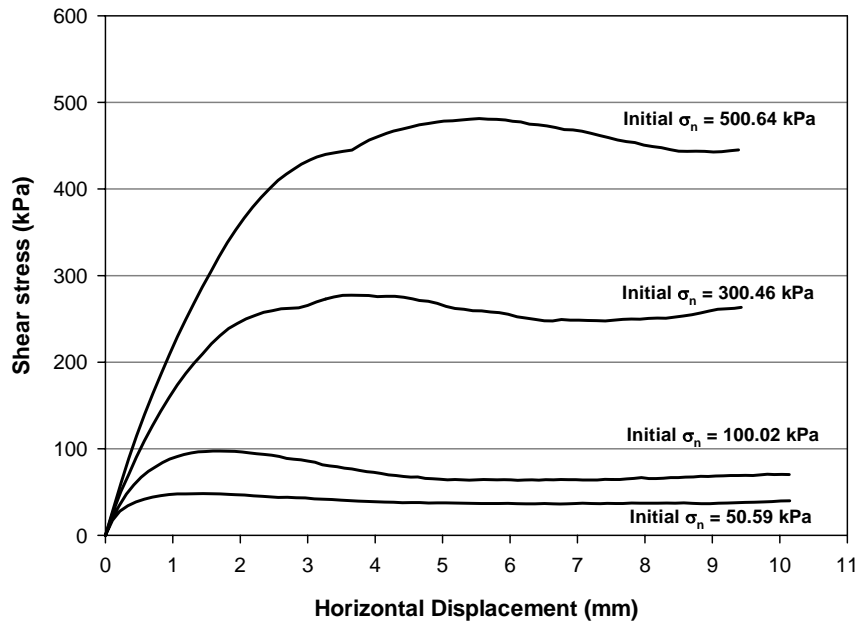


a) Shear stress - displacement curves

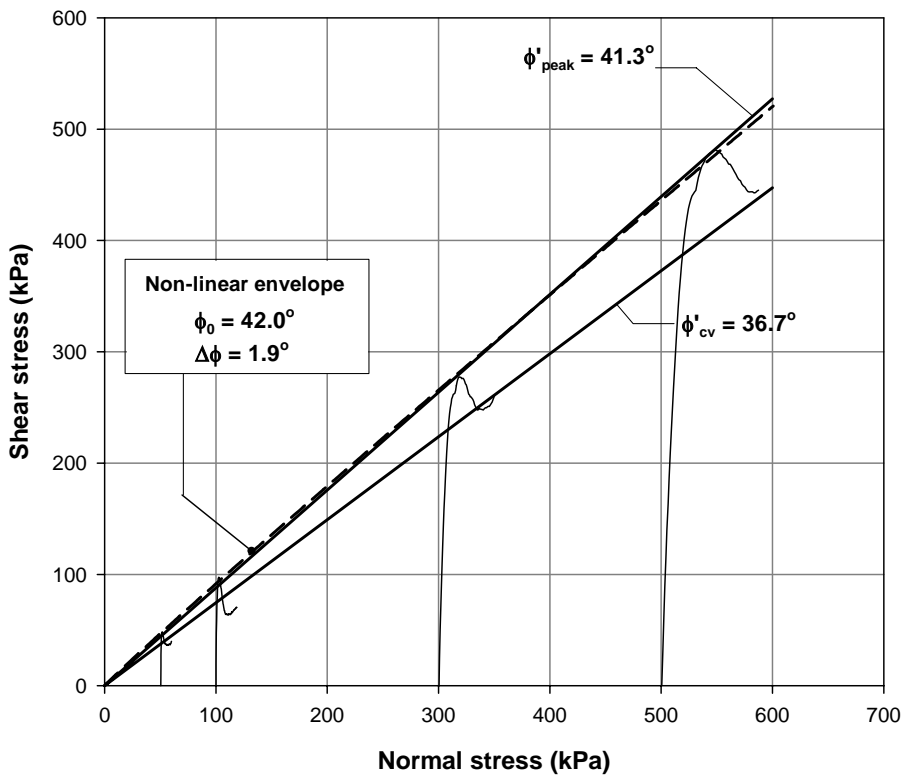


b) Shear strength envelopes

Figure 3.10. Direct shear test results for Cabo Rojo sand, medium relative density.

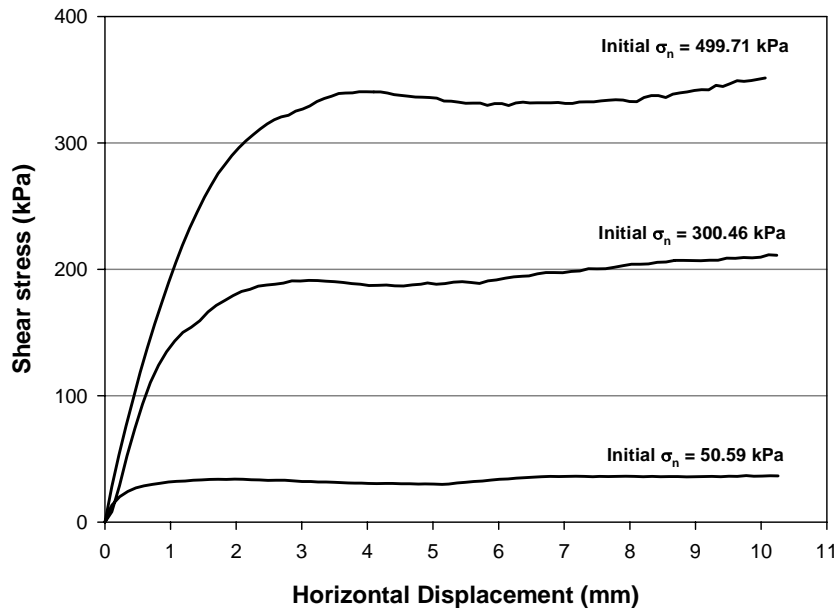


a) Shear stress - displacement curves

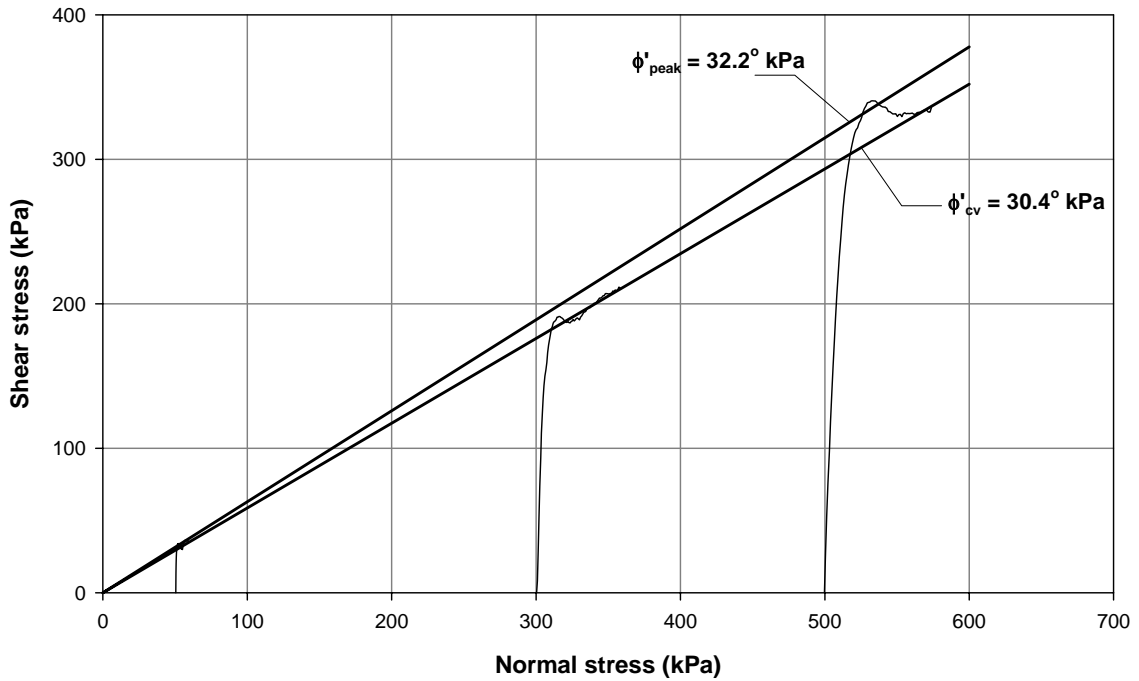


b) Shear strength envelopes

Figure 3.11. Direct shear test results for Cabo Rojo sand, maximum relative density.



a) Shear stress - displacement curves



b) Shear strength envelopes

Figure 3.12. Direct shear test results for South Bend sand, medium relative density.

The calcareous sand dense specimen (Figure 3.11) exhibited a slight decrease in peak friction angles with increasing normal stress. This requires a non-linear shear strength envelope which could be defined using the following expression, proposed by Duncan et al. (1980):

$$\phi = \phi_o - \Delta\phi \log_{10} \left(\frac{\sigma'_n}{P_{atm}} \right) \quad (3.3)$$

where: ϕ_o is the peak secant friction angle at a normal stress equal to the atmospheric pressure ($P_{atm} = 101 \text{ kPa}$); and

$\Delta\phi$ is the reduction in peak secant friction angle for a tenfold increase in normal stress (σ'_n).

The non-linear shear strength envelope, as well as the values for ϕ_o and $\Delta\phi$ for dense Cabo Rojo calcareous sand are shown in Figure 3.11b.

As previously mentioned, the shearing area of the soil specimens decreases during shearing. The stress paths shown in Figures 3.10b, 3.11b and 3.12b have been corrected for this effect.

ICU triaxial testing: Isotropic Consolidated Undrained (ICU) triaxial tests with pore pressure measurements were performed to determine the internal friction angle values of the Cabo Rojo and South Bend sands. Details regarding test procedure, specimen

preparation, and data reduction are presented later in this chapter. A summary of the internal friction angles obtained for both test sands is presented in Table 3.5.

Table 3.5. Summary of shear strength parameters for ICU triaxial tests.

Parameter	Cabo Rojo sand		South Bend sand	
	Loose	Dense	Loose	Dense
ϕ'_{peak}	39.8	41.2	33.4	40.0
$\epsilon'_{\text{axial at peak}}$	18.1	16.9	7.8	4.2
$\phi'_{\text{c.v.}}$	38.7	39.4	29.2	32.3
$\epsilon'_{\text{axial at c.v.}}$	20.0	20.0	20.0	20.0

Notes: ϕ'_{peak} : Peak friction angle, $\epsilon'_{\text{axial at peak}}$: axial strain at ϕ'_{peak} , $\phi'_{\text{c.v.}}$: Residual (nearly constant volume) friction angle, $\epsilon'_{\text{axial at c.v.}}$: axial strain at $\phi'_{\text{c.v.}}$ (20%).

3.2.5 Crushability analyses

As mentioned in Chapter 2, susceptibility to crushing is considered a significant factor that influences the behavior of calcareous sands. A component of the experimental program of this work was designed to assess the crushability potential of both test sands. Crushing susceptibility was quantified using the particle brakeage factor (B_{10}) proposed by Lade et al. (1996). This particle brakeage factor (B_{10}) can be computed as follows:

$$B_{10} = 1 - \frac{D_{10f}}{D_{10i}} \quad (3.4)$$

where D_{10i} is the initial grain diameter corresponding to 10% of the material being smaller by weight, before shearing stresses are applied, and D_{10f} is the final grain diameter corresponding to 10% of the material being smaller by weight after shearing.

This factor ranges from zero when there is no particle breakage to unity for the hypothetical case where there is infinite particle breakage.

Crushing of particles was evaluated by comparing the grain size distributions of the sands before and after each of the following tests: Direct simple shear test, ICU triaxial test, resonant column test, and 1-D compression test. The amount of particle crushing measured for the two test sands in the different tests is summarized in Figure 3.13. This figure shows that compared to the South Bend silica sand, the Cabo Rojo sand was found to be more crushable.

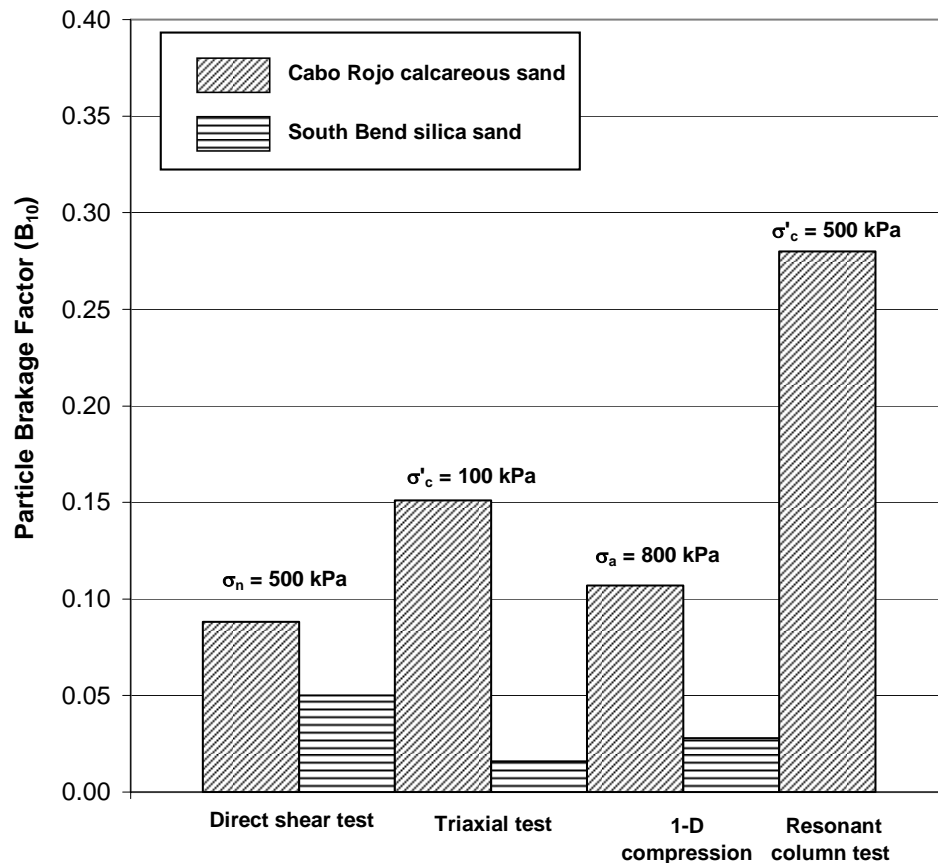


Figure 3.13. Particle breakage factor measured for the two test sands for different tests.

The higher particle breakage factor exhibited by the Cabo Rojo calcareous sand specimens after performing the resonant column tests may be associated to progressive crushing caused by using a single specimen subjected to increasing levels of effective confining pressures. Each specimen was subjected during a test to confining stress levels from 50 kPa to 500 kPa.

3.3 1-D Compression Test

Unidirectional (1-D) compression tests were performed on the Cabo Rojo and South Bend sands to obtain data on their mechanical behavior and to help evaluate their susceptibility to crushing. Two specimens, one for each test sand, were prepared at a loose state using dry air pluviation. Each specimen was subjected to a series of vertical stress increments. The tests were carried out using the LoadTrac II system by Geocomp Corp. Each load increment was maintained for a period of two hours. Figure 3.14 shows the vertical compression of sand specimens versus applied vertical pressure. This figure shows that calcareous sand is more compressible than the silica sand.

The results shown in Figure 3.14 have been corrected for machine deformations or compliance effects. The yield pressure (σ_{yield}) for the Cabo Rojo calcareous sand, determined as the point of maximum curvature, is approximately 327 kPa. This pressure defines the initiation of marked particle crushing in the specimen (Chuhan et al., 2003). Since the curve of the South Bend silica sand did not show a marked point of maximum

curvature, it was difficult to define the yield pressure (σ_{yield}) for this sand. The degree of crushing obtained after each test was discussed in section 3.2.5.

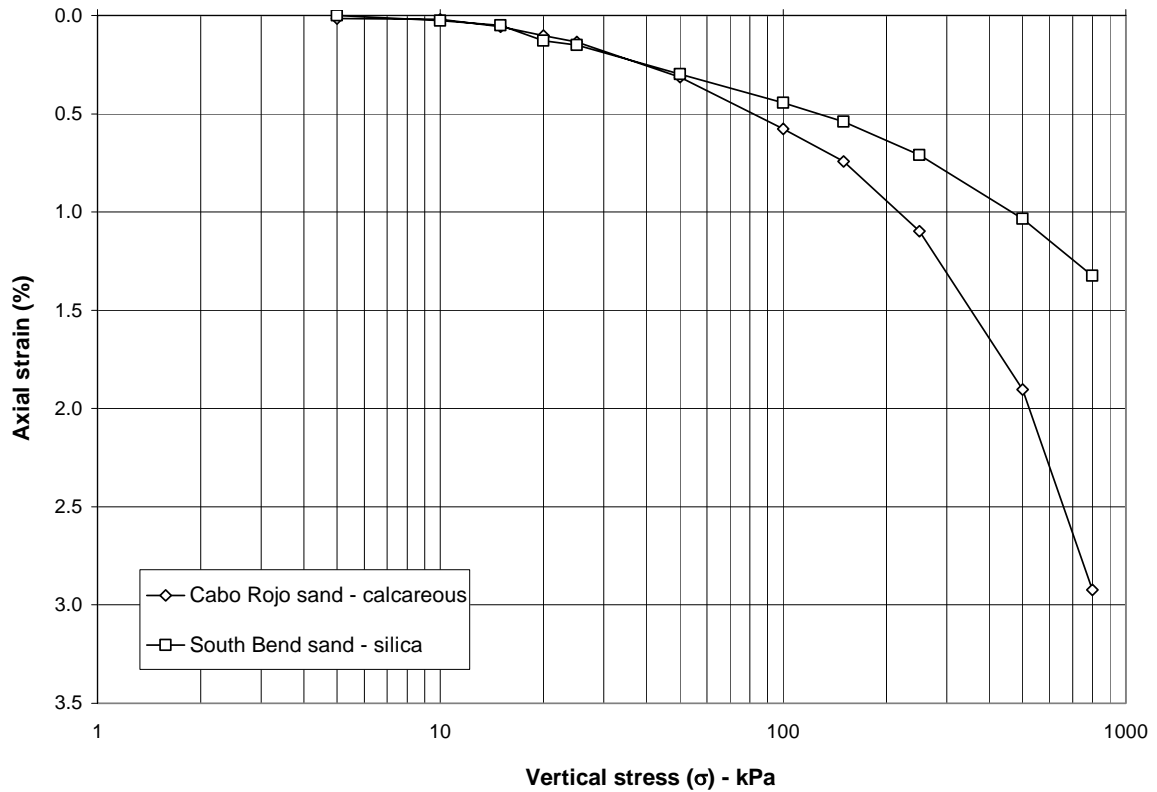


Figure 3.14. Specimen compression versus consolidation pressure, consolidation test.

3.4 Monotonic Triaxial Testing Program

A series of isotropic consolidated undrained strain-controlled triaxial tests (ICU) on calcareous sand specimens were carried out at the graduate geotechnical laboratory of the University of Puerto Rico at Mayagüez. These tests were carried out at three initial relative densities from medium ($D_{r,ini,avg} = 44\%$) to dense ($D_{r,ini,avg} = 87\%$), and at three levels of confining pressures (50, 100 and 300 kPa) to study the stress-strain behavior of the test sands at different density and confining states. This section describes the

followed test procedure, including specimen preparation and data reduction. Test results and respective analyses are presented in Chapter 4.

3.4.1 Triaxial specimen preparation

Triaxial test specimens were approximately 148 mm high and 70 mm in diameter. Specimens were prepared using two different methods: water pluviation method and moist tamping. Most of the specimens were prepared using the water pluviation technique, since it resulted in uniform specimens and best simulated the natural depositional mechanism of the marine calcareous sands. The moist tamping method was used to achieve looser states in some specimens.

Water pluviation method: This technique consisted of wet deposition of sand through de-aired water placed inside a mold lined with a latex membrane. The bottom part of the membrane was placed and secured with an o-ring to the bottom pedestal of the triaxial cell. The membrane was positioned within a forming split mold using a vacuum, which held the membrane open to the 70 mm diameter. A photograph of this setup is shown in Figure 3.15. Prior to sand pluviation, the sand was de-aired in a flask. This consisted of placing a known mass of dry sand into a flask and then adding de-aired water to the flask. A vacuum was then applied for about one hour to remove air bubbles entrapped inside the sand. The flask with de-aired sand was placed upside down into the forming mold, which had been previously filled with de-aired water. The open end of the flask was then carefully and slowly lifted from the base of the mold to initiate a gentle deposition

process. This process is shown in Figure 3.16. When the sand was completely deposited, the top porous stone and top cap were placed, and the upper end of the membrane was flipped up off the mold onto the top cap. The membrane was placed and secured with an o-ring to the top cap. For specimens requiring denser states, a mass of 500g was placed over the top of the specimen while gently tapping the mold laterally. This procedure produced specimens with relative densities ranging between 38% (without weight) and 95% (with weight).

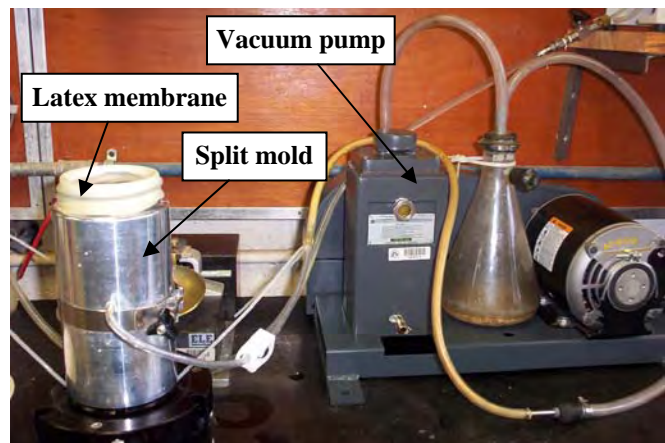


Figure 3.15. Split mold, latex membrane and vacuum pump.



Figure 3.16. Deposition of calcareous sand using the water pluviation method.

Moist tamping method: This technique consisted in pouring consecutive layers of moist sand into a latex membrane and tamping each layer before the next one is placed. For this work the sand was mixed with water to achieve moisture contents (w) between 5% and 20%. The 5% moisture content was used to produce very loose specimens, while specimens prepared with higher moisture contents achieved denser structures. This procedure resulted in specimens with relative densities between 3% ($w=5\%$) and 55% ($w=20\%$). The mixed moist sand was placed in five layers of 30 mm thickness into the latex membrane, whose bottom part was placed in the pedestal of the triaxial cell and positioned within a forming split mold using a vacuum. The vacuum held the membrane open to the 70 mm diameter. O-rings were used to secure the membrane at the bottom and top of the specimen. Each layer was compacted with a tamping rod of 62.3 g mass as shown in Figure 3.17. To compensate the effect of the sand weight supported by the lower layers, the number of blows per layer was increased in the upper layers. When the specimen reached the desired height, the top porous stone and the top cap were placed, and the membrane was flipped up off the mold onto the top cap.

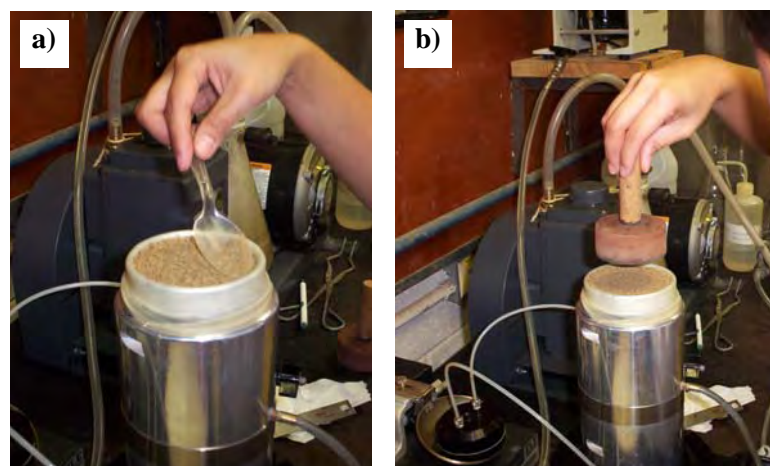


Figure 3.17. Moist tamping method: a) placement of moist sand, b) tamping of sand layer.

3.4.2 Triaxial specimen setup and saturation

Regardless of the specimen preparation technique, once the top cap was placed onto the specimen, a small negative pressure of -20 kPa was applied to the specimen through the lower drainage valve. This small negative pressure helped to support the specimen while the split mold was removed. After removal of the split mold, the dimensions of the specimen were measured. At least three circumference measurements were taken along the specimen to determine the average specimen diameter. The specimen height was based on at least four measurements. After carefully measuring the specimen, the triaxial cell was assembled, sealed, and filled with water. At this point a small cell pressure of 20 kPa was applied to the specimen while removing the small negative pressure of -20 kPa.

To facilitate specimen saturation, specimens were first flushed with carbon dioxide (CO₂) following a procedure similar to the one utilized by Cuning (1994) and by Garga and Zhang (1997). This flushing was carried out by releasing CO₂ through the bottom specimen port at a pressure of 13 kPa. This was done for approximately 30 to 45 minutes. During flushing, the upper port was left open to permit flushing of air. After the CO₂ flushing, the specimen was flushed with de-aired water in an attempt to displace any entrapped air.

After flushing the specimen with CO₂ and de-aired water, the specimen saturation process was completed using standard back pressure saturation. The back pressure

saturation was carried out using the control software “Triaxial” provided by Geocomp Corp. This phase is described next.

3.4.3 Triaxial test setup

The monotonic triaxial tests were performed using an automatic LoadTrac II/FlowTrac II triaxial testing system manufactured by Geocomp Corp. The testing system consists of three main components: a load frame (LoadTrac-II) which applies the vertical load to the specimen, and two flow pumps (FlowTrac-II) for controlling and measuring cell and specimen volume and pressure. More details of this testing apparatus can be found in Geocomp (2006). A diagram of the general test configuration is shown in Figure 3.18. A photograph of the layout of the system at the University of Puerto Rico is shown in Figure 3.19.

All tests were performed with the control software “Triaxial”, which was provided with the LoadTrac II/FlowTrac II System. This software is an interface/control software that permits running the tests while showing the current status of the system. The software includes five sequential phases: Initialization, Consolidation/A, Saturation, Consolidation/B, and Shear. Details of the different stages involved in the monotonic triaxial tests are provided next.

Initialization phase: This phase is used to check if the system has any leaks or problems. This check is done prior to the specimen saturation phase. The initialization

consists of applying a very small cell and specimen pressure. For this work, a cell pressure of 20 kPa and a specimen pressure of 13 kPa were used since these values produce a very low effective stress in the specimen (7 kPa) compared to the stress levels that were imposed to the specimen during the shearing stage of the test.

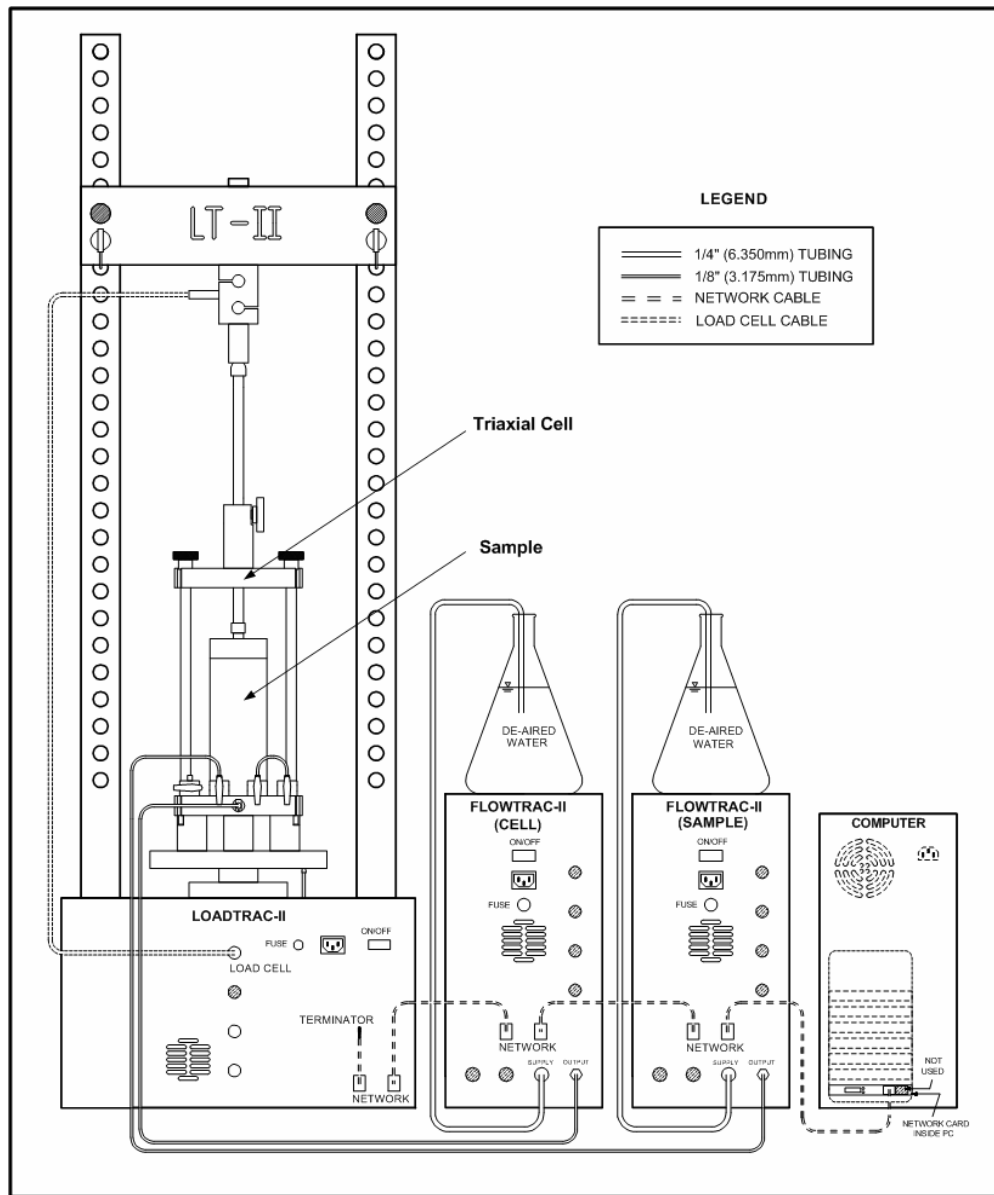


Figure 3.18. Installation diagram for LoadTrac-II/FlowTrac-II system for triaxial testing. (Geocomp, 2006).



Figure 3.19. LoadTrac-II/FlowTrac-II Triaxial system, University of Puerto Rico at Mayagüez.

Saturation phase: As previously mentioned, specimens were initially flushed with CO_2 , and then flushed by de-aired water. However, to ensure saturation, a back pressure was also applied. This automatic system applied successive increments of cell and specimen pressure until a B pore pressure parameter value of at least 0.95 was achieved. The first increment of cell pressure was of 15 kPa applied at a rate of 20 kPa/min, and maintained for at least 2 minutes. During this time, the B value was continuously updated and checked against the target value ($B = 0.95$). If the target B value was not achieved, the system applied a pressure increment of 15 kPa, to ensure a near zero effective stress in the specimen. This condition was maintained for at least 3 minutes before the next cell pressure increment was applied. Saturation ($B \geq 0.95$) was typically achieved at specimen back pressures (u_b) between 200 and 300 kPa.

Consolidation phase: Once specimen saturation was ensured, it was isotropically consolidated to a specified effective confining pressure. The system applied the target cell pressure at a rate of 2 kPa/min, while maintaining the confining pressure until reaching 100% of primary consolidation in the specimen.

Shear phase: Undrained shearing was applied after isotropic consolidation. As strain-controlled tests were performed in this work, specimens were sheared at 0.1% of axial deformation per minute. This phase was completed when the maximum strain was reached, or when steady state conditions were achieved. Since triaxial test specimens experience both vertical and radial deformation during shearing, the expression shown in equation (3.5) (Geocomp, 2006) was used to correct the specimen area at the middle height.

$$A_c = A_o \cdot \frac{1 - \varepsilon_v}{1 - 1.5\varepsilon_a} \quad (3.5)$$

where A_o is the area of the specimen before shearing; ε_v is the volumetric strain (%); and ε_a is the axial strain (%). Using this expression, corrected stress values for the specimen were estimated.

3.4.4 Final specimen void ratio calculations

Changes in void ratios after specimen preparation were calculated based on the changes in volume during the saturation, consolidation, and shear stages. Changes in

specimen volume due to the application of consolidation pressures were obtained directly from the system. To obtain volume changes in the specimen before consolidation (during CO₂ flushing and saturation), an elastic response of the specimen was assumed, as recommended in ASTM D4767-02. The elastic response approach produces the following approximation:

$$\varepsilon_v = 3 \cdot \varepsilon_a \quad (3.6)$$

where, ε_v is the volumetric strain (%) and ε_a is the axial strain (%).

The assessment of specimen volume changes during the shearing phase (ΔV_{shear}) was done using the following equation suggested by Garga and Zhang (1997).

$$\Delta V_{shear} = \Delta V_{tx.cell} - \Delta V_{piston} - \Delta V_{membrane} \quad (3.7)$$

where, $\Delta V_{tx.cell}$ is the measured total volume change of the water in the triaxial cell;

ΔV_{piston} is the calculated volume change of the cell water due to the penetration of the piston rod; and

$\Delta V_{membrane}$ is the calculated specimen volume change due to membrane penetration. (A normalized membrane penetration of 0.0015 cm³/cm² per log cycle of stress as proposed by Sladen and Handford (1987) was used).

The final total volume of the specimen was calculated as subtracting all of the specimen volume changes from the initial volume of the specimen (V_0). Calculations were performed as follows:

$$V_{final} = V_0 - \Delta V_{ini} - \Delta V_{sat} - \Delta V_{cons} - \Delta V_{shear} \quad (3.8)$$

where V_0 is the initial total specimen volume of the specimen after preparation;

ΔV_{ini} is the calculated specimen volume change assuming an elastic response of the specimen during initial saturation with CO₂ flushing;

ΔV_{sat} is the calculated volume change during back pressure saturation assuming an elastic response of the specimen;

ΔV_{cons} is the measured volume change during consolidation; and

ΔV_{shear} is the calculated volume change during shear phase, using equation (3.7).

The final void ratio of the specimen was calculated using equation (3.9), which was derived from the volumetric and weight relationships for a soil mass presented by Bardet (1997).

$$e_{final} = \frac{G_s \rho_w V_{final}}{M_s} - 1 \quad (3.9)$$

where G_s is the specific gravity of solids;

ρ_w is the density of water;

M_s is the mass of solids.

3.4.5 Calibration of sensors used in the triaxial testing

The following sensor transducers of the LoadTrac II/FlowTrac II triaxial system were checked to ensure calibration:

- Load cell

- Cell pressure transducer
- Internal (specimen) pressure transducer
- Displacement (LVDT) transducer

Details of the calibration procedures and results are provided in Appendix 6.

3.5 Resonant Column Testing Program

The dynamic properties of the calcareous sands, namely shear modulus and damping ratio, were determined using a resonant column (RC) device. The experiments on the resonant column device were carried out at the Geotechnical Engineering Laboratory of the University of Notre Dame. The objective was to determine the variation of the dynamic properties of both sands as a function of density, confining pressure, and shear strain levels. Resonant column specimens were prepared at three relative densities (21%, 58% and 91%) and at four levels of effective confining pressures (50, 100, 300 and 500 kPa). This section presents a description of the testing device, the specimen preparation procedure and the testing procedure. A brief overview of the resonant column test is also provided. Additional details are provided in Appendix 5. The results of these RC tests are presented and discussed in Chapter 5.

3.5.1 Resonant column background

The resonant column method is based on the one-dimensional wave equation derived from the theory of linear-elastic vibrations. By assuming linear elastic conditions,

parameters such as stiffness and damping are considered constant and independent of frequency and amplitude. The following discussion will focus on a fix-free system, which was the type of RC used in this research. In this kind of system the soil column is fixed at the base and free to rotate at the top.

Shear modulus (G): The shear modulus is obtained from a curve relating the variation in shear strain amplitude (γ) with frequency, as shown in Figure 3.20. This curve is called the frequency response curve of the system. It is measured by the resonant column system while applying a torsional harmonic load with constant amplitude over a range of frequencies. As the frequency is swept the data acquisition system has to keep track of the shear strain (γ) of the specimen. This procedure is used to obtain the resonant frequency of the rotational mode of vibration.

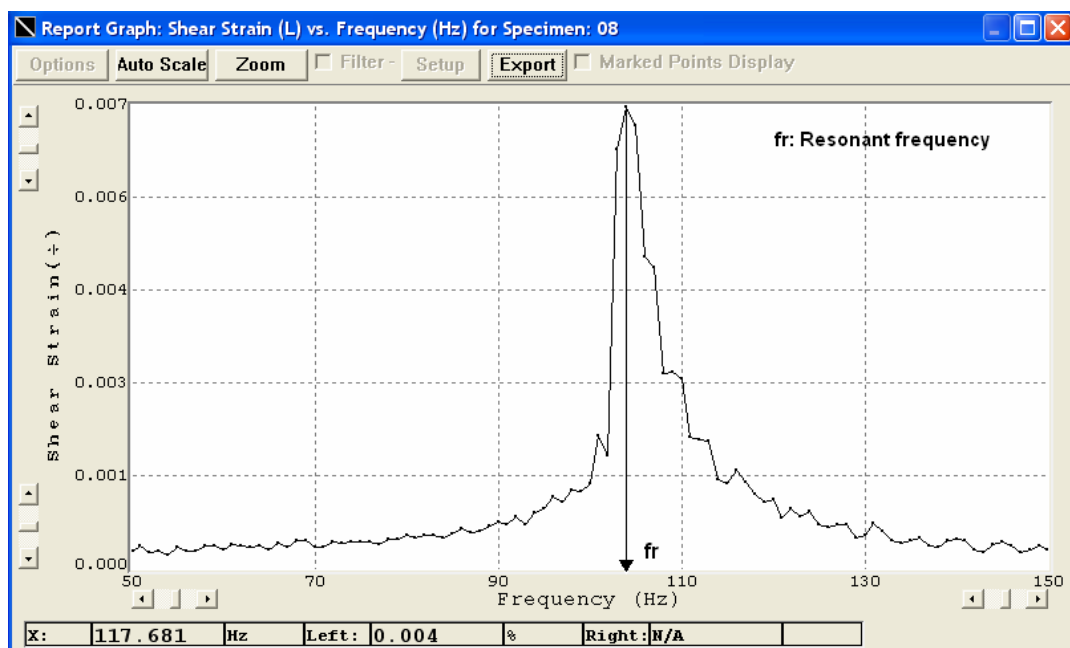


Figure 3.20. Dynamic response curve obtained by CATS© program.

From soil dynamics it is possible to relate the resonant frequency of the rotational mode of vibration with the shear wave velocity of the soil as shown in the equation (3.10), which was obtained from the linear-elastic vibrations solution of the one-dimensional wave equation, as shown by Ishihara (1996).

$$\frac{I}{I_0} = \left(\frac{2\pi f_r H}{V_s} \right) \tan \left(\frac{2\pi f_r H}{V_s} \right) \quad (3.10)$$

where: I is the mass moment of inertia of the soil column;

I_0 is the mass moment of inertia of the driving system;

f_r is the measured resonant frequency;

H is the height of the soil specimen; and

V_s is the shear wave velocity.

Having the shear wave velocity and the soil density, the shear modulus can be obtained using theory of elasticity, as follows (Kramer, 1996):

$$G = \rho V_s^2 \quad (3.11)$$

where G is the shear modulus, and ρ is the soil mass density.

The mass moment of inertia of the driving system (I_0) is obtained from calibration tests. The calibration tests consist of using a specimen of known elastic properties such as an aluminum rod specimen. A value of 827 kg-mm² was obtained for the mass moment of inertia of the driving system (I_0) used in this research. This value includes the mass moment of inertia of the top cap used.

Damping ratio (D): The material damping ratio was evaluated by two different methods: the half power bandwidth method and the free vibration decay method.

The half power bandwidth method consisted of evaluating the damping ratio of the specimen from its frequency response characteristics (Kramer, 1996). The half power damping ratio was obtained from the response curve of the system (Figure 3.20), as follows (GCTS, 2004):

$$D = \frac{1}{2} \frac{f_2 - f_1}{f_r} \quad (3.12)$$

where f_1 and f_2 are called the half-power points, which are the frequencies above and below resonance (f_r), where the response amplitude is 0.707 times the resonant amplitude (see Appendix 5). This method was used for damping ratio determination at small shear strain levels.

The free vibration decay method can also be used to obtain the material damping ratio. This method is based on using the logarithmic decrement, δ , calculated as the natural logarithm of two consecutive shear strain peaks from the free vibration curve, as shown in Figure 3.21.

The logarithmic decrement (δ) can be calculated as follows (Kramer, 1996):

$$\delta = \ln\left(\frac{\gamma_n}{\gamma_{n+1}}\right) = \frac{2\pi D}{\sqrt{1-D^2}} \quad (3.13)$$

where γ_n and γ_{n+1} are the shear strain values of two consecutive peaks.

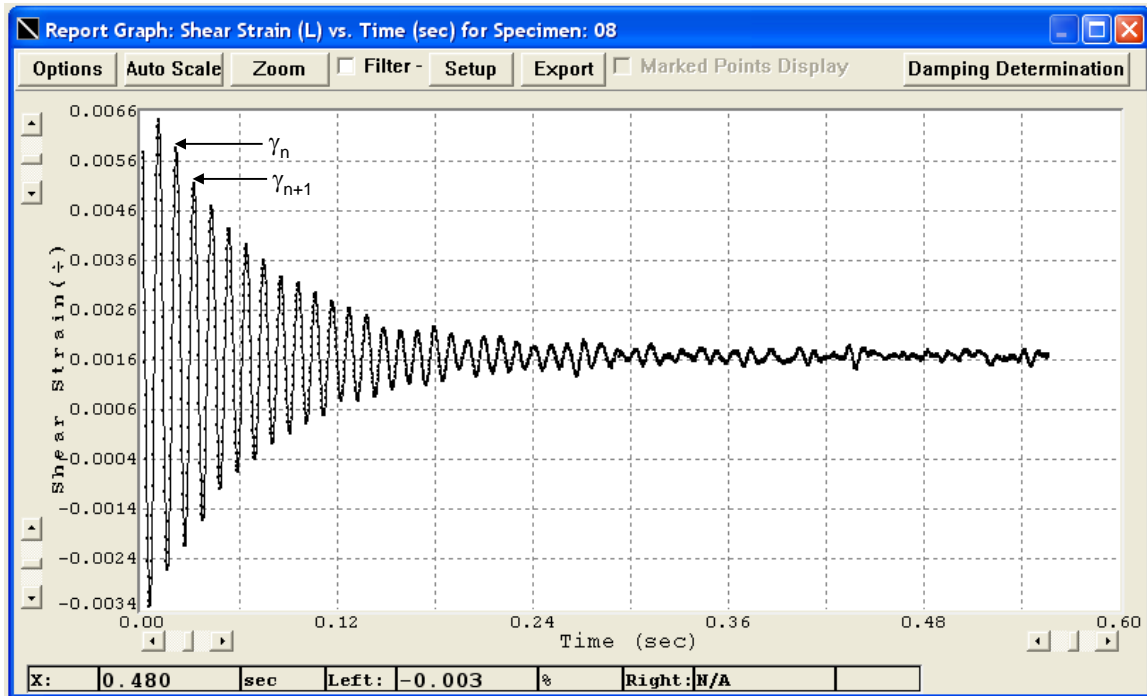


Figure 3.21. Free-vibration decay – CATS© software.

Therefore, the logarithmic decrement is the slope of the shear strain versus numbers of cycles plotted in Figure 3.22. Typically 10 cycles were used in this work to calculate the logarithmic decrement. With the logarithmic decrement, the material damping can be obtained as follows (Kramer, 1996):

$$D = \sqrt{\frac{\delta^2}{4\pi^2 + \delta^2}} \quad (3.14)$$

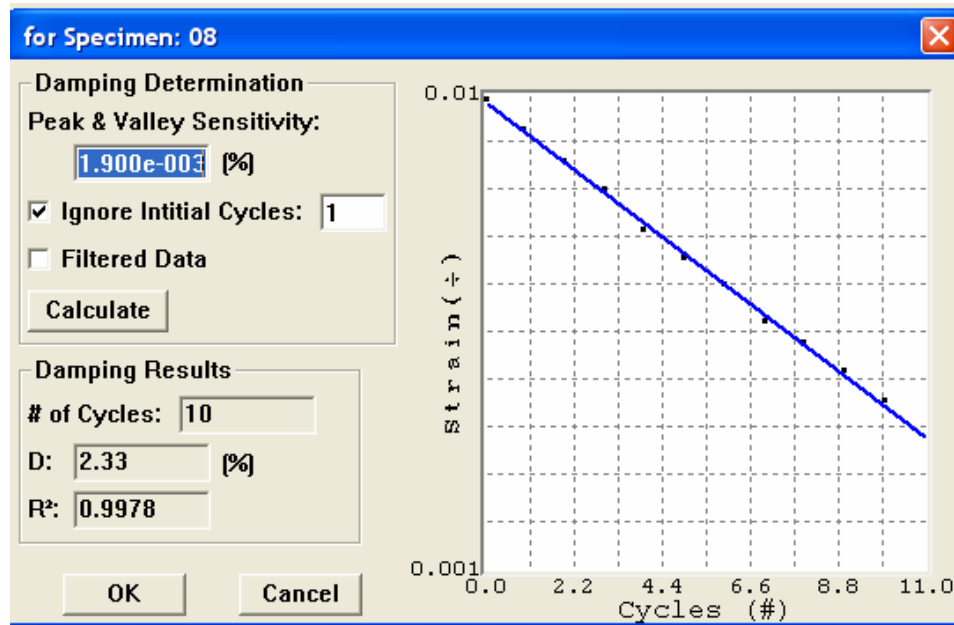


Figure 3.22. Damping determination from free-vibration decay – CATS© program.

Equipment-generated damping (D_{eq}): In both methods described above, the equipment-generated damping (D_{eq}) needs to be subtracted. The equipment-generated damping is an inherent damping of the resonant column drive system which is included in the response of the specimen during testing (Stokoe II et al., 1995). To obtain more realistic material damping ratios one needs to subtract this effect. To measure (D_{eq}), an aluminum specimen was tested. Since the damping associated with the aluminum specimen can be considered negligible in comparison with the equipment-generated damping, the measured damping can be used as an estimate of the resonant column drive system damping (D_{eq}) (Cascante et al., 2005). Several tests were performed with the aluminum calibration specimen to obtain the equipment-generated damping. The average value (D_{eq}) obtained was 0.22%. (For more details see Appendix 6).

Shear strain (γ): With regard to the shear strain measured in the RC test, an equivalent shear strain (γ_{eq}) was used to represent the average shear strain within the soil specimen, as follows (GCTS, 2004):

$$\gamma_{eq} = \frac{\frac{2}{3}r_0\theta_{max}}{h} \quad (3.15)$$

where r_0 is the radius of solid soil specimens, h is the height of the soil specimen, and θ_{max} is the maximum angle of twist at the top of the soil column (for more details see Appendix 5).

The value of θ_{max} is calculated by dividing the sensor displacement output (x) of the system by the radius to the position of the sensor, r_{sensor} . For this work, two proximitors were used, placed at the top of the specimen, one across the other to measure its shear strain. These proximitors used magnetic field changes with respect to a magnet to determine the amount of displacement. The typical configuration of a proximitor is shown in Figure 3.23.

3.5.2 RC test set-up

A diagram of the GCTS Resonant Column apparatus used in this work is shown in Figure 3.24. This device is fully automated and uses modern sensors. Tests are completely controlled using the control software CATS© - Resonant Column Test Mode – v. 1.7, GCTS (2004).

The control software requires the input of several parameters: control parameters (related mainly to torque control and motor control); hardware parameters (related to driving system inertia, equipment damping, and radial distance to proximator); units; specimen type; and dimensions. The software allows the user to specify different levels of excitation and frequencies, among others. Additional details regarding the CATS software can be found in GCTS (2004).

3.5.3 *Specimen preparation*

All specimens used in the resonant column testing program were prepared using dry sand with nominal dimensions of 50 mm in diameter and 115 mm in height. Specimens were prepared using the dry deposition method described by Ishihara (1996). Specimens were placed inside a latex membrane, which was held open against a split mold using a vacuum.

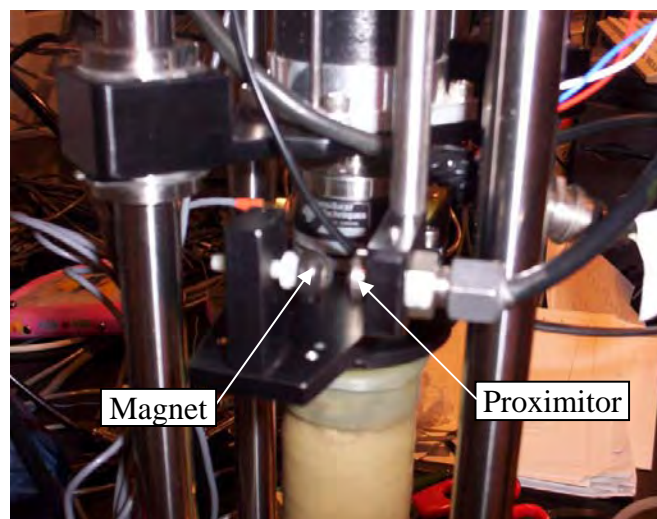


Figure 3.23. Alignment between the proximator and the magnet.

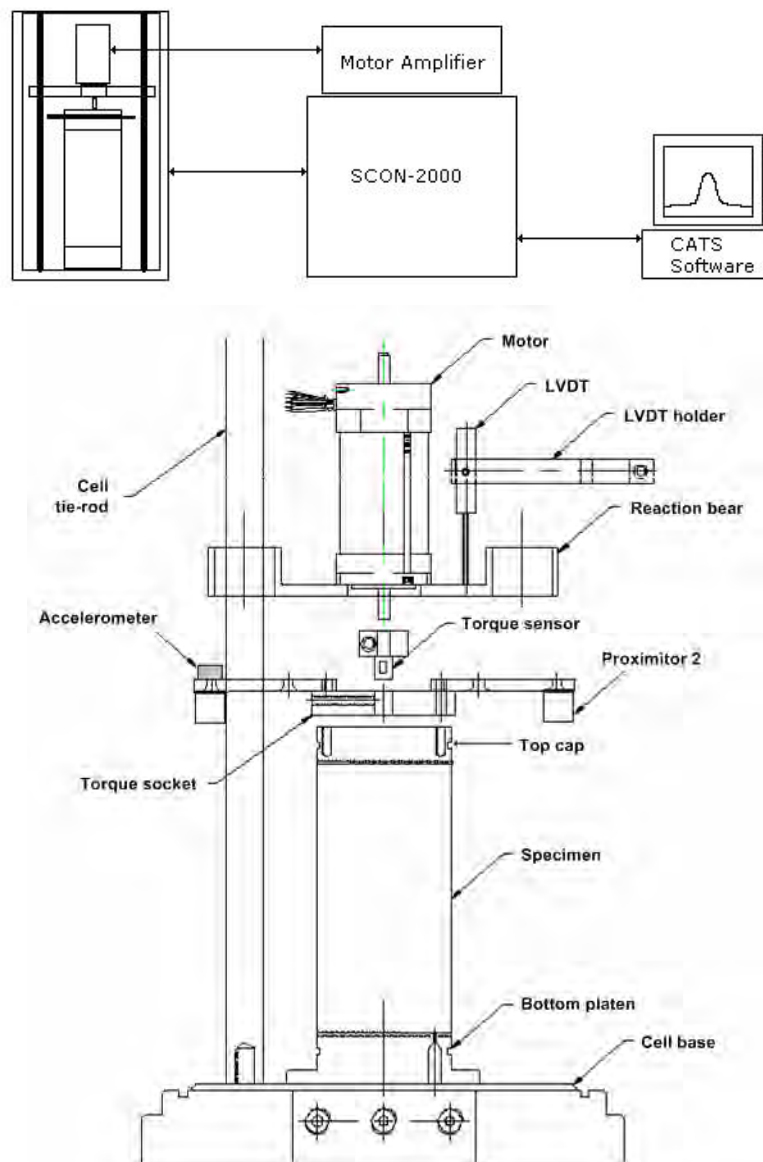


Figure 3.24. Diagram of the GCTS resonant column system.

The preparation method consisted in gently pouring the sand into the membrane with the aid of a slender paper tube. This tube had an external diameter of 46 mm which is slightly smaller than the internal diameter of the mold. The paper tube was fitted with small nozzles at the bottom end. The bottom end of the pouring tube was kept close to the sand surface to ensure the sand was evenly distributed across the surface. Specimen

density using this method yielded relative density values between 21% and 91%. Denser specimens were achieved by applying gentle tapping to the side of the mold during the pouring process. For specimens at the densest state, a mass of 500g was placed on top of the specimen while tapping the mold laterally.

When the specimen reached the desired height, the top cap was placed and the membrane was flipped up off the split mold onto the top cap. O-rings were used to secure the membrane at the bottom and top of the specimen. Once the top cap was placed onto the specimen, a small vacuum was applied to the specimen, through the drainage valve of the RC cell. This vacuum was used to support the specimen when the split mold was removed. At this point the dimensions of the specimen were measured. The average specimen diameter was based on at least three circumferences measurements, while at least four height measurements were used to obtain the average specimen height. When the specimen dimensions were determined, the top cap was screwed to the driving system. The proximity sensors and sensors of the driving system were then connected, and the cell body was assembled. The sensors were then connected to the GCTS RC digital system controller. The required confining pressure for the test was applied using pressurized air that was injected into the RC cell. The air pressure was controlled by a GCTS pressure control panel. The final setup consisted of initializing the proximity sensors by setting them to a zero displacement reading. The test started by using the CATS control software. A photograph of the RC system used is shown in Figure 3.25.

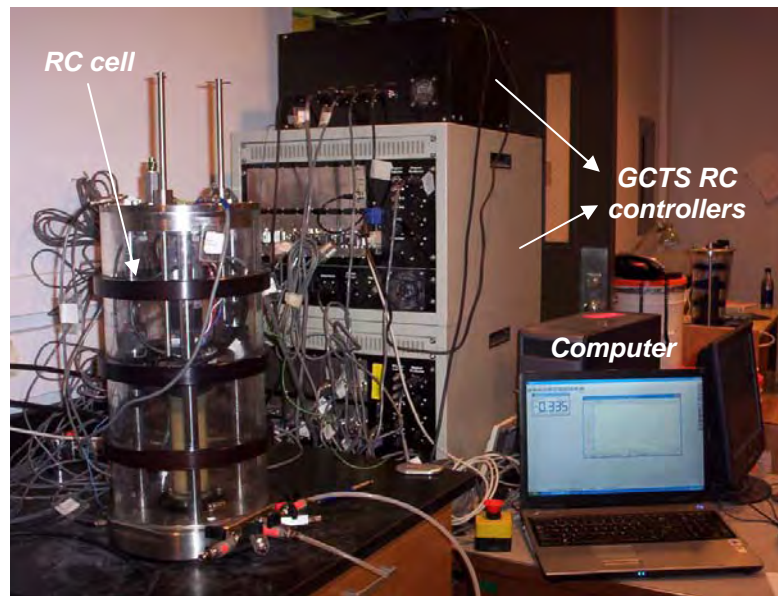


Figure 3.25. GCTS resonant column apparatus, University of Notre Dame.

3.5.4 RC equipment calibrations

As previously mentioned, two important properties of the RC device are required to reduce the data: the mass moment of inertia of the RC driving system (I_0), and the equipment-generated damping ratio (D_{eq}). These parameters were obtained by means of calibration tests described in Appendix 6. Details of the calibration procedures for the displacement sensors (proximitors) of the RC system are also provided in Appendix 6.

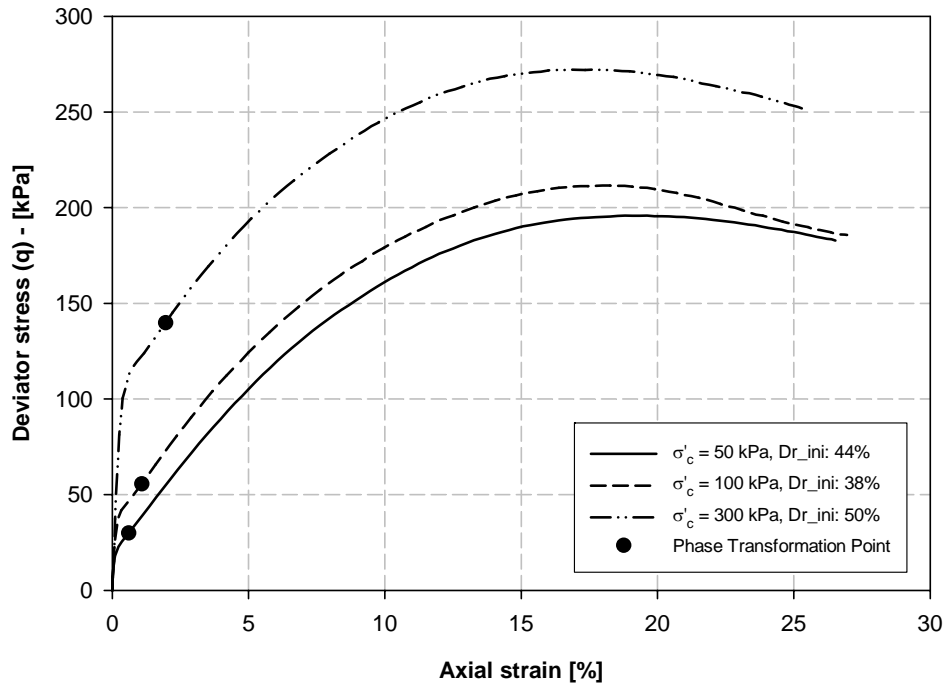
4 STRESS-STRAIN BEHAVIOR OF THE CABO ROJO SAND

4.1 Introduction

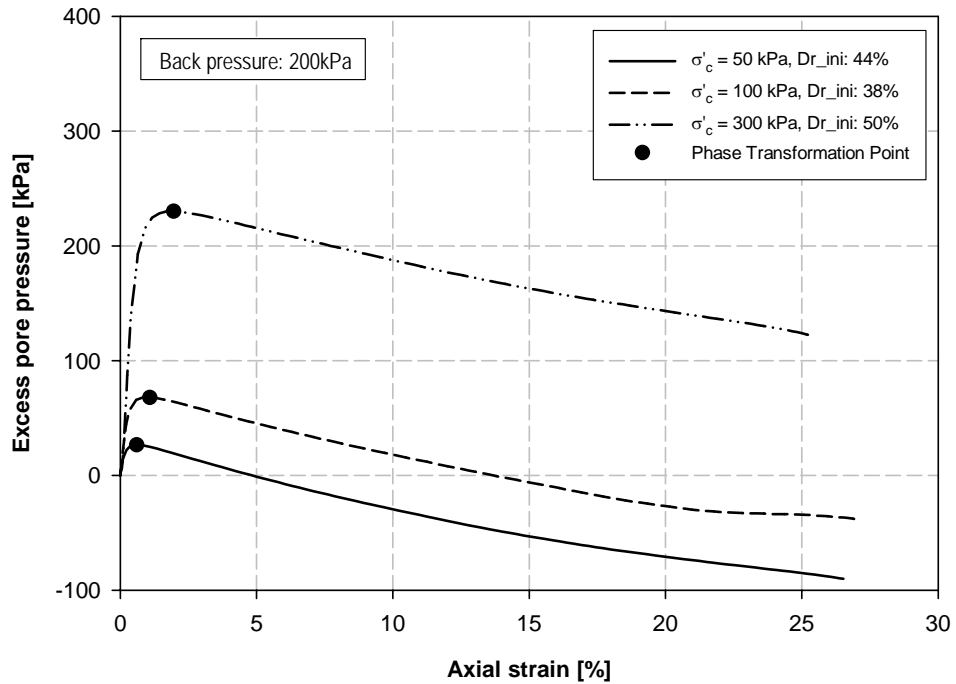
Monotonic triaxial tests were performed to determine the stress-strain behavior and steady state line of the Cabo Rojo calcareous sand. The tests were done on isotropically consolidated specimens that were sheared undrained (ICU). The procedure used for these tests is presented in Chapter 3. Specimens of the South Bend silica sand were also included in the ICU triaxial testing program to compare the stress-strain response of both sands. Test results are presented first for the Cabo Rojo sand, including effective stress paths and the steady state line. Finally a comparison between the stress-strain response of both sands is presented.

4.2 Stress-Strain Behavior of Cabo Rojo Sand

ICU triaxial tests for the Cabo Rojo calcareous sand were carried out for three levels of relative density, varying from medium to a high density state. These test results are shown in Figures 4.1 through 4.3. These graphs show applied deviator stress ($q = \frac{\sigma_1 - \sigma_3}{2}$) versus axial strain and excess pore pressure as a function of axial strain. In these figures, D_{r_ini} refers to the initial relative density of specimens, before the consolidation phase.

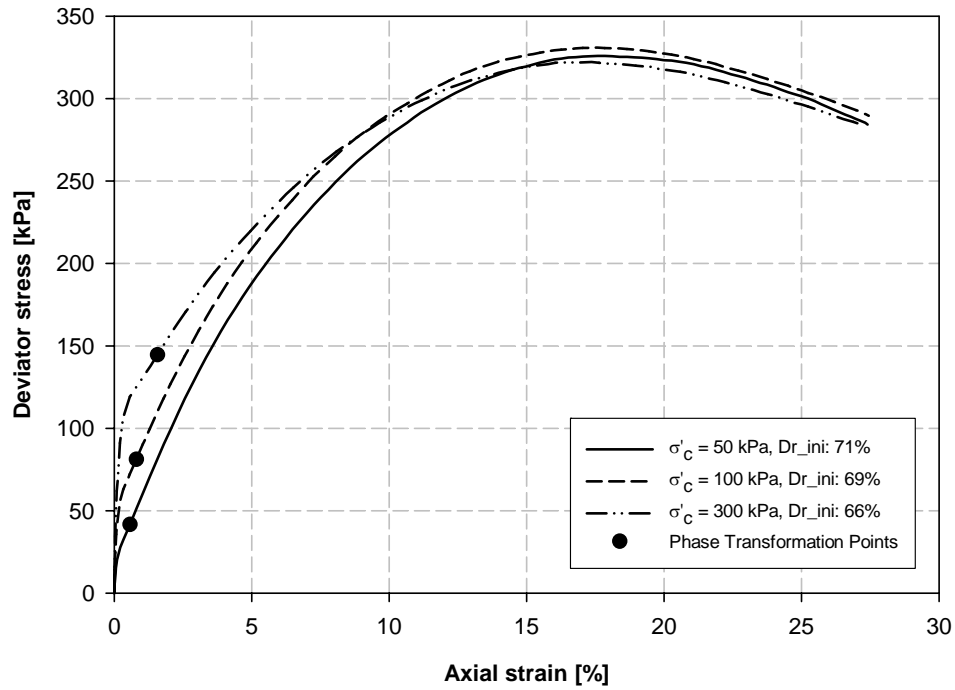


a) Deviator stress vs. axial strain

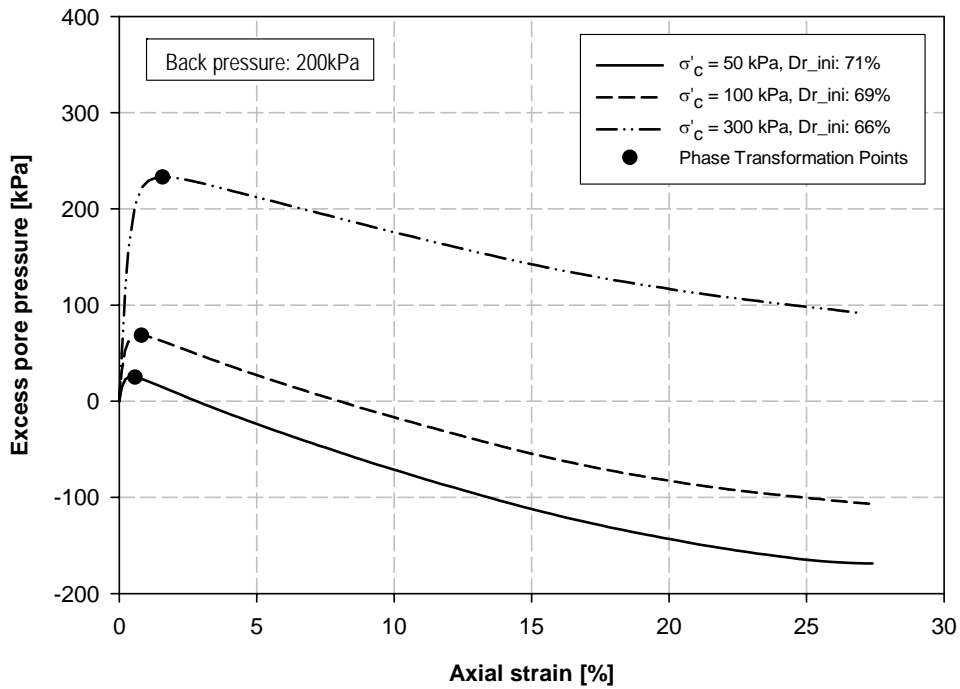


b) Excess pore pressure vs. axial strain

Figure 4.1. ICU test results for Cabo Rojo sand with average $D_{r_ini} = 44\%$.

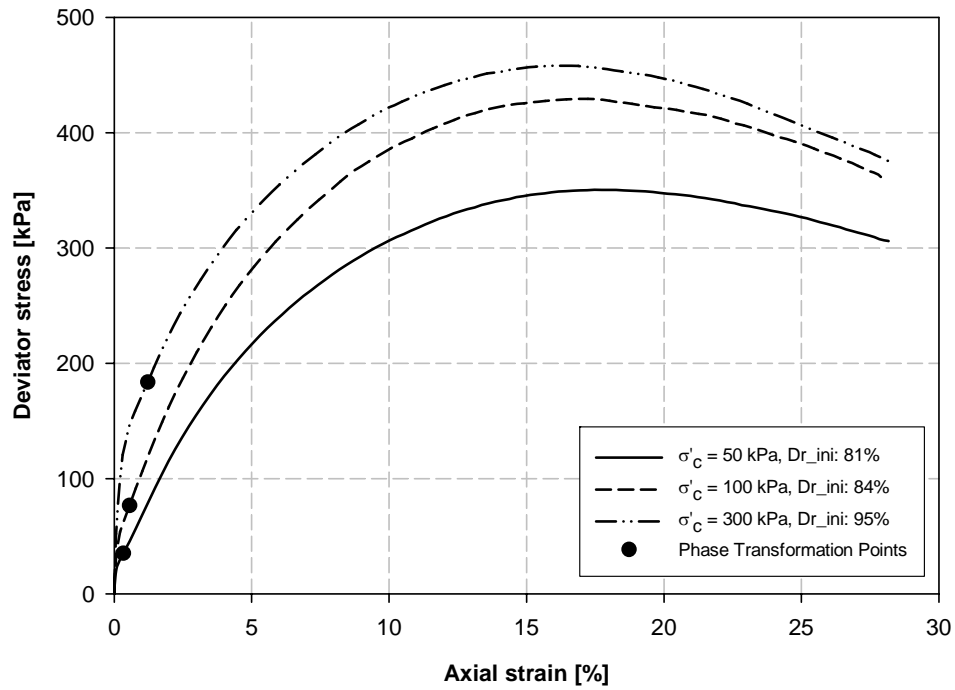


a) Deviator stress vs. axial strain

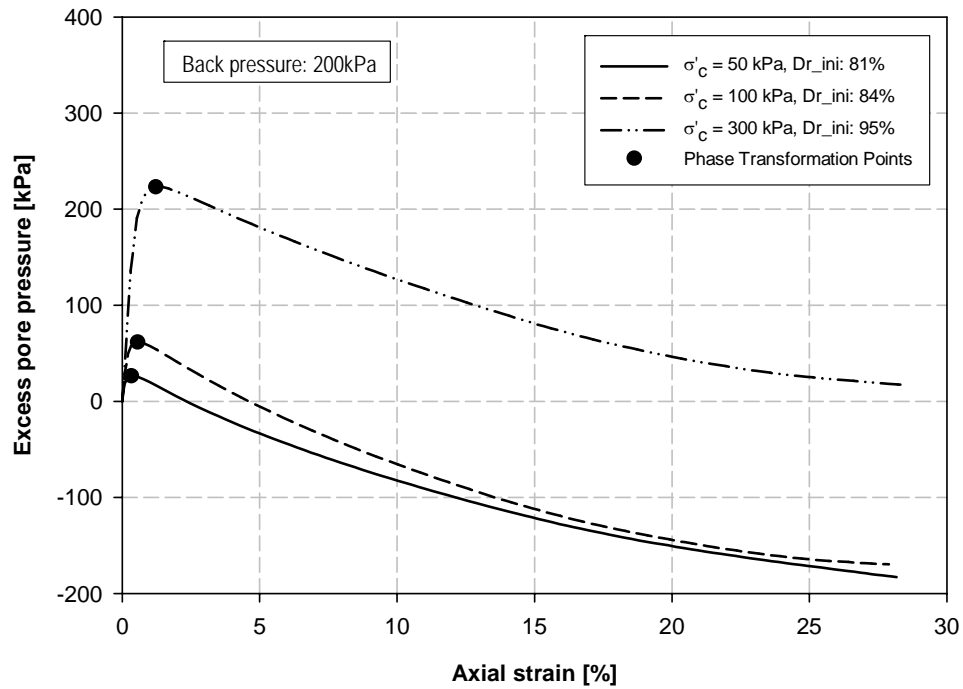


b) Excess pore pressure vs. axial strain

Figure 4.2. ICU test results for Cabo Rojo sand with average $D_{r_ini} = 69\%$.



a) Deviator stress vs. axial strain



a) Excess pore pressure vs. axial strain

Figure 4.3. ICU test results for Cabo Rojo sand with average $D_{r_ini} = 87\%$.

Also indicated in Figures 4.1 through 4.3 are the phase transformation points which correspond to the change from contractive to dilative behavior as defined in Chapter 2.

The peak strength of the Cabo Rojo calcareous sand was found to increase with increasing confining pressure. However, for specimens prepared at a 69% initial relative density, the peak strength showed little dependency on the confining pressure resulting in very similar peak deviator stress values. The peak strength, defined as maximum deviator stress, was reached at large axial strain values ranging between 16% and 20%. The values of peak deviator stress and their corresponding axial strains are summarized in Table 4.1. Also included in Table 4.1 are the deviator stress values at 10% axial strain ($q_{10\% \epsilon_{axial}}$) used to define the strength parameters for the commonly used failure criterion of 10% axial strain.

The stress-strain curves showed very steep initial slopes before reaching the phase transformation points. Phase transformation points occurred at the very early stages of the test, typically at axial strain values between 0.60% and 1.96%. Strain hardening was continued to be observed beyond the phase transformation points until reaching the peak deviator stress. After peaking, all Cabo Rojo sand specimens showed a slight strain softening. Triaxial tests were carried out to axial strain levels in excess of 25%. The usefulness of the test data at high axial strain levels may be questionable. However, other researchers have reported triaxial test results to similar axial strain levels (e.g., Ishihara, 1996, and Castro and Poulos, 1977).

Nevertheless, it is important for the reader to recognize that at high axial strain levels the specimens have experienced large radial deformations that possibly generates errors induced by end effects and other potential problems. ASTM D4767-02 recommends carrying out triaxial tests up to strain levels of about 15%. For this research greater strain levels were used in an attempt to reach steady-state conditions. This condition was only achieved in some tests.

The dilative behavior of the Cabo Rojo sands under different isotropic confining pressures can be observed in the excess pore pressure curves shown in Figures 4.1b, 4.2b, 4.3b. The initial behavior shows an increase in pore pressure up to the phase transformation points. This is indicative of a contractive behavior. After the phase transformation points, specimens experienced a decrease in pore pressures corresponding to a dilative behavior. Table 4.1 shows the maximum excess pore pressure values (Δu_{\max}) for each set of tests and their corresponding axial strains. The points of maximum excess pore pressure (Δu_{\max}) correspond to the phase transformation points.

4.2.1 Initial Young's modulus for Cabo Rojo calcareous sand

The initial undrained Young's modulus for each test was determined from the initial portion of the stress-strain curves in Figures 4.1 through 4.3, redrawn to show results up to 1% axial strain, as shown in Figures 4.4 through 4.6. The values of initial undrained Young's modulus ($E_{u, ini}$) obtained for the Cabo Rojo sand are presented in Table 4.1.

Table 4.1 Summary of ICU triaxial test results on Cabo Rojo calcareous sand.

γ_{dry} kN/m ³	D_{r_ini} %	D_{r_cons} %	σ'_c kPa	E_{u_ini} kPa	q_{peak} kPa	ε_{axial_peak} %	$q_{10\% \varepsilon_{axial}}$ kPa	Δu_{max} kPa	$\varepsilon_{axial \Delta u_{max}}$ %
10.6	44%	62%	50	39060	195.94	19.62	160.87	26.63	0.60
10.5	38%	48%	100	60992	211.55	17.99	179.00	67.96	1.09
10.7	50%	75%	300	73211	272.22	16.81	246.47	230.05	1.96
11.1	71%	80%	50	51307	325.85	17.85	279.46	25.06	0.57
11.0	69%	76%	100	---	330.86	17.58	291.67	68.51	0.80
11.0	66%	81%	300	93568	322.10	17.36	290.00	233.08	1.58
11.3	81%	86%	50	53610	350.45	17.47	306.54	26.52	0.33
11.3	84%	94%	100	73196	429.40	16.97	386.20	61.62	0.56
11.6	95%	111%	300	116388	458.14	16.37	423.81	223.15	1.22

Notes: γ_{dry} : Dry unit weight, D_{r_ini} : Initial relative density, D_{r_cons} : Relative density after consolidation, σ'_c : Effective confining pressure, E_{u_ini} : Initial undrained Young's modulus, q_{peak} : Peak deviator stress, ε_{axial_peak} : Axial strain at peak deviator stress, $q_{10\% \varepsilon_{axial}}$: Deviator stress at 10% axial strain, Δu_{max} : Maximum excess pore pressure, $\varepsilon_{axial \Delta u_{max}}$: Axial strain at maximum excess pore pressure.

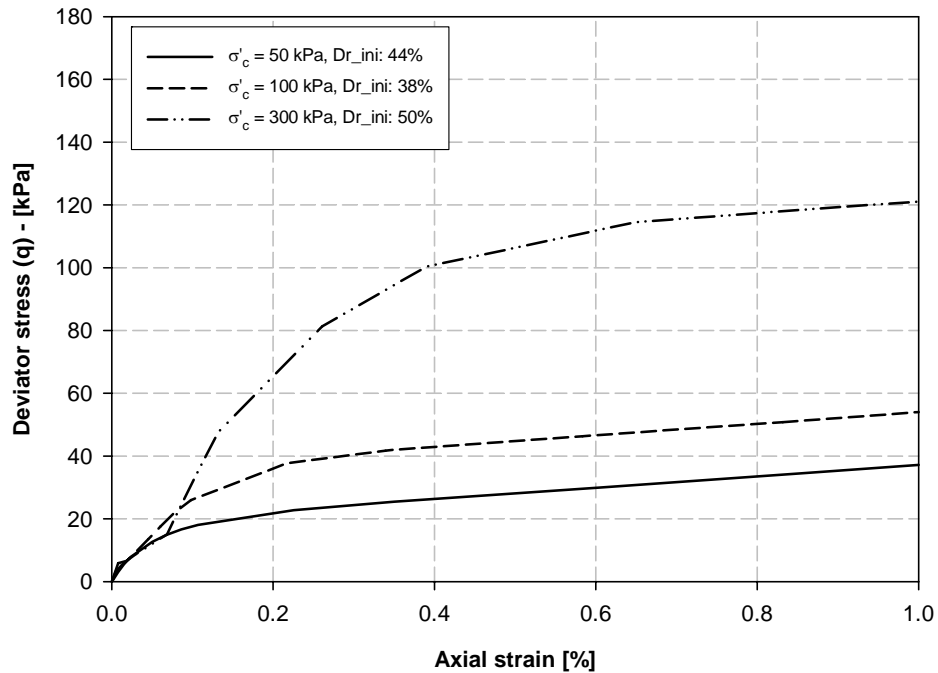


Figure 4.4. Initial portion of the deviator stress curves vs. axial strain curves. (Average $D_{r_ini} = 44\%$).

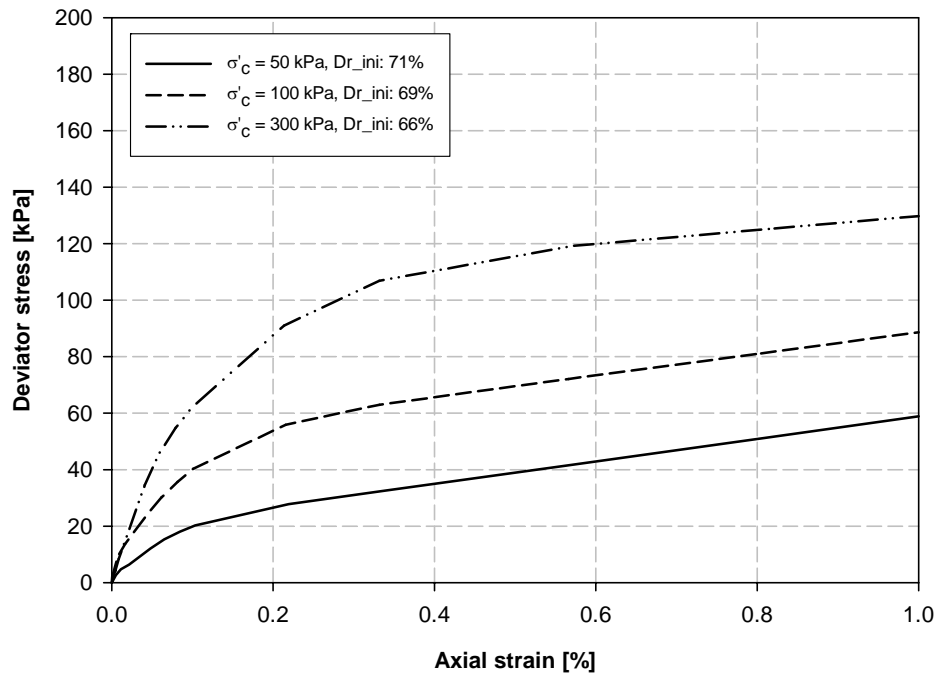


Figure 4.5. Initial portion of the deviator stress curves vs. axial strain curves. (Average $D_{r_ini} = 69\%$).

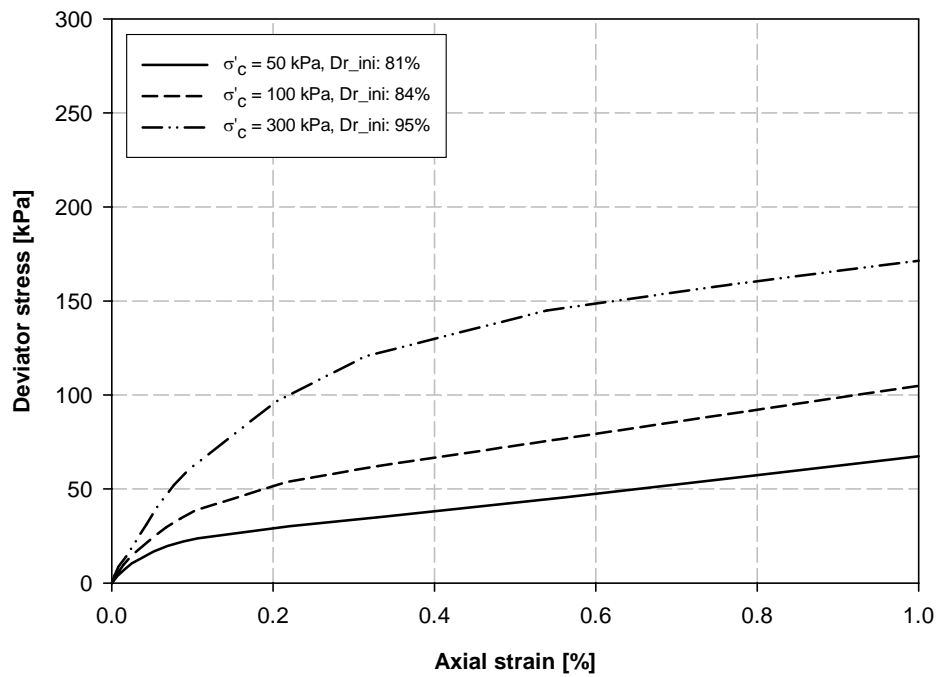


Figure 4.6. Initial portion of the deviator stress curves vs. axial strain curves. (Average $D_{r_ini} = 87\%$).

Janbu (1963) suggested the following relationship between $E_{u, ini}$ and effective confinement:

$$E_{u, ini} = K \cdot P_{atm} \cdot \left(\frac{\sigma'_3}{P_{atm}} \right)^n \quad (4.1)$$

where K is the modulus number (dimensionless); σ'_3 is the effective confining stress (equal to σ'_c); P_{atm} is the atmospheric pressure in the same units as σ'_3 ; and n is the modulus exponent (dimensionless).

The variation of the initial undrained Young's modulus values with effective confining stress for each set of tests is plotted in Figure 4.7. Included in this figure are the power curve fitting of the type shown in equation (4.1). The values of the correlation coefficient (R^2) for the fitting using the power equation given by Janbu (1963) were all found to be between 0.871 and 1.000, indicating reasonable to very good fits. The parameters for the power fits corresponding to the three used densities are provided in Table 4.2.

4.2.2 Internal friction angles for Cabo Rojo calcareous sand

Values of internal friction angle obtained for the Cabo Rojo sands are shown in Tables 4.3 through 4.5. These values correspond to three different types of failure criteria: peak deviator stress, 10% axial strain, and maximum excess pore pressure (i.e., phase transformation points). Internal friction angles at peak deviator stress were

assessed at axial strain values ranging between 16% and 20%; at maximum excess pore pressure, angles were assessed at axial strain values ranging between 0.60% and 1.96%; and the third assessment corresponded to an axial strain of about 10%.

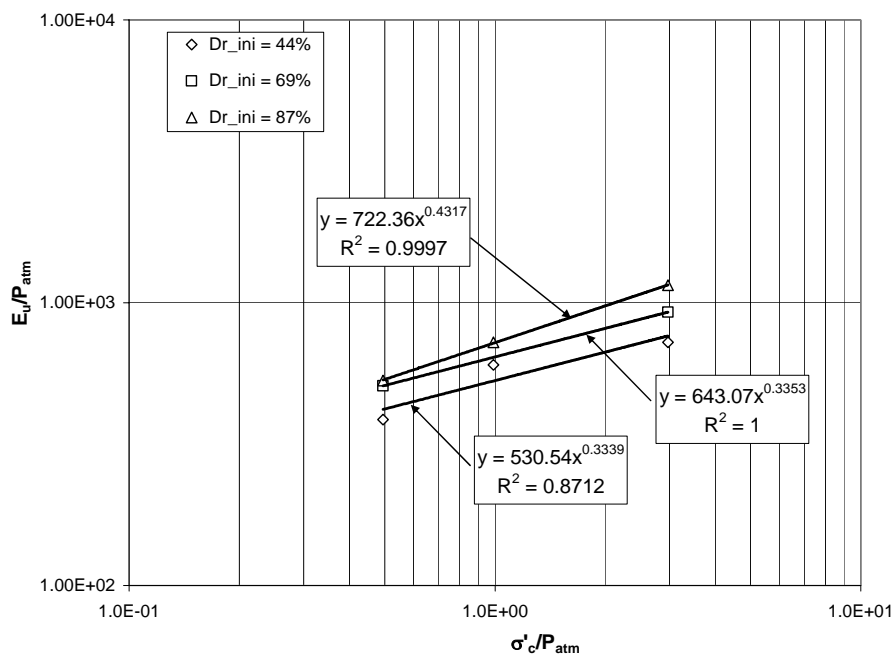


Figure 4.7. Variation of initial undrained Young's modulus with effective confining pressure on Cabo Rojo calcareous sand.

Table 4.2. Power law parameters for Cabo Rojo calcareous sand.

Initial relative density, $D_{r_ini}^{(1)}$	$K^{(2)}$	Exponent, $n^{(2)}$	R^2
44%	530.54	0.334	0.871
69%	643.07	0.335	1.000
87%	722.36	0.432	1.000

(1) D_{r_ini} : Initial relative density, before specimen consolidation

(2) From equation (4.1)

Table 4.3. Friction angles for Cabo Rojo calcareous sand - Peak strength failure criterion.

γ_{dry} kN/m ³	$D_{r,ini}$ %	$D_{r,cons}$ %	σ'_c kPa	Δu_f kPa	σ'_{1f} kPa	σ'_{3f} kPa	ε_{axial_peak} %	$\phi'_{q_{peak}}$ deg.
10.6	44%	62%	50	-69.70	511.61	119.73	19.62	39.8
10.5	38%	48%	100	-19.68	542.81	119.72	17.99	
10.7	50%	75%	300	155.08	689.41	144.98	16.81	
11.1	71%	80%	50	-131.15	832.88	181.18	17.85	40.7
11.0	69%	76%	100	-70.59	832.33	170.62	17.58	
11.0	66%	81%	300	129.02	815.30	171.10	17.36	
11.3	81%	86%	50	-137.20	888.07	187.18	17.47	41.2
11.3	84%	94%	100	-126.66	1085.54	226.75	16.97	
11.6	95%	111%	300	70.03	1146.29	230.02	16.37	

Notes: γ_{dry} : Dry unit weight, $D_{r,ini}$: Relative density before specimen consolidation, σ'_c : Effective confining pressure, Δu_f : Excess pore pressure at failure, σ'_{1f} : Principal major effective stress at failure, σ'_{3f} : Principal minor effective stress at failure, ε_{axial_peak} : Axial strain at peak deviator stress, $\phi'_{q_{peak}}$: Internal friction angle at peak deviator stress failure criterion.

Table 4.4. Friction angles for Cabo Rojo calcareous sand – Maximum Δu failure criterion.

γ_{dry} kN/m ³	$D_{r,ini}$ %	$D_{r,cons}$ %	σ'_c kPa	Δu_f kPa	σ'_{1f} kPa	σ'_{3f} kPa	ε_{axial_umax} %	$\phi'_{\Delta u_{max}}$ deg.
10.6	44%	62%	50	26.63	83.4	23.45	0.60	41.0
10.5	38%	48%	100	67.96	143.24	32.08	1.09	
10.7	50%	75%	300	230.05	349.76	70.01	1.96	
11.1	71%	80%	50	25.06	108.16	24.80	0.57	43.4
11.0	69%	76%	100	68.51	193.77	31.52	0.80	
11.0	66%	81%	300	233.08	356.00	66.98	1.58	
11.3	81%	86%	50	26.52	93.92	23.57	0.33	44.0
11.3	84%	94%	100	61.62	191.72	38.42	0.56	
11.6	95%	111%	300	223.15	444.30	76.90	1.22	

Notes: γ_{dry} : Dry unit weight, $D_{r,ini}$: Relative density before specimen consolidation, σ'_c : Effective confining pressure, Δu_f : Excess pore pressure at failure, σ'_{1f} : Principal major effective stress at failure, σ'_{3f} : Principal minor effective stress at failure, ε_{axial_umax} : Axial strain at maximum excess pore pressure, $\phi'_{\Delta u_{max}}$: Internal friction angle at maximum excess pore pressure failure criterion.

Table 4.5. Friction angles for Cabo Rojo calcareous sand – 10% axial strain failure criterion.

γ_{dry} kN/m ³	$D_{r \text{ ini.}}$ %	$D_{r \text{ cons}}$ %	σ'_c kPa	Δu_f kPa	σ'_{1f} kPa	σ'_{3f} kPa	$\phi'_{10\% \epsilon_{\text{axial}}}$ deg.
10.6	44%	62%	50	-29.27	400.97	79.24	43.0
10.5	38%	48%	100	18.17	439.86	81.87	
10.7	50%	75%	300	187.32	605.67	112.74	
11.1	71%	80%	50	-72.33	681.15	122.24	44.6
11.0	69%	76%	100	-17.83	701.20	117.86	
11.0	66%	81%	300	174.38	705.74	125.74	
11.3	81%	86%	50	-82.47	745.58	132.50	44.6
11.3	84%	94%	100	-66.05	938.43	166.03	
11.6	95%	111%	300	124.92	1022.70	175.08	

Notes: γ_{dry} : Dry unit weight, $D_{r \text{ ini.}}$: Relative density before specimen consolidation, σ'_c : Effective confining pressure, Δu_f : Excess pore pressure at failure, σ'_{1f} : Principal major effective stress at failure, σ'_{3f} : Principal minor effective stress at failure, $\phi'_{10\% \text{ axial strain}}$: Internal friction angle at 10% axial strain failure criterion.

It can be observed that the lowest values of internal friction angle were obtained from failure at peak deviator stress ($\phi'_{q_{\text{peak}}}$). This is a consequence of the dilative behavior exhibited by the Cabo Rojo sand specimens. This dilative behavior resulted in low pore pressure values at peak deviator stress (q_{peak}), most of them negative, which yielded high values of mean principal stress (p'). Therefore, the peak deviator stress points follows up the effective stress path diagram (q vs. p'). In contrast, the deviator stress points for 10% axial strain and for maximum excess pore pressure (Δu_{max}) failure criteria were positioned in the initial to medium parts of the effective stress path diagram due to their low values of mean principal stress (p'). Consequently, failure envelopes for the failure criterion of peak deviator stress have slopes lower than those obtained for the two other failure criteria.

The aforementioned dilative behavior was observed in the effective stress paths shown in Figures 4.8 through 4.10. The early generation of positive pore pressures caused a decrease in the mean principal stress (p') up to the phase transformation points. At these points, the excess pore pressures began to decrease, causing the effective stress paths to move to the right until the end of the tests. This is an indication of the dilative behavior of the sand specimens. The dilatant behavior for the Cabo Rojo sand was observed to decrease with increasing effective confining stress.

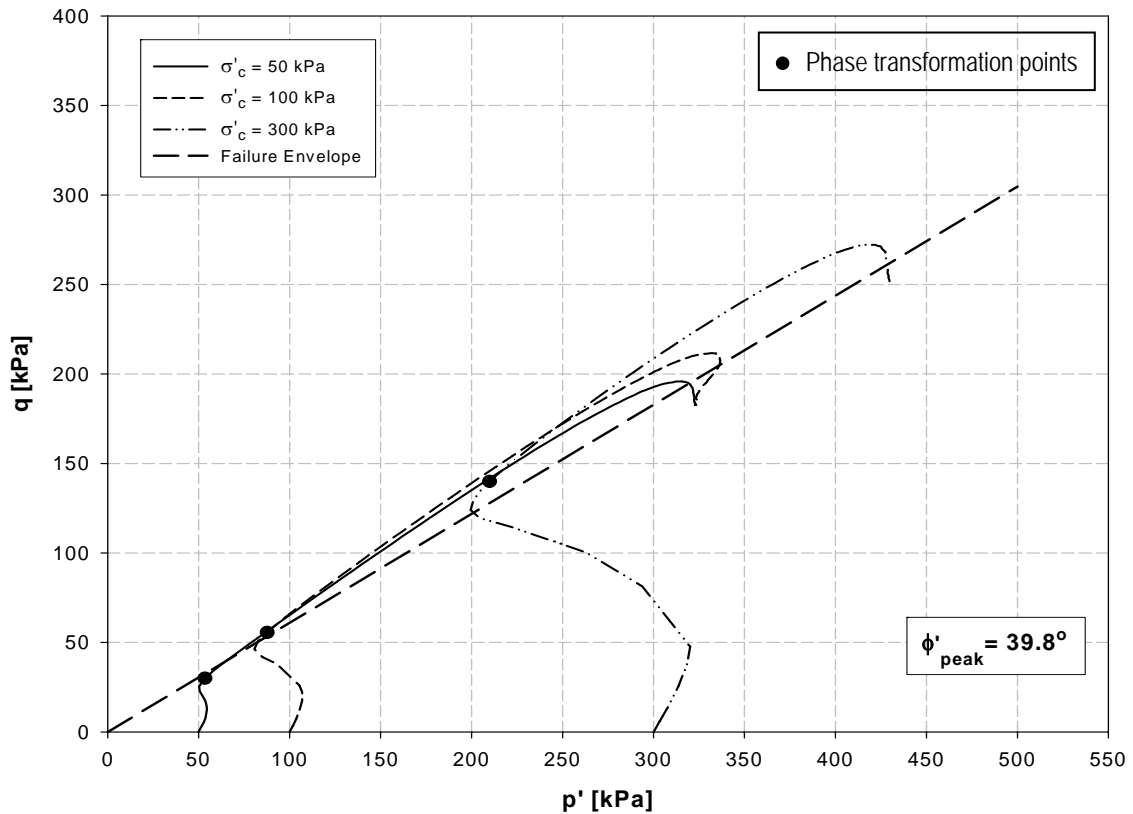


**Figure 4.8. Effective stress paths for Cabo Rojo sand at minimum density.
(Average $D_{r_{ini}} = 44\%$).**

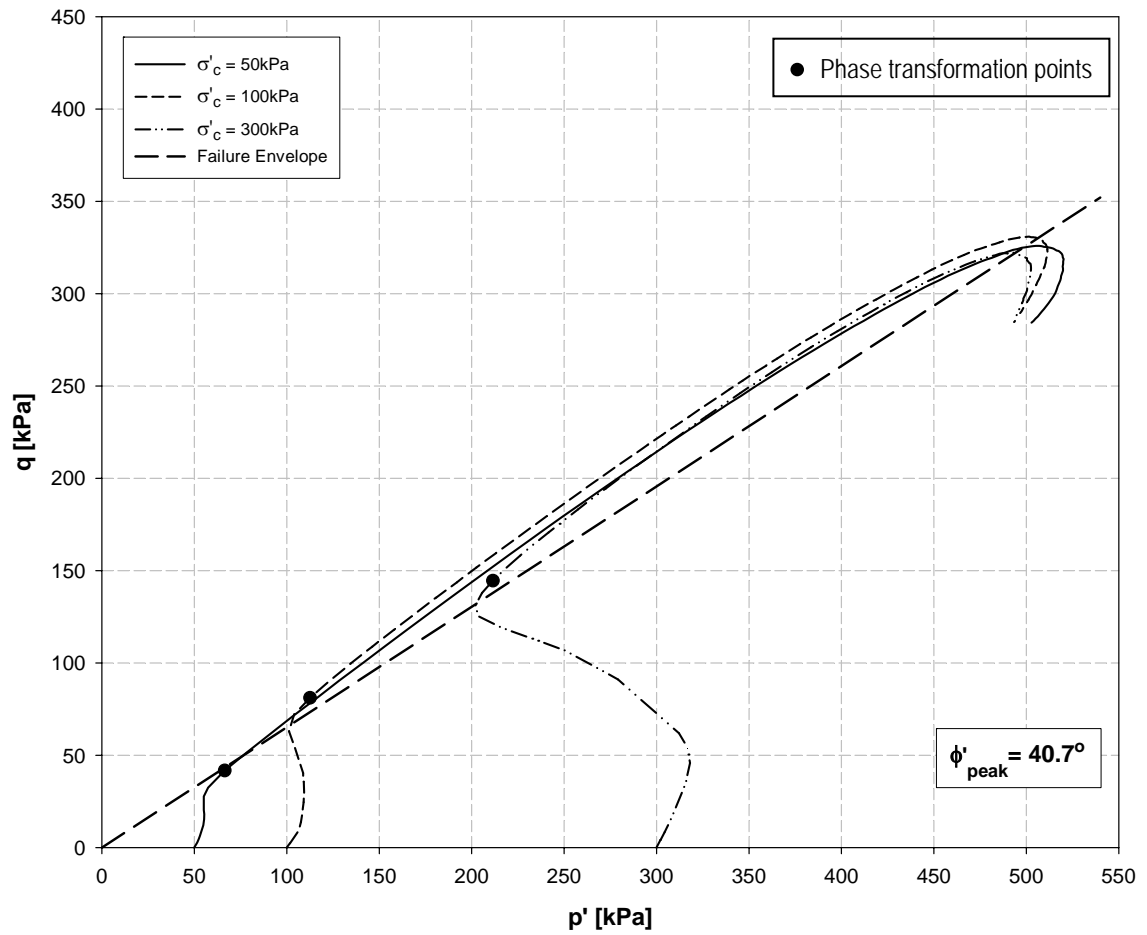


**Figure 4.9. Effective stress paths for Cabo Rojo sand at medium density.
(Average $D_{r_ini} = 69\%$).**

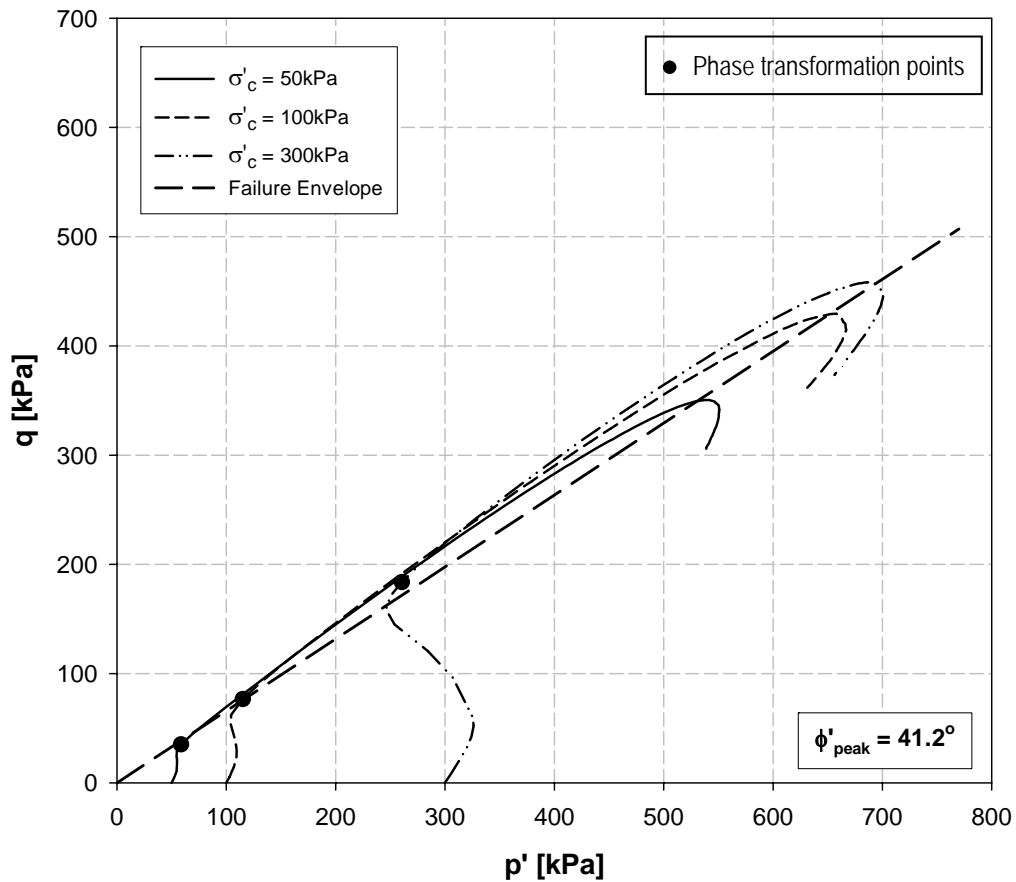


Figure 4.10. Effective stress paths for Cabo Rojo sand at maximum density. (Average $D_{r_{ini}} = 87\%$).

4.3 Steady State Behavior for Cabo Rojo Calcareous Sand

Steady state conditions were not achieved during initial triaxial tests carried out for this research. Results for these tests were presented in the preceding sections. To determine the steady state line of the Cabo Rojo sand, additional tests were required. New specimens were prepared, with a wide range of initial relative densities ($D_{r_{ini}}$: 4% - 104%). From the new set of tests, seven specimens reached steady state conditions at axial strain values ranging between 28% and 33%.

Results for the seven specimens that reached steady state conditions in this new set of ICU triaxial tests are shown in Figure 4.11. They include the steady state line and the paths followed by each specimen during monotonic undrained shearing. Initially, specimens started with an effective minor principal stress equal to the effective confining pressure (σ'_3), shown as open dots. As the undrained loading took place, values for all specimens moved horizontally to the left until the phase transformation point was achieved. After this, σ'_3 increased moving back to the right until reaching steady state conditions (shown as solid black dots). The line drawn through the solid black points is the steady state line (SSL).

Figure 4.12 shows the variations of excess pore pressure with axial strain during undrained shearing for the new specimens that were used to define the steady state line for the Cabo Rojo sand. In this figure, D_{r_cons} refers to the specimen relative density after consolidation, and u_b corresponds to the back pressure used to saturate the specimens. An increase in pore pressure with increasing axial strain can be observed after the steady state conditions were achieved.

This phenomenon was appreciated for all test specimens, independently of their initial density state or the back pressure applied during the saturation phase. This can be related to the change in the internal structure of the calcareous sand due to continuing crushing. As indicated earlier, these sand particles have high crushing potential which can help to explain the observed increase in pore pressures at the interpreted steady state. Continuing

crushing generates an increase of the water pressure inside the voids of the specimen that will keep increasing as axial strain increases, as shown in Figure 4.12.

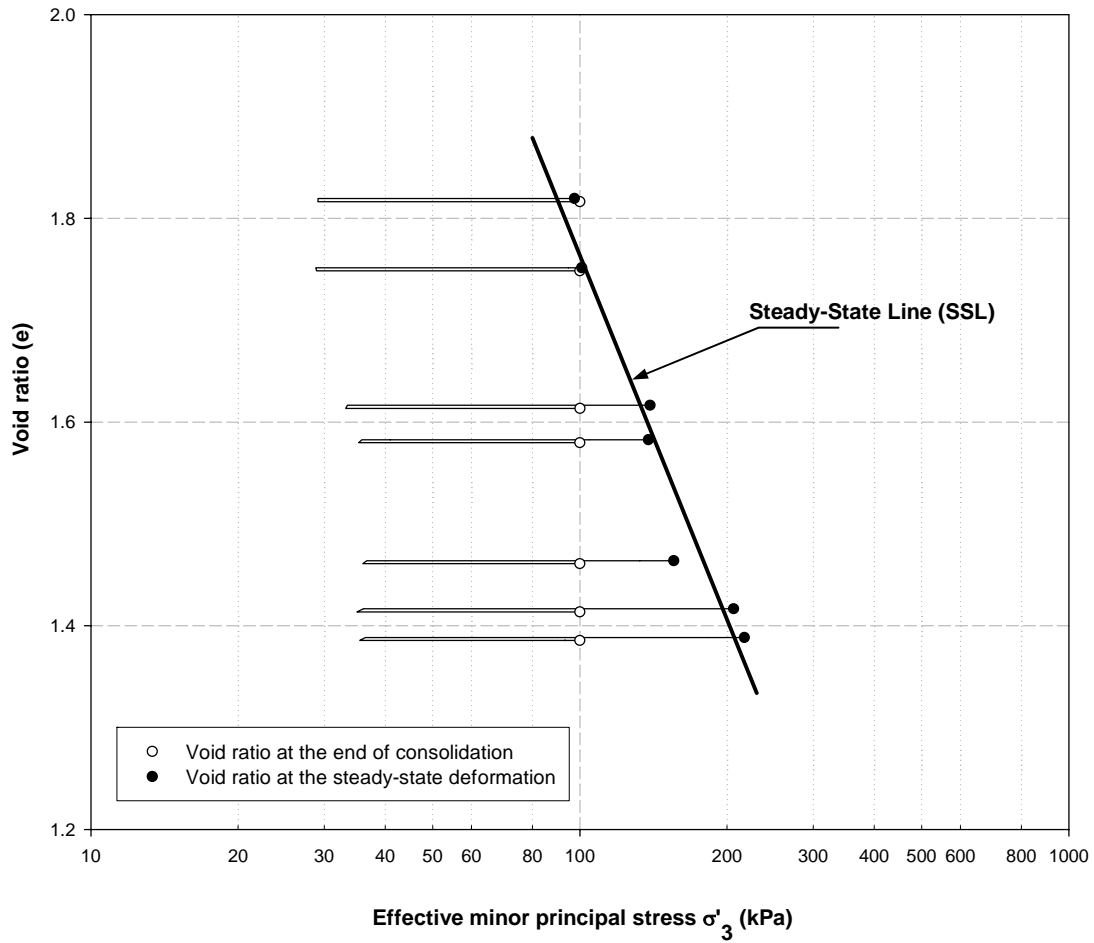


Figure 4.11. Steady state line for Cabo Rojo sand.

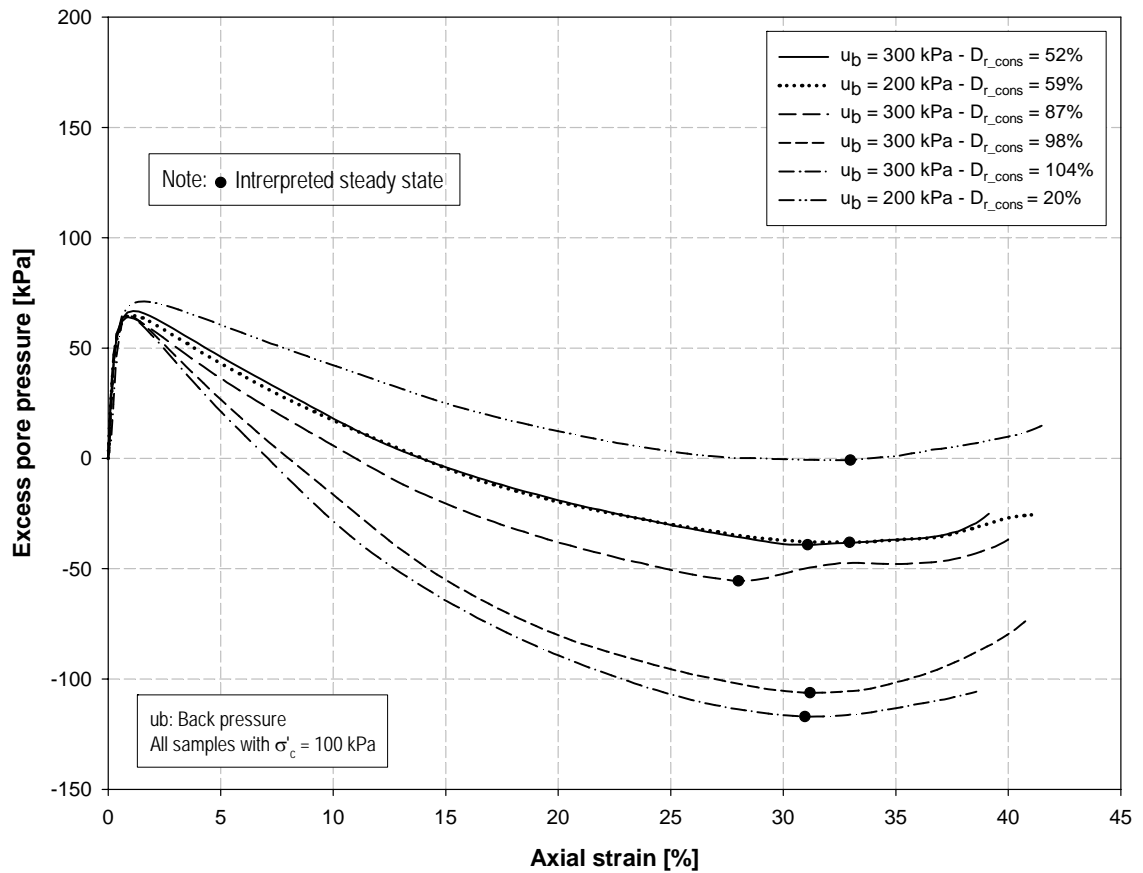
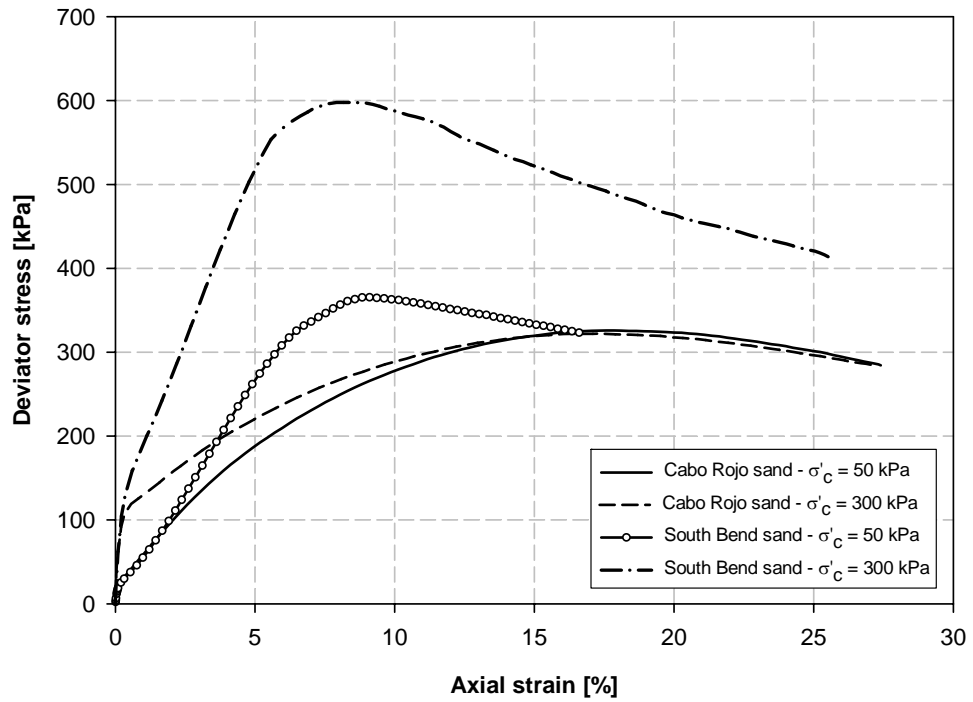


Figure 4.12. Excess pore pressure vs. axial strain curves for “steady-state” specimens of Cabo Rojo sand.

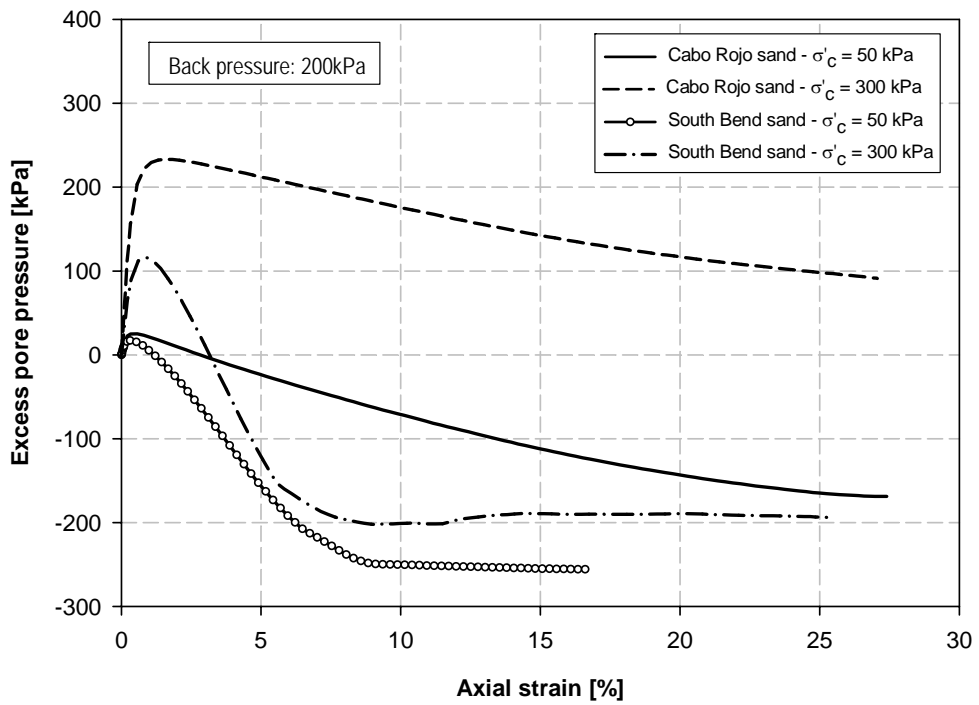
4.4 Stress-Strain Behavior Comparison between the Two Tests Sands

The stress-strain curves and the corresponding excess pore pressures for the Cabo Rojo and the South Bend sand are shown in Figures 4.13 and 4.14 respectively, for medium and maximum relative densities. These figures show results for 50 kPa and 300 kPa confining pressures.



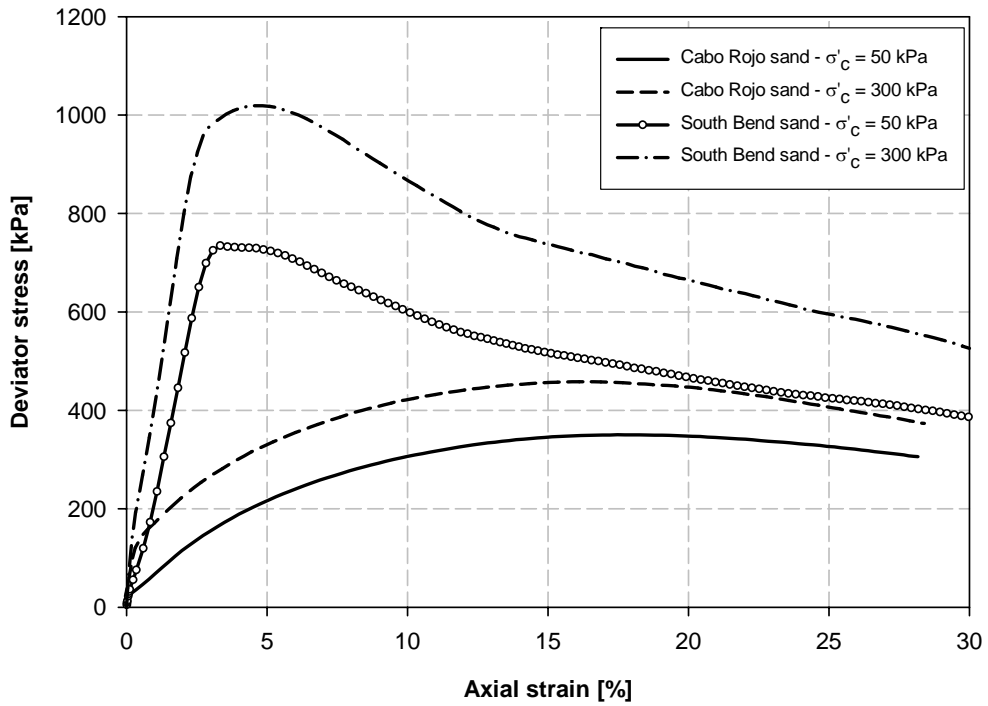
a) Deviator stress vs. axial strain

$D_{r,cons}$ average values:
 Cabo Rojo: 79%
 South Bend: 81%



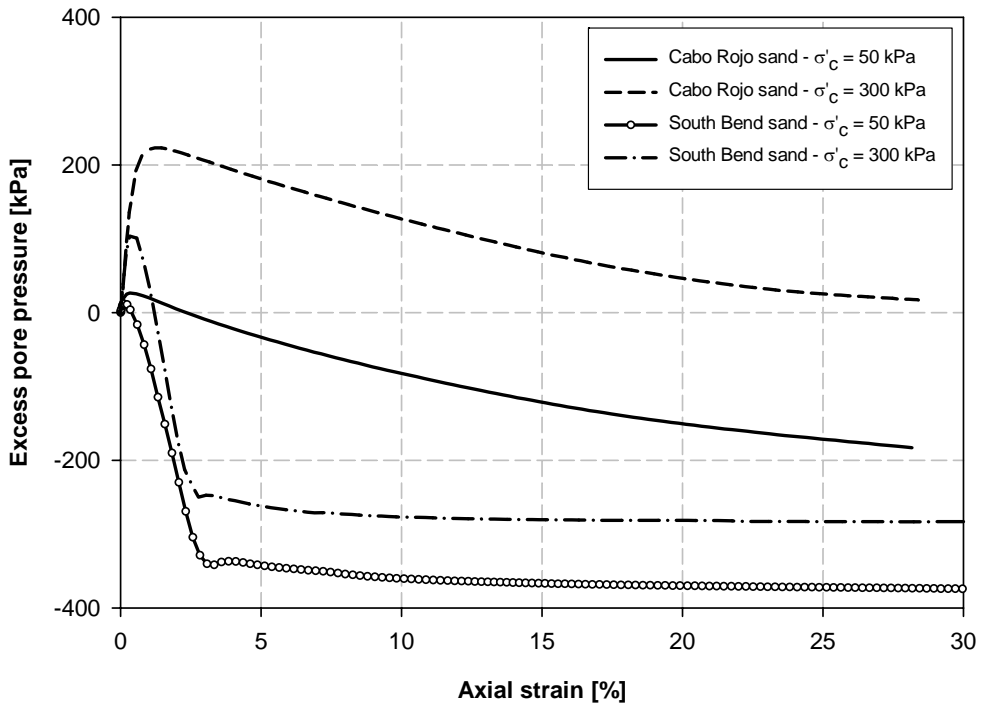
b) Excess pore pressure vs. axial strain

Figure 4.13. Comparison of ICU results for medium relative density.



a) Stress-strain curves

$D_{r,cons}$ average values:
 Cabo Rojo: 97%
 South Bend: 103%



b) Excess pore pressure curves

Figure 4.14. Comparison of ICU results for maximum relative density.

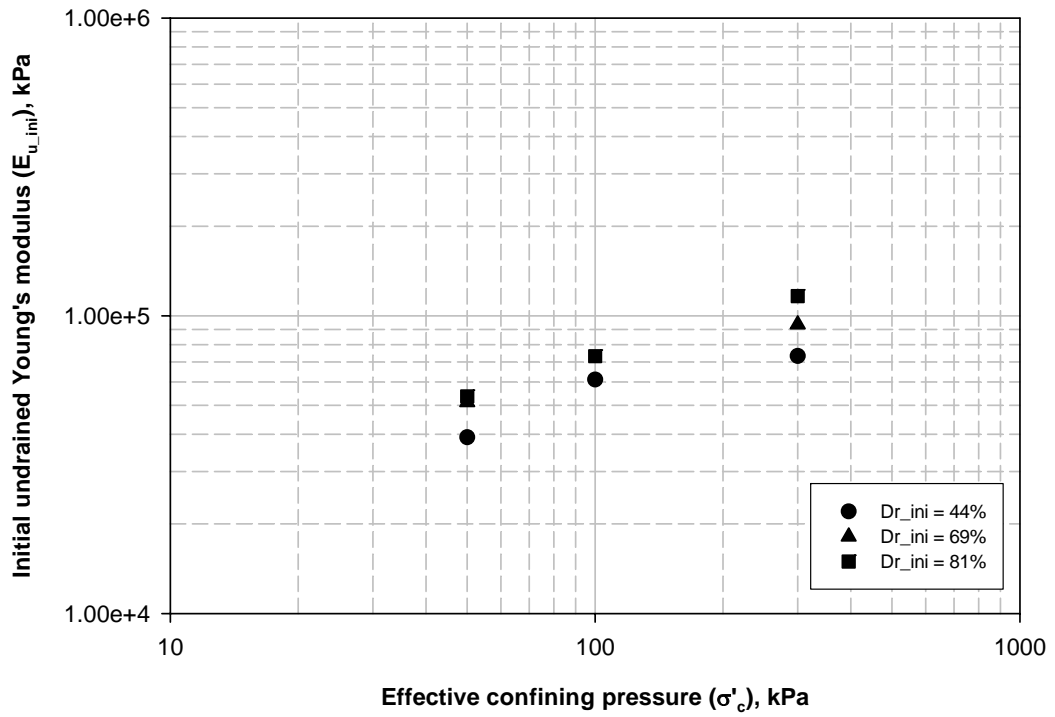
Examination of these curves indicates that strain-stress responses for the calcareous sand are different than those for the silica sand. The Cabo Rojo calcareous sand showed an evidently ductile behavior, where peak strength was achieved after large amounts of axial strain. In contrast, the South Bend silica sand exhibited a brittle response with a clear peak strength and the development of strain-softening behavior after peaking.

Table 4.6 shows the initial undrained Young's modulus values ($E_{u, ini}$) obtained for the Cabo Rojo and the South Bend sands, at the medium and maximum density states. Since the relative density values after consolidation ($D_{r, cons}$) of both sands resulted in appreciable differences, care must be taken when comparing the Young's modulus values provided in this Table. The variation with confining pressure of the $E_{u, ini}$ for both sands is presented in Figure 4.15

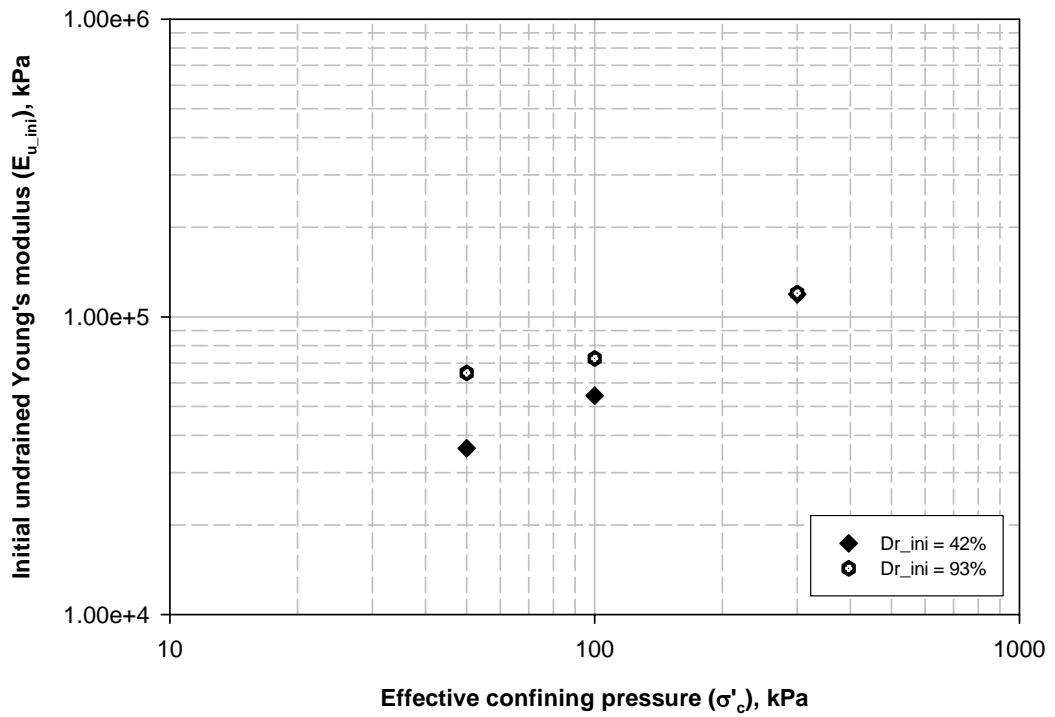
Table 4.6. Initial undrained Young's modulus for Cabo Rojo and South Bend sands.

σ'_c kPa	CABO ROJO SAND				SOUTH BEND SAND			
	γ_{dry} kN/m ³	$D_{r, ini}$ %	$D_{r, cons}$ %	$E_{u, ini}$ kPa	γ_{dry} kN/m ³	$D_{r, ini}$ %	$D_{r, cons}$ %	$E_{u, ini}$ kPa
50	11.08	71%	80%	51307	16.03	36%	79%	36167
100	11.03	69%	76%	---	16.20	44%	65%	54352
300	10.97	66%	81%	93568	16.22	45%	98%	119055
50	11.26	81%	86%	53610	17.51	95%	112%	64822
100	11.32	84%	94%	73196	17.42	92%	96%	72506
300	11.55	95%	111%	116388	17.46	93%	102%	120093

Notes: γ_{dry} : Dry unit weight, $D_{r, ini}$: Initial relative density, $D_{r, cons}$: Relative density after consolidation, $E_{u, ini}$: Initial undrained Young's modulus.



a) Cabo Rojo calcareous sand



b) South Bend silica sand

Figure 4.15. Comparison of the initial undrained Young's modulus.

From Table 4.6 it can be inferred that in the few cases where a comparable D_{r_cons} was obtained for both sands, the Cabo Rojo calcareous sand presented greater E_{u_ini} values. This seems to suggest that this sand has a higher initial stiffness. However, this data is not enough to reach definitive conclusions.

Equation (4.2) shows the shear modulus (G) for an elastic material in terms of its Young's modulus, E_u , and its Poisson's ratio, ν , (Bowles, 1996). This equation indicates that the relationship between the Young's and the shear modulus depends on the volumetric changes in the material determined by the Poisson's ratio.

$$G = \frac{E_u}{2(1 + \nu)} \quad (4.2)$$

When comparing the stress-strain behavior of the Cabo Rojo calcareous with the South Bend silica sands, the first one resulted in a less dilative behavior (see Figures 4.13b and 4.14b), which indicates a lower Poisson's ratio for the calcareous sand. Since the initial undrained Young's modulus values obtained for the Cabo Rojo sand were greater than those for the silica sand, equation (4.2) predicts greater shear modulus values for the Cabo Rojo sand. This is contrary to the findings presented in Chapter 5, which show larger shear modulus values for the South Bend sand. However, one should recognize that the strain levels of the triaxial test measurements are not considered representative of initial modulus values measured using the resonant column test.

Table 4.7 shows a summary of some characteristic values of the stress-strain response for the Cabo Rojo and the South Bend sands. Regarding the peak strength of both sands, the table shows that peak deviator stress values for Cabo Rojo sand ranged between 196 and 458 kPa at axial strains between 16.3% and 19.6% respectively. In contrast, the South Bend sand exhibited peak deviator stress values between 365 and 1019 kPa at axial strains from 3.3% to 9.1%. The same type of response was obtained for the deviator stress values at 10% axial strain, in which the Cabo Rojo sand exhibited lower values than those for the South Bend sands. These results clearly confirm the softer stress-strain behavior of the calcareous sand when compared with the silica sand.

Table 4.7 also compares the maximum excess pore pressure (Δu_{\max}) of the test sands, and their corresponding axial strain ($\epsilon_{\text{axial } \Delta u_{\max}}$). The Cabo Rojo sand exhibited higher positive Δu_{\max} values, which confirms the more contractive behavior of this sand when compared to the South Bend sand. Negligible differences were found in the axial strain at the maximum excess pore pressure of both sands.

Comparison of the curves of excess pore pressure vs. axial strain, included in Figures 4.13b and 4.14b, show that for the same confining pressures, silica sand exhibited a most clearly dilative behavior than calcareous sand. Although calcareous sand show a smooth drop in excess pore pressure with increasing axial strain, positive values were obtained only during the test for 300 kPa of confining pressure. This indicates that contractive behavior could be expected for higher confining pressures.

Table 4.7. Characteristic stress-strain values for Cabo Rojo and South Bend sands.

CABO ROJO SAND							
σ'_c kPa	$D_{r_ini.}$ %	D_{r_cons} %	q_{peak} kPa	ε_{axial_peak} %	$q_{10\% \varepsilon_{axial}}$ kPa	Δu_{max} kPa	$\varepsilon_{axial \Delta u_{max}}$ %
50	71%	80%	325.85	17.85	279.46	25.06	0.57
100	69%	76%	330.86	17.58	291.67	68.51	0.80
300	66%	81%	322.10	17.36	290.00	233.08	1.58
50	81%	86%	350.45	17.47	306.54	26.52	0.33
100	84%	94%	429.40	16.97	386.20	61.62	0.56
300	95%	111%	458.14	16.37	423.81	223.15	1.22
SOUTH BEND SAND							
σ'_c kPa	$D_{r_ini.}$ %	D_{r_cons} %	q_{peak} kPa	ε_{axial_peak} %	$q_{10\% \varepsilon_{axial}}$ kPa	Δu_{max} kPa	$\varepsilon_{axial \Delta u_{max}}$ %
50	36%	79%	365.28	9.10	362.86	15.31	0.54
100	44%	65%	402.40	6.26	376.04	40.48	0.83
300	45%	98%	597.72	7.92	587.71	112.14	1.14
50	95%	112%	734.68	3.33	598.39	10.93	0.23
100	92%	96%	809.69	4.60	680.35	28.32	0.34
300	93%	102%	1018.91	4.58	864.88	100.64	0.57

Notes: σ'_c : Effective confining pressure, $D_{r_ini.}$: Relative density before specimen consolidation, q_{peak} : Peak deviator stress, ε_{axial_peak} : Axial strain at peak deviator stress, $q_{10\% \varepsilon_{axial}}$: Deviator stress at 10% axial strain, Δu_{max} : Maximum excess pore pressure, $\varepsilon_{axial \Delta u_{max}}$: Axial strain at maximum excess pore pressure.

When comparing the stress paths for both sands shown in Figures 4.16 and 4.17, they show that although calcareous sands presented higher friction angles than silica sand, silica sand has great shear strength than calcareous sand, with higher peak deviatoric stress. Cabo Rojo sand showed peak strength values visibly lower than South Bend sand. This soft strength response exhibited by Cabo Rojo calcareous sand confirms what had been stated in technical literature about the anomalous geotechnical behavior of calcareous sands.

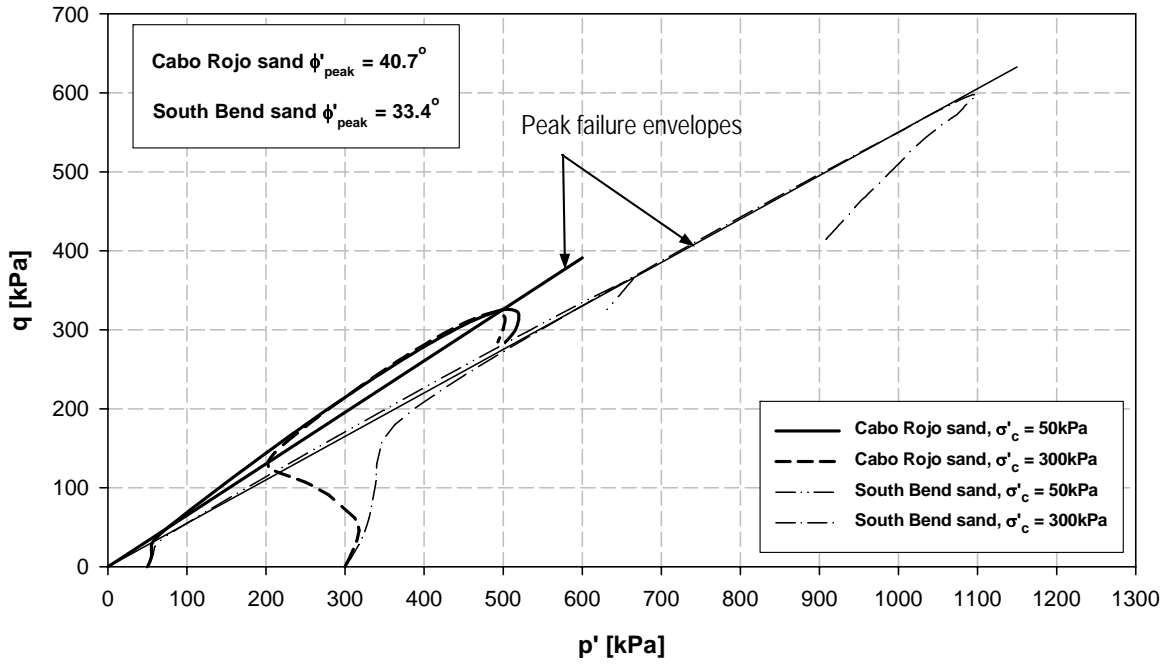


Figure 4.16. Effective stress paths for Cabo Rojo and South Bend sands at medium density.

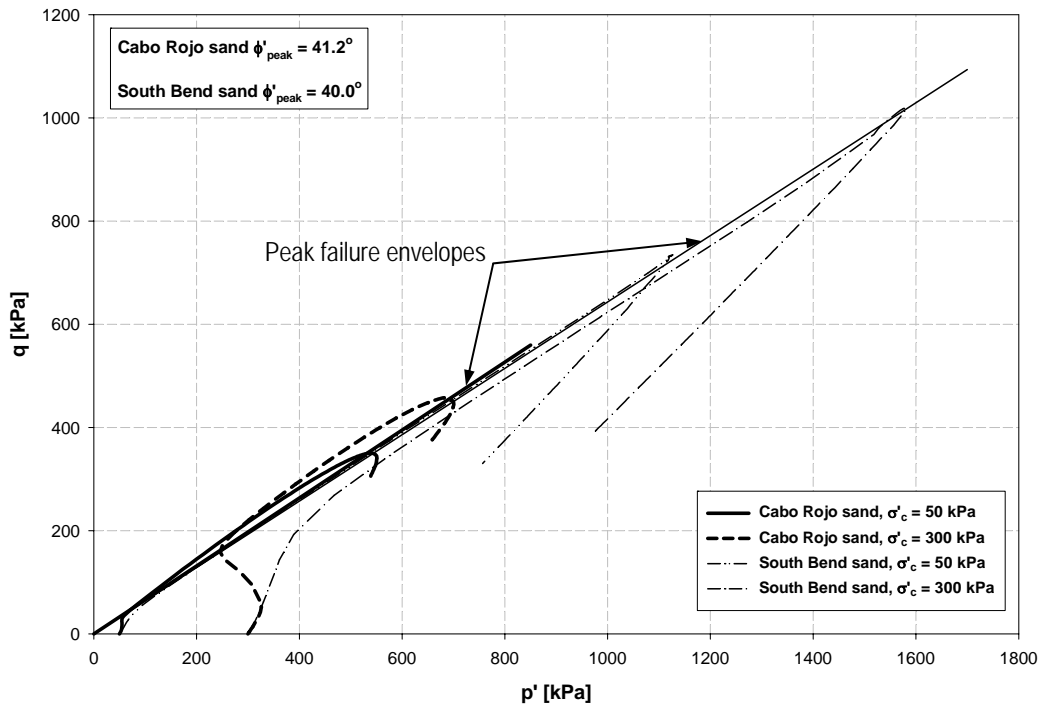


Figure 4.17. Effective stress paths for Cabo Rojo and South Bend sands at maximum density.

With regard to the steady state behavior of both sands, Figure 4.18 shows a comparison of the Cabo Rojo sand steady state line (SSL) and the steady state lines for some subangular and angular non-calcareous sands given by Poulos et al. (1985). Examination of the SSL of both subangular and angular grain sands indicates that the shape of the grains affects the slope of the steady state line (Poulos et al., 1985). Sands with angular grains have a higher SSL slope than subangular grain sands. The SSL of the Cabo Rojo sand presents an even steeper slope than the SSL presented by Poulos et al. (1985) for angular grain sands. This is due to the unique particle shapes of the Cabo Rojo sand, which is illustrated on Chapter 3.

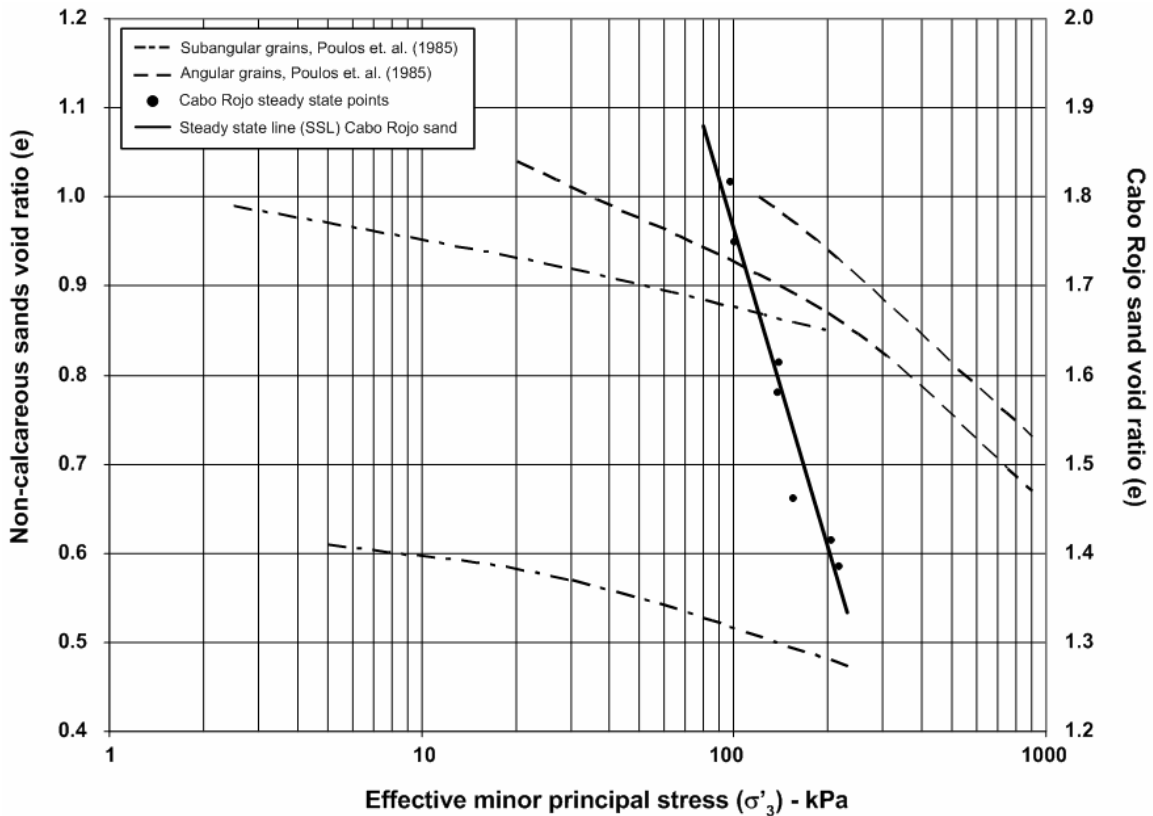


Figure 4.18. Comparison between steady state lines (SSL) for non-calcareous sands and Cabo Rojo sand.

4.5 Summary and Discussion

This chapter provided the results of the ICU triaxial testing program performed on the Cabo Rojo calcareous sand to determine its stress-strain behavior. The analyses of the stress-strain response included the determination of the effective stress paths and the steady state line for Cabo Rojo sand. The results obtained for the South Bend silica sand, for the same the ICU triaxial testing program, were used for comparison purposes.

The stress-strain curves of the Cabo Rojo calcareous sand showed an increment in specimen strength with increasing confining pressure. These curves exhibited very steep initial slopes before reaching the phase transformation points. After this point, universal strain hardening was observed up to the peak deviator stress. After achieving peak deviatoric stress, the Cabo Rojo sand showed a slight softening.

The initial increase in pore pressure, as observed in the excess pore pressure vs. axial strain curves, showed an initial contractive behavior of the Cabo Rojo sand specimens. This was followed by a drop in pore pressure, which indicated a dilative behavior at the effective confining pressures used in this study. This degree of dilatant behavior was observed to decrease with increasing effective confining stress.

Initial undrained Young's modulus values ($E_{u, ini}$) were obtained for the Cabo Rojo sand from the earliest portion of the stress-strain curves. $E_{u, ini}$ values between 51 MPa and 116 MPa were obtained for the specimens. The variations of $E_{u, ini}$ with confining

stress were in good agreement with the relationship proposed by Janbu (1963). Correlation coefficients (R^2) between 0.871 and 0.999 were obtained for the fitting of Cabo Rojo sand data.

Three types of failure criteria were analyzed for the Cabo Rojo calcareous sand: peak deviator stress, 10% of axial strain, and maximum excess pore pressure. For each criterion, the internal friction angle was determined. The criterion that yielded the lowest friction angles was the peak deviator stress. This is due to the lower values of excess pore pressure (Δu) developed in the Cabo Rojo sand specimens at the peak deviator stress, which in turn yielded higher values of mean principal stress (p'). This causes failure envelopes with lower slope values; i.e., peak friction angles. Internal friction angles between 39.8° and 44.6° were obtained. These values are higher than those obtained for the South Bend silica sand, which is in agreement with what had been stated in technical literature.

The stress-strain behavior of the Cabo Rojo calcareous sand was compared with the corresponding stress-strain response of the South Bend silica sand. Examination of the stress-strain curves indicated different strain-stress responses. Cabo Rojo sand showed an evidently ductile behavior; peak strengths were achieved after large amounts of axial strain. In contrast, the silica sand exhibited an evidently brittle response, with a clear peak strength and the development of strain-softening after peaking. The comparison also showed that silica sand exhibited a most clearly dilative behavior than calcareous sand.

The main findings regarding the difference in the stress-strain behavior of the Cabo Rojo calcareous sand and South Bend silica sand are listed below:

- Ductile behavior: the Cabo Rojo sand exhibited higher axial strain values to achieve peak deviator stresses than South Bend sand.
- Soft strength response: the Cabo Rojo sand exhibited lower deviator stresses at peaking and at 10% axial strain than South Bend sand.
- More contractive behavior: the Cabo Rojo sand exhibited higher positive excess pore pressure up to the phase transformation points than South Bend sand.

The steady state line (SSL) for the Cabo Rojo calcareous sand was obtained from the ICU triaxial test results. This line was compared with others obtained by Poulos et al. (1985) for some subangular and angular non-calcareous sands. The steady state line for the Cabo Rojo sand presented a steeper slope than the SSL presented Poulos et al. (1985). It is believed that this is mainly due to the unique characteristics of the Cabo Rojo calcareous sand particles, which differ from silica sand particles in mineralogy, shape and texture.

5 DYNAMIC PROPERTIES OF THE CABO ROJO SANDS

5.1 Introduction

This chapter presents the results of the experimental program performed to obtain the dynamic properties of the Cabo Rojo calcareous sands. For comparison purposes, the dynamic properties for the South Bend silica sand described in Chapter 3 are also presented. These dynamic properties were obtained from the resonant column (RC) testing program described in Chapter 3. The test results are first presented in terms of the maximum shear modulus (G_{\max}) and minimum damping ratio (D_{\min}) for the Cabo Rojo sand. Results are then presented in terms of the variation of the dynamic properties at medium to large shear strain levels. Finally, a comparison between the dynamic properties for both, Cabo Rojo and South Bend sands is presented.

5.2 Dynamic Properties of Cabo Rojo Sands at Small Shear Strains

This section presents the description of the small strain dynamic properties of the Cabo Rojo calcareous sand. The variation of dynamic properties with greater shear strain levels are presented later in section 5.3

5.2.1 Maximum shear modulus of the Cabo Rojo sand

Sands typically behave as linear elastic at very small shear strains of less than about 0.00001 ($\gamma \leq 10^{-3}$ %), (Ishihara, 1996). The limit shear strain at which soil exhibits dynamic properties independent of shear amplitude is called *threshold strain* (γ_{th}). The shear modulus in the range of very small shear strains is often referred to as the “small-strains shear stiffness” or “maximum” shear modulus (G_{max}). Herein it will be referred to as maximum shear modulus, G_{max} . G_{max} is directly related to soil skeleton arrangement, porosity, mineralogy, fabric, and stress state.

From the theory of elastic propagation of torsional waves, G_{max} is related to shear wave speed, V_s , as follows (Kramer, 1996):

$$G_{max} = \rho(V_s)^2 \quad (5.1)$$

where ρ is the soil mass density.

G_{max} was determined as part of the experiments carried out with the resonant column apparatus described in section 3.5. The computed values of G_{max} as a function of confining pressure for different relative densities of the Cabo Rojo calcareous sand are shown in Figure 5.1. This figure shows G_{max} values for specimens prepared at three relative densities: loose ($D_r = 21\%$); medium ($D_r = 58\%$); and dense ($D_r = 91\%$).

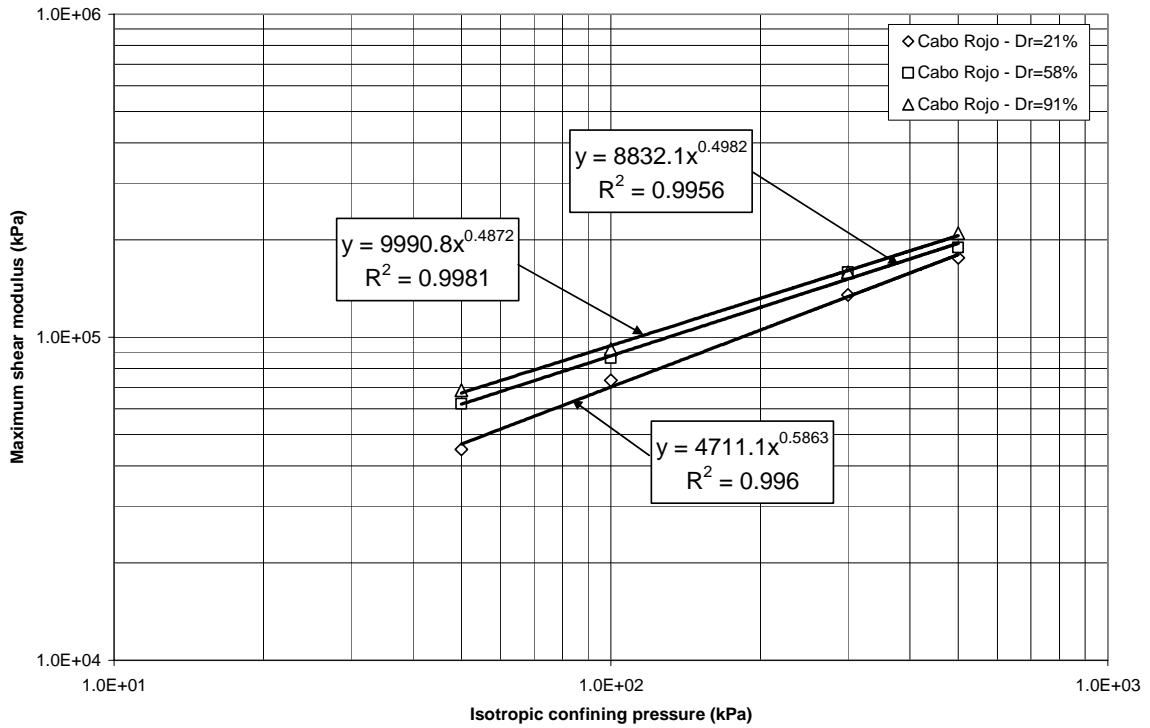


Figure 5.1. Variation of maximum shear modulus with effective confining pressure on Cabo Rojo calcareous sand.

As expected, G_{\max} was found to increase with the isotropic confining stress. For each set of tests, Figure 5.1 shows power law fits of the type proposed by Hardin and Richart (1963), of the following form:

$$G_{\max} = A_0 \left(\frac{\sigma'_0}{1 \text{ kPa}} \right)^n \quad (5.2)$$

where A_0 is the G_{\max} value in kPa corresponding to an effective isotropic confining stress of 1 kPa; σ'_0 is the effective isotropic confining stress in kPa; and n is a dimensionless exponent.

The values of the correlation coefficients (R^2) for the fits using the power equation (5.2) were all found to be above 0.99, indicating very good fits. The parameters for the power law fits corresponding to the three tested densities are provided in Table 5.1.

Table 5.1. Power law parameters for Cabo Rojo calcareous sand.

Specimen void ratio, e	Relative density, D_r	Specimen density (g/cm^3)	$A_0^{(1)}$ (kPa)	Exponent, $n^{(1)}$	R^2
1.50	21%	1.15	4711.1	0.5863	0.9960
1.39	58%	1.20	8832.1	0.4982	0.9956
1.29	91%	1.25	9990.8	0.4872	0.9981

(1): From equation (5.2)

The values of the exponent n ranges between 0.487 and 0.586, and were found to increase with increasing specimen void ratio. The value of this exponent indicates the degree of dependency of G_{\max} to the confining stress level (σ'_o). An exponent value of 0.33 is predicted for a soil composed of elastic spherical particles with a Hertzian contact relationship, while a value of 0.5 is predicted for an ideal soil composed of spherical particles that exhibit yielding at their contact points (Santamarina et al., 2001). The exponent values obtained for the Cabo Rojo sand are closer to the value corresponding to a soil exhibiting yield at their contacts.

The higher the exponent reflects a higher degree of influence of G_{\max} to the stress level. The higher exponent value for the loosest sand specimens can be explained by the fact that a looser initial state has fewer contact points as compared to specimens prepared in a denser initial state. Therefore the effect of increasing the confining stress will be

higher since there is more room to develop newer contacts which result in an increase in G_{\max} .

The values of A_0 increased with decreasing specimen void ratio (or increasing density). This trend is expected since A_0 depends on, among other factors, initial packing or porosity and the coordination number, C_n (Santamarina et al., 2001). The coordination number of a soil (C_n) is the average number of contacts it has per particle. In general, the higher the C_n , the higher the stability and stiffness of the packing of the soil (Santamarina et al., 2001).

The values of A_0 and n can be further evaluated if we compare them with the following velocity-stress relationship proposed by Santamarina et al. (2001) for granular media under isotropic loading:

$$V_s = \alpha \cdot \left(\frac{\sigma'_0}{1 \text{ kPa}} \right)^\beta \quad (5.3)$$

If we incorporate equation (5.1) we obtain:

$$G_{\max} = (\rho \cdot \alpha^2) \left(\frac{\sigma'_0}{1 \text{ kPa}} \right)^{2\beta} \quad (5.4)$$

Therefore α and β are related to A_0 and n as follows:

$$\alpha = \sqrt{\frac{A_0}{\rho}} \quad (\text{m/s}) \quad (5.5)$$

$$\beta = \frac{n}{2} \quad (\text{dimensionless}) \quad (5.6)$$

The experimental values obtained for the Cabo Rojo calcareous sand are plotted in Figure 5.2 as black diamonds. Other experimental values of the coefficients α and β for various granular materials are also shown in this figure as unfilled symbols. The inverse relationship between α and β proposed by Fernandez (2000) is shown as a dashed line. As can be seen, the values of α and β (or A_0 and n) for the Cabo Rojo sands compare reasonably well with the data presented in Figure 5.2.

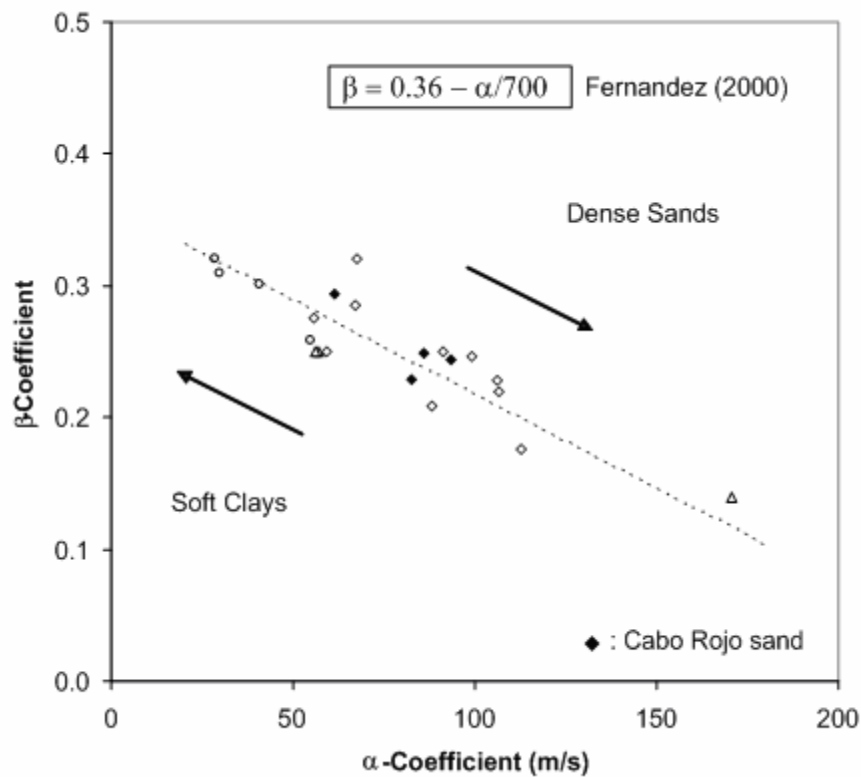


Figure 5.2. Coefficients α and β for Cabo Rojo calcareous sand (After Fernandez, 2000).

Empirical relationship for G_{\max} : Many empirical relationships based on a power relationship between G_{\max} and effective confining stress have been proposed in the literature (Hardin and Richart, 1963; Hardin and Drnevich, 1972; Saxena et al., 1988; Jamiolkowski et al., 1991; Lo Presti, 1995). They all propose a G_{\max} - stress power relationship of the form of equation (5.2). Recognizing the influence of degree of packing, as related to void ratio (e), the following expression is commonly used:

$$G_{\max} = AF(e)P_{atm} \left(\frac{\sigma'_0}{P_{atm}} \right)^n \quad (5.7)$$

where A is a dimensionless constant related to soil shear stiffness; $F(e)$ is a homogenization function related to the soil void ratio; P_{atm} is the atmospheric pressure in the same units as confining pressure (σ'_0); and n is a dimensionless exponent. Typical values for the empirical parameters of equation (5.7) are provided in Table 5.2 for regular quartz sands.

Using a formulation of the type given by equation (5.7) and the parameters shown in Table 5.1, an empirical expression for G_{\max} was obtained for the Cabo Rojo calcareous sand. By combining equations (5.2) and (5.7), equation (5.8) was obtained:

$$G_{\max} = A_0 \left(\frac{\sigma'_0}{1 \text{ kPa}} \right)^n \quad (5.2)$$

$$G_{\max} = AF(e)P_{atm} \left(\frac{\sigma'_0}{P_{atm}} \right)^n \quad (5.7)$$

$$AF(e) = A_0 \frac{P_{atm}^n}{P_{atm}} \quad (5.8)$$

Table 5.2. Typical parameters of G_{max} of quartz sand (After Kokusho, 1987).

Reference	Sand characteristics	A	F(e)	Exponent, n
Hardin-Richart (1963)	Round grained Ottawa sand	700	$\frac{(2.17 - e)^2}{(1 + e)}$	0.5
Hardin-Richart (1963)	Angular grained crushed quartz	330	$\frac{(2.97 - e)^2}{(1 + e)}$	0.5
Shibata-Soelarno (1975)	Three kinds of clean sand	4180	$\frac{0.67 - e}{(1 + e)}$	0.5
Iwasaki et al. (1978)	Eleven kinds of clean sand	515	$\frac{(2.17 - e)^2}{(1 + e)}$	0.38
Kokusho (1980)	Toyoura sand	840	$\frac{(2.17 - e)^2}{(1 + e)}$	0.5
Yu-Richart (1984)	Three kinds of clean sand	700	$\frac{(2.17 - e)^2}{(1 + e)}$	0.5

A power expression was proposed for the homogenization function $F(e)$, which is related to the specimen void ratio, as shown in equation (5.9):

$$F(e) = e^x \quad (5.9)$$

where e is the void ratio of the sand specimens.

Incorporating equation (5.9) into equation (5.8) the following expression was obtained:

$$A \cdot e^x = A_0 P_{atm}^{(n-1)} \quad (5.10)$$

Since the right part of the equation (5.10) is a constant value (see Table 5.1), the unknown values in the expression are: the constant A, related to soil shear stiffness, and the exponent “x” used for the function F(e). If the natural logarithm is applied to the both parts of the expression, equation (5.10) results in:

$$\begin{aligned}\ln(A \cdot e^x) &= \ln(A_0 P_{atm}^{(n-1)}) \\ \ln(A) + x \ln(e) &= \ln(A_0 P_{atm}^{(n-1)})\end{aligned}\quad (5.11)$$

The natural logarithm of the specimen’s void ratio ($\ln(e)$) was called “X” and the right part of the equation (5.11) was called “Y”. Equation (5.11) then results in:

$$\ln(A) + xX = Y \quad (5.12)$$

Equation (5.12) is the equation of a line with a slope equal to the exponent “x” and an intercept equal to the natural logarithm of the constant A. Then, using the values shown in Table 5.1, the values of X and Y were obtained for each specimen’s void ratio, as shown in Table 5.3. These X and Y points were drawn in Figure 5.3. Using a linear regression, the equation of the line shown in this Figure was obtained, which indicates a slope (x) equal to -1.953 and an intercept ($\ln(A)$) equal to 7.3631.

Then, the following parameters were obtained for the Cabo Rojo calcareous sand:

$$\begin{aligned}\ln(A) &= 7.3631 \\ A &= \exp(7.3631) = 1576.64\end{aligned}\quad (5.13)$$

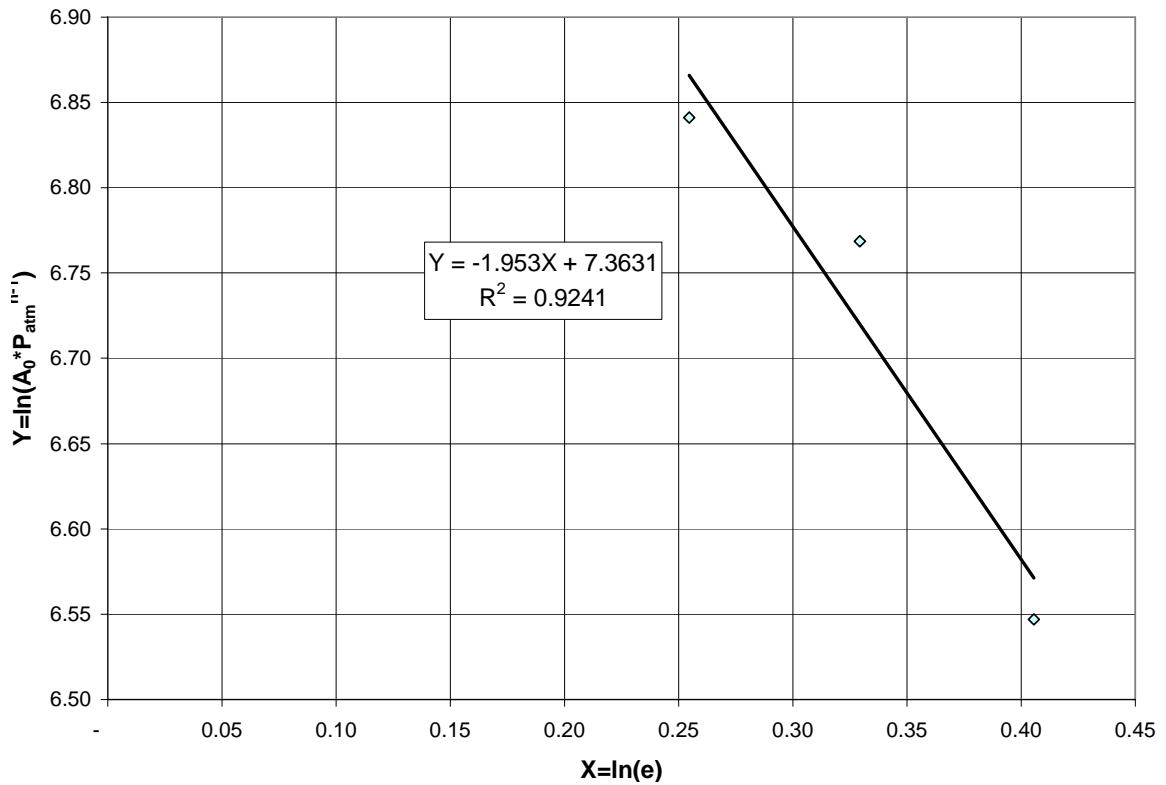
$$F(e) = e^x = e^{-1.953}$$

$$F(e) = \frac{1}{e^{1.953}} \quad (5.14)$$

Table 5.3. Values of X and Y in equation (5.12).

Void ratio, e	$A_0^{(1)}$ (kPa)	Exponent, n (1)	P_{atm} (kPa)	$A_0 * P_{atm}^{n-1}$	$X = \ln(e)$	$Y = \ln(A_0 * P_{atm}^{n-1})$
1.50	4711.10	0.5863	101.325	697.20	0.405	6.547
1.39	8832.10	0.4982		870.15	0.329	6.769
1.29	9990.80	0.4872		935.55	0.255	6.841

(1): From equation (5.2)

**Figure 5.3. Linear regression to obtain the parameters of the G_{max} expression for the Cabo Rojo calcareous sand.**

Using the parameters given in equations (5.13) and (5.14), and with an average value of 0.52 for the exponent n , the empirical formulation for G_{\max} obtained for the Cabo Rojo sand may be expressed as follows:

$$G_{\max} = 1577 \cdot \left(\frac{1}{e^{1.953}} \right) \cdot P_{atm} \cdot \left(\frac{\sigma'_0}{P_{atm}} \right)^{0.52} \quad (5.15)$$

The fits obtained for the Cabo Rojo calcareous sand using equation (5.15) are compared with the actual test data in Figure 5.4.

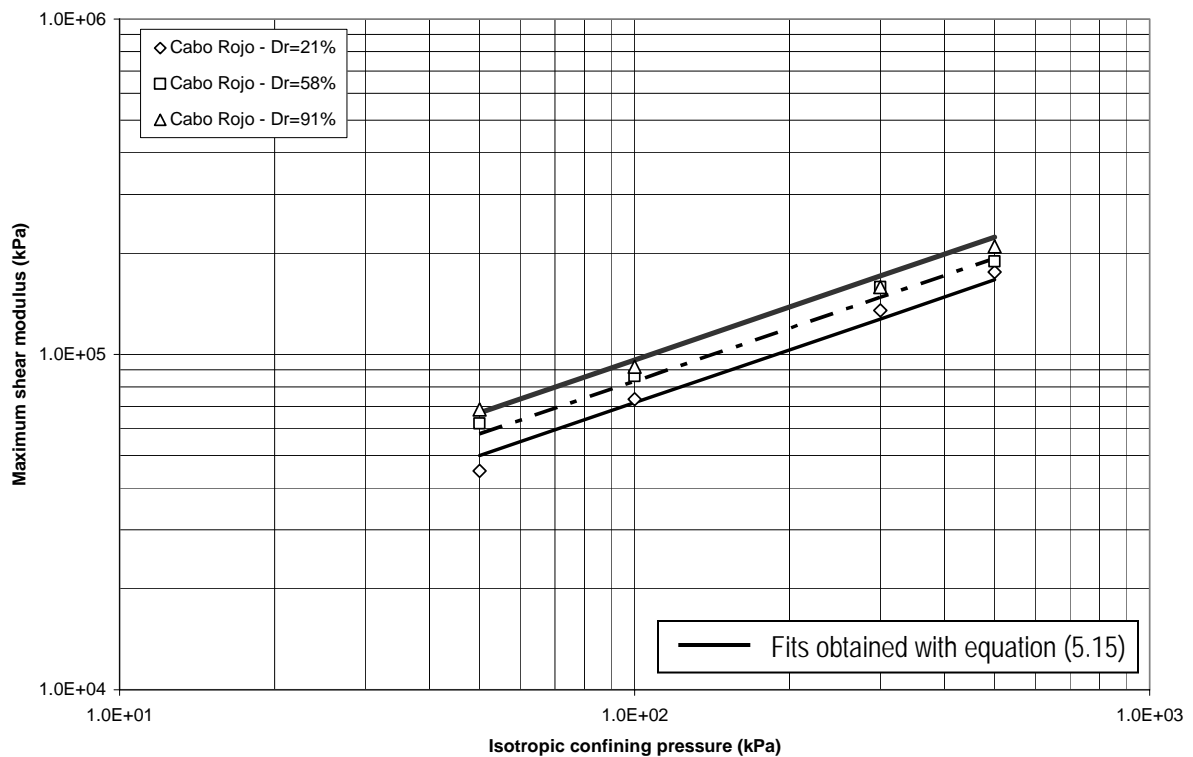


Figure 5.4. Comparison between equation (5.15) for G_{\max} and actual test data.

As shown in Figure 5.4, the values of G_{\max} predicted by equation (5.15) compare reasonably well with the experimental values.

A better fit would be achieved if the exponent n is allowed to vary as a function of specimen void ratio, as it was observed in the experimental data. A preliminary approach would be to use a simple linear regression between the experimental values of n and the sand specimens void ratios, as follows:

$$n = 0.4774 \cdot e - 0.1412 \quad (5.16)$$

Equation (5.16) is preliminary and only applicable to the range of confining stresses used in this study (50 to 500 kPa). Replacing the average exponent value ($n = 0.52$) in equation (5.15) for the new n expression of the equation (5.16), results in:

$$G_{\max} = 1577 \left(\frac{1}{e^{1.953}} \right) \cdot P_{atm} \left(\frac{\sigma'_0}{P_{atm}} \right)^{0.4774e - 0.1412} \quad (5.17)$$

The predicted G_{\max} values using equation (5.17) are shown in Figure 5.5.

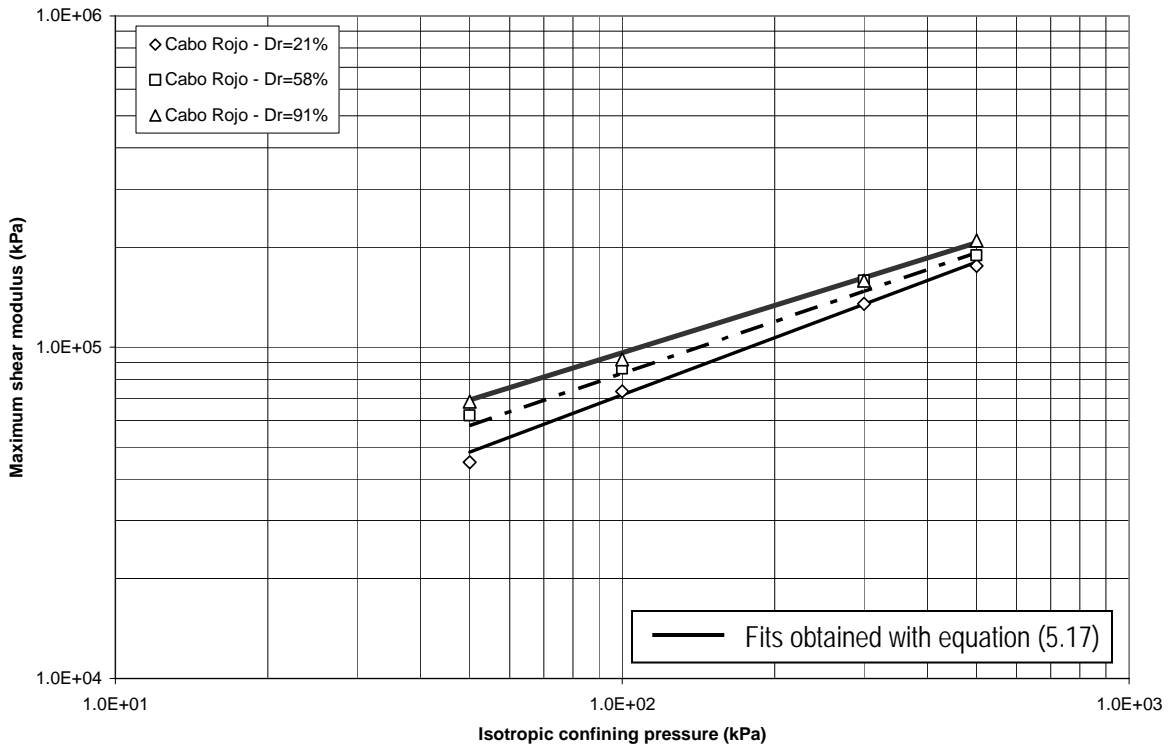


Figure 5.5. Comparison between equation (5.17) for G_{max} and actual test data.

5.2.2 Minimum damping ratio of the Cabo Rojo sand

The damping ratio at very low shear strains (< 0.0001) is referred to as D_{min} . The variation of D_{min} as a function of the confining pressure is shown in Figure 5.6. Even though some scatter may be observed, there is a general trend for minimum damping ratio (D_{min}) to decrease with increasing effective confining pressure. This behavior was very noticeable for specimens with low relative densities ($D_r = 21\%$), and became almost imperceptible for specimens with high relative densities of ($D_r = 96\%$).

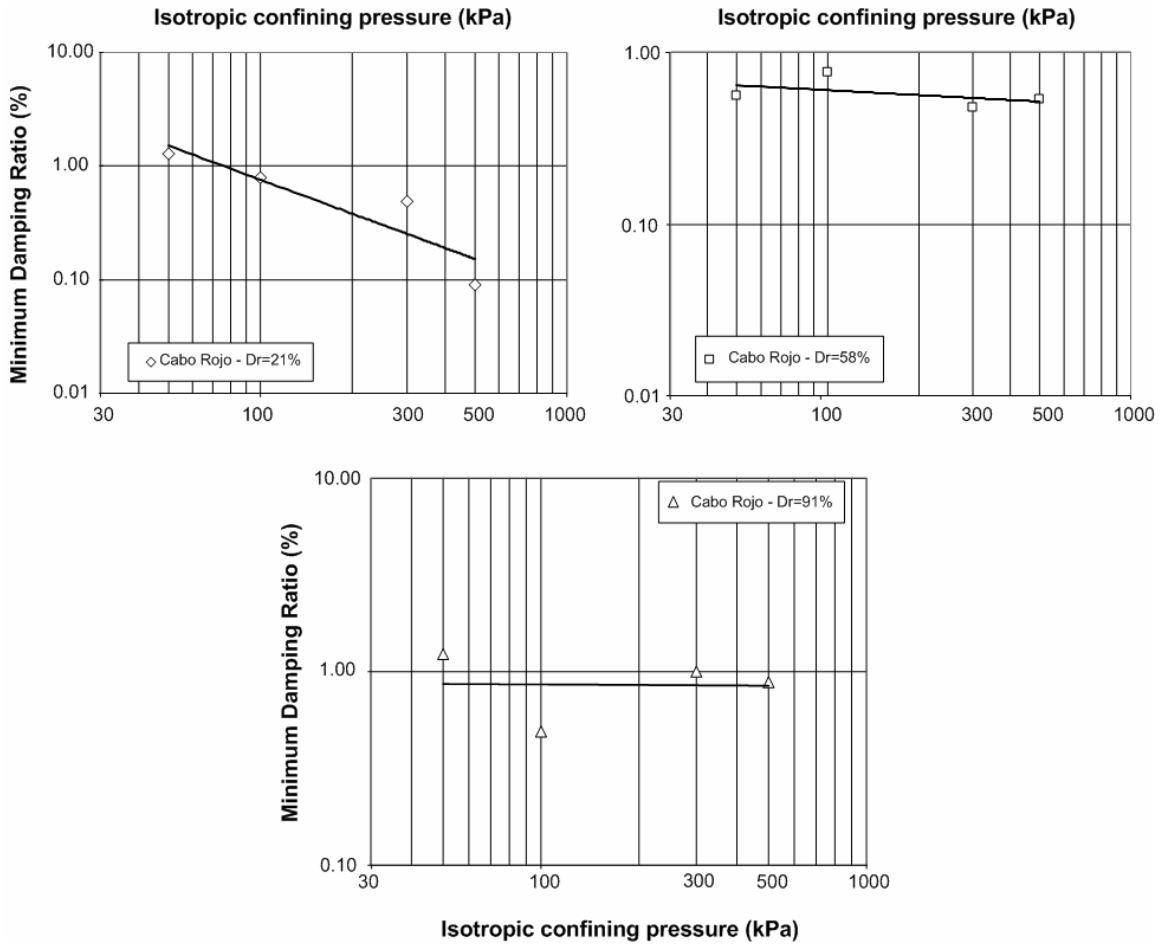


Figure 5.6. Variation of minimum damping ratio (D_{\min}) with effective confining pressure on Cabo Rojo sand.

The results for D_{\min} showed in Figure 5.6 indicated very low influence of the effective confining pressure on the minimum damping ratio of the Cabo Rojo sand specimens at their densest states. This may be caused by the dense packing of the sand particles, which produced a stiffer structure that in turn requires of greater confining stresses to alter the initial damping conditions when sheared at small shear strain amplitudes.

5.3 Variation of Dynamic Properties of Cabo Rojo Sand with Medium to Large Shear Strain

5.3.1 Shear modulus (G)

The variation of the shear modulus with shearing strain for the Cabo Rojo sand at four effective confining pressures (50, 100, 300 and 500 kPa) are plotted in Figures 5.7 through 5.9 for three relative densities: loose ($D_r = 21\%$), medium ($D_r = 58\%$), and dense ($D_r = 91\%$). As expected for conventional sands, the results for the calcareous sands showed that the shear modulus decreases with increasing shear strains beyond the threshold strain (γ_{th}). For shear strain levels below this strain level, the shear modulus is basically independent of the shear strain amplitude, and equal to G_{max} , as discussed in section 5.2. From these figures, higher shear modulus can be observed at higher effective confining pressures and at higher relative density of specimens.

Figures 5.10 and 5.11 show the variation in normalized shear modulus (G/G_{max}) with shearing strain on Cabo Rojo calcareous sand, at confining pressures of 50, 100, 300 and 500 kPa, for minimum and maximum relative densities. Each figure presents the zone of apparent threshold strain that is the range of shear strain at which the threshold strain (γ_{th}) would be located. An apparent threshold strain zone between 0.0007% and 0.004% was obtained for set of tests at minimum relative density. For maximum relative density, the apparent threshold strain zone included shear strain values between 0.0004% and 0.003%.

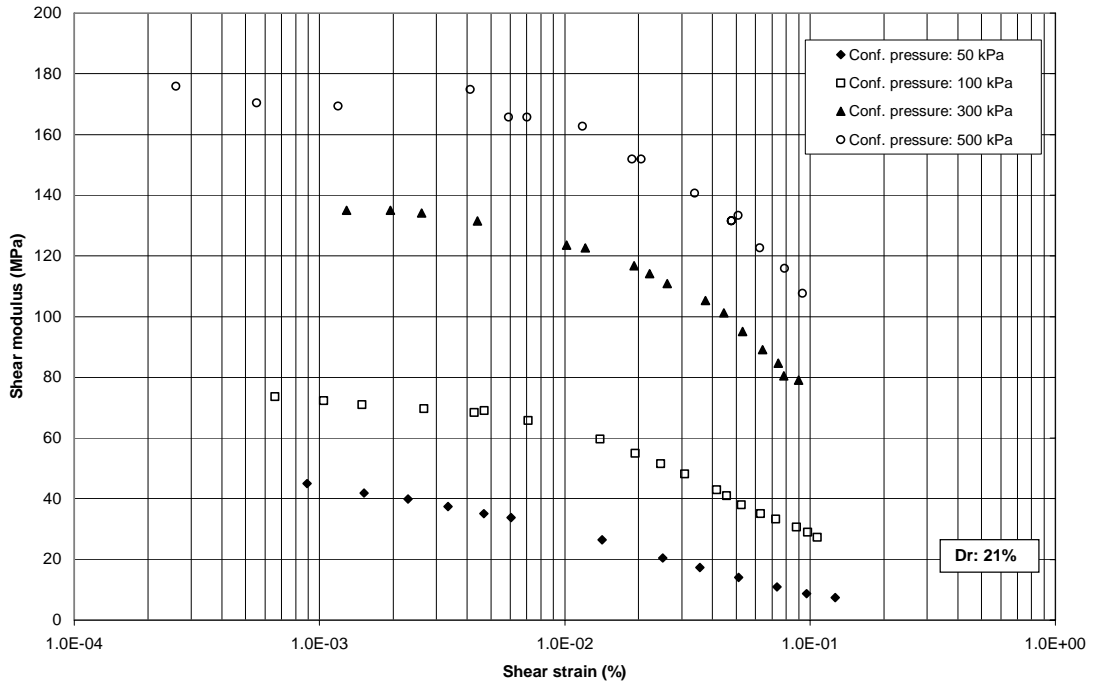
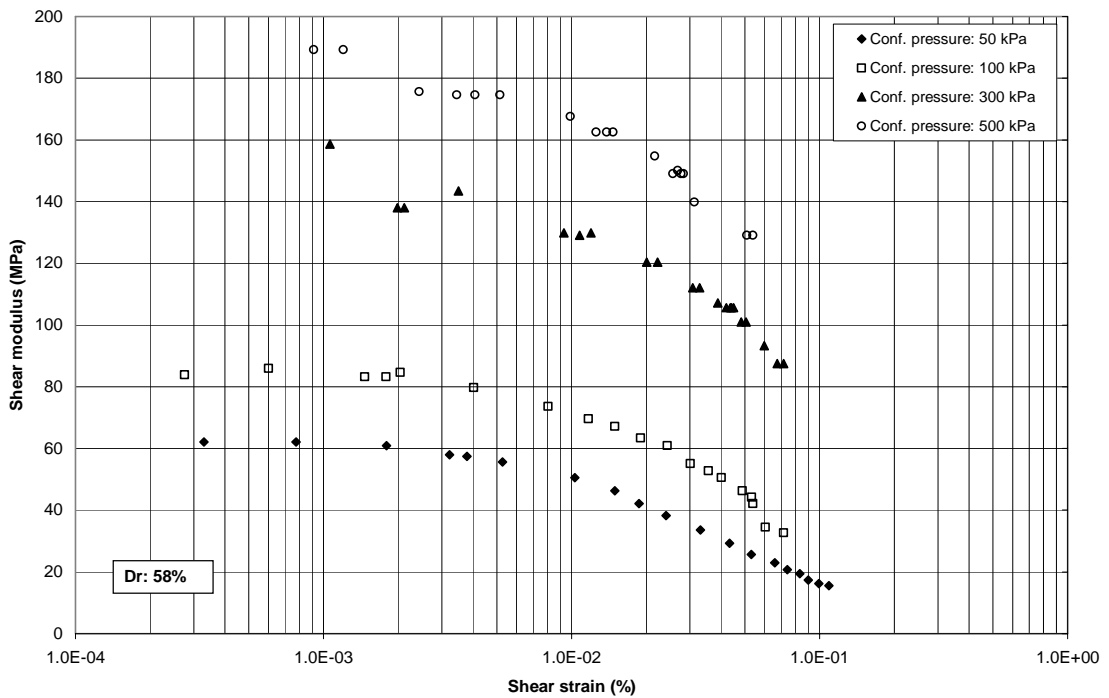


Figure 5.7. Variation in shear modulus with shearing strain on Cabo Rojo sand. Minimum density ($D_r = 21\%$).



X

Figure 5.8. Variation in shear modulus with shearing strain on Cabo Rojo sand. Medium density ($D_r = 58\%$).

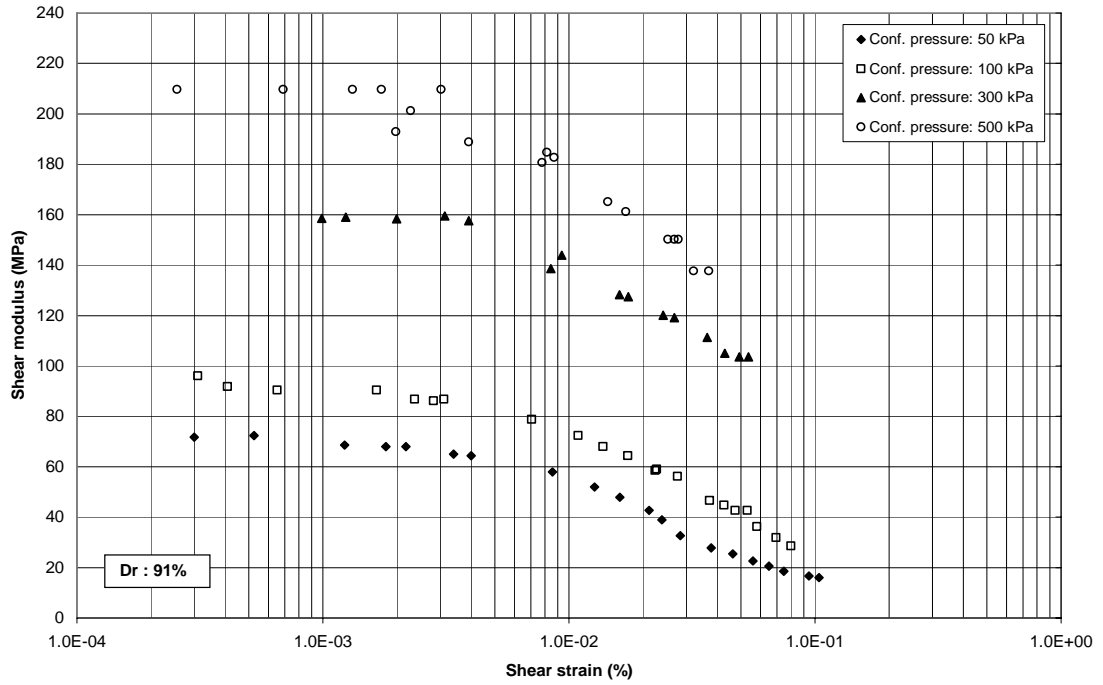


Figure 5.9. Variation in shear modulus with shearing strain on Cabo Rojo sand. Maximum density ($D_r = 91\%$).

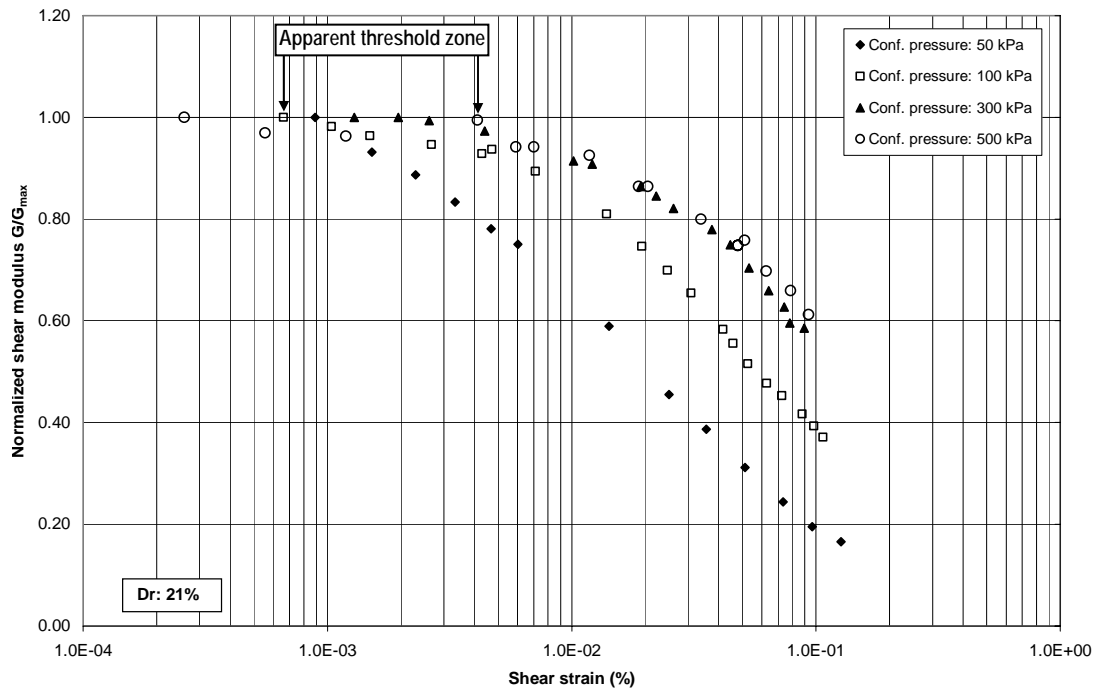


Figure 5.10. Variation of normalized shear modulus with shear strain on Cabo Rojo sand. Minimum density ($D_r = 21\%$).

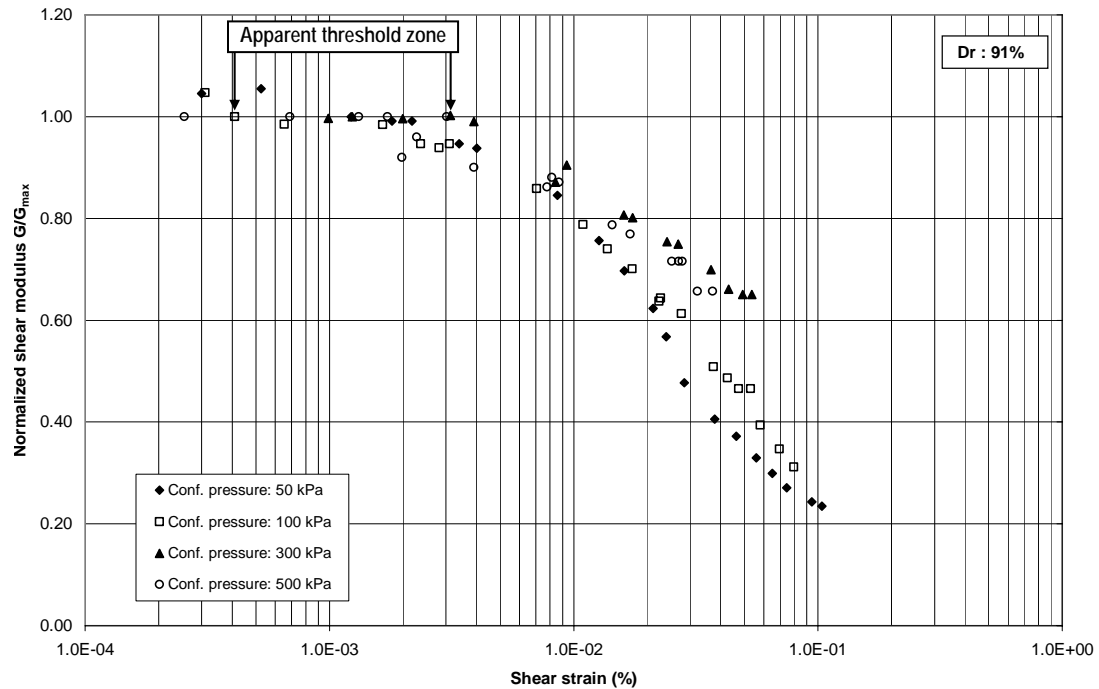


Figure 5.11. Variation of normalized shear modulus with shear strain on Cabo Rojo sand. Maximum density ($D_r = 91\%$).

5.3.2 Damping ratio (D)

Values of material damping for Cabo Rojo calcareous sand, at different confining pressures, are plotted in Figures 5.12 and 5.13, for minimum and maximum relative densities. As illustrated in these figures, damping ratios remained almost constant for the lower levels of shear strain, below the elastic threshold strain (γ_{th}). Beyond this point, they increased with shear strain increasing.

Figures 5.12 and 5.13 also show the reduction in damping ratio with increasing confining pressures, for values of effective confining pressures between 50 and 300 kPa. However, a different situation occurs at 500 kPa confining pressure for both, minimum

and maximum relative densities, where damping ratios were higher than those obtained at 300 kPa confining pressure.

The Cabo Rojo calcareous sand showed a very consistent dynamic behavior at confining pressures of 50, 100 and 300 kPa. However, some differences in behavior were observed at the highest confining pressure level of 500 kPa. This particular response is assumed to be associated to grain crushing. As described in section 3.2.5, particle crushing was observed on calcareous sand specimens subjected to the resonant column testing program. Going back to Figure 3.13, it can be seen that a high level of particle crushing was generated during RC testing at $\sigma'_c = 500$ kPa, due to the progressive crushing caused by the increasing level of effective confining pressures at which each specimen was subjected during the test (from 50 to 500 kPa).

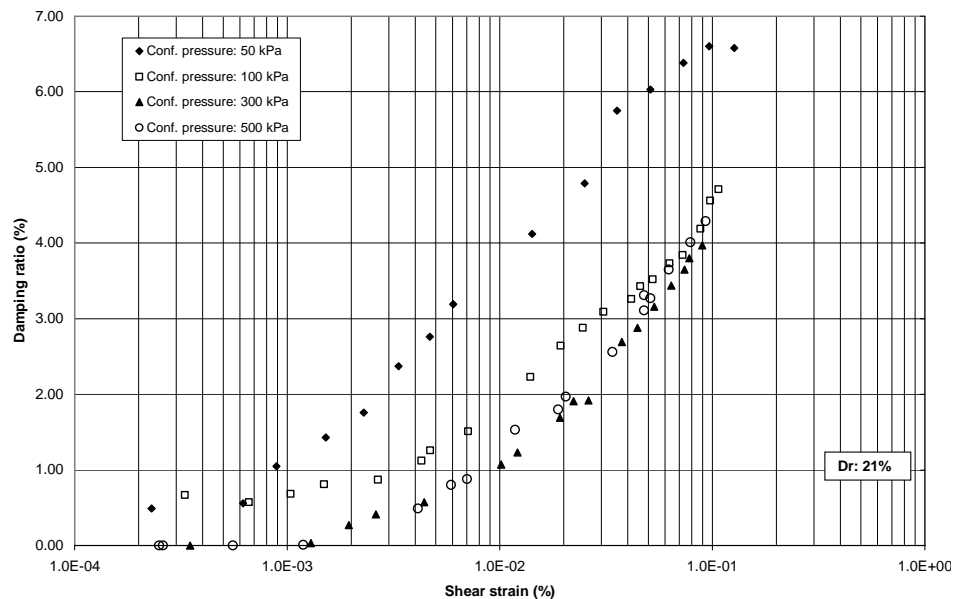


Figure 5.12. Variation of material damping ratio with shear strain on Cabo Rojo sand. Minimum density ($D_r = 21\%$).

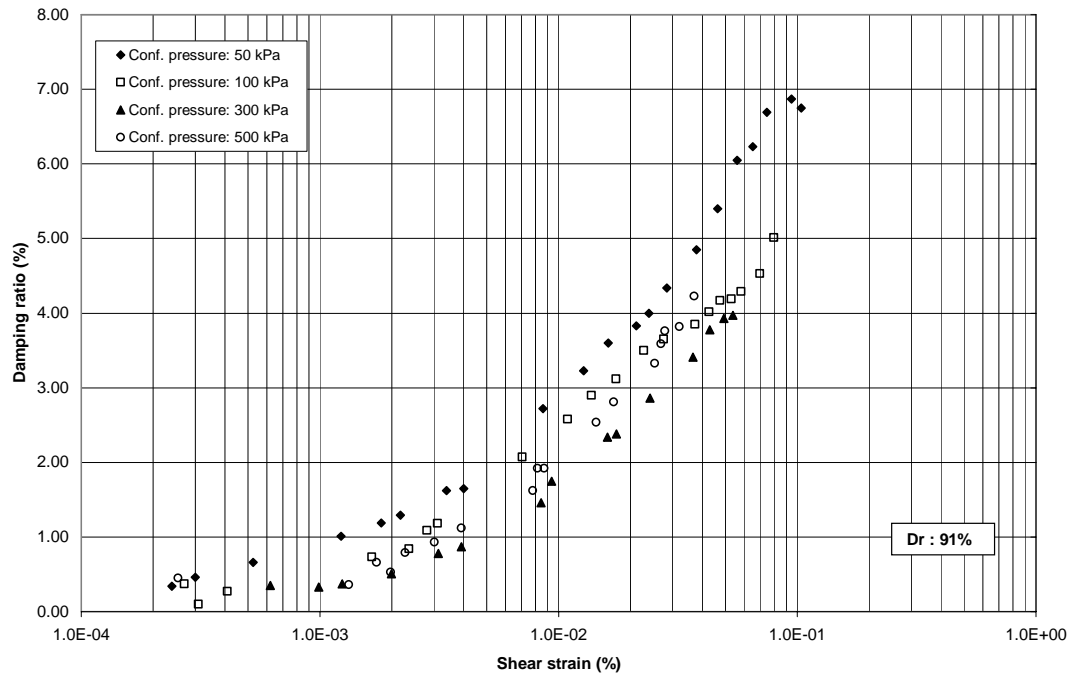
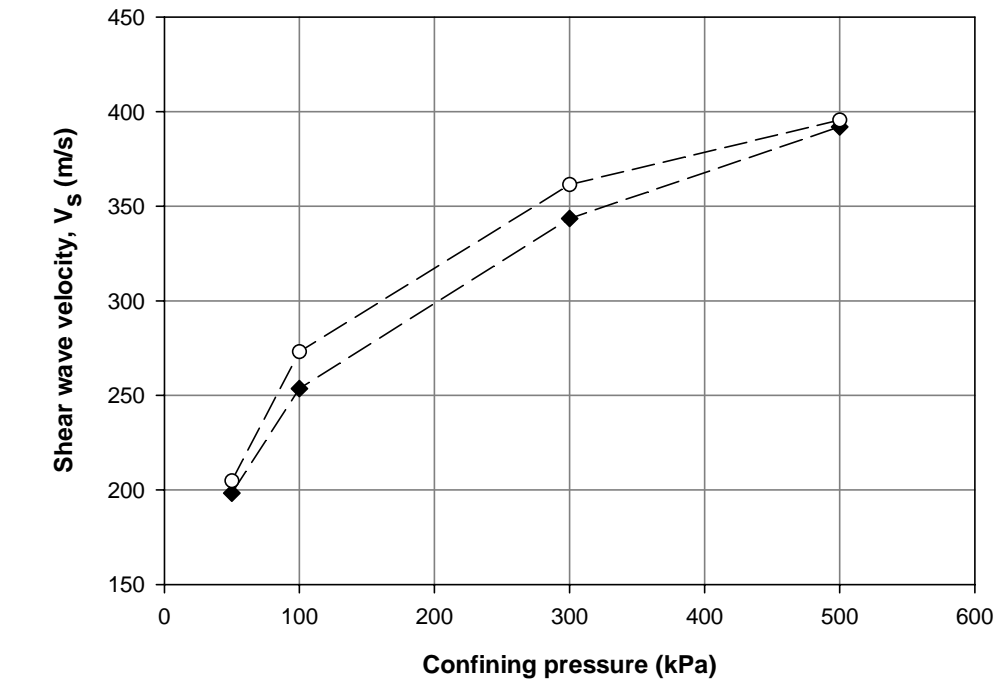


Figure 5.13. Variation of material damping ratio with shear strain on Cabo Rojo sand. Maximum density ($D_r = 91\%$).

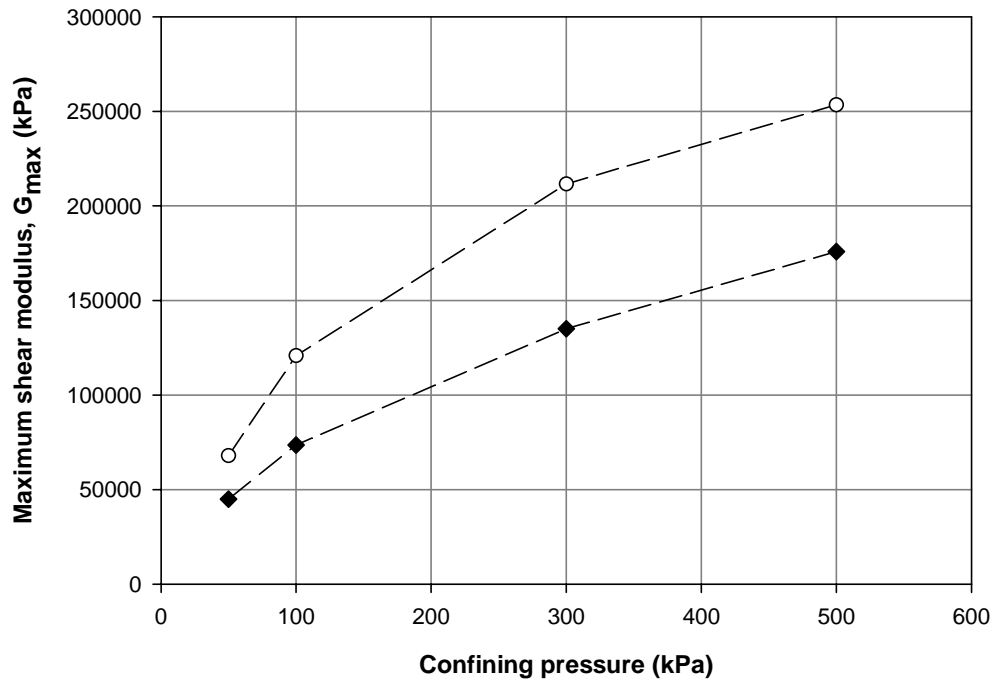
5.4 RC Test Results Comparison for the Cabo Rojo and South Bend Sands

Variations with confining pressure of shear wave velocity (V_s) and maximum shear modulus (G_{max}), for both test sands, are shown in Figures 5.14 and 5.15 for the minimum and maximum relative densities, respectively. Figures 5.14a and 5.15a show no major differences in the shear wave velocity values for both sands. However, Figures 5.14b and 5.15b show greater G_{max} values for the South Bend silica sand compared to the Cabo Rojo calcareous sand. This indicates a less stiff dynamic response for the calcareous sand.



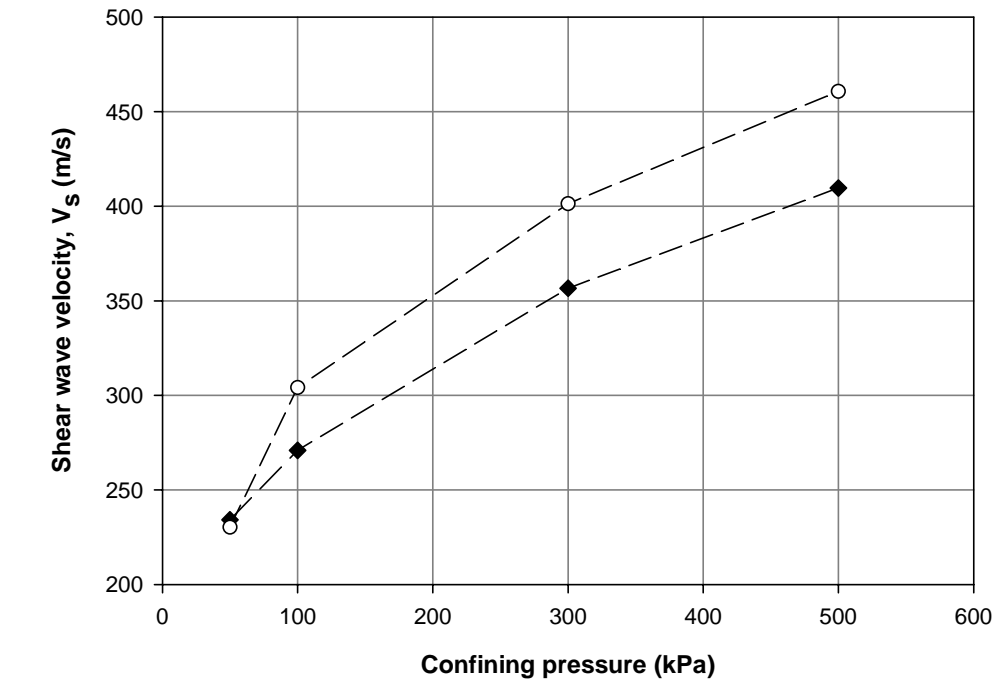
a) Shear wave velocity

—◆— Cabo Rojo calcareous sand ($D_r = 21\%$)
 —○— South Bend silica sand ($D_r = 26\%$)



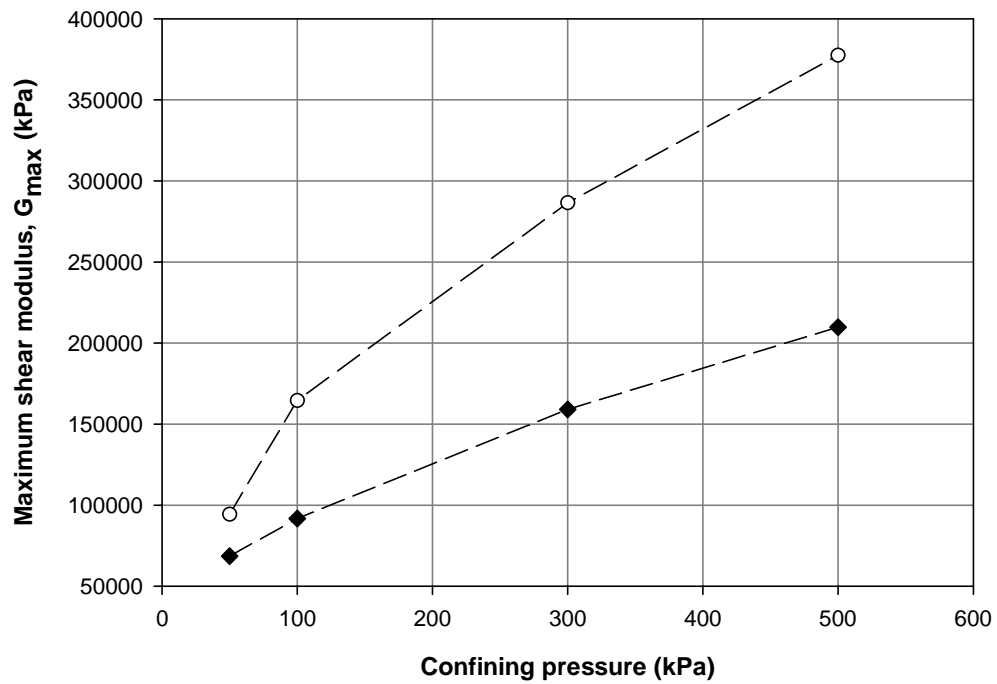
d) Maximum shear modulus

Figure 5.14. Comparison of a) shear wave velocity, and b) maximum shear modulus for Cabo Rojo and South Bend sands at minimum density.



a) Shear wave velocity

—◆— - Cabo Rojo calcareous sand ($D_r = 91\%$)
 —○— - South Bend silica sand ($D_r = 91\%$)



d) Maximum shear modulus

Figure 5.15. Comparison of a) shear wave velocity, and b) maximum shear modulus for Cabo Rojo and South Bend sands at maximum density.

Figures 5.14 and 5.15 illustrate how shear wave velocity is not a good parameter to screen for soil types or for liquefiable soils since two different sands with important differences, such as calcareous and silica sands, show virtually the same V_s values. In this case, G_{\max} was found to be considerably different despite V_s being equal. The differences in the G_{\max} values for both sands are related to the intra-particle porosity of the calcareous sand grains, which resulted in a lower bulk density (ρ), and therefore, in a lower maximum shear modulus (see equation (5.18)).

$$G_{\max} = \sqrt{\frac{V_s}{\rho}} \quad (5.18)$$

Comparison of shear modulus values at higher strain levels for both test sands are shown in Figures 5.16 and 5.17, at confining pressures of 50 and 300 kPa, for the minimum and maximum relative densities, respectively. These figures indicate the silica sand has a greater stiffness than the calcareous sand.

Regarding the variation of material damping ratio, Figure 5.18 shows that at confining pressures of 50 kPa, calcareous sand specimens prepared at minimum relative densities presented greater damping ratio values than silica sand specimens under similar density and stress conditions. The opposite situation was observed for confining pressures of 300 kPa, where silica sand exhibited larger damping ratio values than calcareous sand. Figure 5.19, corresponding to sand specimens prepared at denser states, shows how, contrary to the Cabo Rojo calcareous sand, the South Bend silica sand did

not present a notable range of damping ratio values, indicating little influence of the confining pressure.

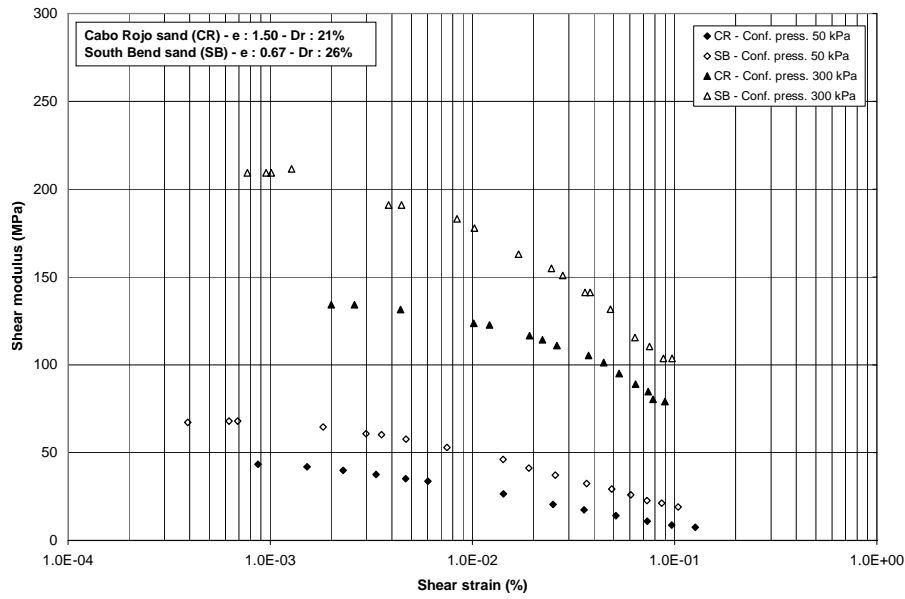


Figure 5.16. Variation in shear modulus with shear strain on Cabo Rojo and South Bend sands at minimum density.

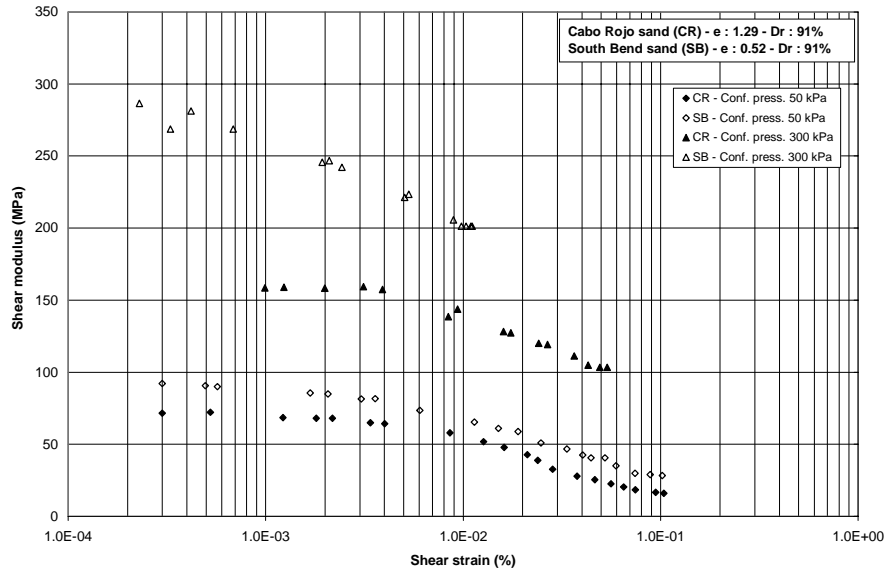


Figure 5.17. Variation in shear modulus with shear strain on Cabo Rojo and South Bend sands at maximum density.

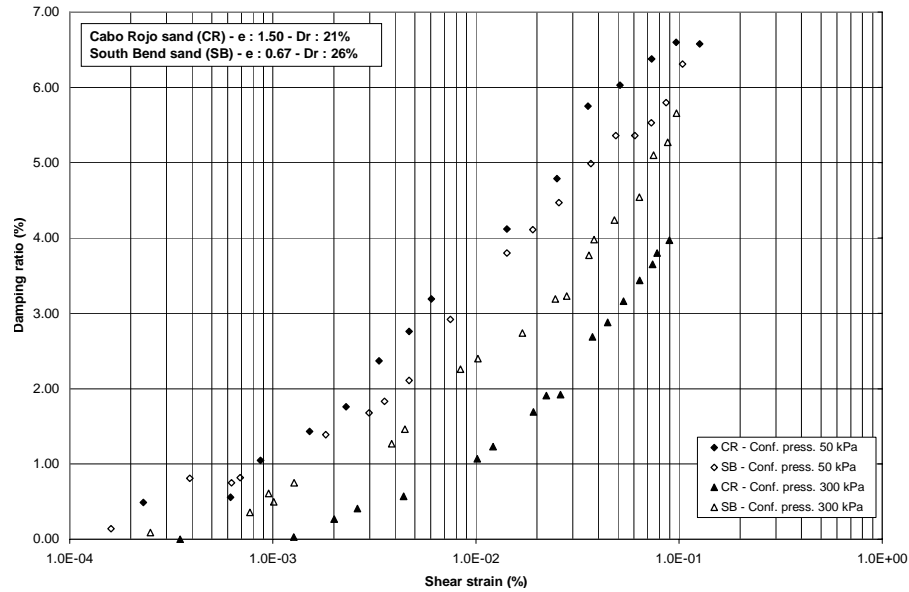


Figure 5.18. Variation in damping ratio with shear strain on Cabo Rojo and South Bend sands at minimum density.

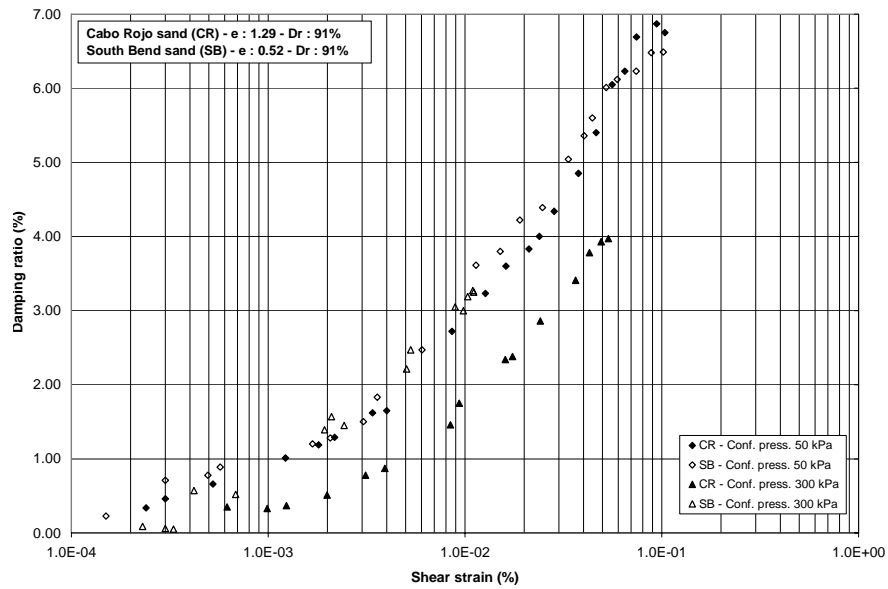


Figure 5.19. Variation in damping ratio with shear strain on Cabo Rojo and South Bend sands at maximum density.

The silica sand exhibited a stiffer dynamic response than calcareous sand under similar relative densities and confining stresses. However, no clear pattern was observed

in terms of the material damping behavior, where the Cabo Rojo calcareous sand exhibited a major dependency on confining pressures than the South Bend silica sand. This agrees with the findings by Seed et al. (1986) that indicated a low dependency of the damping ratio of conventional sands with effective confining pressure. These authors found that the main factor influencing damping ratio was shear strain level.

Figure 5.20 shows the results of the normalized shear modulus (G/G_{\max}) obtained for the Cabo Rojo sand specimens tested in the RC testing program. In dashed lines are also shown the variation curves of G/G_{\max} with shear strain proposed by Seed et al. (1986) for silica sands. The experimental results for the Cabo Rojo sand in general indicate a slower initial degradation compared to the range of results recommended for silica sands by Seed et al. (1986). Furthermore, beyond the threshold strain, the rate of degradation seems to be higher than the one suggested by the trend lines from these authors. This is an important consideration for site response analysis of projects involving calcareous sands.

The observed differences in the modulus degradation curves are significant, highlighting the importance of using appropriate degradation curves that consider the unique nonlinear characteristics and dynamic properties of the Cabo Rojo calcareous sand. Ground response analyses for sites involving uncemented calcareous sands similar to the Cabo Rojo calcareous sand must use specific non-linear curves, and must avoid using published curves that are applicable to conventional silica sands.

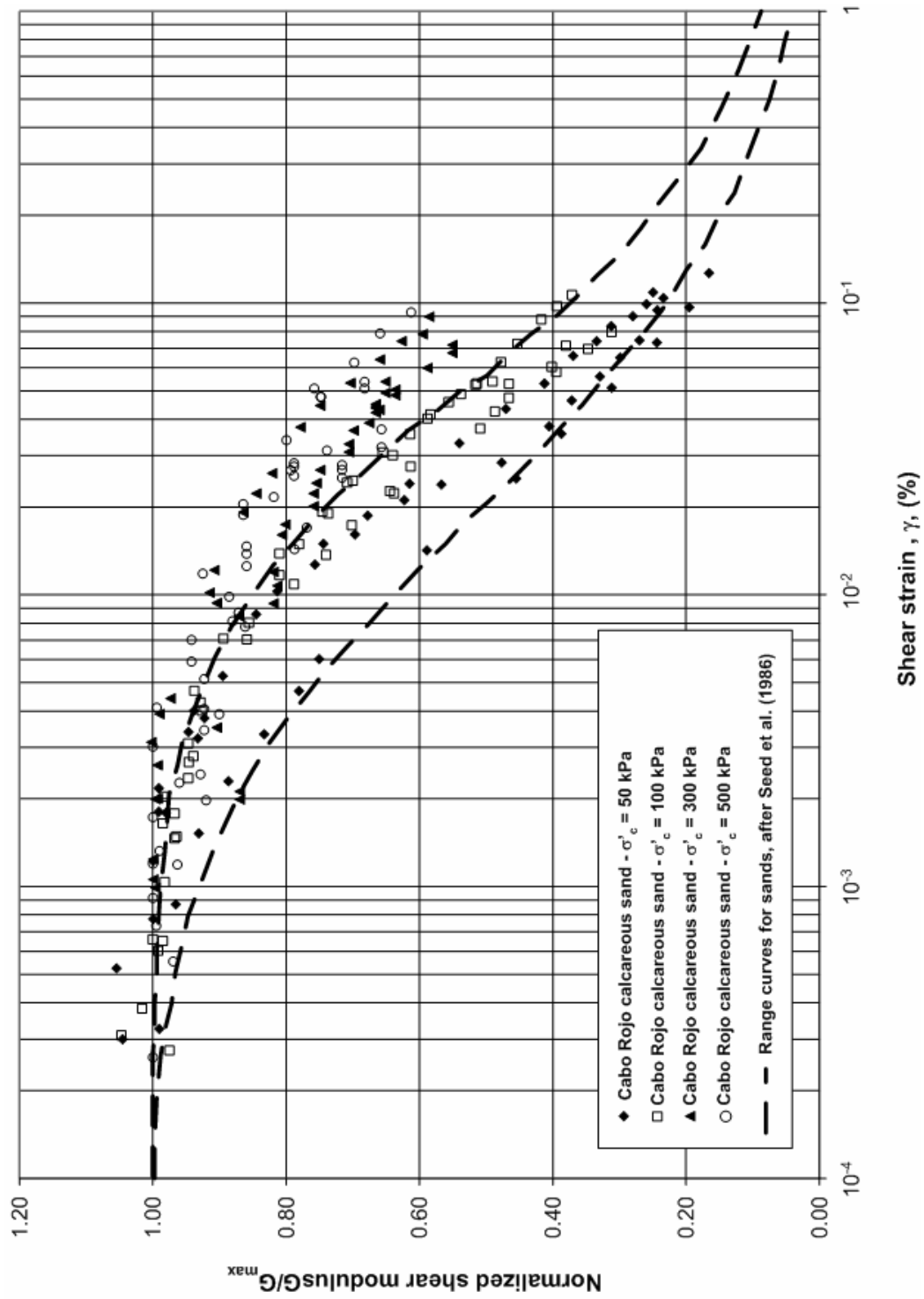


Figure 5.20. Comparison of G/G_{max} curves for Cabo Rojo sand with Seed et al. (1986) range.

5.5 Summary and Discussion

This chapter provided the results of resonant column (RC) testing on Cabo Rojo calcareous sand to determine its dynamic properties at small shear strains (G_{\max} and D_{\min}), and for medium to large shear strains. The results obtained for the South Bend silica sand, were used for comparison purposes.

As expected for conventional sands, the dynamic properties of the Cabo Rojo calcareous sand exhibited strong shear strain dependency for strain levels beyond the elastic threshold strain. Below this threshold strain, shear modulus values (G_{\max}) and damping ratios (D_{\min}) remained almost constant, and basically independent of the strain level. With increasing strain beyond of the elastic threshold, the shear modulus decreases and the damping ratio increases, which demonstrates the non-linear behavior of Cabo Rojo sand for medium to large strains. Apparent elastic threshold strain values from 0.0004% to 0.004% were obtained.

The maximum shear modulus of the Cabo Rojo sand was found to increase with the isotropic confining stress. The following empirical formulation for G_{\max} , which includes the effective confining pressure and void ratio effect, was obtained for the Cabo Rojo sand:

$$G_{\max} = 1577 \left(\frac{1}{e^{1.953}} \right) \cdot P_{atm} \left(\frac{\sigma'_0}{P_{atm}} \right)^{0.4774e-0.1412} \quad (5.17)$$

where 1577 is a constant related to soil shear stiffness and e is the void ratio.

It was found that the minimum damping ratio of the Cabo Rojo sand tends to decrease with increasing effective confining pressure. However, this trend was barely visible in specimens with high relative densities.

At effective confining pressures of 50, 100 and 300 kPa, the Cabo Rojo calcareous sand showed a dynamic behavior that is consistent with the typical dynamic behavior exhibited by other conventional silica sands. However, some differences in the trend were observed at higher confining pressures (500 kPa). This behavior can be associated with the generation of grain crushing processes in the calcareous particles of the Cabo Rojo sand, as previously described in Chapter 3.

Regarding the comparison of the dynamic properties of the Cabo Rojo and the South Bend silica sand, the silica sand exhibited a stiffer dynamic response than the calcareous sand, under similar density and confining stress conditions. This was concluded from the higher shear modulus values obtained for the silica sand in comparison with that of the calcareous sand. The shear wave velocity showed not to be a good parameter to determine the dynamic stiffness of calcareous sands due to the intra-particle porosity exhibited by its grains, which resulted in a lower bulk density. This effect could only be contemplated by the shear modulus as shown in equation (5.1).

No clear pattern was observed in terms of the material damping behavior, where the Cabo Rojo calcareous sand exhibited more dependency on confining pressures than the South Bend silica sand.

Finally, since notable differences were obtained in the degradation with shear strain of the Cabo Rojo sand shear modulus when compared to the degradation curves proposed by Seed et al. (1986) for silica sands, it can be concluded that the ground response analyses for sites involving uncemented calcareous sands similar to the Cabo Rojo calcareous sand must use adequate non-linear curves and must avoid using published curves that are applicable to conventional silica sands.

6 SUMMARY AND CONCLUSIONS

6.1 Introduction

This thesis presented results of a research program to study the geotechnical behavior of uncemented calcareous sands from Cabo Rojo, southwest Puerto Rico, in terms of their stress-strain behavior and dynamic properties. This chapter provides a summary of the work carried out, followed by conclusions and recommendations for future work.

6.2 Summary

The results of this research were presented in five chapters. Chapter 2 presented a review of basic definitions and concepts of critical state soils mechanics that were used in this study to describe the geotechnical behavior of the Cabo Rojo calcareous sand. Background information about calcareous sands and their distribution in the insular shelf of Puerto Rico was also included, together with a comprehensive literature review related to the geotechnical behavior of calcareous sands.

The reviewed publications indicated that the most relevant factors influencing the behavior of uncemented calcareous sands are:

- Mineralogy
- Particle crushing susceptibility

- Grain characteristics (shape, intraparticle porosity, texture)

Therefore, these factors were evaluated for the particular case of the Cabo Rojo sand. A mineralogical and geotechnical characterization was presented in Chapter 3. This characterization included index properties, uniaxial compressive behavior, and shear strength for the Cabo Rojo calcareous sand and for the South Bend silica sand, both with comparable gradation.

The Cabo Rojo calcareous sand was described as a fine to medium poorly graded sand (SP), with subangular to angular grains, specific gravity of 2.86, and average maximum and minimum void ratios of 1.71 and 1.34, respectively. The main minerals found in this sand were aragonite (CaCO_3) and calcite magnesian (MgCaCO_3), with calcium carbonate contents ranging between 91% and 97%. The particles commonly found in this sand were fragments of the skeletal type (biogenic), and also non-skeletal particles, both with peculiar shapes, rough texture, and intraparticle porosity. On the other hand, the South Bend silica sand, used for comparison purposes, was described as a fine to medium quartzitic sand, poorly graded, with subrounded to subangular grains, specific gravity of 2.70, and maximum and minimum void ratios of 0.74 and 0.50, respectively. The particles of this silica sand exhibited predominantly even surfaces with occasional textural changes. A noteworthy difference was the range of void ratio values for both sands, which was found to be related to the intraparticle porosity of calcareous sands.

The direct shear tests included in Chapter 3 resulted in a peak internal friction angle of 37.0° for the Cabo Rojo calcareous sand, at medium density state. The peak friction angle obtained for the South Bend silica sand at the same level of relative density was and 32.2° .

The results of a crushability analysis were also presented in Chapter 3. The evaluation was carried out for four different types of loading: uniaxial, direct shear, axial monotonic and torsional harmonic. These analyses indicated that in general the Cabo Rojo sand exhibited a more crushable behavior than the South Bend silica sand when subjected to similar stress levels and loading stress paths.

Chapter 4 included a study of the geotechnical behavior of the Cabo Rojo sand in terms of its initial state with respect to its steady state line. To that effect, Chapter 4 shows the results of monotonic triaxial tests performed to study their stress-strain behavior and to define the steady state line of the Cabo Rojo calcareous sand.

For the range of effective confining pressures used (50 to 300 kPa), the Cabo Rojo calcareous sand exhibited peak deviator stress values ranging between 196 kPa and 458 kPa, at axial strains between 16.3% and 19.6%, respectively. In contrast, the South Bend sand exhibited peak deviator stress values between 365 kPa and 1019 kPa at axial strains from 3.3% to 9.1%, for the same values of effective confining pressures. An important difference between the two sands is the higher peak stresses of the silica sand and the considerably lower axial strains needed to reach these peaks. In terms of the initial

undrained Young's modulus values ($E_{u, ini}$), the Cabo Rojo calcareous sand has values ranging between 51 MPa and 116 MPa. Whereas, the South Bend silica sand had modulus values between 36 MPa and 120 MPa. These values were comparable but overall, the calcareous sand was less stiff than the silica sand. Peak friction angles between 39.8° and 41.2° were obtained for the Cabo Rojo sand, while the South Bend silica sand resulted in lower peak friction angles ranging between 33.4° and 40.0° .

Chapter 4 also presented the steady state line (SSL) obtained for the Cabo Rojo calcareous sand. This line was found to be steeper than other SSL's reported in the literature. For comparison purposes, the line was plotted against lines obtained by Poulos et al. (1985).

Finally, Chapter 5 presented results of the resonant column test program performed to determine the dynamic properties of the Cabo Rojo calcareous sand for small shear strains (G_{max} and D_{min}), and for medium to large shear strains (G and D). The results obtained for the calcareous sand were compared with results for the South Bend silica sand.

Maximum shear modulus (G_{max}) ranging between 45 MPa and 210 MPa were obtained for the Cabo Rojo calcareous sand. The influence of the effective confining stresses and void ratio on the maximum shear modulus of the Cabo Rojo sand was analyzed. This resulted in an empirical expression for estimating the maximum shear modulus (G_{max}) of these sands (see equation (5.17)).

Curves of variation of shear modulus and damping ratio with shear strain, for both sands were also presented in Chapter 5. Both sands exhibited a decrease in the shear modulus and an increase in the damping ratio with increasing shearing strain beyond of the elastic threshold strain level. Apparent elastic threshold strain values from 0.0004% to 0.004% were observed for the Cabo Rojo calcareous sand.

Finally, the degradation with shear strain of the shear modulus of the Cabo Rojo calcareous sand were compared to the degradation curves proposed by Seed et al. (1986) for silica sands. Important differences were found between both types of sands.

6.3 Conclusions

This study revealed that the Cabo Rojo calcareous sand exhibited a different geotechnical behavior when compared to a conventional silica sand. This behavior was mainly characterized by a less stiff response of the Cabo Rojo sand that resulted in lower values of peak strength and dynamic properties than those of the silica sand used for comparative purposes.

The different geotechnical behavior of the Cabo Rojo calcareous sand is highly related to the presence of particles of biogenic nature, which resulted on different mineralogy and particle shapes when compared to a conventional silica sand. Such unique particle characteristics determined the soft mechanical response of this sand, making it highly crushable and compressible.

More specific conclusions are:

1. The geotechnical characterization performed on the Cabo Rojo calcareous sand and the South Bend silica sand allowed to define important differences in their index properties, which directly influence on the geotechnical behavior of both sands. Although the test sands were selected to have very similar gradation curves, the Cabo Rojo sand resulted in greater values of specific gravity and total void ratios. This was found to be due to its carbonate mineralogy and the intraporosity of its grains. This is in agreement with what had been stated in the technical literature on calcareous sands.

The direct shear tests yielded peak friction angles between 39.8° and 41.2° for the Cabo Rojo sand, while the South Bend sand resulted in lower peak friction angles between 33.4° and 40.0° . This is in agreement with the findings of the literature review.

2. The mineralogical characterization conducted on the Cabo Rojo sand confirmed its carbonate nature with calcium carbonate content (CaCO_3) greater than 91%, and the predominant presence of carbonate minerals such as aragonite and magnesian calcite. Likewise, the South Bend sand exhibited quartz (SiO_2) as its predominant mineral, which indicated the convenience of using this sand as a comparison silica sand. The SEM micrographs obtained as part of the mineralogical characterization showed marked differences in the grain shape and texture of the test sands. Product of its geological formation process, the Cabo Rojo sand was found to contain abundant

- skeletal remains of marine organisms which resulted in particles with peculiar shapes, high intraparticle porosity, and very rough surface texture.
3. The evaluation of the grain crushing potential of the test sands indicated that the Cabo Rojo sand exhibited a more crushable behavior than the South Bend silica sand when subjected to stress. This is directly related to the mineralogy and unique characteristics of the Cabo Rojo sand particles. Additionally, their intraparticle porosity and unique grain shapes increased their fragility and made them more susceptible to suffer crushing. The crushability analysis results were complemented with the results of the 1-D compression test presented in Chapter 3, which indicated a more compressible behavior of the Cabo Rojo sand as compared to the South Bend silica sand.
 4. From the evaluation of the stress-strain behavior of the Cabo Rojo calcareous sand presented in Chapter 4, its stress-strain response could be described as ductile, with a maximum strength (peak deviator stress) achieved at very large axial deformations. In general terms, the initial undrained Young's modulus values ($E_{u, ini}$) obtained for the Cabo Rojo sand were some what greater than those obtained for the South Bend sands at comparable relative densities, indicating an apparent higher initial stiffness of the Cabo Rojo sand at very small axial strain ($< 0.01\%$). However, in terms of secant modulus values and based on the stress-strain curves, the calcareous sand was in general less stiff than the silica sand.

Comparison of the stress-strain behavior of the Cabo Rojo and the South Bend sands indicated that the Cabo Rojo sand exhibited a less stiff behavior than the South Bend sand, with lower values of deviator stresses at peaking and at 10% axial strain. Moreover, the excess pore pressure vs. axial strain curves and the effective stress paths for both sands indicated that for the same confining pressures, the silica sand specimens exhibited a more dilative behavior than the calcareous sand specimens.

The triaxial tests carried out for the stress-strain behavior study showed higher friction angles for the Cabo Rojo sand than for the South Bend sand. This is related to the higher degree of dilation observed for the silica sand, which resulted in higher mean effective stresses (p') and thus lower friction angles. The same results for the friction angles were obtained for the direct shear tests performed on dry specimens as part of the geotechnical characterization presented in Chapter 3.

5. The steady state line (SSL) obtained for the Cabo Rojo sand was found to be steeper in slope than those presented by Poulos et al. (1985) for silica sands. This may be related to the unique particle shape and grain characteristics of the Cabo Rojo calcareous sand, which makes it comparable to angular sands. This is in agreement with the findings by Poulos et al. (1985) which indicated steeper SSL's for angular sands.
6. The determination of the dynamic properties at small strain levels; i.e. maximum shear modulus (G_{\max}) and minimum damping ratio (D_{\min}); showed that the maximum

shear modulus of the Cabo Rojo sand increases with increasing effective confining pressure. Moreover, G_{\max} was found to be primarily controlled by the isotropic confining stress level and the packing of the sand particles (i.e., void ratio). On the other hand, the minimum damping ratio (D_{\min}) of the Cabo Rojo was found to decrease with increasing effective confining pressure. However, this trend was not as noticeable for samples prepared at higher relative densities.

For higher shear strain levels, the Cabo Rojo sand showed a dynamic behavior that is consistent with the typical dynamic behavior exhibited in silica sands, i.e. when increasing shearing strain beyond of the elastic threshold strain level the shear modulus decreases and the damping ratio increases, which confirms the non-linear behavior of these sands. However, some differences in trend were observed at higher confining pressure (500 kPa). This behavior was associated to the generation of particle crushing processes in the Cabo Rojo sand during the resonant column tests.

An important finding was the less stiff response of the Cabo Rojo sand compared with the South Bend sand. Resonant column test results showed greater shear modulus for the South Bend sand compared with the Cabo Rojo sand.

No clear pattern was observed in terms of the material damping behavior, where the Cabo Rojo calcareous sand exhibited a major dependency on confining pressures than the South Bend silica sand.

- Notable differences were obtained in the degradation of the Cabo Rojo sand shear modulus when compared to the degradation curves proposed by Seed et al. (1986) for silica sands, indicating a slower initial degradation in the Cabo Rojo calcareous sand. This is a clear indication that the ground response analyses for sites involving uncemented calcareous sands similar to the Cabo Rojo calcareous sand must use adequate non-linear curves and avoid using published curves that are applicable to conventional silica sands.
7. From the resonant column test results obtained in this study it is possible to conclude that shear wave velocity is not a good parameter to screen for soil types or for liquefiable soils. Two different sands with important differences, such as calcareous and silica sands show virtually the same V_s values. In contrast, shear modulus values reflect a less stiff response for the calcareous sand. The differences in the G_{max} values for both sands are related to the intra-particle porosity of the calcareous sand grains, which resulted in a lower bulk density (ρ), and therefore, in a lower maximum shear modulus

Given the lower values of peak strength and dynamic properties obtained for the Cabo Rojo calcareous sand, special considerations must be taken in the design and construction of coastal structures on deposits involving this sand. Even though Cabo Rojo sand resulted in relatively high peak friction angles, it exhibited particle crushing when subjected to stress and required large amounts of axial strain to mobilize its peak strength. Therefore the convenience of using conventional methods in the geotechnical

analysis and design of geosystems founded in this type of calcareous sand deposits must be evaluated for each particular project.

6.4 Recommendations for Future Work

Recommendations for further research into the geotechnical behavior of the Cabo Rojo calcareous sands are as follows:

- Further study of the micro mechanical behavior of the calcareous particles of the Cabo Rojo sand. A more detailed study on the crushability potential is recommended. Since the unique particle features of the Cabo Rojo calcareous sand were found to be the main factor controlling the mechanical behavior of these sands, a more detailed study at the particle level is considered useful to improve the understanding of the geotechnical behavior of these calcareous sands.
- A detailed study of the cyclic behavior and liquefaction potential of the Cabo Rojo sand is highly recommended. This is particularly important given the high seismicity of Puerto Rico and the saturated conditions of the Cabo Rojo beach deposits. The coastal infrastructure built on calcareous sands warrants such a study.
- Since these sands can also exist in a cemented state, a study of the influence of the interparticle cementation is also recommended. The warm marine environment of the insular shelf of Puerto Rico is conducive to the precipitation of the carbonate minerals

present in these calcareous sands resulting in interparticle cementation. This cementation is expected to influence the geotechnical behavior of these sands. It is desirable to include in the study of cementation the strength of these bond and how it behaves at different load and strain levels.

REFERENCES

Airey, D. W. (1993). "Triaxial Testing of Naturally Cemented Carbonate Soil". J. Geotech. Engrg., ASCE, 119(9), 1379-1398.

Allman, M. A., and Poulos, H. G. (1988). "Stress-strain Behavior of an Artificially Cemented Calcareous soil". Engineering for Calcareous Sediments, Vol. 1. Balkema, Perth, 69-78.

ASTM D 422 – 63 (2002). "Standard Test Method for Particle-Size Analysis of Soils". ASTM International.

ASTM D 854 – 02. "Standard Test Methods for Specific Gravity of Soil Solids by Water Pycnometer". ASTM International.

ASTM D 934 – 80 (2003). "Standard Practices for Identification of Crystalline Compounds in Water-Formed Deposits by X-Ray Diffraction". ASTM International.

ASTM D 2488 – 00. "Standard Practice for Description and Identification of Soils (Visual-Manual Procedure)". ASTM International.

ASTM D 3080 – 03. "Standard Test Method for Direct Shear Test of Soils Under Consolidated Undrained Conditions". ASTM International.

ASTM D 4254 – 00. "Standard Test Methods for Minimum Index Density and Unit Weight of Soils and Calculation of Relative Density". ASTM International.

ASTM D 4767 – 02. "Standard Test Method for Consolidated Undrained Triaxial Compression Test for Cohesive Soils". ASTM International.

ASTM D 5550 – 00. "Standard Test Method for Specific Gravity of Soil Solids by Gas Pycnometer". ASTM International.

Bardet, J. P. (1997). "Experimental Soil Mechanics". Prentice Hall, Inc., Upper Saddle River, NJ, USA.

Been, K., Jefferies, M. G., and Hachey, J. (1991). "The Critical State of Sands". *Geotechnique*, 41(3), 365-381.

Bowles, J. E. (1996). "Foundation Analysis and Design". 5th Ed. McGraw-Hill Companies, Inc.

Cascante, G., Vanderkooy, J., and Chung, W. (2005). "A New Mathematical Model for Resonant-Column Measurements Including Eddy-Current Effects". *Can. Geotech. J.*, 42, 121-135.

Castro, G., and Poulos, S. J. (1977). "Factors Affecting Liquefaction and Cyclic Mobility". *J. Geotech. Engrg., ASCE*, 103(6), 501-516.

Chaney, R. C., Slonim, S. M., and Slonim, S. S. (1982). "Determination of Calcium Carbonate Content in Soils". *Geotechnical Properties, Behavior and Performance of Calcareous Soils*, ASTM Special Technical Publication 777, 3-15.

Chuhan, F. A., Kjeldstad, A., Bjørlykke, K., and Høeg, K. (2003). "Experimental Compression of Loose Sands: Relevance to Porosity Reduction during Burial in Sedimentary Basins". *Can. Geotech. J.*, 40, 995-1011.

Cunning, J. C. (1994). "Shear Wave Velocity Measurement of Cohesionless Soils for Evaluation of In-Situ State". M.Sc. Thesis, University of Alberta, Edmonton, Canada.

Datta, M., Gulhati, S. K., and Rao, G. V. (1982). "Engineering Behavior of Carbonate Soils of India and Some Observations on Classification of Such Soils". *Geotechnical Properties, Behavior and Performance of Calcareous Soils*, ASTM Special Technical Publication 777, 113-140.

Demars, K. R., and Chaney, R. C. (1982). "Symposium Summary" *Geotechnical Properties, Behavior and Performance of Calcareous Soils*, ASTM Special Technical Publication 777, 395-404.

Duncan, J. M., Byrne, P., Wong, K. S., and Mabry, P. (1980). "Strength, Stress Strain and Bulk Modulus Parameters for Finite Element Analyses of Stresses and Movements in Soil Masses". Report No. UCB/GT/80-01, Department of Civil Engineering, University of California, Berkeley.

Fernandez, A. L. (2000). "Tomographic Imaging the State of Stress". Ph.D. Dissertation, Georgia Institute of Technology, Atlanta, GA, USA.

Fioravante, V., Capoferri, R., Hameury, O., and Jamiolkowski, M. (1994). "Deformational Characteristics of Uncemented Carbonate Quiou Sand". Pre-failure Deformation of Geomaterials. Balkema, Sapporo, 55-61.

Garga, V. K., and Zhang, H. (1997). "Volume Changes in Undrained Triaxial Tests on Sands". Can. Geotech. J., 34, 762-772.

GCTS (2004). "CATS 1.7 Resonant Column Test Mode – User's Guide and Reference". Geotechnical Consulting and Testing Systems, Tempe, AR, USA.

Geocomp (2006). "Triaxial, User's Manual". GEOCOMP Corporation, Boxborough, MA, USA.

Golightly, C. R., and Hyde, A. F. L. (1988). "Some Fundamental Properties of Carbonates Sands". Engineering for Calcareous Sediments, Vol. 1. Balkema, Perth, 69-78.

Hardin, B. O., and Drnevich, V. P. (1972). "Shear Modulus and Damping in Soils: Design Equations and Curves". J. Soil Mech. and Found. Div., ASCE, 98(7), 667-692.

Hardin, B. O., and Richart, F. E. (1963). "Elastic Wave Velocities in Granular Soils". J. Soil Mech. and Found. Div., ASCE, 89(1), 33-65.

Hoyos, L. R. (1993). "Dynamic properties of Puerto Rican Residual Soils Using the Resonant Columns Device". M.Sc. Thesis, University of Puerto Rico, Mayagüez, Puerto Rico.

Hull, T. S., Poulus, H. G., and Alehossein, H. (1988). "The Static Behavior of Various Calcareous Sediments". Engineering for Calcareous Sediments, Vol. 1. Balkema, Perth, 87-96.

Hurlbut, C. S. (1971). "Dana's Manual of Mineralogy". 18th Ed. John Wiley & Sons, Inc., New York.

Hyodo, M., Hyde, A. F. L., and Aramaki, N. (1998). "Liquefaction of Crushable Soils". Geotechnique, 48(4), 527-543.

Ishihara, K. (1996). "Soil Behavior in Earthquake Geotechnics". Clarendon Press, Oxford.

Jamiolkowski, M., Leroueil, S., and LoPresti, D. C. F. (1991). "Design Parameters from Theory to Practice". Geo-Coast 1991, Yokohama, Japan, 877-917.

Janbu, N. (1963). "Soil Compressibility as Determined by Oedometer and Triaxial Tests". European Conf. on Soil Mech. and Found. Engrg., Vol. 1, Wiesbaden, Germany, 19-25.

Kramer, S. L. (1996). "Geotechnical Earthquake Engineering". Prentice Hall, Inc., Upper Saddle River, NJ, USA.

Kokusho, T. (1987). "In Situ Dynamic Soil Properties and their Evaluation". Proc., 8th Asian Reg. Conf. on Soil. Mech. and Found. Engrg., Vol. 2, Kyoto, 215-435.

Lade, P. V., Yamamuro, J. A., and Bopp, P. A. (1996). "Significance of Particle Crushing in Granular Materials". J. Geotech. Engrg., ASCE, 122(4), 309-316.

LoPresti, D. C. F., Pallara, O., Lancellotta, R., and Maniscalco, R. (1993). "Monotonic and Cyclic Loading Behavior of two Sands at Small Strains". Geotech. Testing J., 16(4), 409-424.

LoPresti, D. C. F. (1995). "Measurement of Shear Deformation of Geomaterials in the Laboratory". Pre-Failure Deformation of Geomaterials, Balkema, Sapporo, 1067-1088.

Metrodata Inc. (2002). "All Puerto Rico - Pro". CD-ROM.

Mitchell, J. K. (1993). "Fundamentals of Soil Behavior". 2nd Ed. John Wiley & Sons, Inc, New York.

Morelock, J., and Ramirez, W. (2004). "Marine Sediments". Marine Geology, <http://geology.uprm.edu/Morelock/GEOLOCN_/sedimt.htm> (February 12, 2006)

Morioka, B. T. (1999). "Evaluation of the Static and Cyclic Strength Properties of Calcareous Sand using Cone Penetrometer Tests". Ph.D. Dissertation, University of Hawaii, Manoa, USA.

Morse, J. W., and Mackenzie, F. T. (1990). "Geochemistry of Sedimentary Carbonates". Elsevier Science Publishers B. V., Amsterdam

Poulos, S. J., Castro G., and France, J. W. (1985). "Liquefaction Evaluation Procedure". J. Geotech. Engrg., ASCE, 111(6), 772-792.

Santamarina, J.C., Klein, K.A., and Fam, M.A. (2001). "Soils and Waves. Particulate Material Behavior, Characterization and Process Monitoring". John Wiley & Sons, Inc. New York.

Saxena, S. K., Avramidis, A. S., and Reddy, K. R. (1988). "Dynamic Moduli and Damping Ratios for Cemented Sands at Low Strains". Can. Geotech. J., 25, 353-368.

Saxena, S. K., and Lastrico, R. (1978). "Static Properties of Lightly Cemented Sands". J. Geotech. Engrg., ASCE, 104(12), 1449-1464.

Scanlon, K. M., Rodriguez, R. W., Trias, J. L, and Delorey, C. M (1998). "Offshore Sediments and Sand and Gravel Resources on the Insular Shelf of Puerto Rico". U.S. Geological Survey, Open-File Report 98-38, 202-217.

- Seed, H. B., Wong, R. T., Idriss, I. M., and Tokimatsu, K. (1986). "Moduli and Damping Factors for Dynamic Analyses of Cohesionless Soils". *J. Geotech. Engrg., ASCE*, 112(11), 1016-1032.
- Sladen, J. A., and Handford, G. (1987). "A potential Systematic Error in Laboratory Testing of Very Loose Sands". *Can. Geotech. J.*, 24, 462-466.
- Stokoe, K. H., II, Hwang, S. K., Lee, J. N.-K., and Andrus, R. D. (1995). "Effects of Various Parameters on the Stiffness and Damping of Soils at Small to Medium Strains". *Pre-Failure Deformation of Geomaterials, Vol. 1. Balkema, Sapporo*, 785-816.
- Sweet, J. (1988). "Estimation of the Drained End Bearing Capacity of Calcareous Material". *Engineering for Calcareous Sediments. Balkema, Perth*, 69-78.
- Terzaghi, K., Peck, R. B., and Mesri, G. (1993). "Soil Mechanics in Engineering Practice". 3rd Ed. John Wiley & Sons, Inc, New York.
- Todor, D. N. (1976). "Thermal Analysis of Minerals". Abacus Press, Tunbridge Wells, UK.
- Valle, C., Stokoe II, K. H., Camacho, B. I., and Rauch, A. F. (2003). "Comparison of the Dynamic Properties and Undrained Shear Strength of Offshore Calcareous Sand and Artificially Cemented Sand". *Proc. 22nd International Conference on Offshore Mechanics and Arctic Engineering, Cancun*, 1-9.
- Volckmann, R. P. (1984). "Geologic Map of the Puerto Real Quadrangle, Southwest Puerto Rico". U.S. Geological Survey, Map I-1559.
- Webb, P. A. (2001). "Volume and Density Determinations for Particle Technologists", Micromeritics Instrumental Corp.
< http://www.micromeritics.com/pdf/app_articles/density_determinations.pdf> (April 1, 2006)

APPENDIX 1 SEM Micrographs

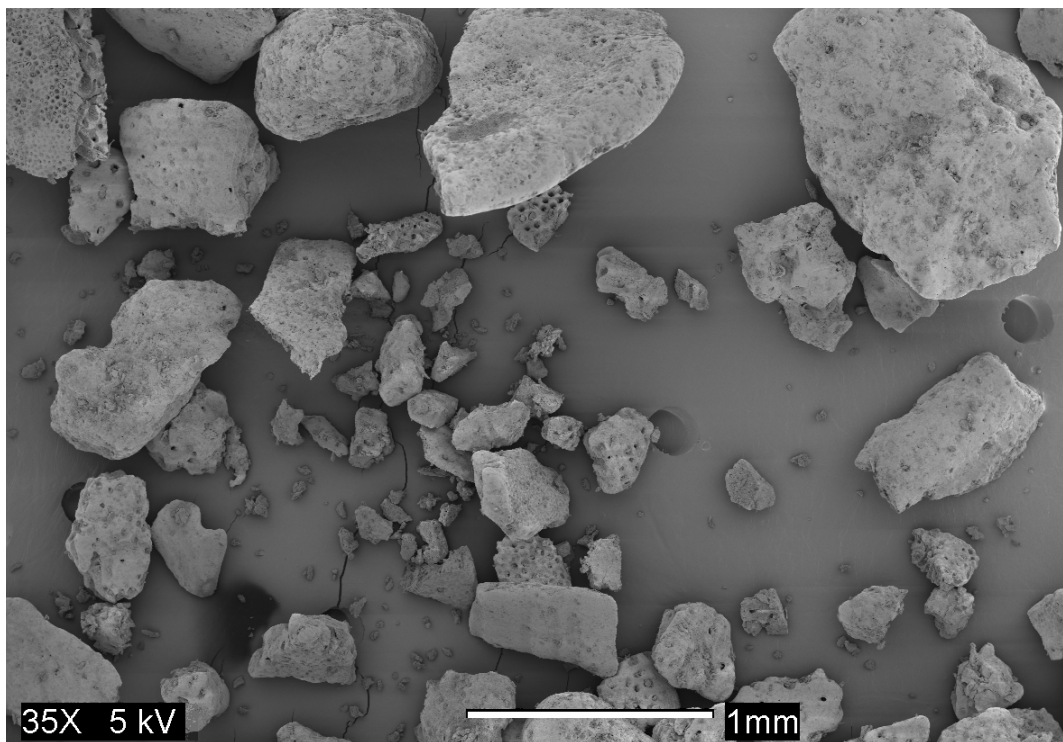


Figure A.1.1. General view of the Cabo Rojo sand particles, scale = 1000 μm .

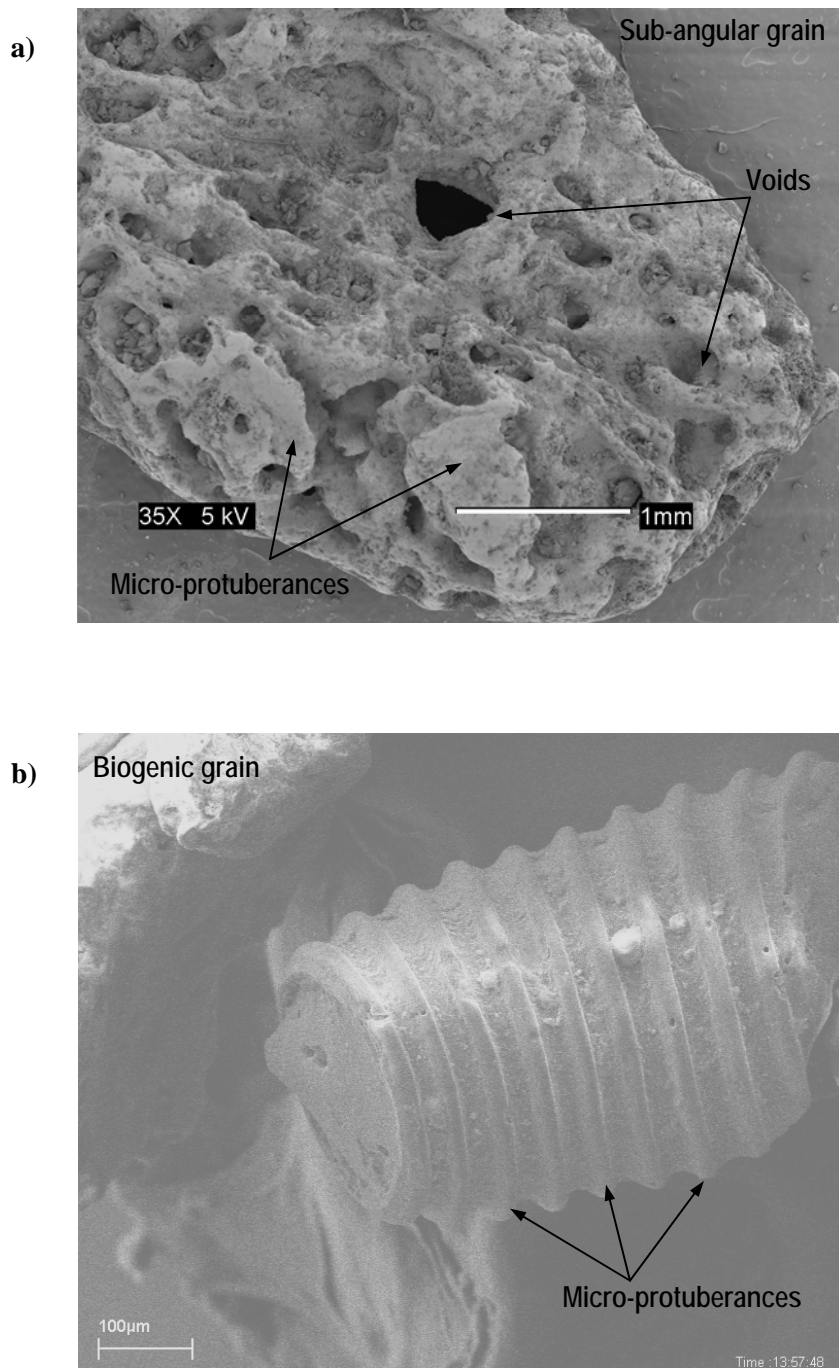


Figure A.1.2. Particle features, Cabo Rojo sand, a) scale = 1000 µm, b) scale = 100 µm.

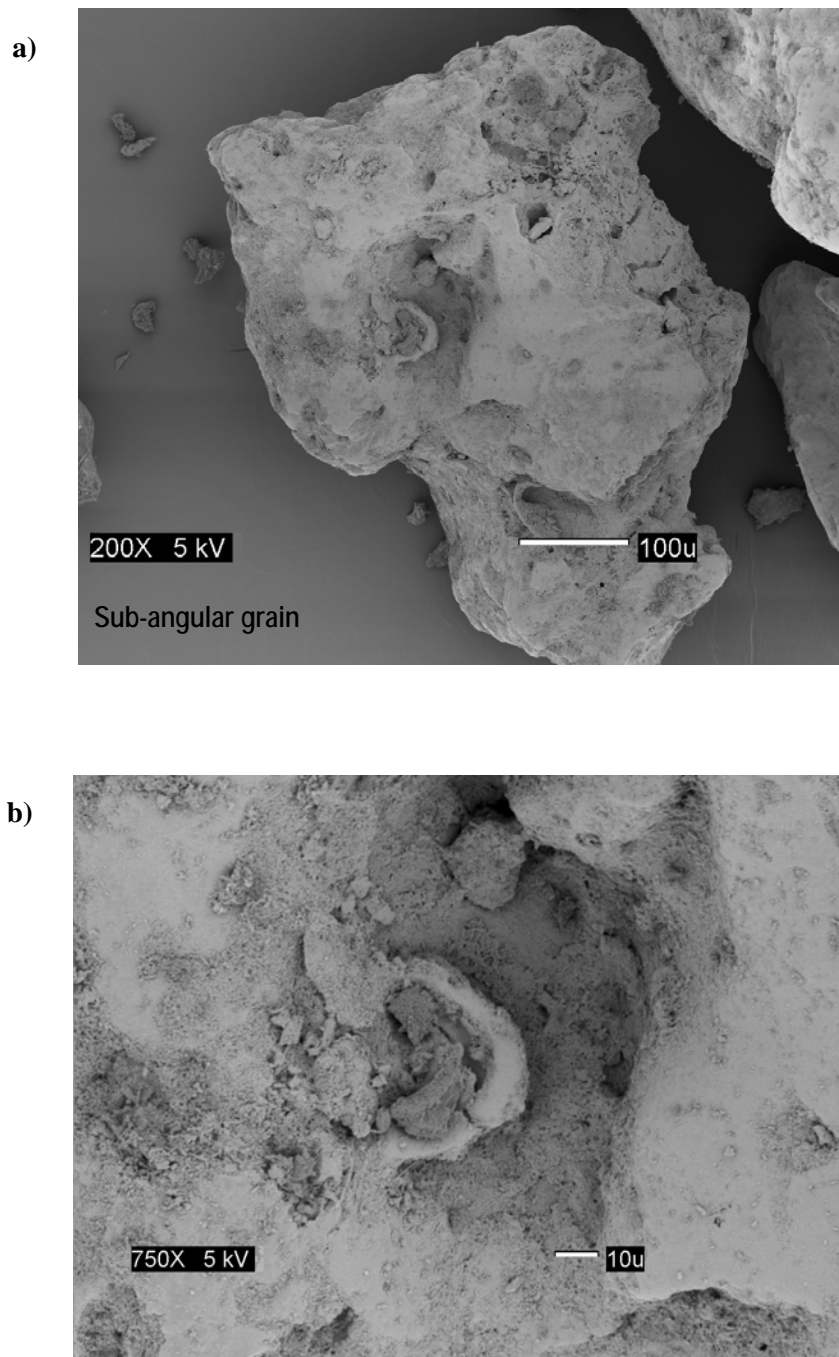


Figure A.1.3. Detail of the surface texture for a Cabo Rojo sand particle, a) scale = 100 μm , b) scale = 10 μm .

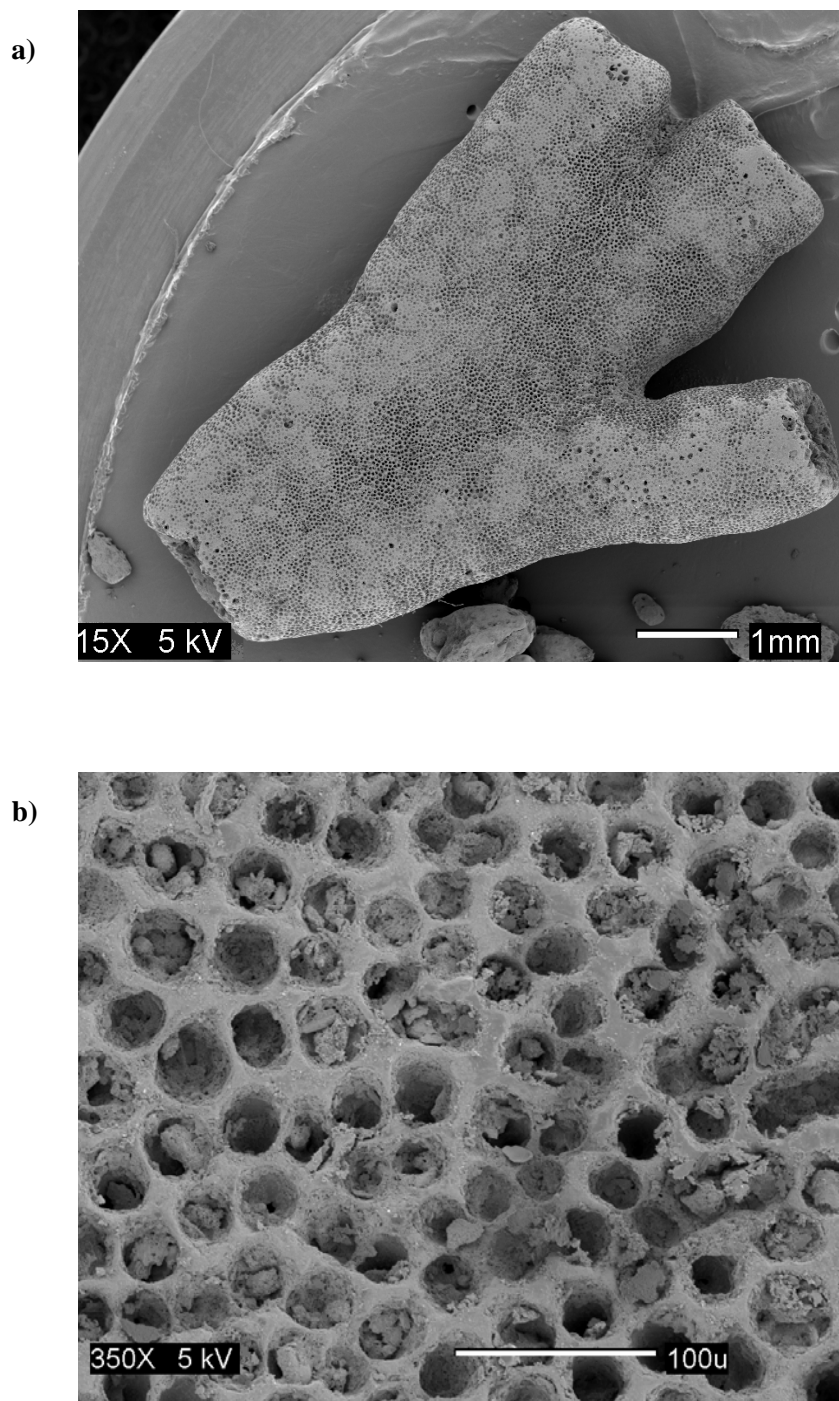
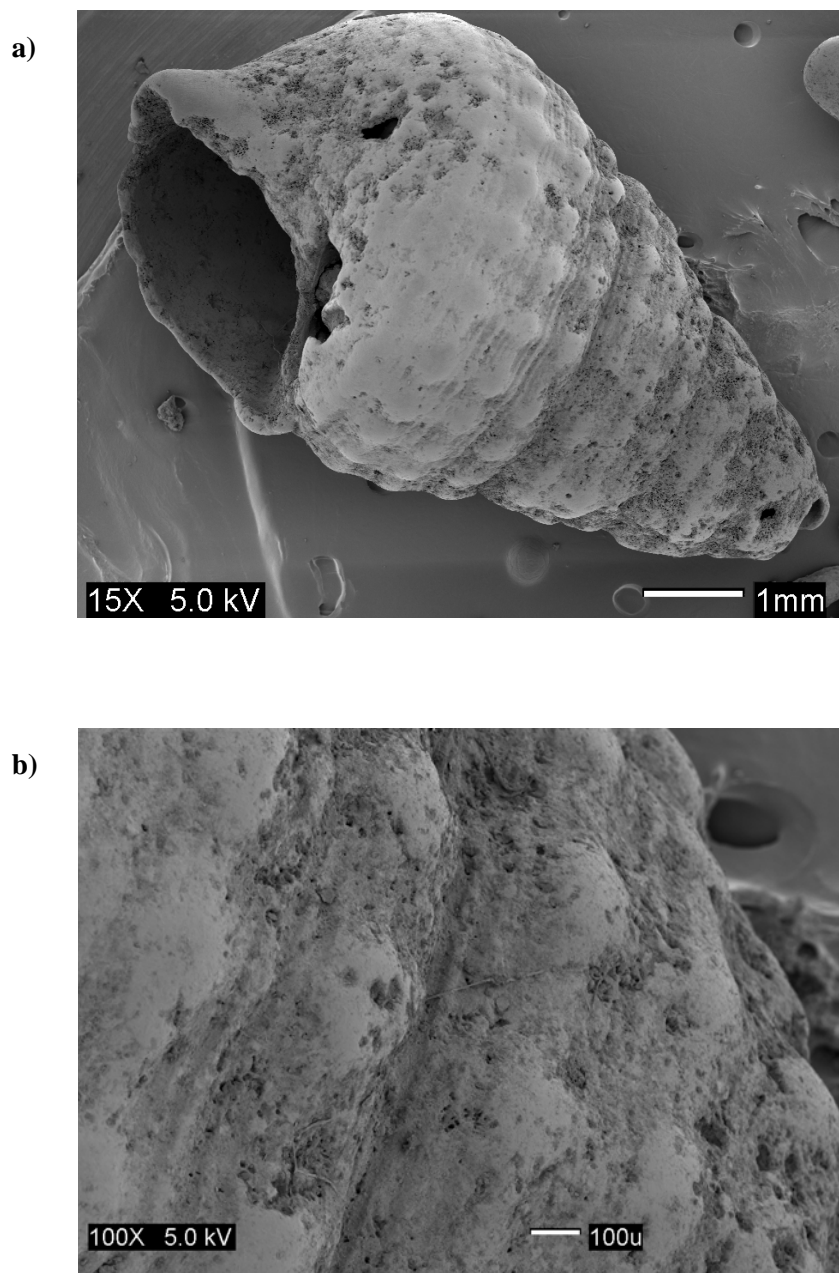


Figure A.1.4. Biogenic grain, Cabo Rojo sand. (*Halimeda*, aragonite alga),
a) scale = 1000 μm , b) scale = 100 μm .



**Figure A.1.5. Biogenic grain, Cabo Rojo sand. (calcite-aragonite gastropod),
a) scale = 1000 μm , b) scale = 100 μm .**

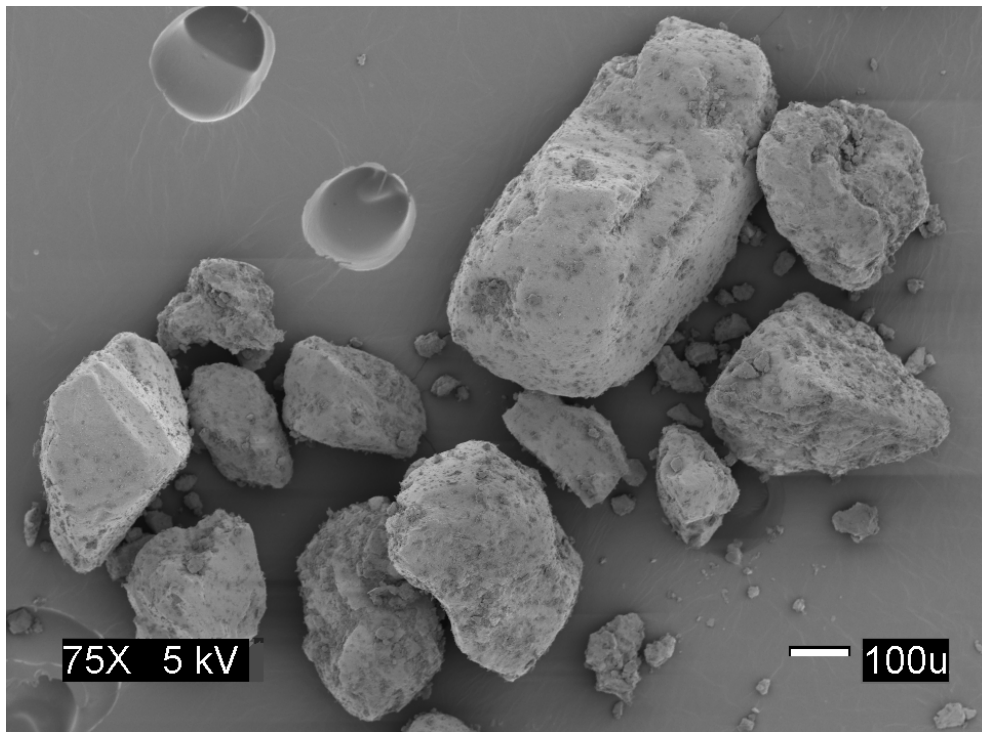


Figure A.1.6. General view of the South Bend sand particles, scale = 100 μm .

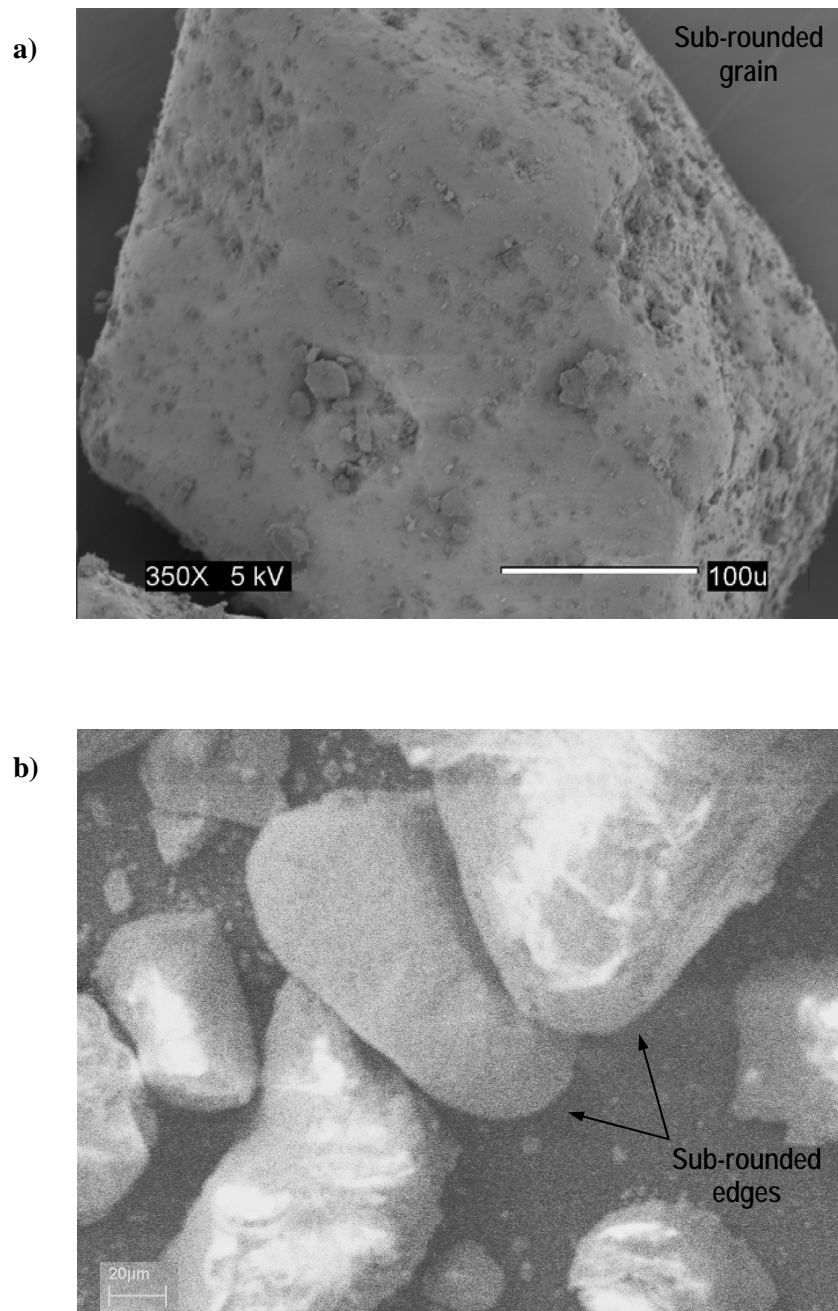


Figure A.1.7. Shape particle features, South Bend sand, a) scale = 100 µm, b) scale = 20 µm.

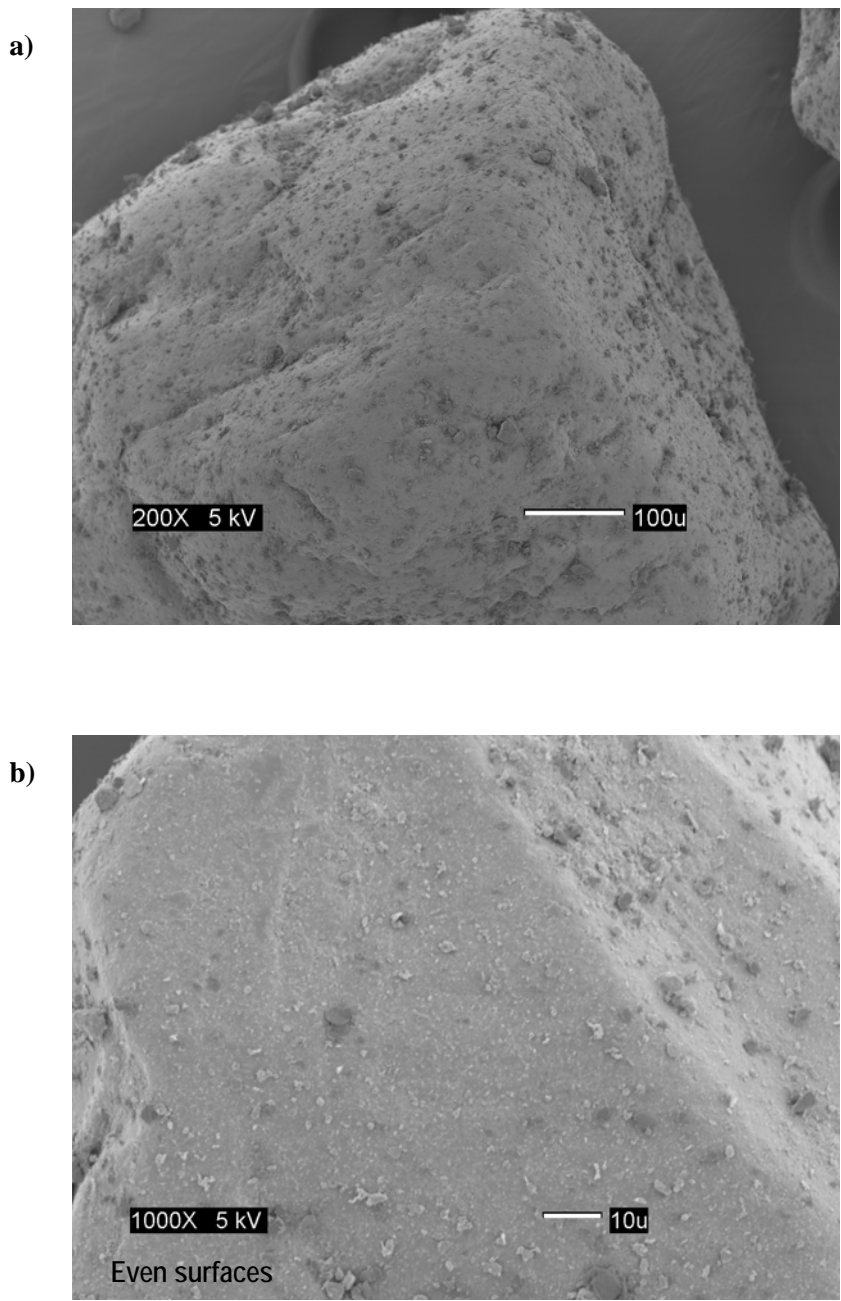


Figure A.1.8. Detail of the surface texture for a South Bend sand particle, a) scale = 100 μm , b) scale = 10 μm .

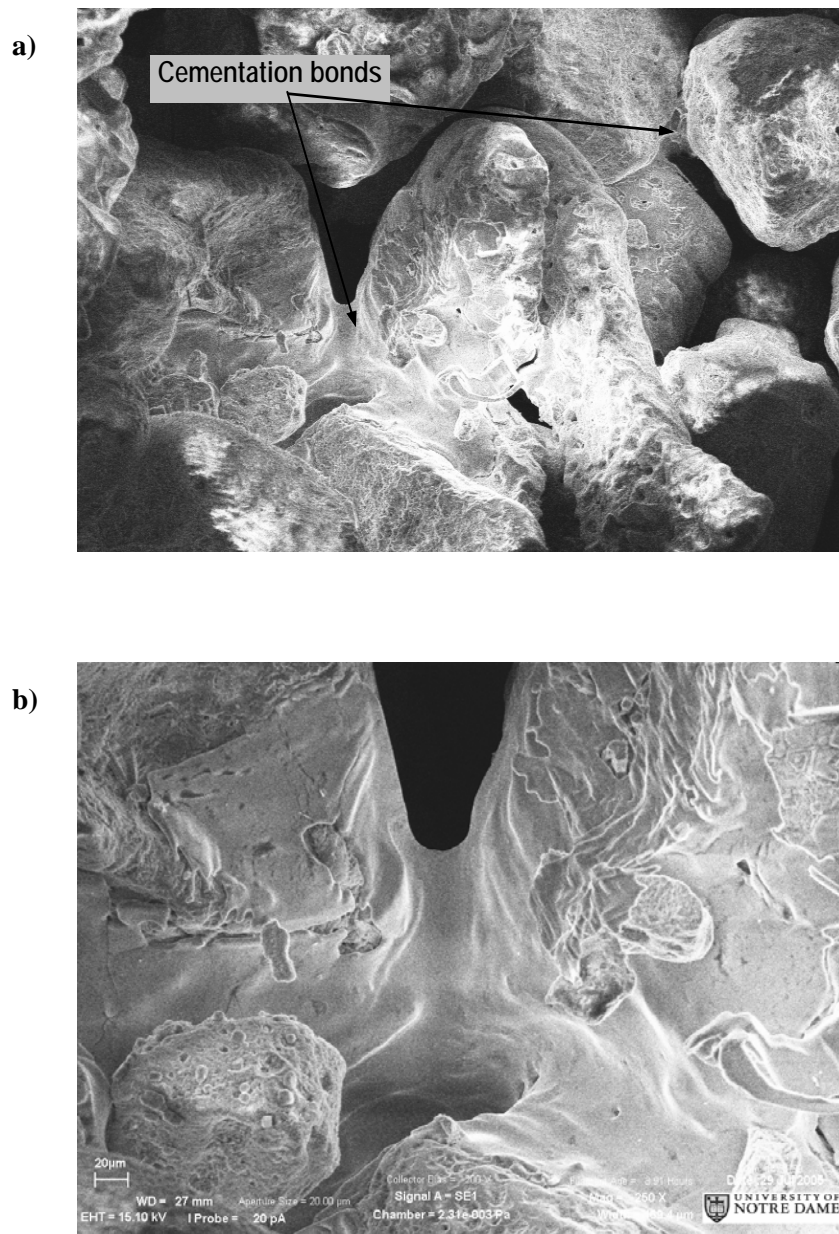


Figure A.1.9. Induced cementation on Cabo Rojo sand. Cementing material in the form of a coating, a) scale = 100 μm, b) scale = 20 μm.

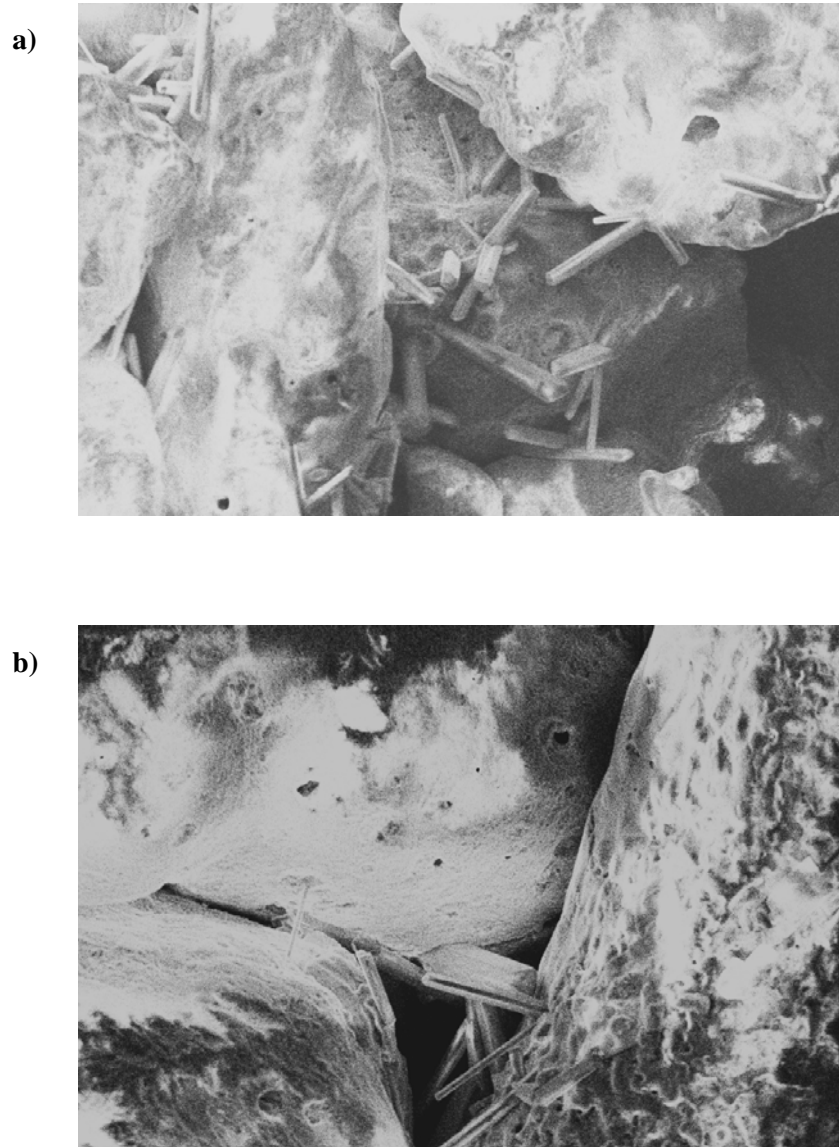


Figure A.1.10. Induced cementation on Cabo Rojo sand. Cementing material in the form of a needle-like, a) scale = 100 μm , b) scale = 20 μm .

APPENDIX 2.

Non-standardized Tests for Sands Characterization.

Alternative Method to Determine Maximum Density

The maximum density test was initially done following the standard ASTM D4253-93, but since this method involves the mechanical compaction of sand samples, some anomalous behavior was observed for Cabo Rojo sand, as shown in Figure A.2.1. This behavior is related to the crushability of calcareous sand particles.

For this reason, an alternate method was used for both Cabo Rojo and South Bend sands to avoid grain crushing. In this method, sand was placed in a cylindrical mold (D=102 mm, H=116 mm) using a funnel with a 45° angle and 15 mm in diameter. A 20 mm extension piece was added to the mold. The sand was spread in the mold with zero height of fall, in 10 layers of approximately 17 mm each. The mold was tapped to the side with a wooden mallet, 100 times per layer for a total of 1000 times. The extension piece was then removed and the sand was leveled using a straight-edge. Then the mass was determined and the maximum density assessed.

Figure A.2.2 shows the materials used for the alternative method described.

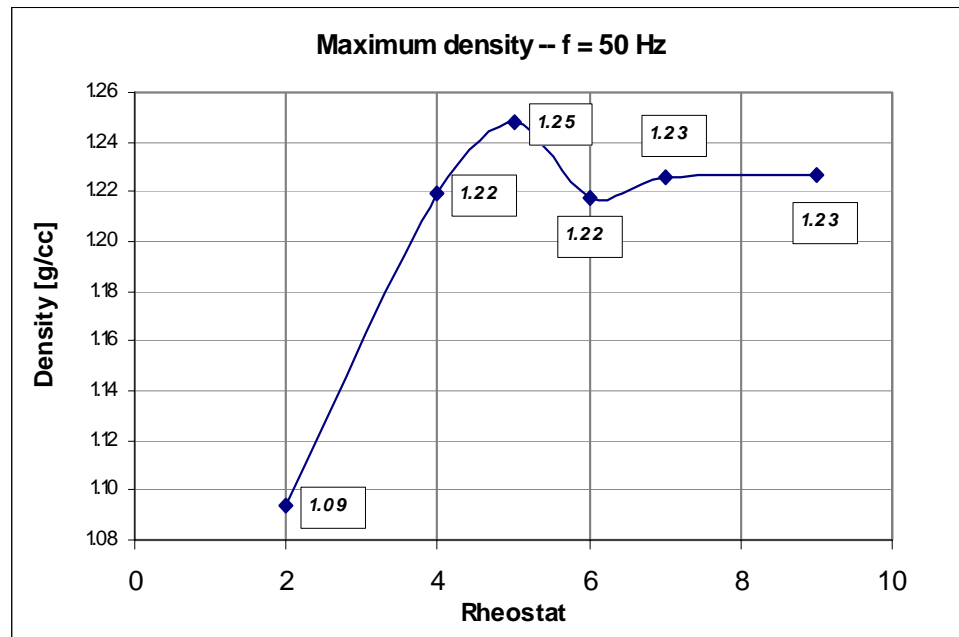


Figure A.2.1. Initial results for maximum density test, ASTM D4253-93.



Figure A.2.2. Alternative method for maximum density test.

Gas pycnometer for Specific Gravity of Solids Determination

Since calcareous sand particles exhibits unique shapes and texture with intraparticle porosity, high probability exists on air bubbles remaining inside the water pycnometer when performing the conventional specific gravity (G_s) of solids test (ASTM D854-02). The Micromeritics–AccuPyc 1330 gas pycnometer (see Figure A.2.3) from the Material Characterization Laboratory at the University of Notre Dame was used to determine the G_s values of the test sands.

Gas pycnometer method is faster and more accurate than the water pycnometer method. A gas pycnometer operates by detecting the pressure change resulting from gas displacement by solid objects (Webb, 2001). This way the skeletal volume of the solid could be determined using the gas law given by the following expression:

$$P \cdot V = n \cdot R \cdot T \quad (\text{A.2.1})$$

where P is the gas pressure, V is the volume occupied by the gas, n is the number of gas molecules, T is its temperature and R is the gas constant.

The sample of unknown volume (V_x) is placed into a chamber with known volume, (V_s). When chamber is sealed, the pressure within the sample chamber is measured (P_s). Then, a reference chamber of known volume (V_r) is charged to a pressure P_r greater than

the pressure in the sample chamber (P_s). A valve isolating the two chambers is opened and the pressure of the system (P_{sys}) is allowed to equilibrate.



**Figure A.2.3 Micromeritics–AccuPyc 1330 gas pycnometer.
University of Notre Dame.**

Figure A.2.4 shows the initial and final condition of the system. Assuming the temperature (T) and the number of gas molecules (n) are constant through the experiment, the gas law (A.2.1) permits to determine de sample volume V_x as shown in Figure A.2.4.

The accuracy and precision of the gas pycnometer in the determination of skeletal volume and density can be quite high, but it relies greatly on letting the sample material and gas be free of moisture (Webb, 2001). The sample also must be free of any volatile substances that can contribute to partial pressures and cause error and instability.

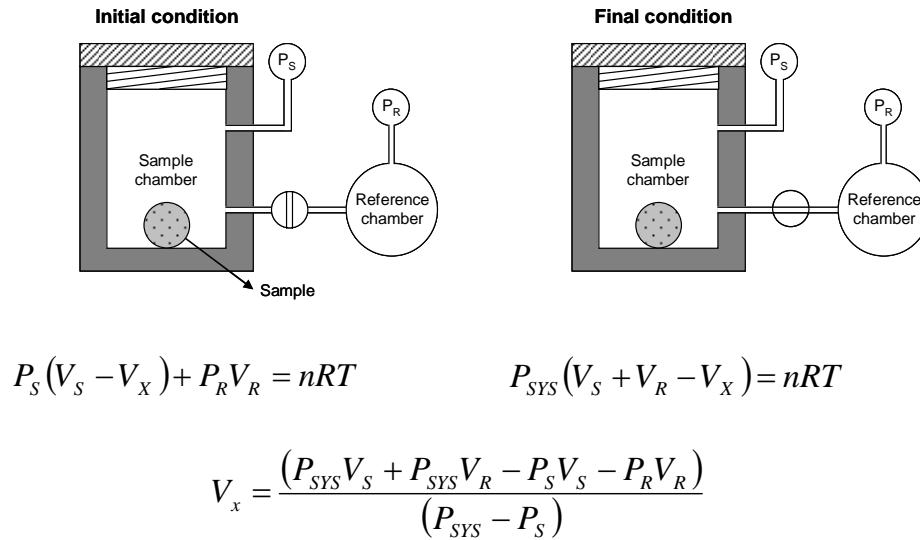


Figure A.2.4 Fundamental of the operation of gas pycnometer.

Thermogravimetric Analyses for Calcium Carbonate Content Determination

Thermogravimetric analyses (TGA) were performed at the Material Characterization Laboratory of the University of Notre Dame to determine the calcium carbonate content of soil samples using a NETZSCH TG 209 device (see Figure A.2.5). In this method, the sample is placed into a small tared pan, which is then placed into a high temperature furnace. A sensitive microbalance measures the initial sample weight at room temperature and then continuously monitors changes in sample weight (losses or gains) as heat is applied to the sample.



Figure A.2.5 NETZSCH TG 209 device, University of Notre Dame.

All TGA tests done in this study were run with the following heating program:

1. Initial phase: 25°C
2. Dynamic phase: 900°C – rate: 5°K/min.
3. Isothermal phase: 900°C – total phase duration: 30 min.
4. Emergency phase: 950°C

Todor (1976) indicates that calcium carbonate (CaCO_3) loses carbon dioxide (CO_2) at about 675°C and reaches complete outgassing at about 950°C. This can be represented in the following chemical reaction that occurs in calcium carbonate when heated to these temperatures:



Because the aforementioned chemical reaction has a 1:1 ratio, the moles lost of CO_2 are the same as the amount moles lost of calcium carbonate (CaCO_3). By this way, and

using the molecular weight of calcium carbonate, the amount of calcium carbonate in the specimen could be determined as shown in Figure A.2.6.

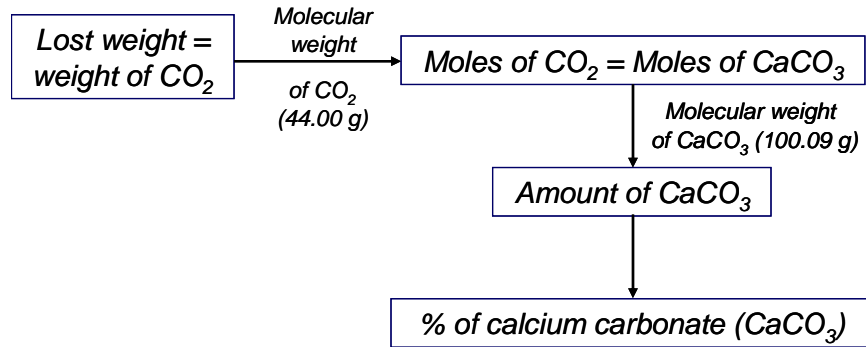


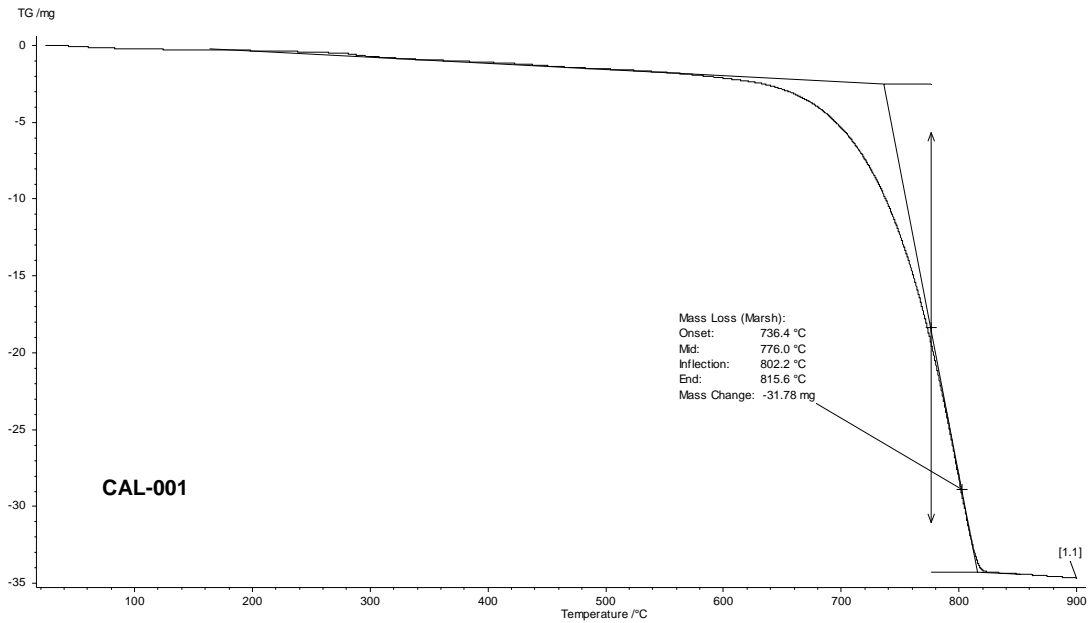
Figure A.2.6 Procedure to determine calcium carbonate content from TGA results.

Shown next are the results obtained for samples analyzed by the TGA method:

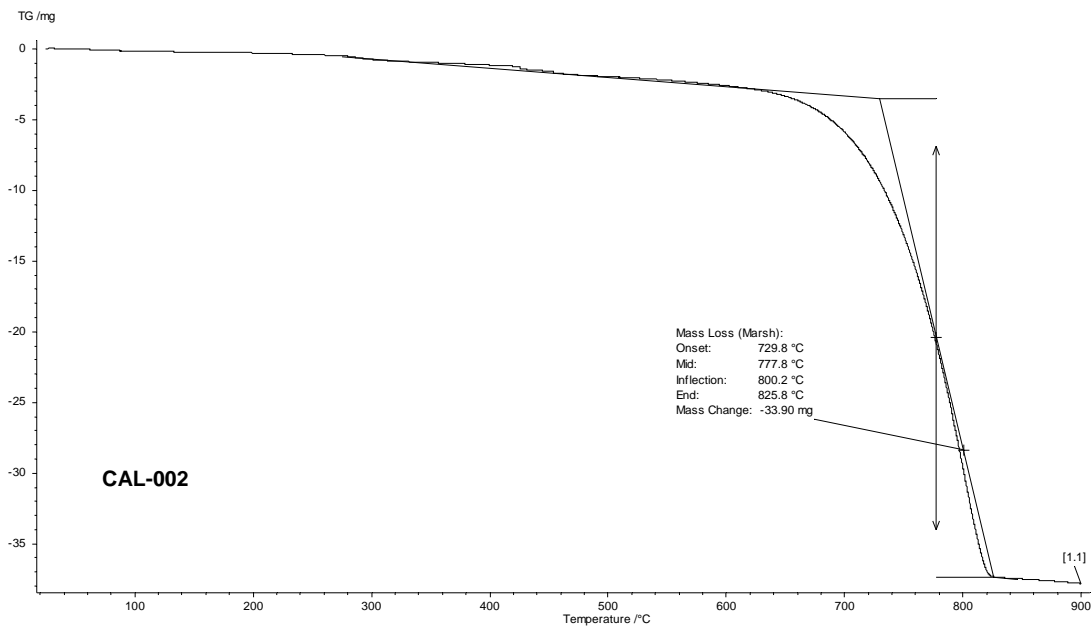
MOLECULAR WEIGHT

CaCO₃		CO₂	
Ca	40.078	C	12.0107
C	12.0107	O	15.9994
O	15.9994		<u>44.0095</u>
	<u>100.0869</u>		
1 mole of CaCO ₃	100.0869 g 100086.9 mg	1 mole of CO ₂	44.0095 g 44009.5 mg

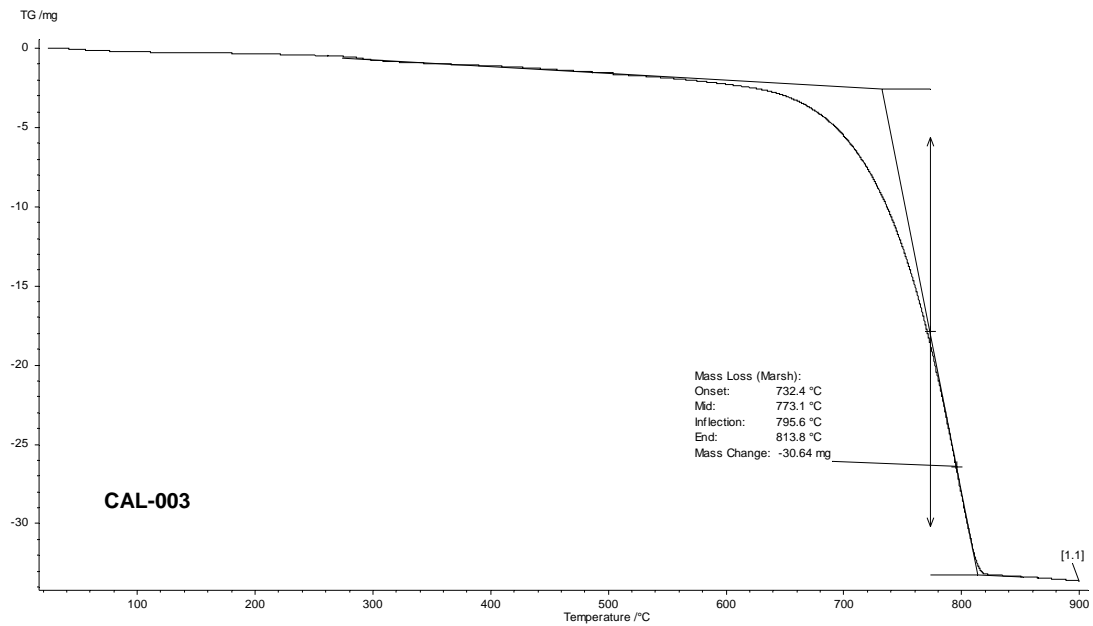
Sample 1 - CAL-001		
Mass Loss (CO ₂)	31.78 mg 0.0007 moles of CO ₂	
Mass Loss (CaCO ₃)	0.0007 moles of CaCO ₃ 72.274 mg	
Calcium carbonate	72.274 mg	91.31% of CaCO₃
Total mass	79.151 mg	



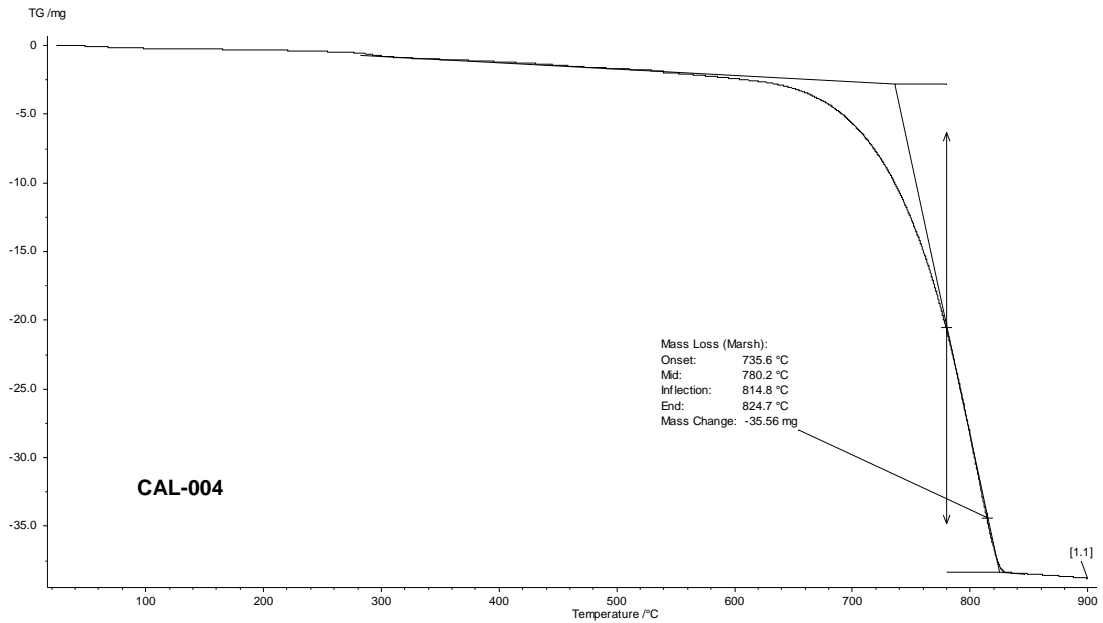
Sample 2 - CAL-002		
Mass Loss (CO ₂)	33.90 mg	
	0.0008 moles of CO ₂	
Mass Loss (CaCO ₃)	0.0008 moles of CaCO ₃	
	77.096 mg	
Calcium carbonate	77.096 mg	97.29% of CaCO₃
Total mass	79.246 mg	



Sample 3 - CAL-003		
Mass Loss (CO₂)	30.64 mg 0.0007 moles of CO ₂	
Mass Loss (CaCO₃)	0.0007 moles of CaCO ₃ 69.682 mg	
Calcium carbonate	69.682 mg	91.07% of CaCO₃
Total mass	76.517 mg	



Sample 4 - CAL-004		
Mass Loss (CO₂)	35.56 mg 0.0008 moles of CO ₂	
Mass Loss (CaCO₃)	0.0008 moles of CaCO ₃ 80.871 mg	
Calcium carbonate	80.871 mg	91.41% of CaCO₃
Total mass	88.469 mg	



Sample 5 - SIL-001		
Mass Loss (CO₂)	4.37 mg	
	0.0001 moles of CO ₂	
Mass Loss (CaCO₃)	0.0001 moles of CaCO ₃	
	9.938 mg	
Calcium carbonate	9.938 mg	10.56% of CaCO₃
Total mass	94.133 mg	

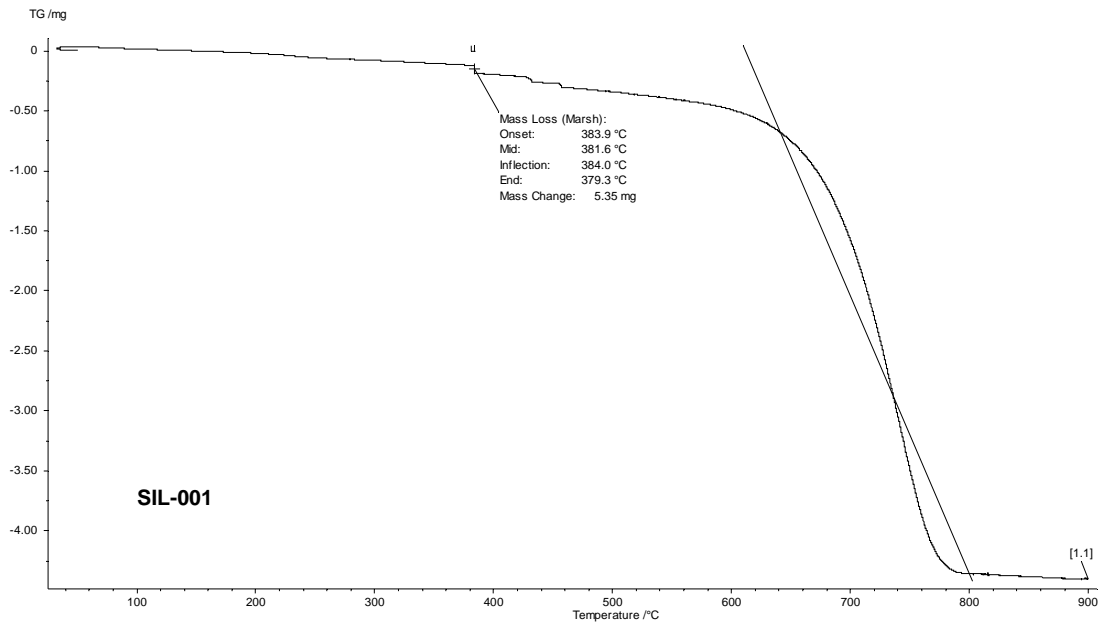


Figure A.2.7 shows the curves of mass change with temperature obtained for the samples analyzed by the TGA method. It could be noticed that the Cabo Rojo calcareous sand samples have very similar curves, while notable differences exist between them and the South Bend silica sand.

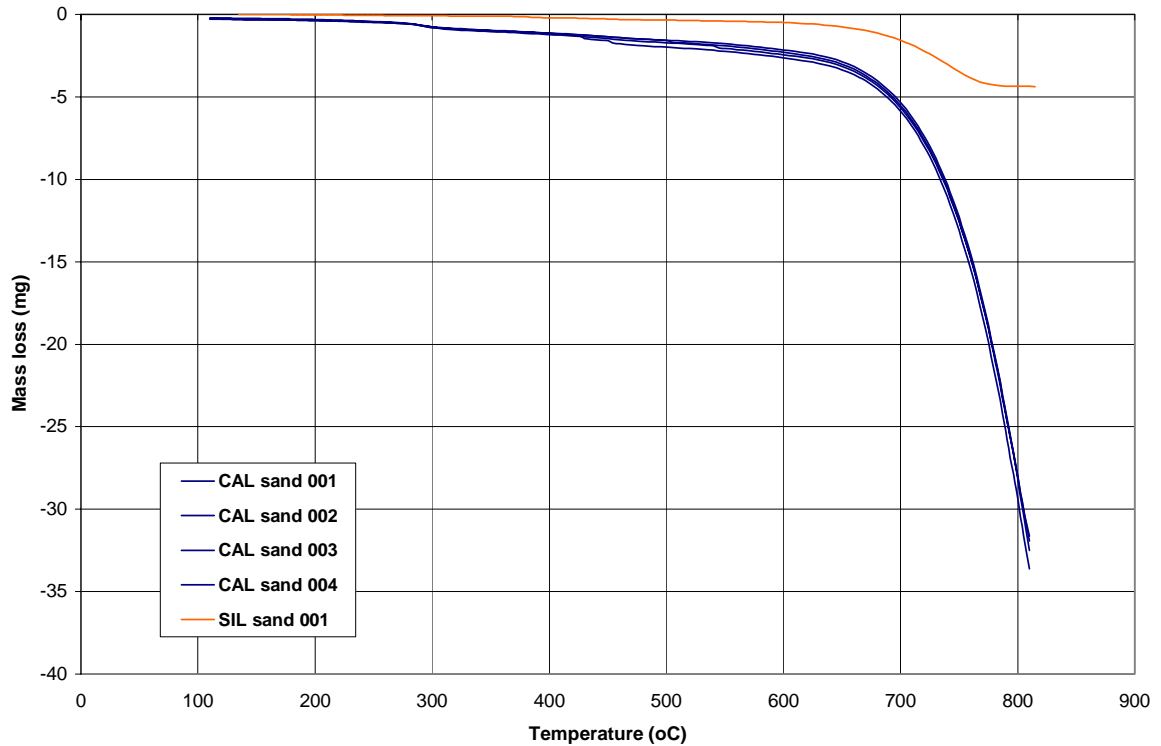


Figure A.2.7 Mass changes with temperature obtained from the TGA tests.

APPENDIX 3

Direct Shear Test (DST)

- Other results -

Initial state of DST samples

Cabo Rojo calcareous sand:

	Test #	σ_{normal} kPa	Mass g	Area mm ²	Height mm	γ dry kN/m ³	Ini. void ratio e_0	Initial $D_{r \text{ ini}}$
Minimum density	CD-033	50	119.94	4032.25	27.20	10.73	1.61	52%
	CD-037	200	120.90	4032.25	27.72	10.61	1.64	45%
	CD-035	300	119.83	4032.25	27.32	10.67	1.63	49%
	CD-036	500	119.78	4032.25	27.25	10.69	1.62	50%
Maximum density	CD-029	50	124.13	4032.25	26.49	11.40	1.46	88%
	CD-038	100	124.00	4032.25	25.88	11.66	1.41	101%
	CD-031	300	124.75	4032.25	26.15	11.61	1.42	98%
	CD-032	500	123.57	4032.25	26.72	11.25	1.49	80%

South Bend silica sand:

	Test #	σ_{normal} kPa	Mass g	Area mm ²	Height mm	γ dry kN/m ³	Ini. void ratio e_0	Initial $D_{r \text{ ini}}$
Minimum density	CD-015	50	195.68	4032.25	29.25	16.27	0.63	47%
	CD-018	300	188.85	4032.25	28.48	16.13	0.64	41%
	CD-039	500	193.03	4032.25	28.86	16.27	0.63	47%

After consolidation state of DST samples

Cabo Rojo calcareous sand:

	Test #	σ_{normal} kPa	Mass g	Area mm ²	Height mm	ΔH cons. mm	void ratio e_{con}	Rel. Dens. D_r cons.
Minimum density	CD-033	50	119.94	4032.25	27.20	-0.22	1.59	57%
	CD-037	200	120.90	4032.25	27.72	-0.39	1.61	54%
	CD-035	300	119.83	4032.25	27.32	-0.51	1.58	60%
	CD-036	500	119.78	4032.25	27.25	-0.79	1.55	68%
Maximum density	CD-029	50	124.13	4032.25	26.49	-0.03	1.46	89%
	CD-038	100	124.00	4032.25	25.88	-0.12	1.40	103%
	CD-031	300	124.75	4032.25	26.15	-0.29	1.39	104%
	CD-032	500	123.57	4032.25	26.72	-0.47	1.45	90%

South Bend silica sand:

	Test #	σ_{normal} kPa	Mass g	Area mm ²	Height mm	ΔH cons. mm	void ratio e_{con}	Rel. Dens. D_r cons.
Minimum density	CD-015	50	195.68	4032.25	29.25	-0.28	0.61	53%
	CD-018	300	188.85	4032.25	28.48	-0.52	0.61	53%
	CD-039	500	193.03	4032.25	28.86	-0.48	0.60	58%

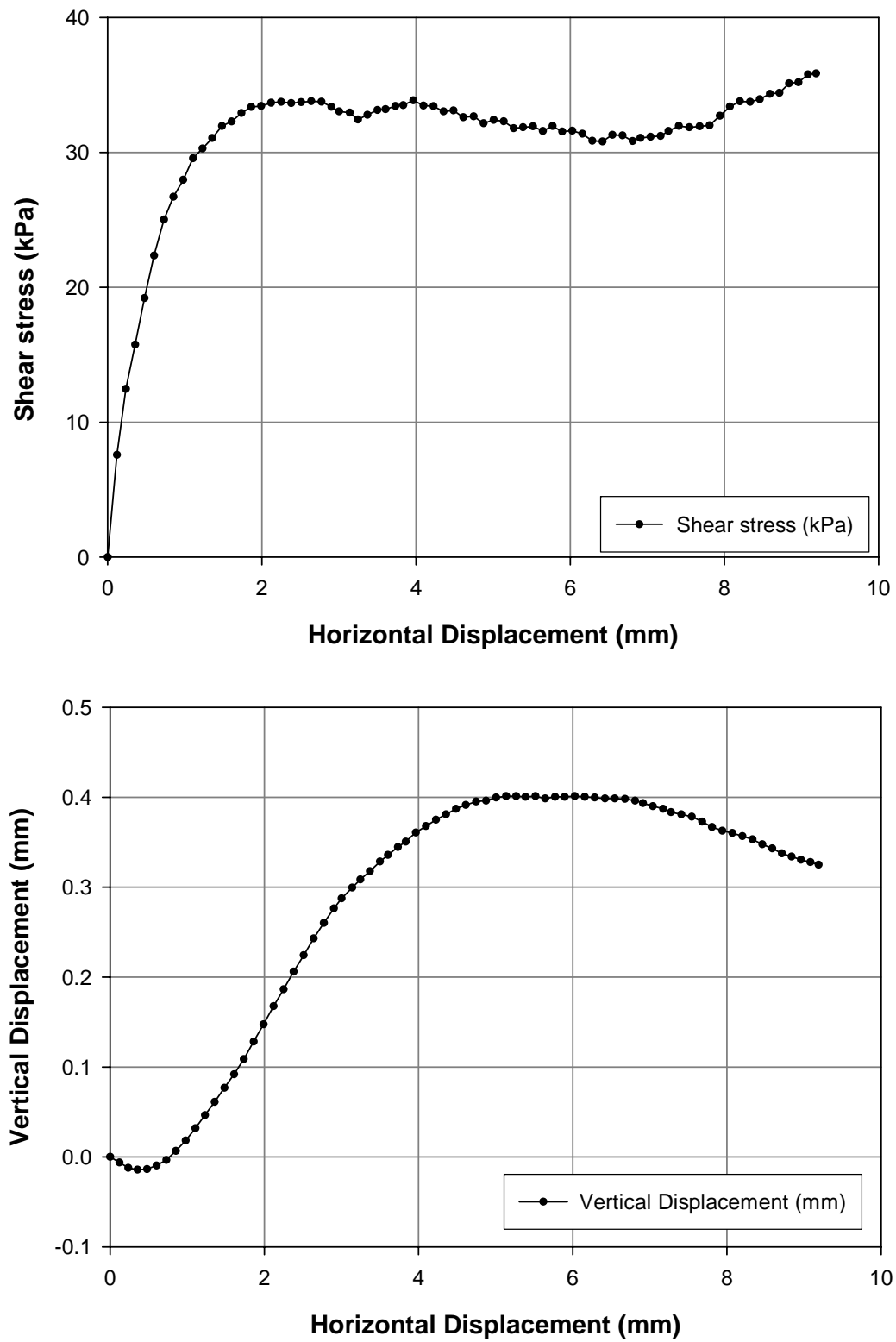


Figure A.3.1. DST results for Cabo Rojo sand sample, Normal stress = 50 kPa, $D_r = 57\%$.

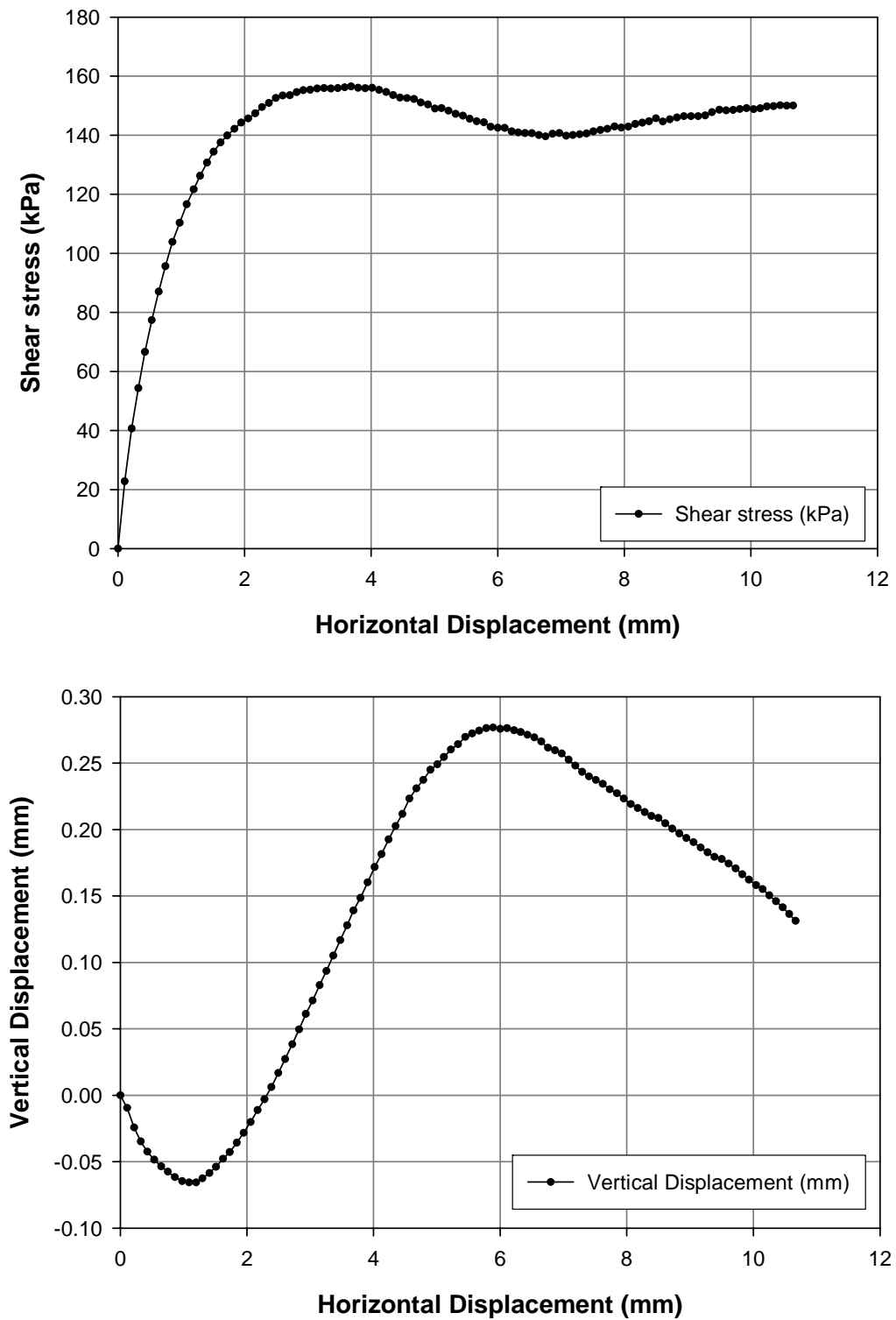


Figure A.3.2. DST results for Cabo Rojo sand sample, Normal stress = 200 kPa, $D_r = 54\%$.

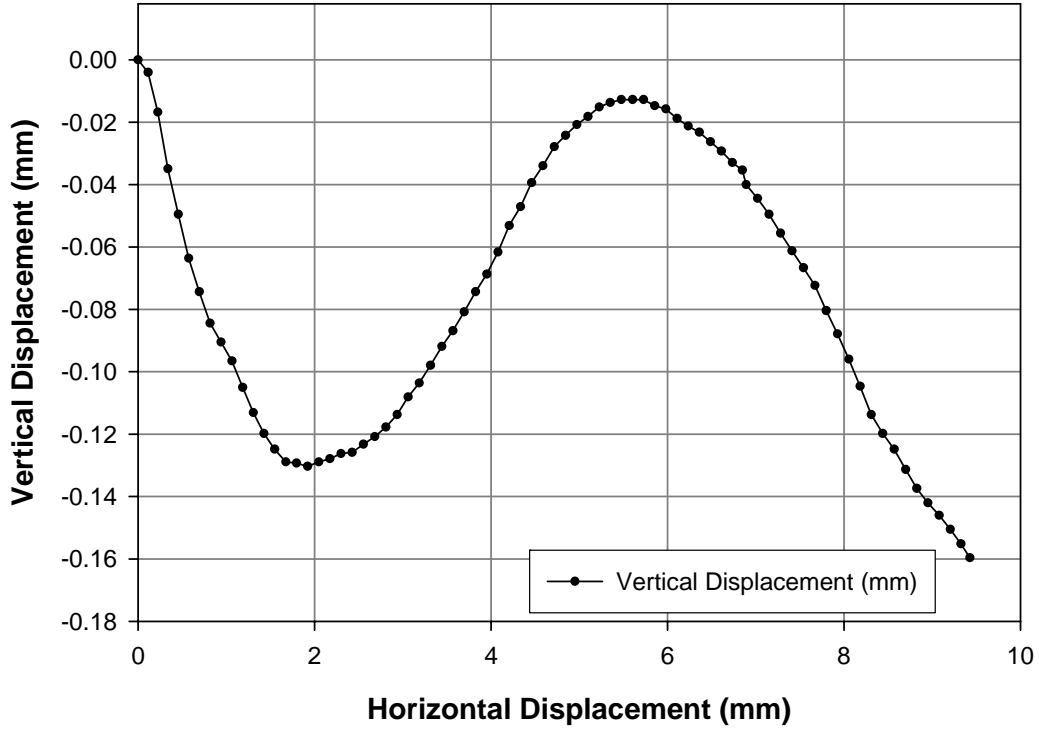
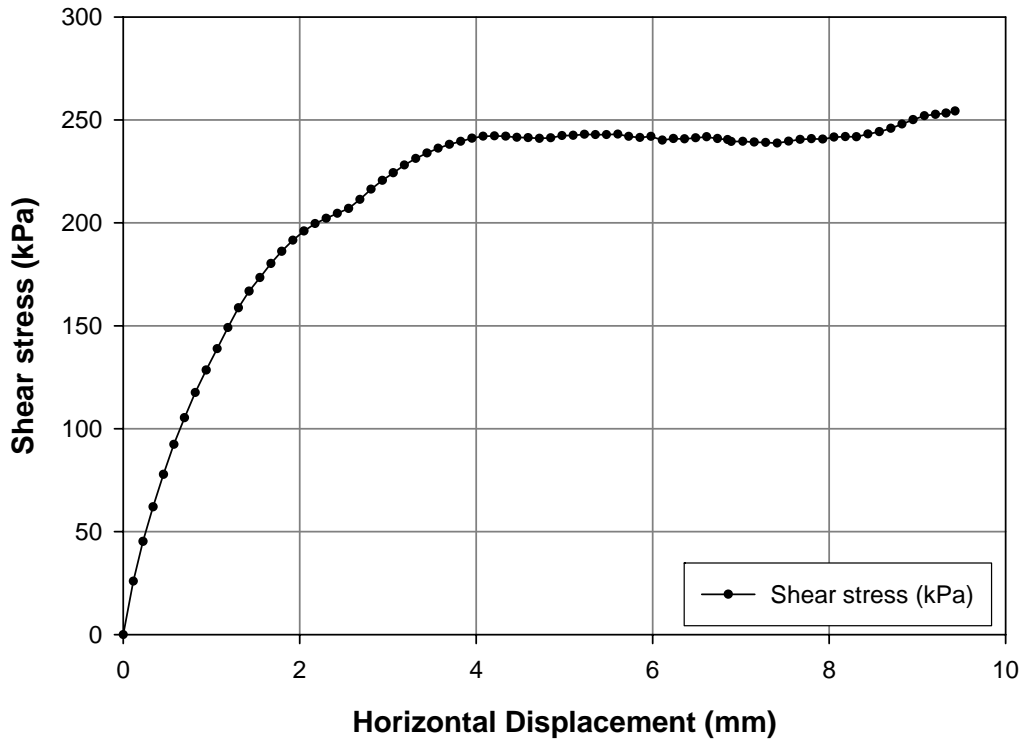


Figure A.3.3. DST results for Cabo Rojo sand sample, Normal stress = 300 kPa, Dr = 60%.

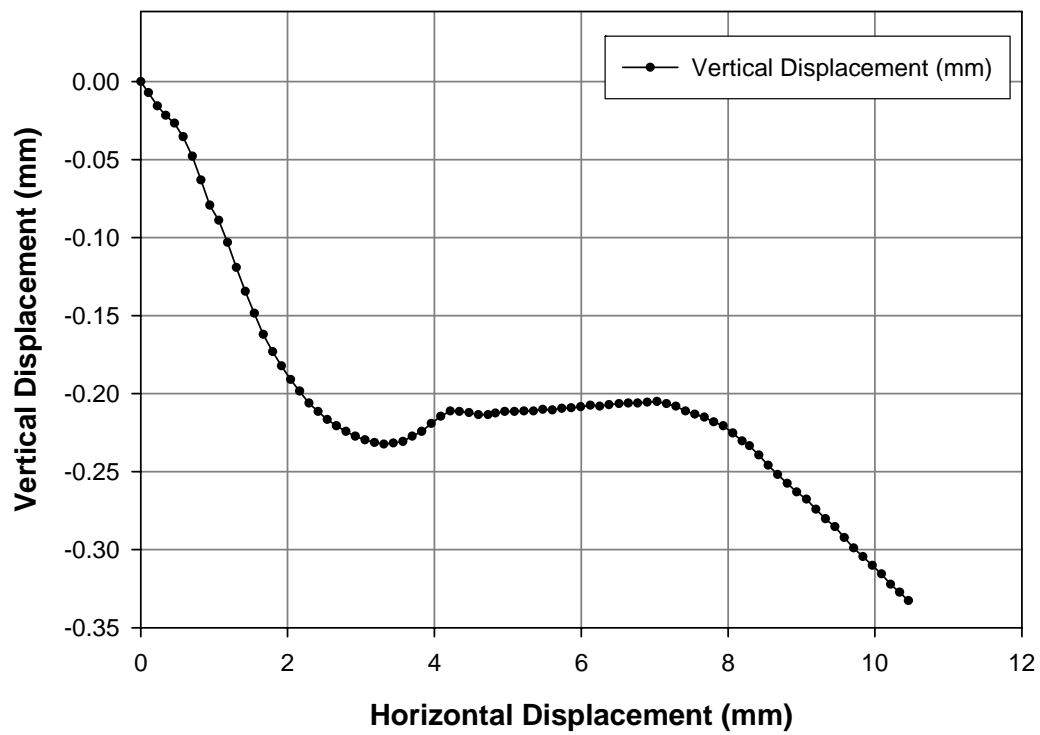
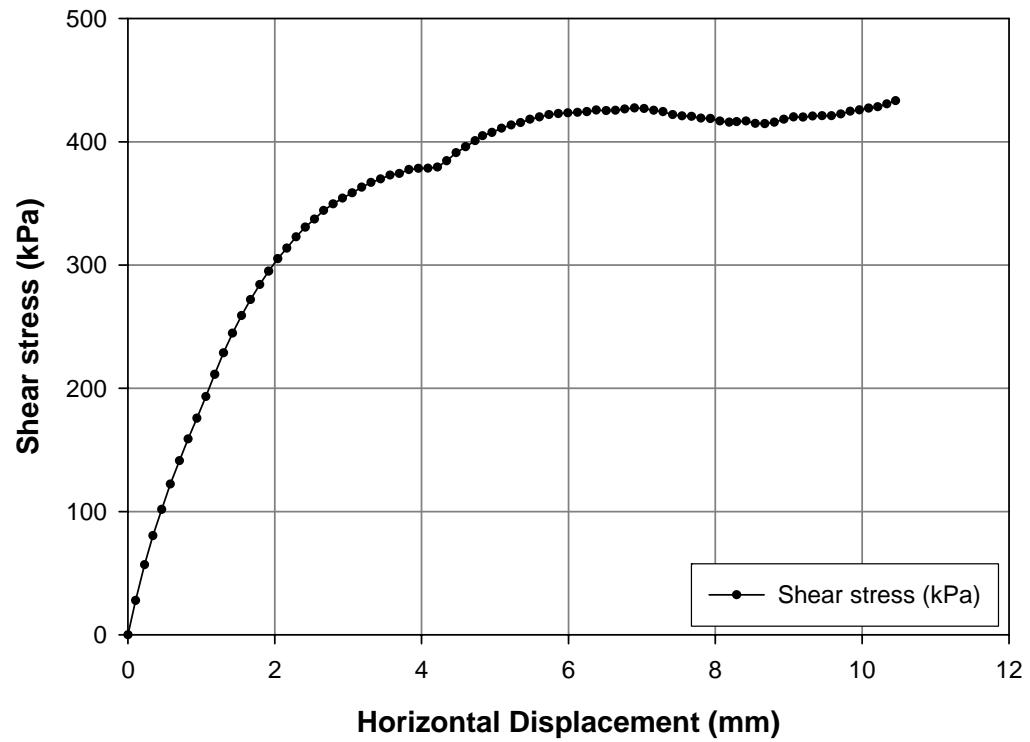


Figure A.3.4. DST results for Cabo Rojo sand sample, Normal stress = 500 kPa, $D_r = 68\%$.

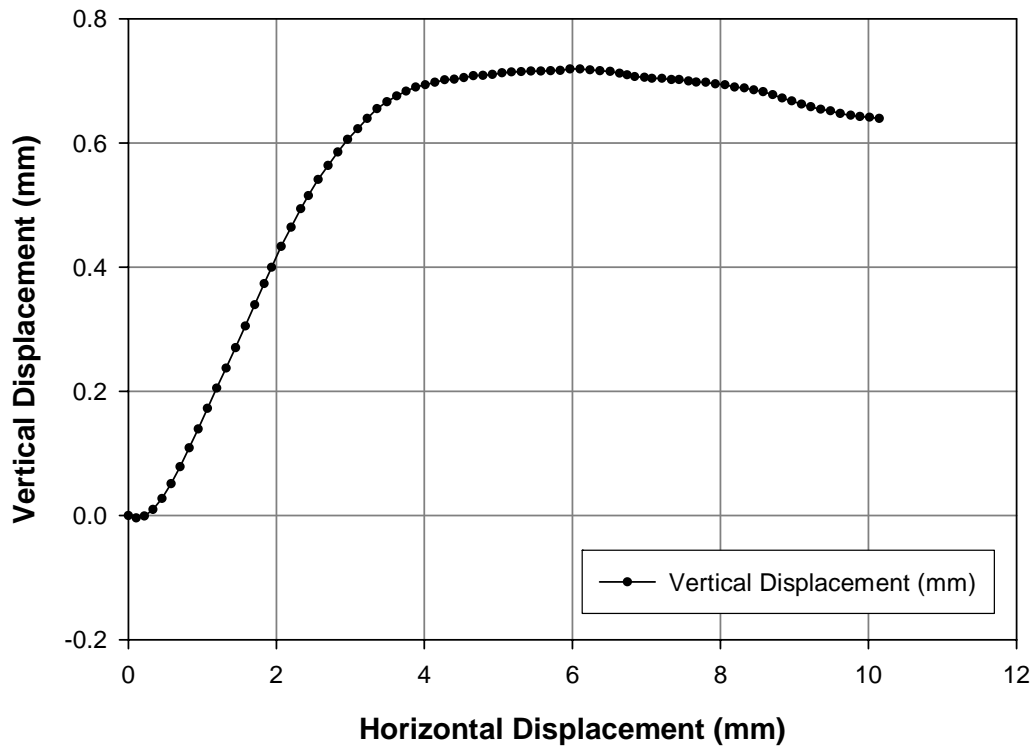
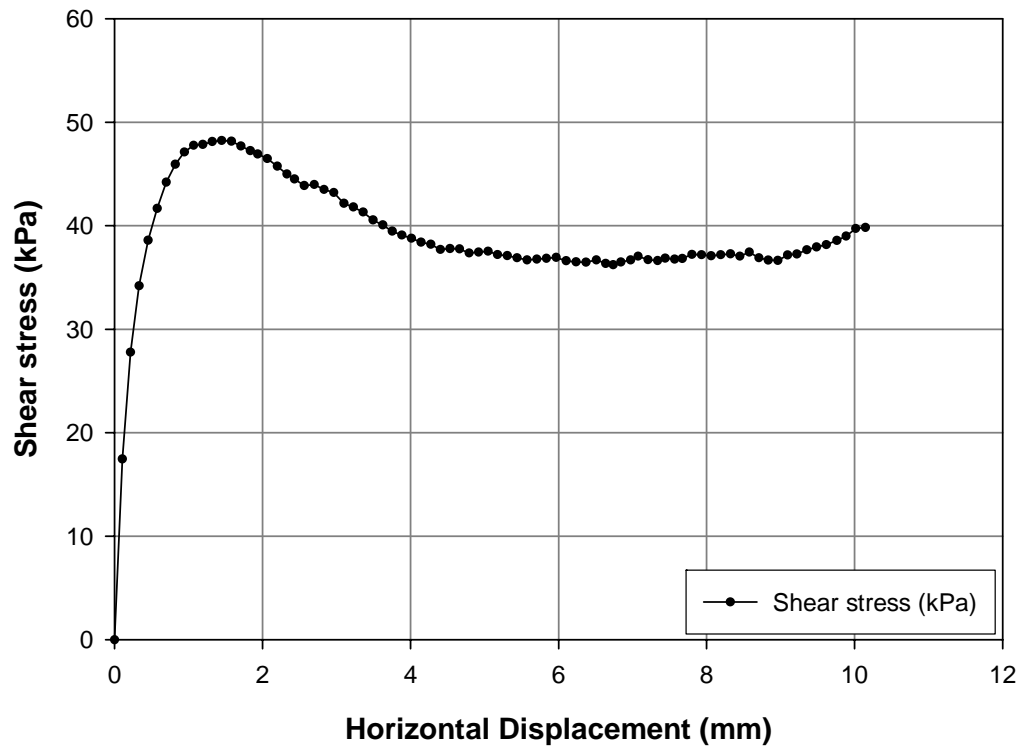


Figure A.3.5. DST results for Cabo Rojo sand sample, Normal stress = 50 kPa, Dr = 89%.

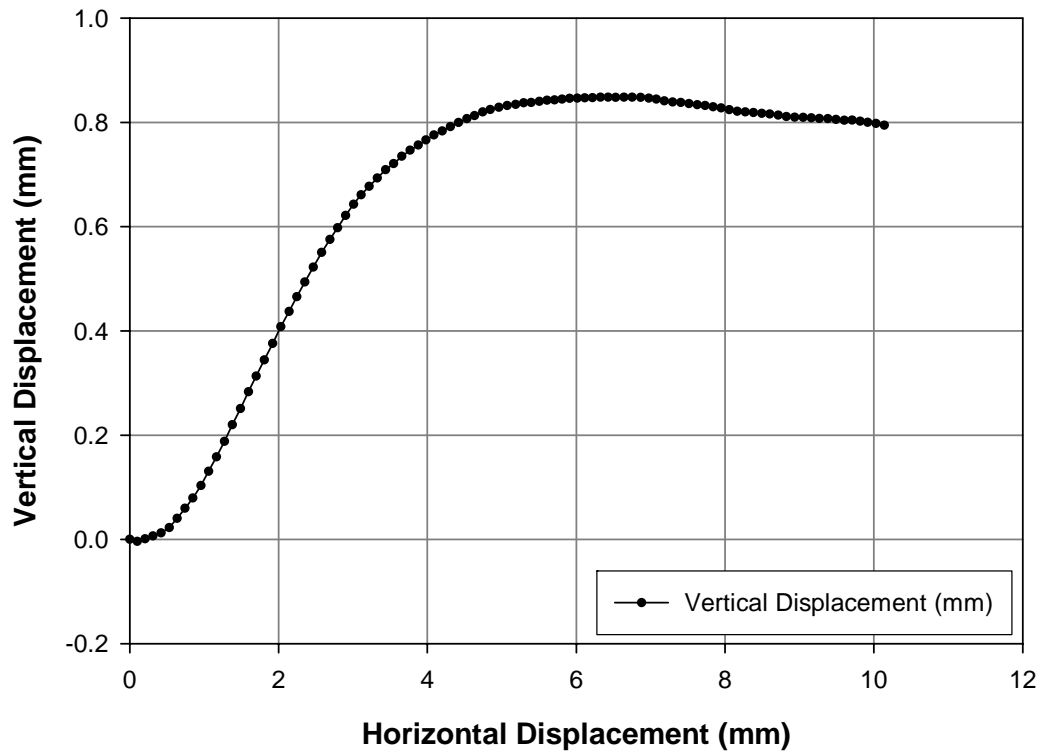
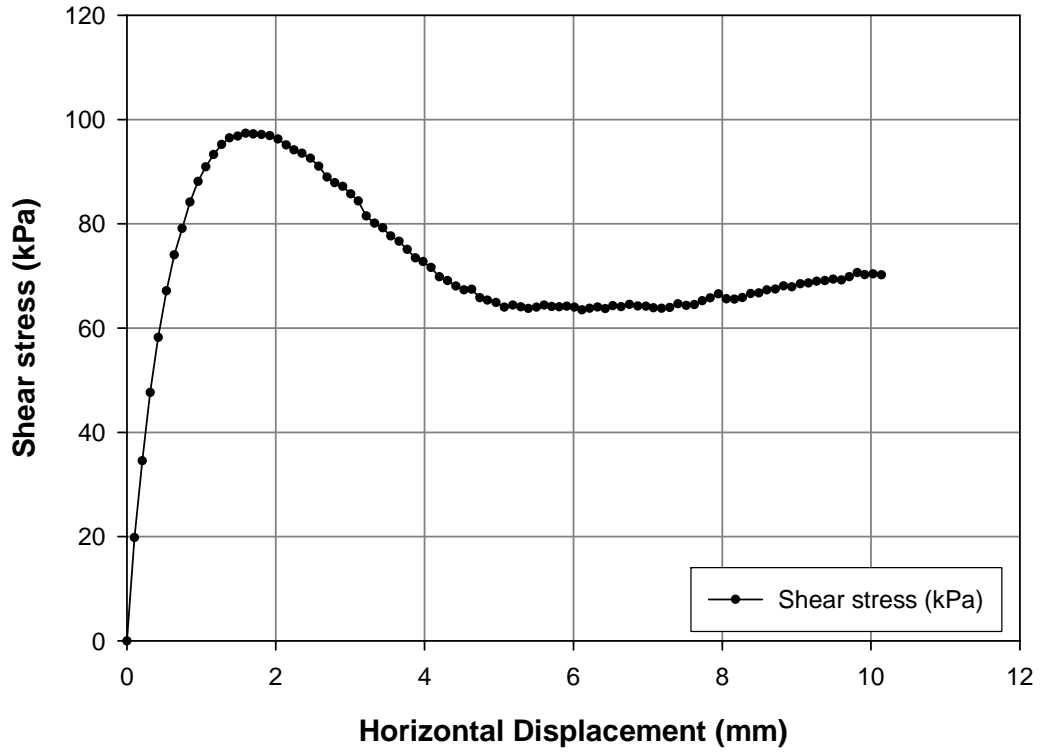


Figure A.3.6. DST results for Cabo Rojo sand sample, Normal stress = 100 kPa, Dr = 103%.

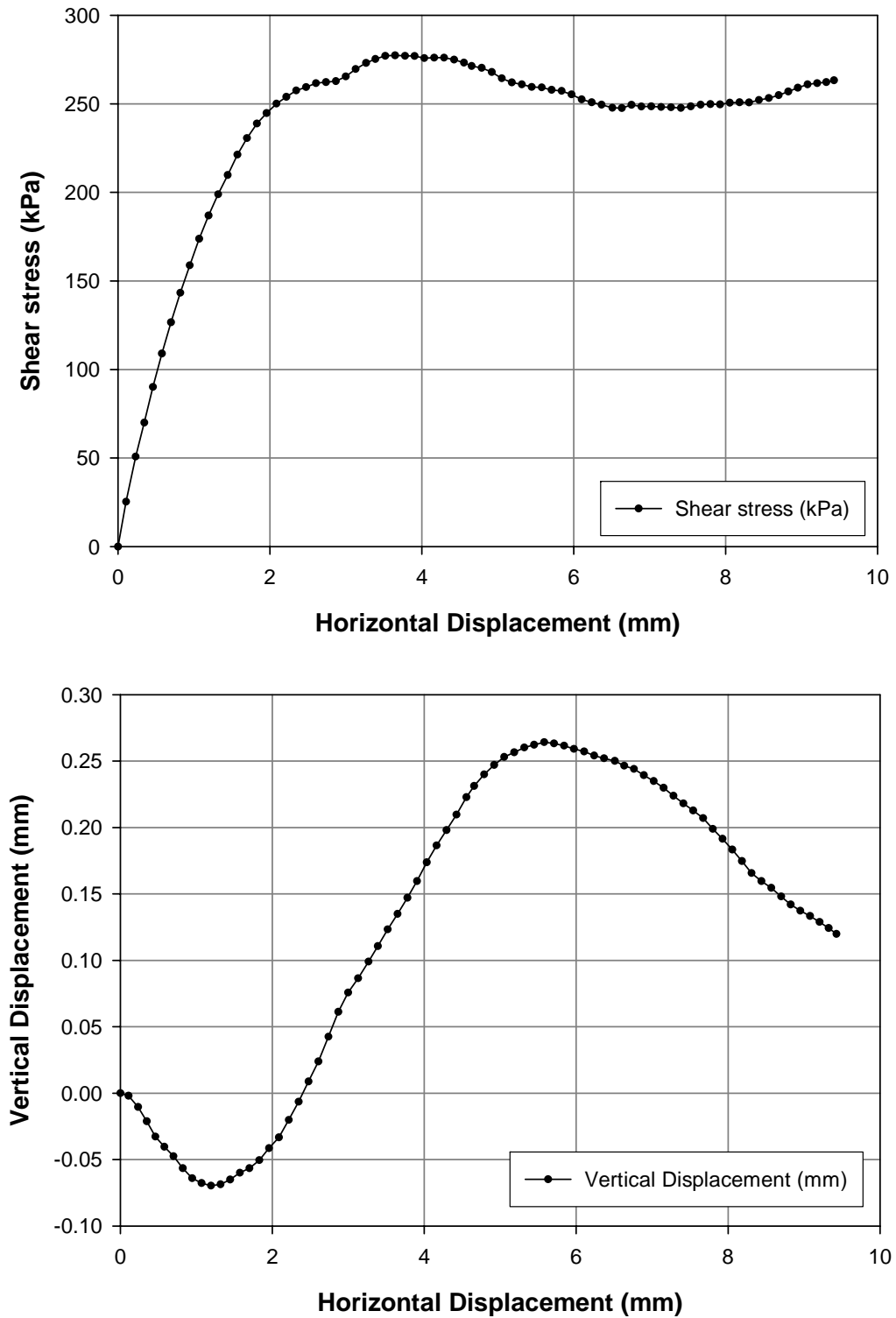


Figure A.3.7. DST results for Cabo Rojo sand sample, Normal stress = 300 kPa, $D_r = 104\%$.

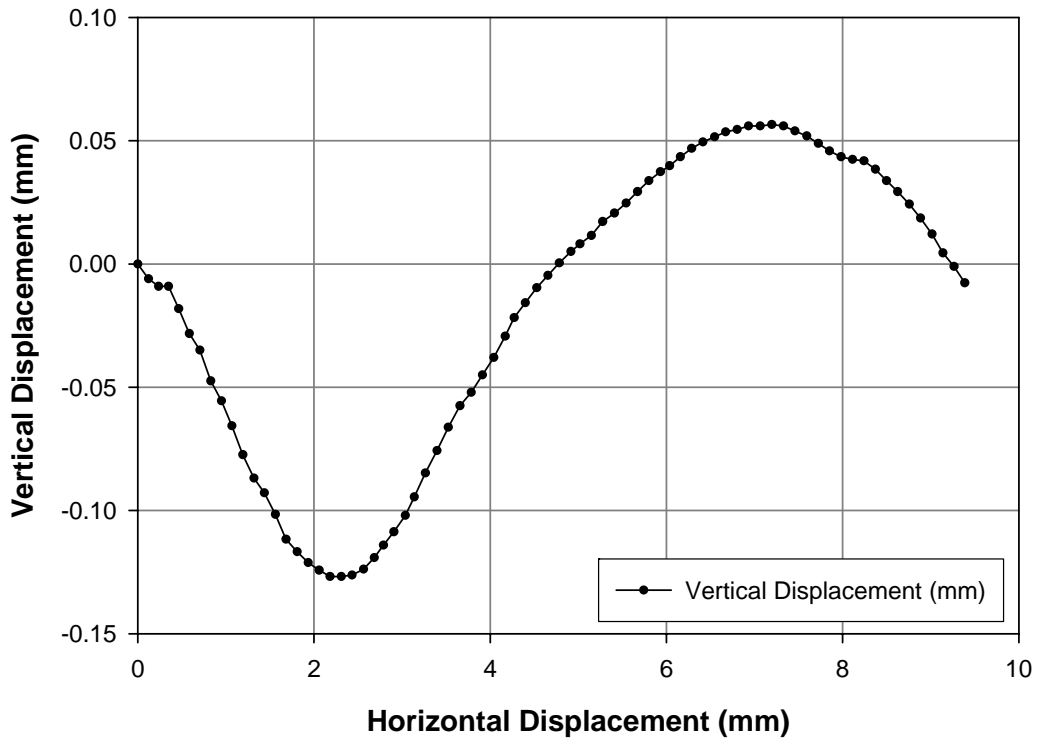
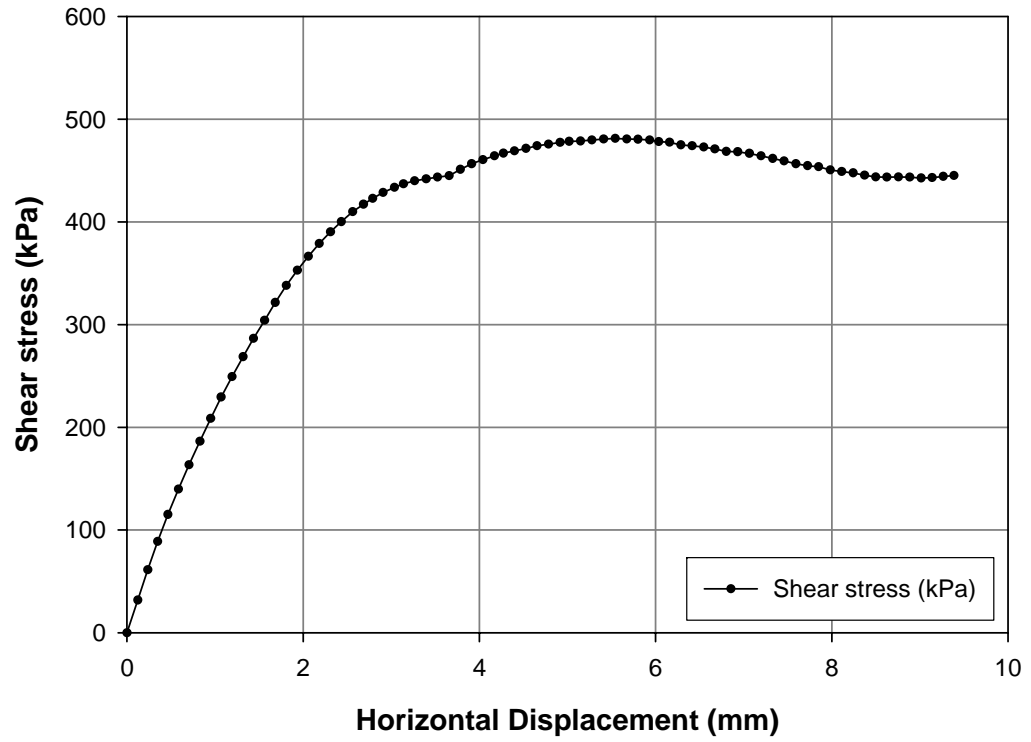


Figure A.3.8. DST results for Cabo Rojo sand sample, Normal stress = 500 kPa, Dr = 90%.

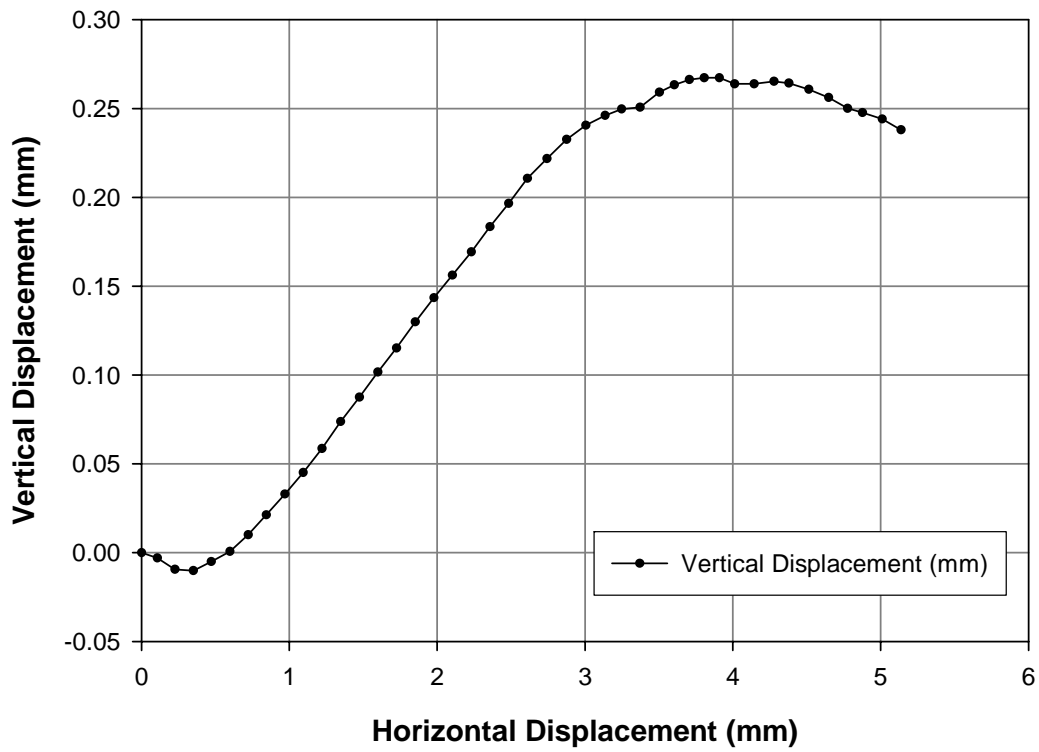
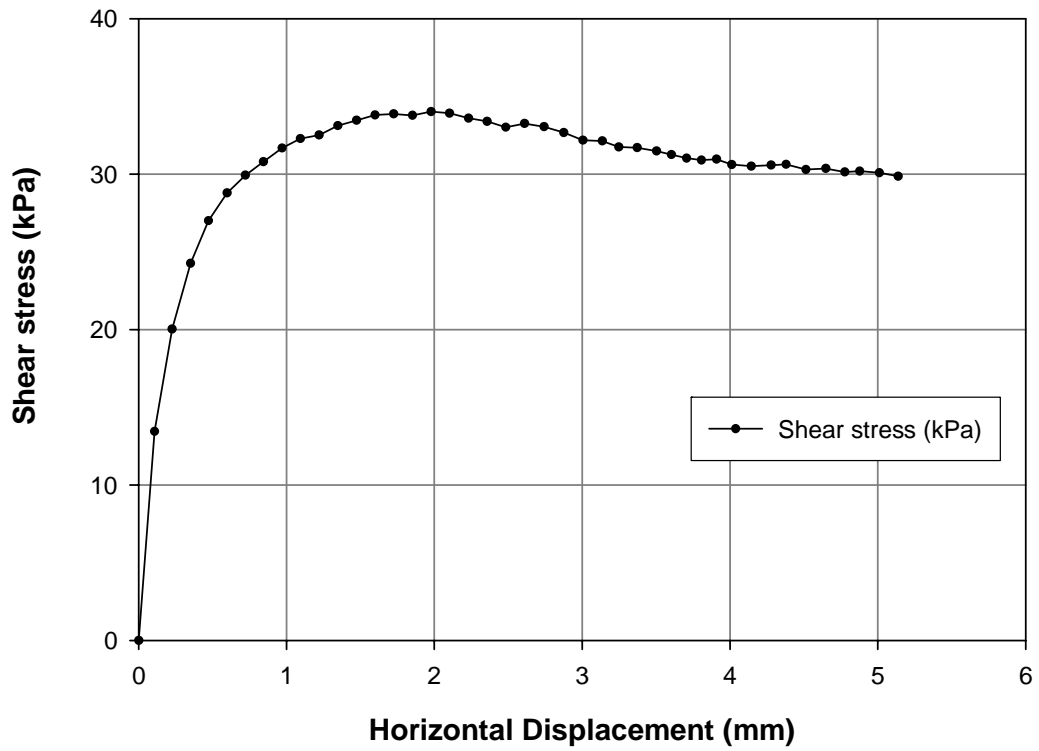


Figure A.3.9. DST results for South Bend sand sample, Normal stress = 50 kPa, Dr = 53%.

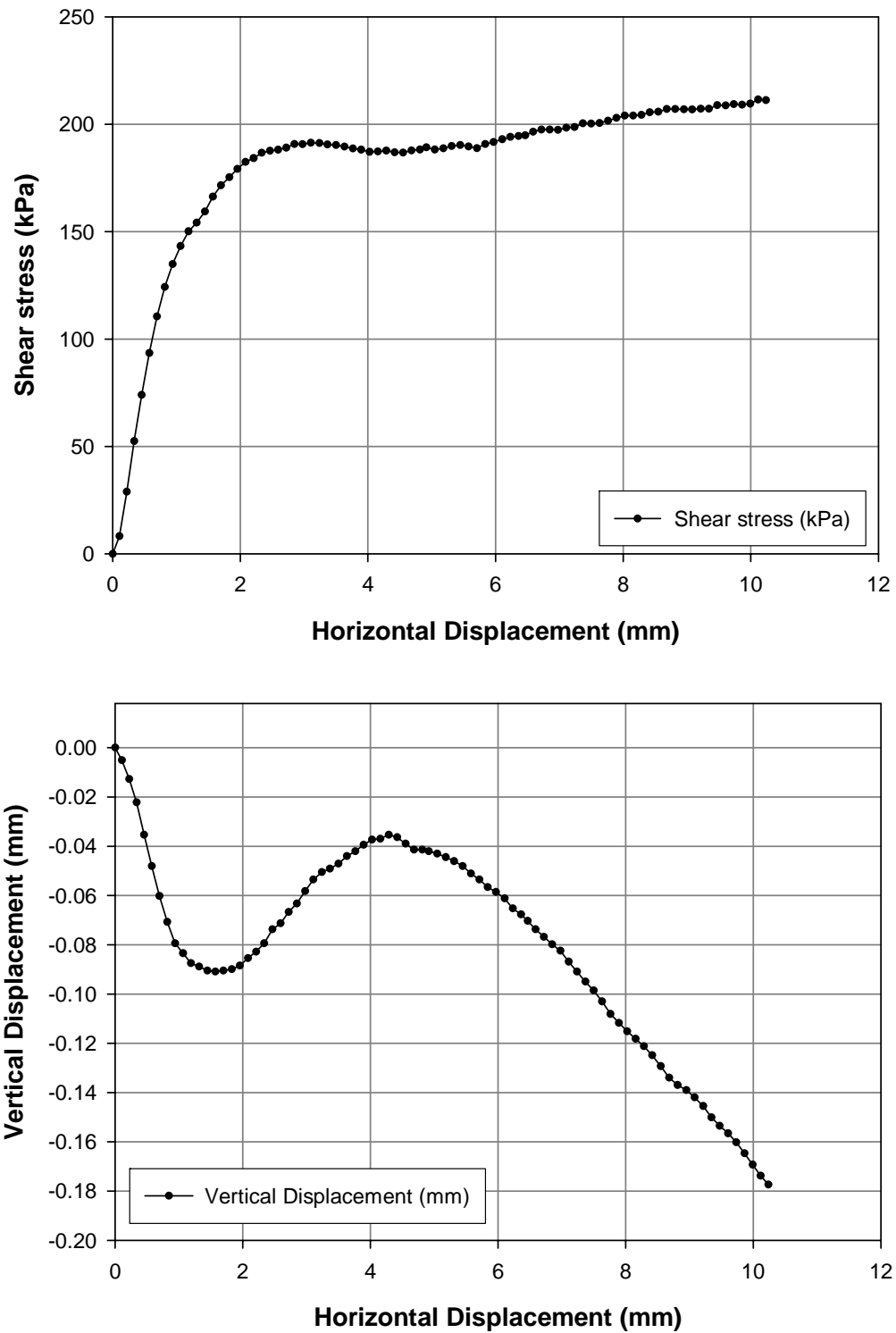


Figure A.3.10. DST results for South Bend sand sample, Normal stress = 300 kPa, $D_r = 53\%$.

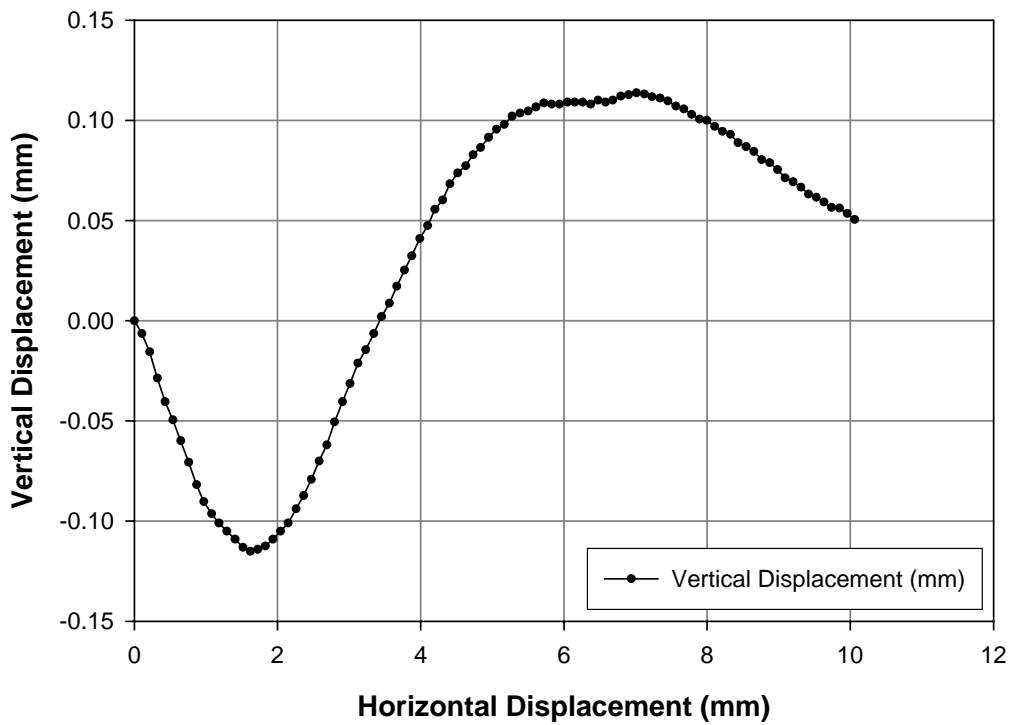
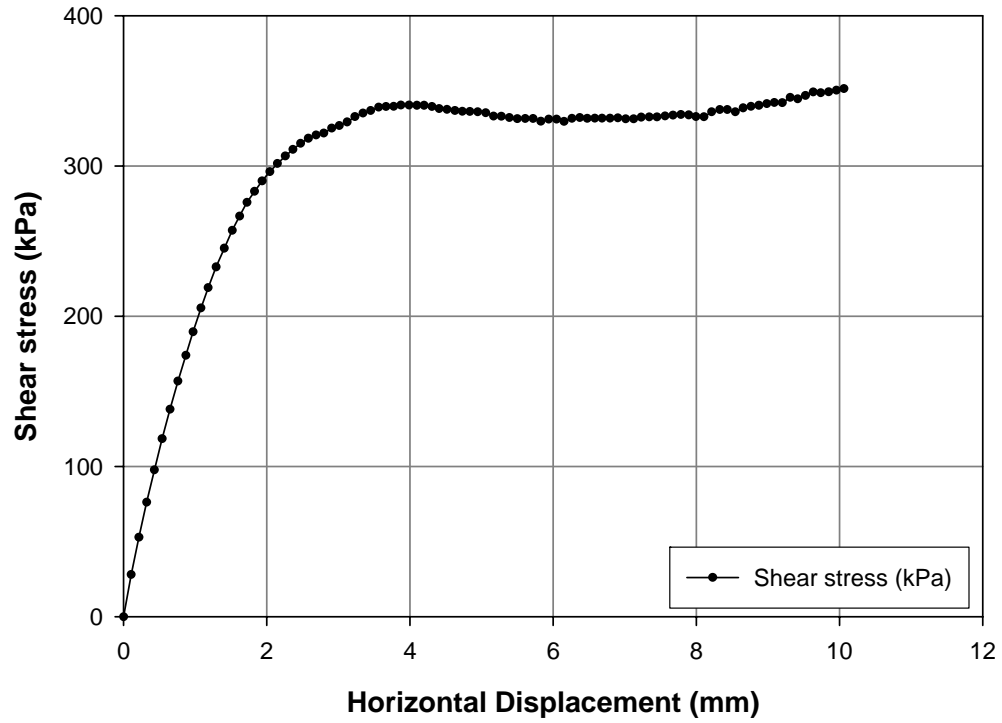


Figure A.3.11. DST results for South Bend sand sample, Normal stress = 500 kPa, Dr = 58%.

APPENDIX 4.

Isotropic Consolidated Undrained (ICU) Triaxial Test - Other results -

Initial state of ICU samples

Cabo Rojo calcareous sand:

Table A.4. 1. Initial state of CIU-TX Cabo Rojo sand samples

	Test #	σ'_o kPa	Ini. Mass g	Diam. mm	Height mm	Tot. Vol INI. cm ³	Sol. Vol. cm ³	Ini. Void ratio e_0	INI. Dr %
Minimum density	TX-011A	50	617	70.44	146.67	571.57	215.73	1.65	44%
	TX-012A	100	617	70.73	147.00	577.58	215.73	1.68	38%
	TX-020A	300	617	70.50	145.00	566.03	215.73	1.62	50%
Medium density	TX-021A	50	648	70.44	147.25	573.83	226.57	1.53	71%
	TX-022A	100	648	70.54	147.50	576.44	226.57	1.54	69%
	TX-016A	300	648	70.74	147.38	579.24	226.57	1.56	66%
Maximum density	TX-017A	50	678	71.17	148.50	590.76	237.06	1.49	81%
	TX-023A	100	678	71.11	147.94	587.54	237.06	1.48	84%
	TX-019A	300	678	69.97	149.75	575.81	237.06	1.43	95%

South Bend silica sand:

Table A.4. 2. Initial state of CIU-TX South Bend sand samples

	Test #	σ'_o kPa	Ini. Mass g	Diam. mm	Height mm	Tot. Vol INI. cm ³	Sol. Vol. cm ³	Ini. Void ratio e_0	INI. Dr %
Minimum density	TX-040A	50	973	70.83	151.13	595.49	360.37	0.65	36%
	TX-041A	100	943	70.23	147.38	570.92	349.26	0.63	44%
	TX-042A	300	928	70.11	145.38	561.25	343.70	0.63	45%
Maximum density	TX-045A	50	1065	70.78	151.63	596.62	394.44	0.51	95%
	TX-046A	100	1062	70.95	151.25	597.98	393.33	0.52	92%
	TX-047A	300	1065	70.92	151.50	598.47	394.44	0.52	93%

After consolidation state of ICU samples

Cabo Rojo calcareous sand:

Table A.4. 3. After consolidation state. CIU-TX Cabo Rojo sand samples

	Test #	Δvol bef. saturation		Δvol Sat. Ph. cm ³	Δvol Cons. Ph. cm ³	B value	After cons. void ratio e_{cons}	After cons. Dr %
		CO ₂ cm ³	Intial. Ph. cm ³					
Minimum density	TX-011A	-1.881	0.229	11.826	6.025	1.004	1.57	62%
	TX-012A	-0.118	0.507	1.167	7.218	1.004	1.64	47%
	TX-020A	0.000	0.384	7.877	14.684	0.993	1.52	75%
Medium density	TX-021A	-0.031	-0.199	3.871	4.909	1.000	1.49	80%
	TX-022A	-0.046	0.215	0.261	6.645	0.997	1.51	76%
	TX-016A	-0.015	0.833	0.602	12.766	1.001	1.49	80%
Maximum density	TX-017A	0.016	-0.078	0.672	3.700	1.003	1.47	85%
	TX-023A	0.000	0.016	3.492	7.413	0.997	1.43	95%
	TX-019A	0.015	-0.046	2.492	11.922	1.000	1.37	109%

South Bend silica sand:

Table A.4. 4. After consolidation state. CIU-TX South Bend sand samples

	Test #	Δvol bef. saturation		Δvol Sat. Ph. cm ³	Δvol Cons. Ph. cm ³	B value	After cons. void ratio e_{cons}	After cons. Dr %
		CO ₂ cm ³	Intial. Ph. cm ³					
Minimum density	TX-040A	1.067	0.572	21.384	13.867	1.008	0.55	79%
	TX-041A	0.015	0.213	5.306	12.140	1.008	0.58	65%
	TX-042A	0.092	0.075	23.859	19.889	0.997	0.51	98%
Maximum density	TX-045A	0.142	0.390	10.618	5.398	0.985	0.47	112%
	TX-046A	0.190	0.451	0.546	2.960	0.993	0.51	96%
	TX-047A	0.118	0.249	1.943	6.527	1.016	0.49	102%

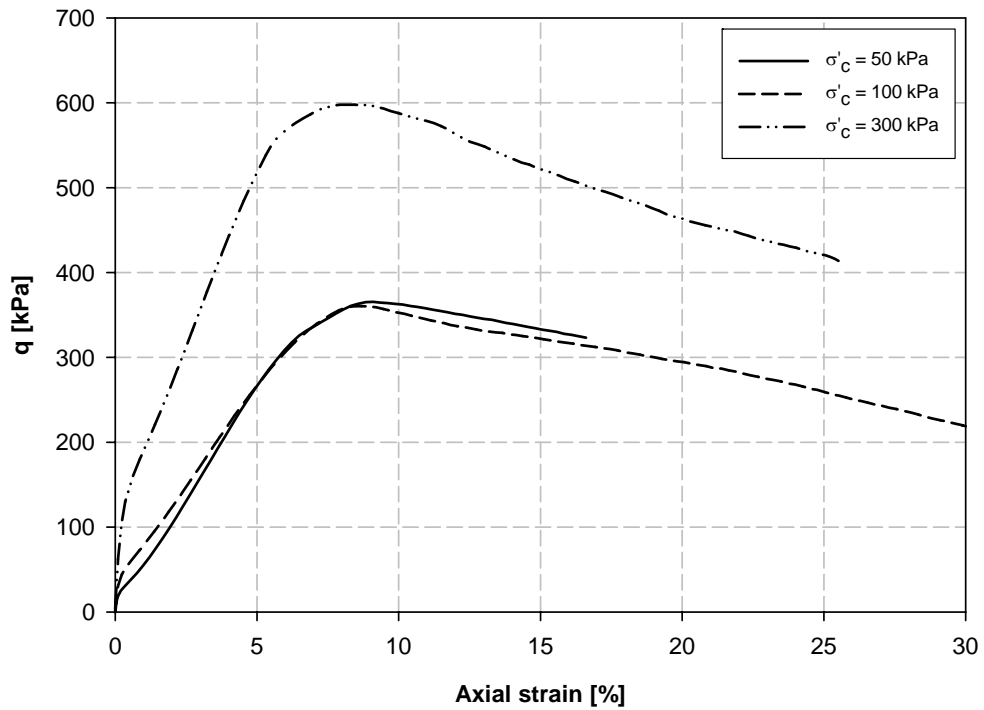
After shearing state of ICU samples

Cabo Rojo calcareous sand:

Table A.4. 5. After shearing state. CIU-TX South Bend sand samples

	Test #	Δvol shear phase			Δvol Shear. Ph. cm^3	Final void ratio e_{fin}	Final Dr %
		Δvol tx. cell water, cm^3	Δvol piston movm, cm^3	Δvol membr. penet., cm^3			
Minimum density	TX-011A	-5.139	-5.726	-0.066	0.653	1.57	62%
	TX-012A	-5.358	-5.858	0.085	0.415	1.63	48%
	TX-020A	-4.567	-5.380	0.251	0.562	1.51	75%
Medium density	TX-021A	-5.738	-5.967	-0.141	0.369	1.49	80%
	TX-022A	-5.611	-6.004	0.015	0.377	1.51	76%
	TX-016A	-4.530	-5.877	0.242	1.106	1.49	81%
Maximum density	TX-017A	-5.629	-6.197	-0.150	0.719	1.47	86%
	TX-023A	-6.473	-6.099	-0.029	-0.345	1.43	94%
	TX-019A	-4.760	-6.269	0.198	1.311	1.36	111%

a)



b)

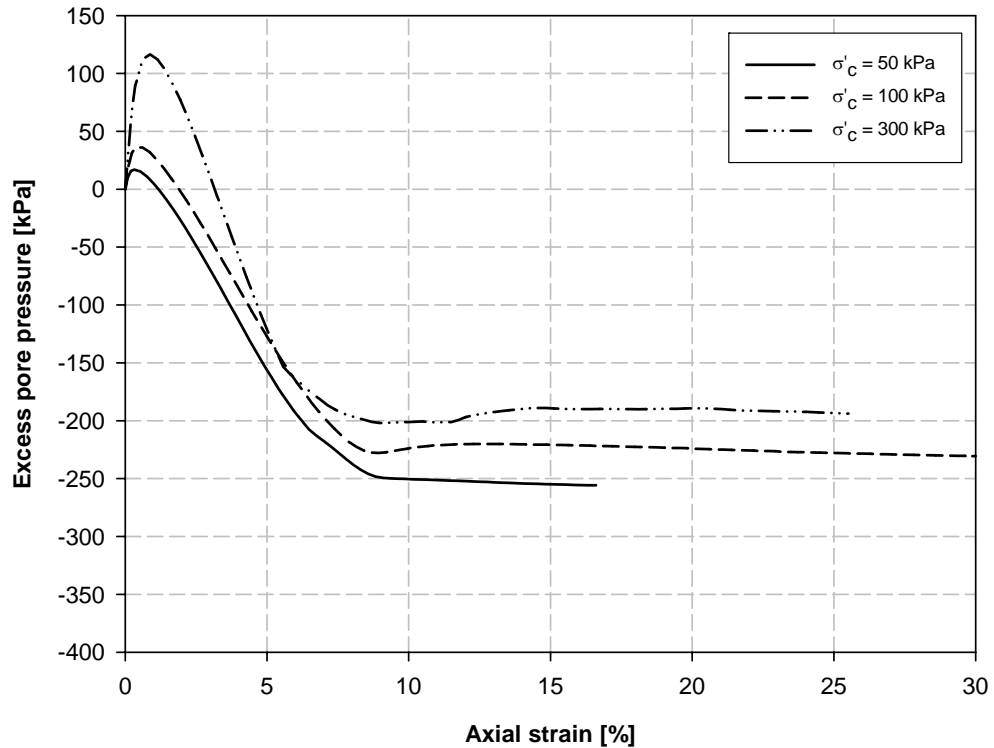
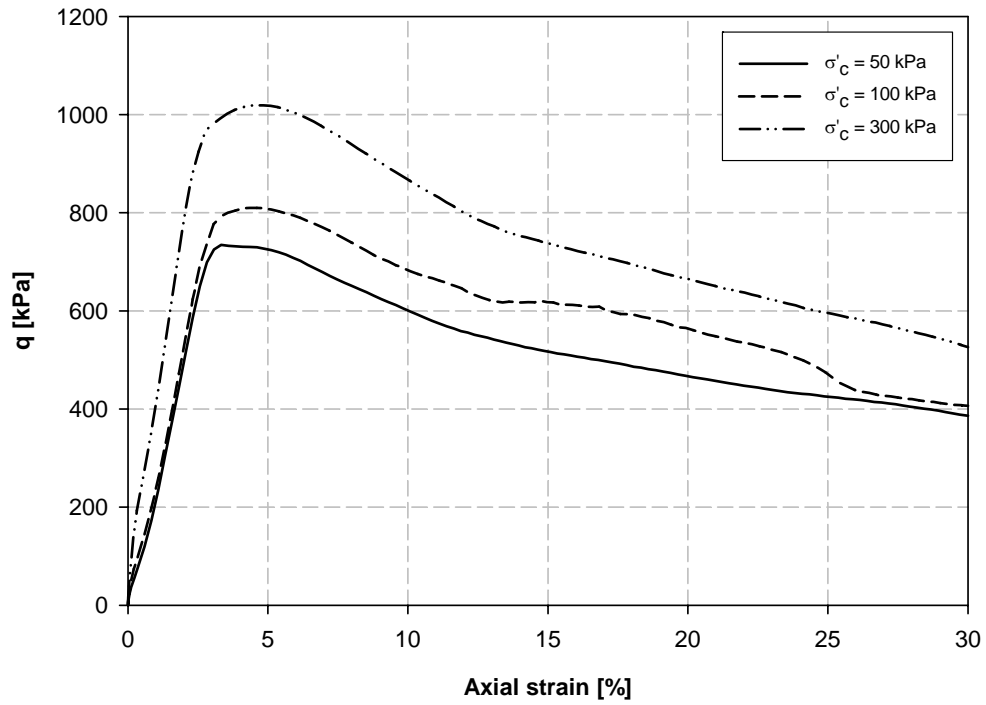


Figure A.4.1. a) Deviator stress curves vs. axial strain and b) excess pore pressure curves vs. axial strain for South Bend sand. (Average $D_r = 81\%$).

a)



b)

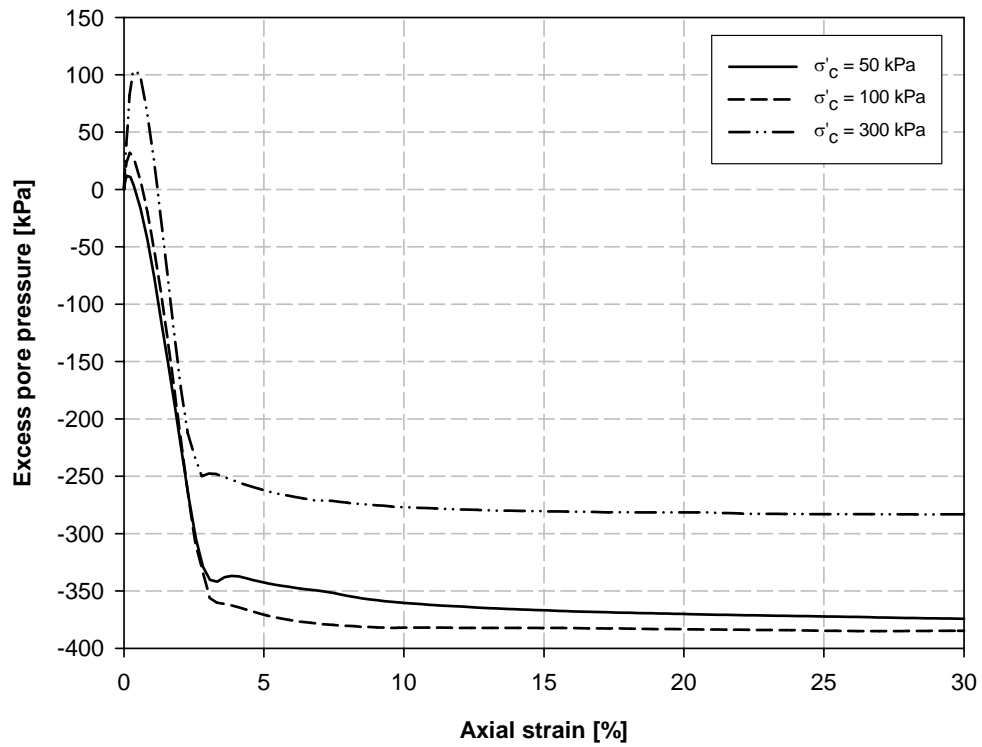


Figure A.4.2. a) Deviator stress curves vs. axial strain and b) excess pore pressure curves vs. axial strain for South Bend sand. (Average $D_r = 103\%$).

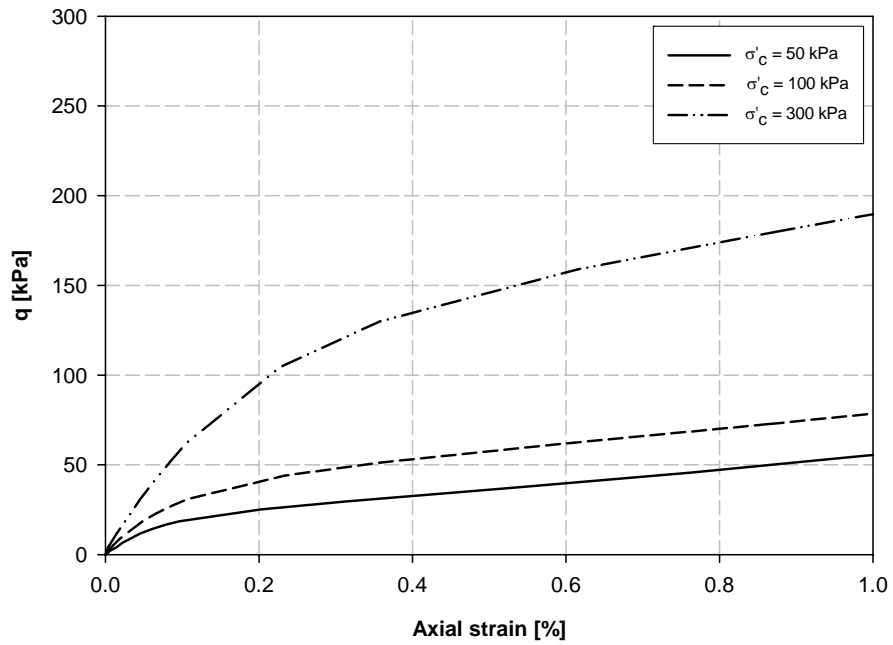


Figure A.4.3. Initial portion of the deviator stress curves vs. axial strain curves for South Bend sand, (Average $D_r = 81\%$).

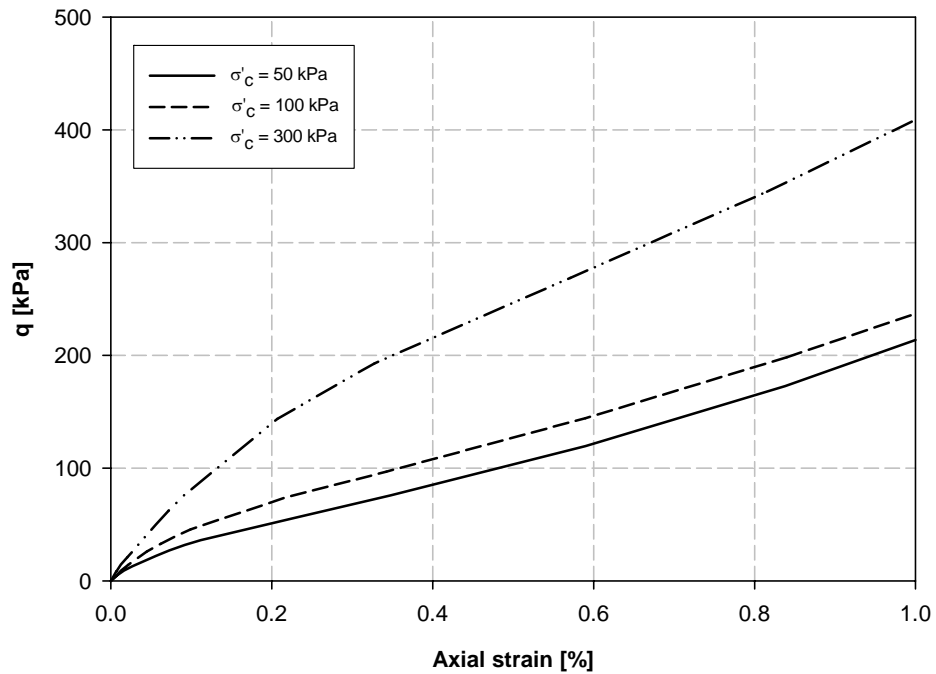
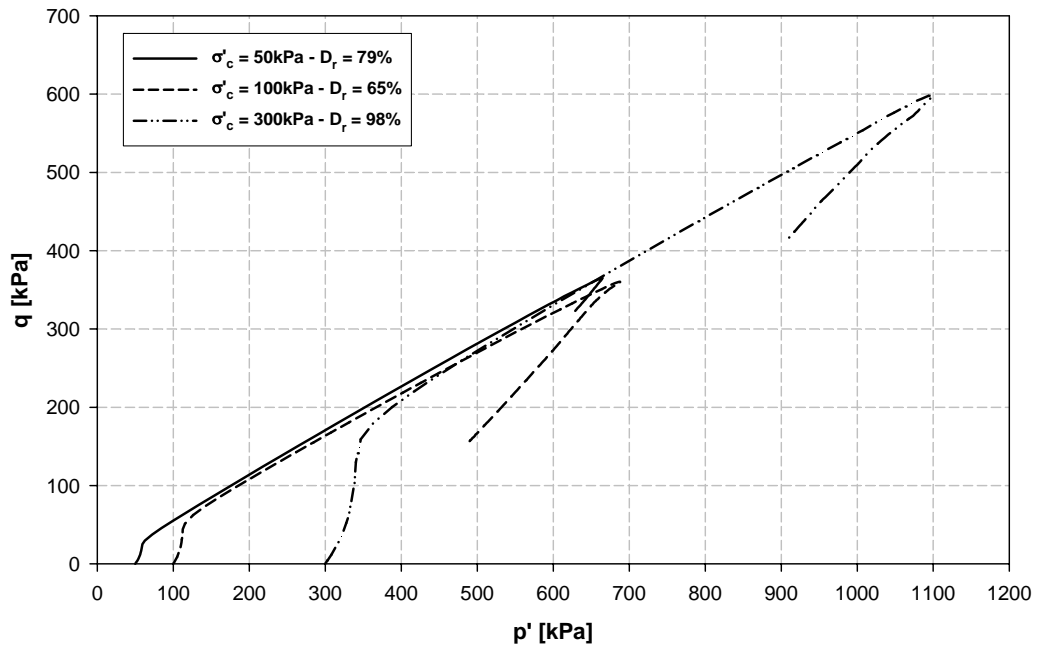
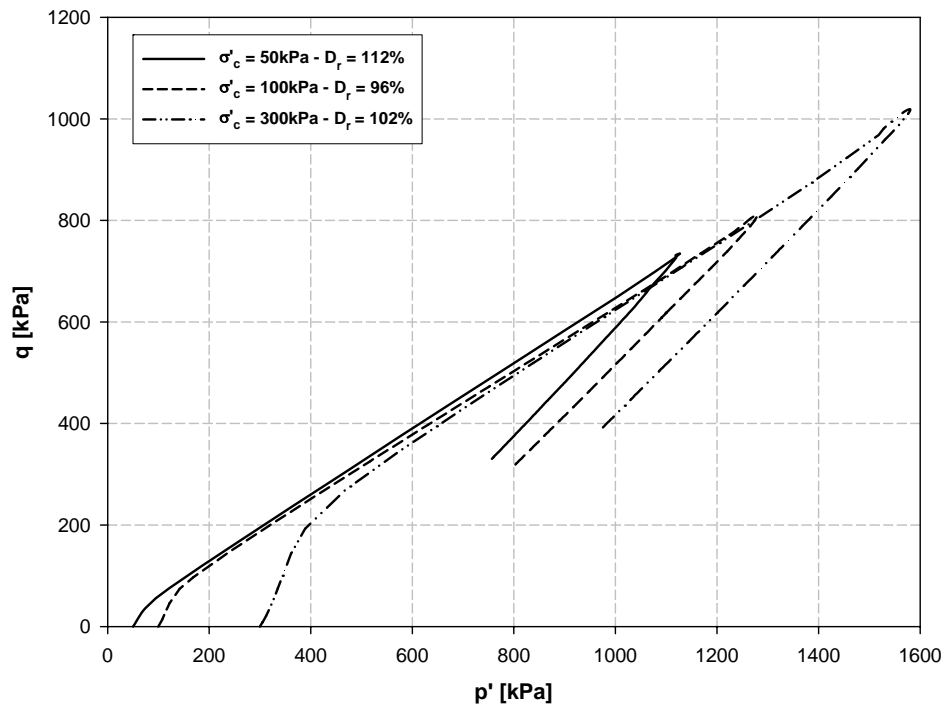


Figure A.4.4. Initial portion of the deviator stress curves vs. axial strain curves for South Bend sand, (Average $D_r = 103\%$).



**Figure A.4.5. Effective Stress Paths for South Bend sand at minimum density.
(Average $D_r = 81\%$).**



**Figure A.4.6. Effective Stress Paths for South Bend sand at maximum density.
(Average $D_r = 103\%$).**

APPENDIX 5.

Resonant Column (RC) Test

Theoretical Background and other results.

Theoretical Background of the RC Test

The resonant column test is the most commonly used laboratory test for measuring the dynamic soil properties at low and medium strains (GCTS, 2004). The equipment used in this study was a GCTS Resonant Column apparatus. This device consists of a soil column, solid or hollow, placed inside a triaxial cell and set in a fixed-free configuration. The configuration fixed-free is based on fixing the base of the column and leaving the top free to rotate. After setting the GCTS Resonant Column apparatus, harmonic torsional excitations with constant amplitude are applied over a range of frequencies at the top of the specimen using an electromagnetic loading motor system. In this way, the resonant frequency of the first-mode is determined, which in turn can be used to obtain the shear wave velocity of the material. Based on the dynamic response of the soil measured by the resonant column apparatus, shear moduli and material damping ratios can also be determined for different shear strain amplitudes.

The resonant column method is based on the one-dimensional wave equation derived from the theory of linear-elastic vibrations (GCTS, 2004). In the linear vibrations theory

parameters such stiffness and viscous damping are assumed to be constant and independent of frequency and amplitude (Hoyos, 1993).

Shear modulus

To obtain the shear modulus of the soil, the solution of the equation of motion for forced torsional vibration is used. In this solution fixed-free soil column is represented by the Kelvin-Voigt model as shown in Figure A.5.1. In this model the soil is idealized by a spring with a stiffness G and a dashpot with a viscous damping coefficient c .

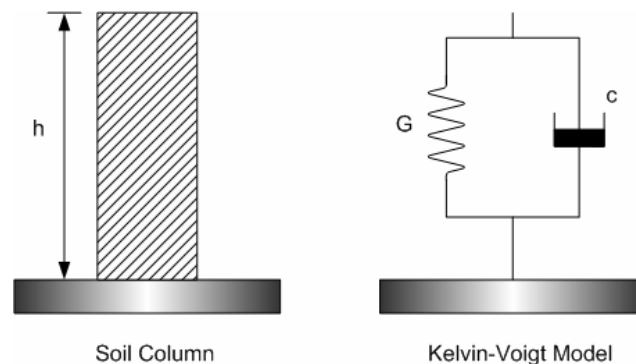


Figure A.5.1. Kelvin-Voigt model used to represent the soil column.

Although the complete development of the solution aforementioned is presented in the CATS© - Resonant Column Test Mode, User's Guide and Reference (GCTS, 2004), some of the principal expressions of the solution are summarized next.

For the derivation of the torsional motion equation the sketch shown in Figure A.5.2 is used. When the RC machine applies a sinusoidal torsional excitation ($T = T_0 \sin \Omega t$) at

the top of the soil specimen, a torque T applied to an elastic soil element an incremental angle of twist ($d\theta$), along to an incremental length (dz), generates in the element of soil a torque T equal to:

$$T = GJ \frac{d\theta}{dz} \quad (\text{A.3.1})$$

where G is the shear modulus of the soil and J is the polar moment of inertia of area of the cross section. At the other face of the elastic soil element, the torsional stress will be

equal to $T + \frac{\partial T}{\partial z} dz$, where:

$$\frac{\partial T}{\partial z} dz = GJ \frac{\partial^2 \theta}{\partial z^2} dz \quad (\text{A.3.2})$$

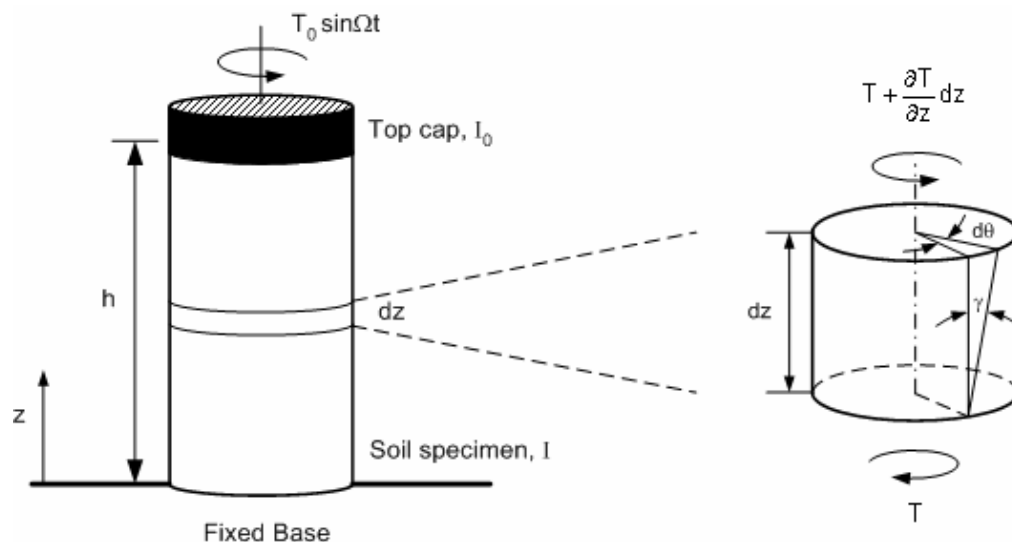


Figure A.5.2. Idealization of the fixed-free RC specimen.

By applying Newton's second law to the element of soil with length dz , the equation

A.3.3 for $\frac{\partial T}{\partial z} dz$ is obtained:

$$\frac{\partial T}{\partial z} dz = I \frac{\partial^2 \theta}{\partial t^2} = \rho J dz \frac{\partial^2 \theta}{\partial t^2} \quad (\text{A.3.3})$$

where I is the polar mass moment of inertia of the soil element, and equal to $(\rho * J * dz)$, where ρ is the soil mass density.

Substituting $\frac{\partial T}{\partial z} dz$ from equation A.3.2 in equation A.3.3, and using the relationship between shear wave velocity (V_s) and shear modulus ($G = \rho V_s^2$) the following expression for wave equation in torsion for an elastic rod is obtained:

$$\frac{\partial^2 \theta}{\partial z^2} = \frac{1}{V_s^2} \frac{\partial^2 \theta}{\partial t^2} \quad (\text{A.3.4})$$

The general solution found to equation (A.3.4) is:

$$\theta(z, t) = \left[A \sin\left(\frac{\omega}{V_s} z\right) + B \cos\left(\frac{\omega}{V_s} z\right) \right] * e^{i\omega t} \quad (\text{A.3.5})$$

where ω is the circular natural frequency and A and B are constants that depend on the boundary conditions of the soil column. The boundary conditions in the GCTS RC system are (GCTS, 2004):

- Zero angular displacement at the bottom (fixed end).
- Torque at the top of the soil specimen (free end) equal to the inertia torque of the drive system but opposite.

From the first boundary condition, it is found that $B = 0$. The new expression for Equation A.3.5 is now:

$$\theta(z, t) = A \sin\left(\frac{\omega}{V_s} z\right) e^{i\omega t} \quad (\text{A.3.6})$$

To evaluate equation A.3.6 at the second boundary condition the second derivative with respect to time needs to be found:

$$\frac{\partial^2 \theta}{\partial t^2} = \frac{\partial^2 \left(A \sin\left(\frac{\omega z}{V_s}\right) e^{i\omega t} \right)}{\partial t^2} = -\omega^2 A \sin\left(\frac{\omega z}{V_s}\right) e^{i\omega t} \quad (\text{A.3.7})$$

The torque at the free end of soil specimen is:

$$T_{z=h} = -I_0 \left(\frac{d^2 \theta}{dt^2} \right) \quad (\text{A.3.8})$$

where I_0 is the mass moment of inertia of the driving system and h is the height of the soil specimen. Substituting equation A.3.7 in A.3.8 results in:

$$T_{z=h} = I_0 \omega^2 A \sin\left(\frac{\omega z}{V_s}\right) e^{i\omega t} \quad (\text{A.3.9})$$

Combining equations A.3.1 and A.3.9 and rearranging the terms, the following equation is obtained:

$$\frac{I}{I_0} = \frac{\omega h}{V_s} \tan\left(\frac{\omega h}{V_s}\right) \quad (\text{A.3.10})$$

where I is the mass moment of inertia of the soil column. Equation A.3.10 is used by the GCTS software (CATS) to determine the shear wave velocity of the soil once the resonant frequency has been determined from the response curve of the system as shown in Figure A.5.3. Knowing the soil density and shear wave velocity, the shear modulus can be obtained as follows:

$$G = \rho V_s^2 \quad (\text{A.3.11})$$

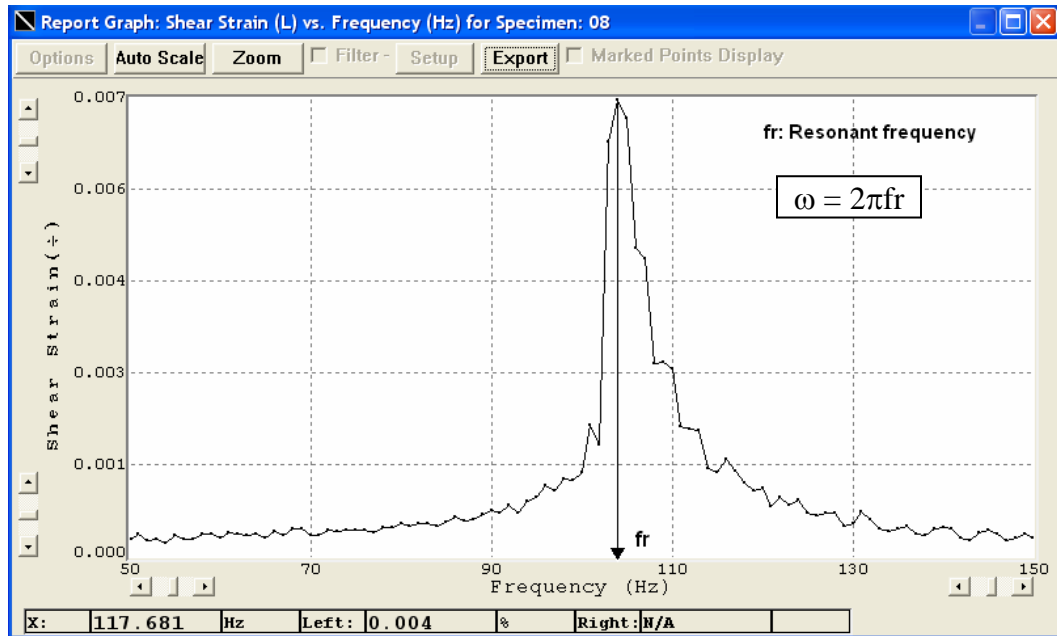


Figure A.5.3. Response curve of the system obtained by CATS© program.

Shear strain

The shear strain in a RC system varies from zero at the center line of the soil column to a maximum value at its outer edges, as shown in Figure A.5.4. So then shear strain could be calculated with the next equation:

$$\gamma(r) = \frac{r\theta_{\max}}{h} \quad (\text{A.3.12})$$

where r is the radial distance from the soil column axis; θ_{\max} is the maximum angle of twist and h is the height of the soil specimen.

Since shearing strain varies within the soil column, an equivalent shear strain (γ_{eq}) is required to represent the average shear strain. Equation A.3.13 shows the formulation for (γ_{eq}), using an equivalent radius (r_{eq}) which is generally taken as $\frac{2}{3} r_0$ for solid specimens with radius r_0 :

$$\gamma_{eq} = \frac{\frac{2}{3} r_0 \theta_{max}}{h} \quad (A.3.13)$$

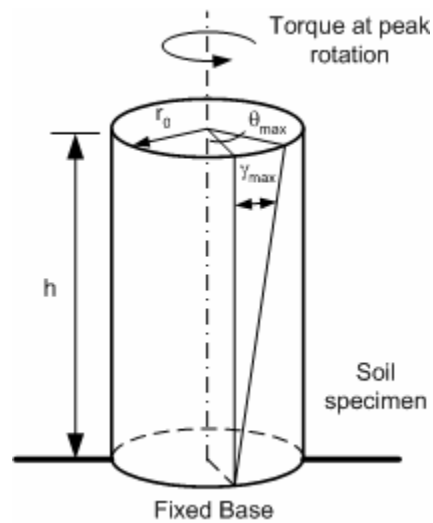


Figure A.5.4. Shearing strain, γ , for solid soil column

The maximum angle of twist (θ_{max}) at the top of the specimen is calculated by dividing the sensor displacement output (x) by the radius to the position of the sensor (r_{sensor}). In the tests performed for this study, two proximitors were used to measure the shear strain, this type of transducers uses magnetic field changes with respect to a magnet to determine the amount of displacement. The proximitors were mounted at the top of the

specimen, one a cross the other. The position of each sensor (r_{sensor}) was determined and introduced to CATS software. The GCTS RC apparatus obtained the displacement output directly in real time from the proximitors. This way, θ_{max} is given by:

$$\theta_{\text{max}} = \frac{x}{r_{\text{sensor}}} \quad (\text{A.3.14})$$

Damping ratio

The material damping ratio was evaluated with two different methods: The half power bandwidth method and the free vibration decay method.

The free vibration decay method is based on using the logarithmic decrement, δ , calculated as the natural logarithm of two successive positive shear strain peaks from the free vibration curve, as shown in Figure A.5.5.

The logarithmic decrement (δ) can be calculates as follows:

$$\delta = \ln\left(\frac{\gamma_n}{\gamma_{n+1}}\right) = \frac{2\pi D}{\sqrt{1-D^2}} \quad (\text{A.3.15})$$

where γ_n and γ_{n+1} are the shear strain values of two consecutive peaks. With the logarithmic decrement, the material damping can be obtained as follows:

$$D = \sqrt{\frac{\delta^2}{4\pi^2 + \delta^2}} \quad (\text{A.3.16})$$

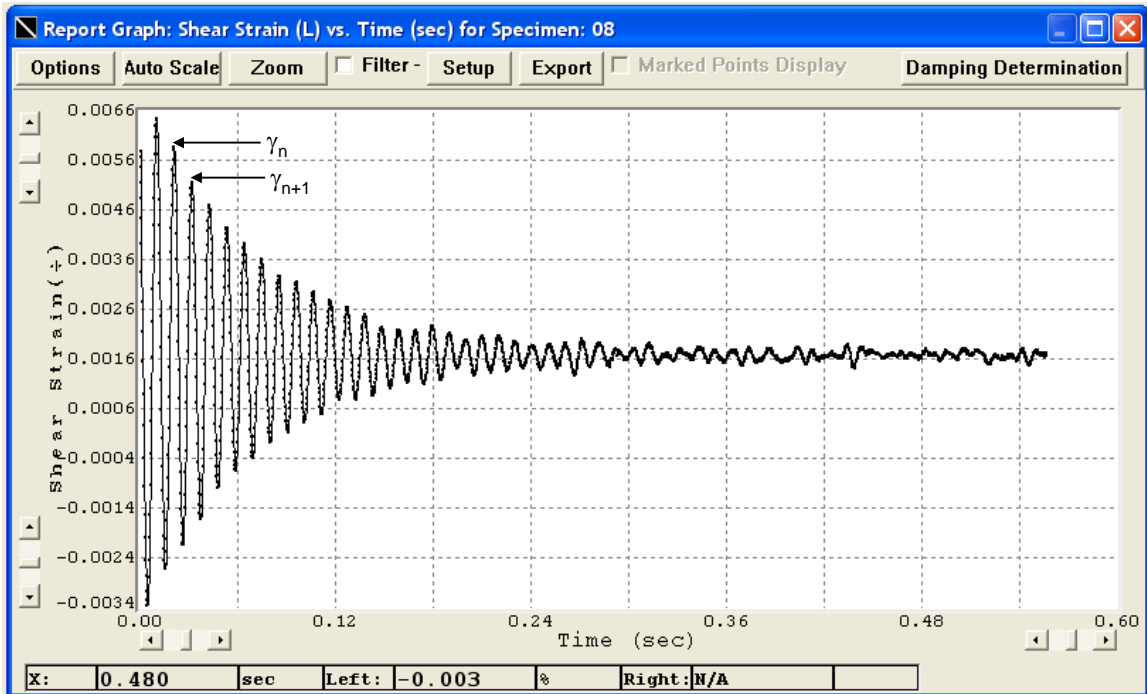


Figure A.5.5. Free-vibration decay – CATS© software.

Notice that δ is the linear slope in the curve shown in Figure A.5.6.

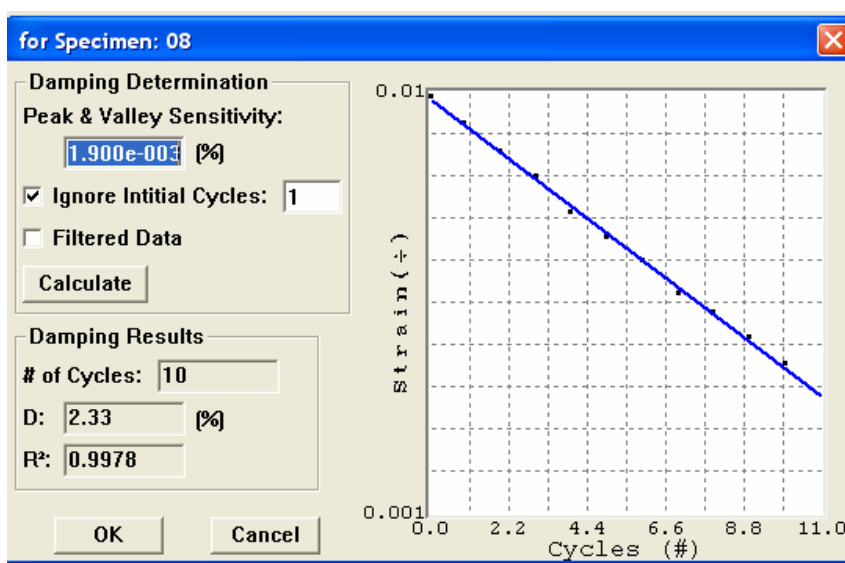


Figure A.5.6. Damping determination from Free-vibration decay – CATS© program.

A second method used to determine the material damping in the resonant column test is the Half-Power Bandwidth Method. This approach is based on measuring the width of the dynamic response curve of the system near resonance as shown in Figure A.5.7. Frequencies above and below resonance, where the response amplitude is 0.707 times the resonant amplitude ($\gamma_{\max}/\sqrt{2}$), are referred to as the half-power points.

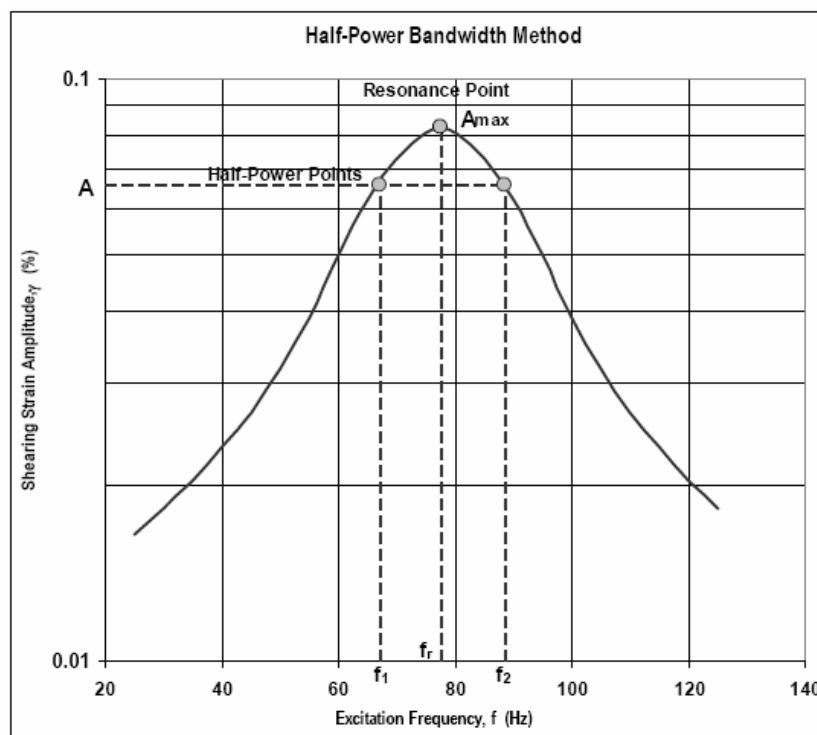


Figure A.5.7. Dynamic response curve obtained by CATS© program. (From GCTS, 2004)

The damping ratio obtained with the Half-Power Bandwidth Method is:

$$D = \frac{1}{2} \frac{f_2 - f_1}{f_r} \quad (\text{A.3.17})$$

where f_1 and f_2 are called the half-power points, which are the frequencies above and below resonance (f_r), where the response amplitude is 0.707 times the resonant amplitude.

This method was used for damping ratio determination at small shear strain levels.

RC Test Other Results

RC – Cabo Rojo sand – 50 kPa – Dr: 21%

Specific gravity (Gs) 2.864
 Min. void ratio 1.264
 Max. void ratio 1.566

Mass 270.50 g
 Actual diameter 50.71 mm
 Height 117 mm

Total volume 236299.59 mm³ Void ratio (e) 1.502
 236.300 cm³ Relative density (Dr) 21%

Solid volume (Vs) 94.448 cm³

G max 45.00 MPa

PSF %	Average			Damping %	R2	D DEF. %	Cycles N	Ignored Ini. cycles
	γ max %	G avg MPa	G/Gmax					
0.01	2.30E-04			0.71	0.6755	0.49	10	1
0.05	6.20E-04			0.78	0.3804	0.56	10	1
0.1	8.90E-04	45.00	1.00	1.27		1.05		
0.2	1.52E-03	41.92	0.93	1.65	0.7600	1.43	10	1
0.3	2.30E-03	39.92	0.89	1.98	0.9115	1.76	10	1
0.5	3.34E-03	37.50	0.83	2.59	0.9395	2.37	10	1
0.7	4.68E-03	35.14	0.78	2.98	0.9733	2.76	10	1
1.0	6.03E-03	33.78	0.75	3.41	0.9823	3.19	10	1
3.0	1.42E-02	26.51	0.59	4.34	0.9591	4.12	10	1
5.0	2.51E-02	20.48	0.5	5.01	0.9564	4.79	9	1
7.0	3.56E-02	17.42	0.4	5.97	0.9739	5.75	8	1
10.0	5.12E-02	14.03	0.3	6.25	0.9475	6.03	8	1
15.0	7.32E-02	10.99	0.2	6.60	0.9485	6.38	7	1
20.0	9.67E-02	8.79	0.20	6.82	0.9460	6.60	7	1
25.0	1.27E-01	7.45	0.17	6.80	0.9620	6.58	6	1

RC Internal Damping **0.22 %**

RC – Cabo Rojo sand – 100 kPa – Dr: 21%

Specific gravity (Gs)	2.864		
Min. void ratio	1.264		
Max. void ratio	1.566		
Mass	270.50 g		
Actual diameter	50.71 mm		
Height	117 mm		
Total volume	236299.59 mm ³	Void ratio (e)	1.502
	236.300 cm ³	Relative density (Dr)	21%
Solid volume (Vs)	94.448 cm ³		

G max 73.62 MPa

PSF %	Average			Damping %	R2	D _{DEF.} %	Cycles N	Ignored Ini. cycles
	γ max %	G avg MPa	G/Gmax					
0.01	3.30E-04			0.89	0.8199	0.67	10	1
0.05	6.60E-04	73.62	1.00	0.79	0.8174	0.57	10	1
0.1	1.04E-03	72.29	0.98	0.90	0.9254	0.68	10	1
0.2	1.49E-03	70.98	0.96	1.03	0.9576	0.81	10	1
0.3	2.67E-03	69.66	0.95	1.09	0.9825	0.87	10	1
0.5	4.29E-03	68.37	0.93	1.34	0.9953	1.12	10	1
0.7	4.71E-03	69.02	0.94	1.48	0.9767	1.26	10	1
1	7.10E-03	65.81	0.89	1.73	0.9962	1.51	10	1
3.000	1.39E-02	59.65	0.81	2.45	0.9911	2.23	10	1
5.000	1.94E-02	54.92	0.75	2.86	0.9865	2.64	10	1
7.000	2.46E-02	51.50	0.70	3.10	0.9859	2.88	10	1
10.000	3.08E-02	48.20	0.65	3.31	0.9759	3.09	10	1
15.000	4.16E-02	42.93	0.58	3.48	0.9608	3.26	10	1
17.000	4.58E-02	40.92	0.56	3.65	0.9644	3.43	10	1
20.000	5.26E-02	37.97	0.52	3.74	0.9578	3.52	10	1
25.000	6.29E-02	35.14	0.48	3.95	0.9512	3.73	10	1
30	7.26E-02	33.32	0.45	4.06	0.9490	3.84	10	1
35	8.80E-02	30.67	0.42	4.41	0.9527	4.19	9	1
40	9.79E-02	28.97	0.39	4.78	0.9497	4.56	8	1
45	1.07E-01	27.31	0.37	4.93	0.9520	4.71	8	1

RC Internal Damping 0.22 %

RC – Cabo Rojo sand – 300 kPa – Dr: 21%

Specific gravity (Gs) 2.864
 Min. void ratio 1.264
 Max. void ratio 1.566

Mass 270.50 g
 Actual diameter 50.71 mm
 Height 117 mm

Total volume 236299.59 mm³ Void ratio (e) 1.502
 236.300 cm³ Relative density (Dr) 21%

Solid volume (Vs) 94.448 cm³

G max 135.08 MPa

PSF %	Average			Damping %	R2	D DEF. %	Cycles N	Ignored Ini. cycles
	γ max %	G avg MPa	G/Gmax					
0.1	3.50E-04			0.01	0.0007	0.00	10	1
0.5	1.29E-03	135.08	1.00	0.25	0.1513	0.03	10	1
0.8	1.95E-03	135.08	1.00	0.49	0.6107	0.27	10	1
1	2.61E-03	134.18	0.99	0.63	0.7742	0.41	10	1
2	4.41E-03	131.49	0.97	0.79	0.9390	0.57	10	1
3	1.02E-02	123.56	0.91	1.29	0.9961	1.07	10	1
5	1.21E-02	122.69	0.91	1.45	0.9976	1.23	10	1
7	1.92E-02	116.73	0.86	1.91	0.9964	1.69	10	1
10	2.22E-02	114.20	0.85	2.13	0.9983	1.91	10	1
15.0	2.61E-02	110.92	0.82	2.14	0.9972	1.92	10	1
20	3.75E-02	105.23	0.78	2.91	0.9891	2.69	10	1
25	4.45E-02	101.25	0.75	3.10	0.9908	2.88	10	1
30	5.32E-02	95.07	0.70	3.38	0.9869	3.16	10	1
40	6.41E-02	89.08	0.66	3.66	0.9797	3.44	10	1
50	7.40E-02	84.72	0.63	3.87	0.9720	3.65	10	1
60	7.81E-02	80.47	0.60	4.02	0.9733	3.80	10	1
70	8.97E-02	79.07	0.59	4.19	0.9671	3.97	10	1

RC Internal Damping 0.22 %

RC – Cabo Rojo sand – 500 kPa – Dr: 21%

Specific gravity (Gs) 2.864
 Min. void ratio 1.264
 Max. void ratio 1.566

Mass 270.50 g
 Actual diameter 50.71 mm
 Height 117 mm

Total volume 236299.59 mm³ Void ratio (e) 1.502
 236.300 cm³ Relative density (Dr) 21%

Solid volume (Vs) 94.448 cm³

G max 175.84 MPa

PSF %	Average			Damping %	R2	D DEF. %	Cycles N	Ignored Ini. cycles
	γ max %	G avg MPa	G/Gmax					
0.05	2.50E-04			0.03	0.0089	0.00	10	1
0.1	2.60E-04	175.84	1.00	0.09	0.0691	0.00	10	1
0.5	5.55E-04	170.39	0.97	0.12	0.1325	0.00	10	1
1	1.19E-03	169.37	0.96	0.23	0.1720	0.01	10	1
2	4.12E-03	174.81	0.99	0.71	0.7742	0.49	10	1
3	5.91E-03	165.65	0.94	1.02	0.9572	0.80	10	1
5	7.01E-03	165.65	0.94	1.10	0.9677	0.88	10	1
10	1.18E-02	162.67	0.93	1.75	0.9995	1.53	10	1
15	1.88E-02	151.90	0.86	2.02	0.9973	1.80	10	1
20	2.05E-02	151.90	0.86	2.19	0.9984	1.97	10	1
30	3.39E-02	140.58	0.80	2.78	0.9946	2.56	10	1
40	4.78E-02	131.48	0.75	3.33	0.9915	3.11	10	1
50	5.11E-02	133.28	0.76	3.49	0.9893	3.27	10	1
60	4.78E-02	131.48	0.75	3.53	0.9903	3.31	10	1
70	6.25E-02	122.69	0.70	3.87	0.9850	3.65	10	1
80	7.89E-02	115.87	0.66	4.23	0.9781	4.01	10	1
90	9.32E-02	107.63	0.61	4.51	0.9743	4.29	10	1

RC Internal Damping 0.22 %

RC – Cabo Rojo sand – 50 kPa – Dr: 58%

Specific gravity (Gs) 2.864
 Min. void ratio 1.264
 Max. void ratio 1.566

Mass 280.5 g
 Actual diameter 50.80 mm
 Height 115.5 mm

Total volume 234098.855 mm³ Void ratio (e) 1.390
 234.099 cm³ Relative density (Dr) 58%

Solid volume (Vs) 97.940 cm³

Gmax 62.14 MPa

PSF %	Average			Damping %	R2	D _{DEF.} %	Cycles N	Ignored Ini. cycles
	γ max %	G avg MPa	G/Gmax					
0.005	1.30E-04			0.31	0.2670	0.09	10	1
0.010	1.20E-04			0.51	0.4237	0.29	10	1
0.050	3.30E-04	62.14	1.00	0.45	0.4853	0.23	7	1
0.100	7.75E-04	62.14	1.00	0.56	0.8661	0.34	10	1
0.300	1.80E-03	60.92	0.98	1.38	0.9710	1.16	10	1
0.500	3.23E-03	57.95	0.93	1.61	0.9767	1.39	10	1
0.700	3.78E-03	57.36	0.92	1.80	0.9950	1.58	10	1
1.000	5.28E-03	55.62	0.89	2.09	0.9976	1.87	10	1
3.000	1.03E-02	50.55	0.81	2.88	0.9955	2.66	10	1
5.000	1.50E-02	46.25	0.74	3.25	0.9883	3.03	10	1
7.000	1.87E-02	42.14	0.68	3.39	0.9776	3.17	10	1
10.000	2.40E-02	38.23	0.62	3.66	0.9706	3.44	10	1
15.000	3.31E-02	33.59	0.54	3.60	0.9894	3.38	10	1
20.000	4.34E-02	29.26	0.47	3.71	0.9877	3.49	10	1
25.000	5.30E-02	25.63	0.41	3.75	0.9810	3.53	10	1
30.000	6.59E-02	22.96	0.37	4.85	0.9541	4.63	9	1
35.000	7.41E-02	20.79	0.33	5.16	0.9505	4.94	8	1
40.000	8.33E-02	19.40	0.31	3.84	0.9791	3.62	10	1
45.000	9.02E-02	17.42	0.28					
50.000	9.92E-02	16.15	0.26	5.35	0.9445	5.13	8	1
55.000	1.09E-01	15.53	0.25	5.42	0.9431	5.20	8	1

RC Internal Damping 0.22 %

RC – Cabo Rojo sand – 100 kPa – Dr: 58%

Specific gravity (Gs) 2.864
 Min. void ratio 1.264
 Max. void ratio 1.566

Mass 280.5 g
 Actual diameter 50.80 mm
 Height 115.5 mm

Total volume 234098.855 mm³ Void ratio (e) 1.390
 234.099 cm³ Relative density (Dr) 58%

Solid volume (Vs) 97.940 cm³

Gmax 86.00 MPa (Ignoring 1st cycle)

PSF %	Average			N=10 cycl.		
	γ max %	G avg MPa	G/Gmax	Damping %	R2	D _{DEF.} %
0.005	1.30E-04			0.00		0.00
0.010	1.50E-04			0.00		0.00
0.050	2.75E-04	83.87	0.98	0.00		0.00
0.100	6.00E-04	86.00	1.00	0.76	0.8494	0.54
0.300	1.47E-03	83.16	0.97	0.78	0.9948	0.56
0.500	1.79E-03	83.16	0.97	1.03	0.9820	0.81
0.700	2.04E-03	84.58	0.98	0.92	0.9751	0.70
1	4.03E-03	79.68	0.93	1.34	0.9949	1.12
3	8.06E-03	73.59	0.86	2.00	0.9969	1.78
5	1.17E-02	69.66	0.81	2.39	0.9956	2.17
7	1.49E-02	67.11	0.78	2.66	0.9927	2.44
10	1.90E-02	63.36	0.74	2.92	0.9887	2.70
15	2.43E-02	60.92	0.71			
20	3.02E-02	55.04	0.64			
25	3.57E-02	52.77	0.61			
30	4.02E-02	50.55	0.59			
35	4.89E-02	46.25	0.54			
40	5.32E-02	44.17	0.51	4.02	0.9597	3.80
45	5.39E-02	42.14	0.49	4.01	0.9669	3.79
55	6.05E-02	34.50	0.40	3.88	0.9643	3.66
60	7.16E-02	32.71	0.38	4.10	0.9652	3.88

RC Internal Damping 0.22 %

RC – Cabo Rojo sand – 300 kPa – Dr: 58%

Specific gravity (Gs) 2.864
 Min. void ratio 1.264
 Max. void ratio 1.566

Mass 280.5 g
 Actual diameter 50.80 mm
 Height 115.5 mm

Total volume 234098.855 mm³ Void ratio (e) 1.390
 234.099 cm³ Relative density (Dr) 58%

Solid volume (Vs) 97.940 cm³

Gmax 158.69 MPa (Ignoring 1st cycle)

PSF %	Average			N=10 cycl.		
	γ max %	G avg MPa	G/Gmax	Damping %	R2	D _{DEF.} %
0.1	3.50E-04			0.00		0.00
0.5	3.80E-04			0.00		0.00
0.6	1.06E-03	158.69	1.00			
0.7	1.99E-03	137.99	0.87	0.48	0.5482	0.26
1	2.12E-03	137.99	0.87	0.51	0.7308	0.29
3	3.51E-03	143.49	0.90	0.82	0.9136	0.60
5	9.33E-03	129.94	0.82	1.43	0.9957	1.21
7	1.08E-02	129.06	0.81	1.48	0.9971	1.26
10	1.20E-02	129.94	0.82	1.61	0.9976	1.39
15	2.01E-02	120.43	0.76	2.23	0.9977	2.01
20	2.22E-02	120.43	0.76	2.49	0.9977	2.27
25	3.08E-02	112.10	0.71	2.83	0.9948	2.61
30	3.28E-02	112.10	0.71	2.93	0.9931	2.71
35	3.88E-02	107.24	0.68	3.22	0.9923	3.00
40	4.21E-02	105.65	0.67	3.29	0.9887	3.07
45	4.36E-02	105.65	0.67	3.39	0.9905	3.17
50	4.41E-02	105.65	0.67	3.41	0.9877	3.19
55	4.50E-02	105.65	0.67	3.44	0.9898	3.22
60	4.84E-02	100.93	0.64	3.51	0.9855	3.29
65	5.05E-02	100.93	0.64	3.64	0.9845	3.42
70	5.99E-02	93.32	0.59	3.86	0.9783	3.64
75	6.75E-02	87.44	0.55	3.98	0.9730	3.76
80	7.18E-02	87.44	0.55	4.13	0.9718	3.91

RC Internal Damping 0.22 %

RC – Cabo Rojo sand – 500 kPa – Dr: 58%

Specific gravity (Gs) 2.864
 Min. void ratio 1.264
 Max. void ratio 1.566

Mass 280.5 g
 Actual diameter 50.80 mm
 Height 115.5 mm

Total volume 234098.855 mm³ Void ratio (e) **1.390**
 234.099 cm³ Relative density (Dr) **58%**

Solid volume (Vs) 97.940 cm³

Gmax 189.23 MPa (Ignoring 1st cycle)

PSF %	Average			N=10 cycl.		
	γ max %	G avg MPa	G/Gmax	Damping %	R2	D _{DEF.} %
0.1	6.60E-04			0.00		0.00
0.7	9.15E-04	189.23	1.00	0.48	0.6275	0.26
1	1.20E-03	189.23	1.00	0.53	0.7947	0.31
2	2.43E-03	175.67	0.93			
3	3.45E-03	174.64	0.92	0.84	0.9668	0.62
5	4.08E-03	174.64	0.92	0.97	0.9960	0.75
10	5.15E-03	174.64	0.92	1.16	0.9968	0.94
12	9.88E-03	167.58	0.89			
15	1.26E-02	162.60	0.86	1.83	0.9984	1.61
20	1.39E-02	162.60	0.86	1.94	0.9988	1.72
25	1.47E-02	162.60	0.86	2.07	0.9988	1.85
30	2.17E-02	154.81	0.82	2.57	0.9973	2.35
35	2.56E-02	149.10	0.79	2.73	0.9957	2.51
45	2.76E-02	149.10	0.79	2.97	0.9947	2.75
50	2.83E-02	149.10	0.79	3.02	0.9940	2.80
60	2.68E-02	150.05	0.79	3.01	0.9919	2.79
70	3.13E-02	139.81	0.74	3.22	0.9886	3.00
80.0	5.10E-02	129.06	0.68	3.60	0.9804	3.38
85.0	5.39E-02	129.06	0.68	3.79	0.9820	3.57

RC Internal Damping 0.22 %

RC – Cabo Rojo sand – 50 kPa – Dr: 91%

Specific gravity (Gs) 2.864
 Min. void ratio 1.264
 Max. void ratio 1.566

Mass 287.8 g
 Actual diameter 51.35 mm
 Height 111.17 mm

Total volume 230198.239 mm³ Void ratio (e) 1.291
 230.198 cm³ Relative density (Dr) 91%

Solid volume (Vs) 100.489 cm³

Gmax 68.58 MPa

PSF %	Average			Damping %	R2	D _{DEF.} %	Cycles N	Ignored Ini. cycles
	γ max %	G avg MPa	G/Gmax					
0.01	2.40E-04			0.56		0.34		
0.05	3.00E-04	71.68	1.05	0.68	0.6828	0.46	10	1
0.1	5.25E-04	72.32	1.05	0.88	0.6739	0.66	10	1
0.2	1.23E-03	68.58	1.00	1.23	0.9589	1.01	10	1
0.3	1.81E-03	67.96	0.99	1.41	0.9134	1.19	10	1
0.5	2.18E-03	67.96	0.99	1.51	0.9856	1.29	10	1
0.7	3.40E-03	64.94	0.95	1.84	0.9850	1.62	10	1
1	4.01E-03	64.34	0.94	1.87	0.9781	1.65	10	1
3	8.59E-03	57.96	0.85	2.94	0.9924	2.72	10	1
5	1.27E-02	51.90	0.76	3.45	0.9823	3.23	10	1
7	1.61E-02	47.80	0.70	3.82	0.9783	3.60	10	1
10	2.11E-02	42.71	0.62	4.05	0.9504	3.83	10	1
12	2.39E-02	38.92	0.57	4.22	0.9264	4.00	10	1
15	2.84E-02	32.71	0.48	4.56		4.34		
20	3.78E-02	27.80	0.41	5.07		4.85		
25	4.64E-02	25.50	0.37	5.62		5.40		
30	5.59E-02	22.59	0.33	6.27		6.05		
35	6.51E-02	20.52	0.30	6.45	0.9501	6.23	7	1
40	7.45E-02	18.55	0.27	6.91	0.9424	6.69	6	1
50	9.44E-02	16.68	0.24	7.09	0.9445	6.87	6	1
55	1.04E-01	16.08	0.23	6.97	0.9472	6.75	6	1

RC Internal Damping 0.22 %

RC – Cabo Rojo sand – 100 kPa – Dr: 91%

Specific gravity (Gs) 2.864
 Min. void ratio 1.264
 Max. void ratio 1.566

Mass 287.8 g
 Actual diameter 51.35 mm
 Height 111.17 mm

Total volume 230198.239 mm³ Void ratio (e) 1.291
 230.198 cm³ Relative density (Dr) 91%

Solid volume (Vs) 100.489 cm³

Gmax 91.79

PSF %	Average			Damping %	R2	D _{DEF.} %	Cycles N	Ignored Ini. cycles
	γ max %	G avg MPa	G/Gmax					
0.01	2.70E-04			0.59		0.37		
0.05	3.10E-04	96.11	1.05	0.32	0.1756	0.10	10	1
0.1	4.10E-04	91.79	1.00	0.49	0.4574	0.27	10	1
0.2	6.53E-04	90.39	0.98				10	1
0.3	1.65E-03	90.37	0.98	0.95	0.8879	0.73	10	1
0.5	2.36E-03	86.88	0.95	1.06	0.9555	0.84	10	1
0.7	2.81E-03	86.19	0.94	1.31	0.9673	1.09	10	1
1.0	3.11E-03	86.88	0.95	1.40	0.9932	1.18	10	1
3.0	7.05E-03	78.78	0.86	2.29	0.9954	2.07	10	1
5.0	1.09E-02	72.32	0.79	2.80	0.9880	2.58	10	1
7.0	1.37E-02	67.96	0.74	3.12	0.9941	2.90	10	1
10.0	1.74E-02	64.34	0.70	3.34	0.9952	3.12	10	1
15.0	2.27E-02	59.09	0.64	3.72		3.50		
20.0	2.76E-02	56.27	0.61	3.87		3.65		
25.0	2.24E-02	58.52	0.64					
30.0	3.73E-02	46.68	0.51	4.07		3.85		
35.0	4.26E-02	44.68	0.49	4.24		4.02		
40.0	4.74E-02	42.71	0.47	4.39		4.17		
45.0	5.30E-02	42.71	0.47	4.41	0.9532	4.19	9	1
50.0	5.81E-02	36.19	0.39	4.51	0.9538	4.29	8	1
60.0	6.96E-02	31.86	0.35	4.75	0.9608	4.53	8	1
70.000	7.98E-02	28.59	0.31	5.23	0.9565	5.01	7	1

RC Internal Damping 0.22 %

RC – Cabo Rojo sand – 300 kPa – Dr: 91%

Specific gravity (Gs) 2.864
 Min. void ratio 1.264
 Max. void ratio 1.566

Mass 287.8 g
 Actual diameter 51.35 mm
 Height 111.17 mm

Total volume 230198.239 mm³ Void ratio (e) 1.291
 230.198 cm³ Relative density (Dr) 91%

Solid volume (Vs) 100.489 cm³

Gmax 159.04 MPa

PSF %	Average			Damping %	R2	D _{DEF.} %	Cycles N	Ignored Ini. cycles
	γ max %	G avg MPa	G/Gmax					
0.1	6.20E-04			0.57		0.35		
0.5	1.24E-03	159.04	1.00	0.59	0.8358	0.37	10	1
0.8	9.90E-04	158.47	1.00	0.55	0.8519	0.33	10	1
1	2.00E-03	158.38	1.00	0.73	0.9292	0.51	10	1
3	3.13E-03	159.40	1.00	1.00	0.9825	0.78	10	1
5	3.91E-03	157.53	0.99	1.09	0.9805	0.87	10	1
7	8.44E-03	138.57	0.87	1.68	0.9933	1.46	10	1
10	9.36E-03	143.86	0.90	1.97	0.9962	1.75	10	1
15	1.60E-02	128.28	0.81	2.56	0.9983	2.34	10	1
20	1.74E-02	127.43	0.80	2.60	0.9972	2.38	10	1
25	2.41E-02	120.01	0.75	3.08	0.9927	2.9	10	1
30	2.68E-02	119.19	0.75					
40	3.65E-02	111.22	0.70	3.63	0.9836	3.41	10	1
50	4.30E-02	105.04	0.66	4.00	0.9811	3.78	10	1
60	4.92E-02	103.52	0.65	4.15	0.9744	3.93	10	1
70	5.37E-02	103.52	0.65	4.19	0.9809	3.97	10	1

RC Internal Damping 0.22 %

RC – Cabo Rojo sand – 500 kPa – Dr: 91%

Specific gravity (Gs) 2.864
 Min. void ratio 1.264
 Max. void ratio 1.566

Mass 287.8 g
 Actual diameter 51.35 mm
 Height 111.17 mm

Total volume 230198.239 mm³ Void ratio (e) 1.291
 230.198 cm³ Relative density (Dr) 91%

Solid volume (Vs) 100.489 cm³

Gmax 209.73 MPa

PSF %	Average			Damping %	R2	D _{DEF.} %	Cycles N	Ignored Ini. cycles
	γ max %	G avg MPa	G/Gmax					
0.05	2.90E-04							
0.1	2.55E-04	209.73	1.00	0.67		0.45		
0.5	6.90E-04	209.73	1.00					
1	1.32E-03	209.73	1.00	0.58	0.3695	0.36	10	1
2	1.73E-03	209.73	1.00	0.88	0.9332	0.66	10	1
3	1.98E-03	192.88	0.92	0.75	0.4395	0.53	10	1
5	2.28E-03	201.31	0.96	1.01	0.9734	0.79	10	2
10	3.02E-03	209.73	1.00	1.15	0.9854	0.93	10	2
12	3.91E-03	188.77	0.90	1.34	0.9816	1.12	10	1
15	7.79E-03	180.72	0.86	1.84	0.9952	1.62	10	2
20	8.15E-03	184.70	0.88	2.14	0.9984	1.92	10	1
25	8.71E-03	182.70	0.87	2.14	0.9937	1.92	10	2
30	1.44E-02	165.08	0.79	2.76	0.9950	2.54	10	1
40	1.70E-02	161.28	0.77	3.03	0.9892	2.81	10	1
50	2.53E-02	150.16	0.72	3.55	0.9835	3.33	10	1
60	2.69E-02	150.16	0.72	3.81	0.9804	3.59	10	1
70	2.79E-02	150.16	0.72	3.98	0.9788	3.76	10	1
80.0	3.21E-02	137.69	0.66	4.04	0.9817	3.82	9	1
90.0	3.70E-02	137.69	0.66	4.45	0.9719	4.23	9	1

RC Internal Damping 0.22 %

RC – South Bend sand – 50 kPa – Dr: 26%

Specific gravity (Gs) 2.698
 Min. void ratio 0.497
 Max. void ratio 0.726

Mass 377.40 g
 Actual diameter 50.10 mm
 Height 118.17 mm

Total volume 232955.29 mm³ Void ratio (e) 0.665
 232.955 cm³ Relative density (Dr) 26%

Solid volume (Vs) 139.881 cm³

Gmax 67.94 MPa

PFS %	Average			Damping %	R2	D _{DEF.} %	Cycles N	Ignored Ini. cycles
	γ max %	G avg MPa	G/Gmax					
0.01	1.60E-04			0.36		0.14		
0.05	3.90E-04	67.28	0.99	1.03		0.81		
0.08	6.25E-04	67.94	1.00	0.97	0.7944	0.75	10	1
0.1	6.90E-04	67.94	1.00	1.04	0.9163	0.82	10	1
0.2	1.83E-03	64.66	0.95	1.61	0.9607	1.39	10	1
0.5	2.98E-03	60.82	0.90	1.90	0.9986	1.68	10	1
0.7	3.56E-03	60.20	0.89	2.05	0.9918	1.83	10	1
1.0	4.69E-03	57.70	0.85	2.33	0.9978	2.11	10	1
2.0	7.49E-03	52.90	0.78	3.14	0.9936	2.92	10	1
5.0	1.42E-02	46.09	0.68	4.02	0.9894	3.80	10	1
7.0	1.90E-02	41.28	0.61	4.33	0.9881	4.11	10	1
10.0	2.57E-02	37.23	0.55	4.69	0.9749	4.47	10	1
15.0	3.68E-02	32.46	0.48	5.21	0.9726	4.99	9	1
20.0	4.89E-02	29.32	0.43	5.58	0.9708	5.36	8	1
25.0	6.06E-02	25.92	0.38	5.58	0.9634	5.36	8	1
30.0	7.30E-02	22.73	0.33	5.75	0.9598	5.53	8	1
35.0	8.64E-02	21.22	0.31	6.02	0.9535	5.80	7	1
40.0	1.04E-01	19.04	0.28	6.53	0.9664	6.31	6	1

RC Internal Damping 0.22 %

RC – South Bend sand – 100 kPa – Dr: 26%

Specific gravity (Gs)	2.698		
Min. void ratio	0.497		
Max. void ratio	0.726		
Mass	377.40 g		
Actual diameter	50.10 mm		
Height	118.17 mm		
Total volume	232955.29 mm ³	Void ratio (e)	0.665
	232.955 cm ³	Relative density (Dr)	26%
Solid volume (Vs)	139.881 cm ³		

Gmax 120.79

PSF %	Average			Damping %	R2	D _{DEF.} %	Cycles N	Ignored Ini. cycles
	γ max %	G avg MPa	G/Gmax					
0.05	4.40E-04	117.26	0.97	0.76		0.54		
0.1	8.43E-04	117.86	0.98	0.95	0.7540	0.73	10	1
0.2	1.41E-03	115.52	0.96	1.07	0.9423	0.85	10	1
0.5	2.04E-03	117.27	0.97	0.96	0.9502	0.74	10	1
0.7	2.57E-03	113.79	0.94	1.12	0.9875	0.90	10	1
1.0	4.50E-03	108.68	0.90	1.48	0.9972	1.26	10	1
2.0	7.69E-03	103.69	0.86	1.93	0.9996	1.71	10	1
5.0	1.46E-02	92.49	0.77	2.83	0.9972	2.61	10	1
7.0	2.00E-02	85.62	0.71	3.26	0.9983	3.04	10	1
10.0	2.56E-02	80.46	0.67	3.64	0.9971	3.42	10	1
15.0	3.37E-02	74.08	0.61	4.04	0.9904	3.82	10	1
20.0	4.15E-02	67.95	0.56	4.30	0.9865	4.08	10	1
25.0	5.01E-02	62.72	0.52	4.45	0.9807	4.23	10	1
30.0	5.63E-02	57.70	0.48	4.66	0.9780	4.44	9	1
40.0	6.72E-02	46.08	0.38	4.85	0.9512	4.63	8	1
45	7.44E-02	46.08	0.38	4.83	0.9560	4.61	8	1
50	8.10E-02	39.73	0.33	5.15	0.9512	4.93	8	1
55	8.94E-02	36.73	0.30	5.50	0.9535	5.28	7	1

RC Internal Damping 0.22 %

RC – South Bend sand – 300 kPa – Dr: 26%

Specific gravity (Gs) 2.698
 Min. void ratio 0.497
 Max. void ratio 0.726

Mass 377.40 g
 Actual diameter 50.10 mm
 Height 118.17 mm

Total volume 232955.29 mm³ Void ratio (e) 0.665
 232.955 cm³ Relative density (Dr) 26%

Solid volume (Vs) 139.881 cm³

Gmax 211.59

PSF %	Average			Damping %	R2	D _{DEF.} %	Cycles N	Ignored Ini. cycles
	γ max %	G avg MPa	G/Gmax					
0.1	2.50E-04			0.31		0.09		
0.5	7.70E-04	209.25	0.99	0.58	0.6892	0.36	10	1
0.8	9.55E-04	209.25	0.99	0.83	0.8377	0.61	10	2
1	1.01E-03	209.25	0.99	0.72	0.8186	0.50	10	2
2	1.28E-03	211.59	1.00	0.97	0.9376	0.75	10	2
3	3.85E-03	190.96	0.90	1.49	0.9967	1.27	10	2
5	4.47E-03	190.96	0.90	1.68	0.9963	1.46	10	2
7	8.39E-03	183.24	0.87	2.48	0.9994	2.26	10	1
10	1.02E-02	177.79	0.84	2.62	0.9993	2.40	10	1
15	1.69E-02	163.03	0.77	2.96	0.9990	2.74	10	1
20	2.46E-02	154.88	0.73	3.41	0.9966	3.19	10	1
25	2.79E-02	150.88	0.71	3.45	0.9970	3.23	10	1
30	3.60E-02	141.12	0.67	3.99	0.9971	3.77	10	1
40	3.82E-02	141.12	0.67	4.20	0.9962	3.98	10	1
50	4.81E-02	131.68	0.62	4.46	0.9918	4.24	10	1
60	6.37E-02	115.52	0.55	4.76	0.9871	4.54	10	1
70	7.50E-02	110.37	0.52	5.32	0.9841	5.10	9	1
80	8.80E-02	103.68	0.49	5.49	0.9782	5.27	9	1
90	9.73E-02	103.68	0.49	5.88	0.9710	5.66	9	1

RC Internal Damping 0.22 %

RC – South Bend sand – 500 kPa – Dr: 26%

Specific gravity (Gs) 2.698
 Min. void ratio 0.497
 Max. void ratio 0.726

Mass 377.40 g
 Actual diameter 50.10 mm
 Height 118.17 mm

Total volume 232955.29 mm³ Void ratio (e) 0.665
 232.955 cm³ Relative density (Dr) 26%

Solid volume (Vs) 139.881 cm³

Gmax 253.44

PSF %	Average			Damping %	R2	D _{DEF.} %	Cycles N	Ignored Ini. cycles
	γ max %	G avg MPa	G/Gmax					
0.1	1.90E-04			0.54		0.32		
0.5	3.05E-04	252.16	0.99	0.85		0.63	10	1
1	2.48E-04	253.44	1.00	0.74	0.8251	0.52	10	1
2	1.44E-03	250.88	0.99	0.92	0.9378	0.70	10	2
5	1.94E-03	250.88	0.99	1.13	0.9911	0.91	10	3
7	4.85E-03	229.60	0.91	1.70	0.9979	1.48	10	2
10	5.51E-03	228.37	0.90	1.75	0.9922	1.53	10	3
15	1.06E-02	213.98	0.84	2.67	0.9969	2.45	10	1
20	1.21E-02	209.25	0.83	2.69	0.9937	2.47	10	2
25	1.62E-02	202.29	0.80	3.25	0.9973	3.03	10	1
30	2.00E-02	190.96	0.75	3.75	0.9953	3.53	10	1
35	2.20E-02	190.96	0.75	3.89	0.9929	3.67	10	1
40	2.35E-02	193.20	0.76	4.05	0.9935	3.83	10	1
50	2.51E-02	190.96	0.75	4.13	0.9941	3.91	9	2
60	4.32E-02	163.03	0.64	4.61	0.9904	4.39	9	1
70	4.94E-02	163.03	0.64	4.73	0.9813	4.51	9	1
80	6.57E-02	150.88	0.60	5.79	0.9761	5.57	9	1
90	7.93E-02	141.12	0.56	6.17	0.9737	5.95	9	1

RC Internal Damping 0.22 %

RC – South Bend sand – 50 kPa – Dr: 91%

Specific gravity (Gs)	2.698		
Min. void ratio	0.497		
Max. void ratio	0.726		
Mass	415.00 g		
Actual diameter	51.23 mm		
Height	113.166667 mm		
Total volume	233299.40 mm ³	Void ratio (e)	0.517
	233.299 cm ³	Relative density (Dr)	91%
Solid volume (Vs)	153.818 cm ³		

Gmax 94.38 MPa

PSF %	Average			Damping %	R2	D DEF. %	Cycles N	Ignored Ini. cycles
	γ max %	G avg MPa	G/Gmax					
0.01	1.50E-04			0.45		0.23		
0.05	3.00E-04	92.19	0.98	0.93	0.9296	0.71	10	1
0.08	4.95E-04	90.73	0.96	1.00	0.9359	0.78	10	1
0.1	5.70E-04	90.00	0.95	1.11	0.9537	0.89	10	2
0.3	1.69E-03	85.74	0.91	1.42	0.9731	1.20	10	1
0.5	2.07E-03	85.04	0.90	1.50	0.9497	1.28	10	1
0.7	3.05E-03	81.57	0.86	1.72	0.9944	1.50	10	1
1	3.59E-03	81.58	0.86	2.05	0.9859	1.83	10	1
2	6.05E-03	73.56	0.78	2.69	0.9442	2.47	10	1
5	1.14E-02	65.34	0.69	3.83	0.9942	3.61	9	1
7	1.51E-02	61.11	0.65	4.02	0.9939	3.80	9	1
10	1.90E-02	58.76	0.62	4.44	0.9858	4.22	9	1
15	2.48E-02	50.90	0.54	4.61	0.9683	4.39	9	1
20	3.35E-02	46.66	0.49	5.26	0.9652	5.04	8	1
25	4.03E-02	42.60	0.45	5.58	0.9693	5.36	8	1
30	4.44E-02	40.64	0.43	5.82	0.9652	5.60	7	1
40	5.22E-02	40.64	0.43	6.23	0.9698	6.01	6	1
50	5.95E-02	35.05	0.37	6.34	0.9590	6.12	6	1
60	7.41E-02	29.86	0.32	6.45	0.9743	6.23	6	1
70	8.86E-02	29.04	0.31	6.70	0.9682	6.48	6	1
80	1.02E-01	28.23	0.30	6.71	0.9645	6.49	6	1

RC Internal Damping **0.22 %**

RC – South Bend sand – 100 kPa – Dr: 91%

Specific gravity (Gs) 2.698
 Min. void ratio 0.497
 Max. void ratio 0.726

Mass 415.00 g
 Actual diameter 51.23 mm
 Height 113.166667 mm

Total volume 233299.40 mm³
 233.299 cm³ Void ratio (e) 0.517
 Relative density (Dr) 91%

Solid volume (Vs) 153.818 cm³

Gmax 164.52 MPa

PSF %	Average			Damping %	R2	D DEF. %	Cycles N	Ignored Ini. cycles
	γ max %	G avg MPa	G/Gmax					
0.01	3.00E-04			0.34		0.12		
0.05	2.30E-04			0.20		0.00		
0.1	3.40E-04	164.52	1.00	0.31		0.09		
0.2	5.25E-04	157.78	0.96	0.67		0.45		
0.5	7.20E-04	159.69	0.97					
0.7	9.35E-04	159.69	0.97	0.66	0.4369	0.44	10	1
1	1.14E-03	159.69	0.97	0.85	0.4440	0.63	10	1
2	2.98E-03	143.80	0.87	1.34	0.8289	1.12	10	1
5	6.22E-03	134.84	0.82	2.03	0.9537	1.81	10	1
7	9.65E-03	124.47	0.76	2.70	0.9801	2.48	10	1
10	1.24E-02	121.13	0.74	3.32	0.9986	3.10	10	1
15	1.94E-02	109.70	0.67	3.65	0.9899	3.43	10	1
20	2.51E-02	104.21	0.63	4.01	0.9922	3.79	10	1
25	3.13E-02	95.86	0.58	4.57	0.9952	4.35	10	1
30	3.49E-02	95.86	0.58	4.67	0.9914	4.45	10	1
40	4.09E-02	88.57	0.54	5.10	0.9863	4.88	10	1
50	4.70E-02	84.34	0.51	5.23	0.9826	5.01	10	1
60	5.75E-02	74.86	0.46	5.89	0.9870	5.67	9	1
70	6.80E-02	72.26	0.44	6.22	0.9793	6.00	8	1
80	7.74E-02	69.70	0.42	6.37	0.9722	6.15	8	1
90	8.53E-02	64.72	0.39	6.46	0.9673	6.24	8	1

RC Internal Damping 0.22 %

RC – South Bend sand – 300 kPa – Dr: 91%

Specific gravity (Gs) 2.698
 Min. void ratio 0.497
 Max. void ratio 0.726

Mass 415.00 g
 Actual diameter 51.23 mm
 Height 113.166667 mm

Total volume 233299.40 mm³ Void ratio (e) 0.517
 233.299 cm³ Relative density (Dr) 91%

Solid volume (Vs) 153.818 cm³

Gmax 286.45 MPa

PSF %	Average			Damping %	R2	D DEF. %	Cycles N	Ignored Ini. cycles
	γ max %	G avg MPa	G/Gmax					
0.1	3.00E-04			0.28		0.06		
0.5	2.30E-04	286.45	1.00	0.31		0.09		
1	3.30E-04	268.75	0.94	0.27	0.4168	0.05	10	1
2	4.20E-04	281.35	0.98	0.79	0.5291	0.57	10	1
5	6.85E-04	268.75	0.94	0.74	0.4822	0.52	10	1
7	1.94E-03	245.63	0.86	1.61	0.9889	1.39	10	2
10	2.10E-03	246.82	0.86	1.79	0.9667	1.57	10	2
15	2.44E-03	242.08	0.85	1.67	0.9715	1.45	10	1
20	5.05E-03	221.29	0.77	2.43	0.9966	2.21	10	2
25	5.30E-03	223.55	0.78	2.69	0.9939	2.47	10	2
30	8.92E-03	205.76	0.72	3.27	0.9905	3.05	10	1
35	9.81E-03	201.43	0.70	3.22	0.9935	3.00	10	2
40	1.03E-02	201.43	0.70	3.41	0.9877	3.19	10	2
45	1.10E-02	201.43	0.70	3.49	0.9911	3.27	10	2
50	1.11E-02	201.43	0.70	3.47	0.9927	3.25	10	2

RC Internal Damping 0.22 %

RC – South Bend sand – 500 kPa – Dr: 91%

Specific gravity (Gs) 2.698
 Min. void ratio 0.497
 Max. void ratio 0.726

Mass 415.00 g
 Actual diameter 51.23 mm
 Height 113.166667 mm

Total volume 233299.40 mm³ Void ratio (e) 0.517
 233.299 cm³ Relative density (Dr) 91%

Solid volume (Vs) 153.818 cm³

Gmax 377.50 MPa

PSF %	Average			Damping %	R2	D DEF. %	Cycles N	Ignored Ini. cycles
	γ max %	G avg MPa	G/Gmax					
0.5	1.70E-04			0.22		0.00		
1	1.17E-03	370.20	0.98					
2	2.45E-04	368.76	0.98					
5	3.95E-04	358.59	0.95					
7	4.40E-04	373.10	0.99					
10	7.00E-04	299.44	0.79	0.58	0.4616	0.36	10	2
12	7.80E-04	312.86	0.83					
15	1.40E-03	310.09	0.82					
20	1.71E-03	299.44	0.79	1.79	0.9652	1.57	10	1
25	1.80E-03	299.44	0.79	1.84	0.9816	1.62	10	2
30	3.67E-03	271.24	0.72	2.13	0.8946	1.91	10	2
35	3.96E-03	268.75	0.71	2.34	0.9597	2.12	10	2
40	4.16E-03	268.75	0.71	2.54	0.9799	2.32	10	2
50	4.45E-03	268.75	0.71	2.63	0.9814	2.41	8	2
60	4.35E-03	278.80	0.74	2.55	0.9888	2.33	9	2

RC Internal Damping 0.22 %

APPENDIX 6.

Equipment and Sensors Calibration.

Calibration of sensors used by the triaxial testing system

The load, displacement and pressure transducers in the LoadTrac II/FlowTrac II System were calibrated to determine if the calibration factors provided by Geocomp in the “Triaxial” software were correct.

Force Transducer:

To perform the calibration of the system load cell, a series of loads were applied to the load cell and checked by an independent calibrated load cell, which was placed between the platen in the LoadTrac device and the load cell extension rod, as shown in Figure A.6.1. The Load Control window in the “Triaxial” software was used to applying the desired load for the calibration process. When a load value was entered, the platen moved up until the reading of the system load cell best matches (as per previous Geocomp calibration) the force value entered. Both values were recorded every time a load was applied, to produce the calibration line shown in Figure A.6.2.

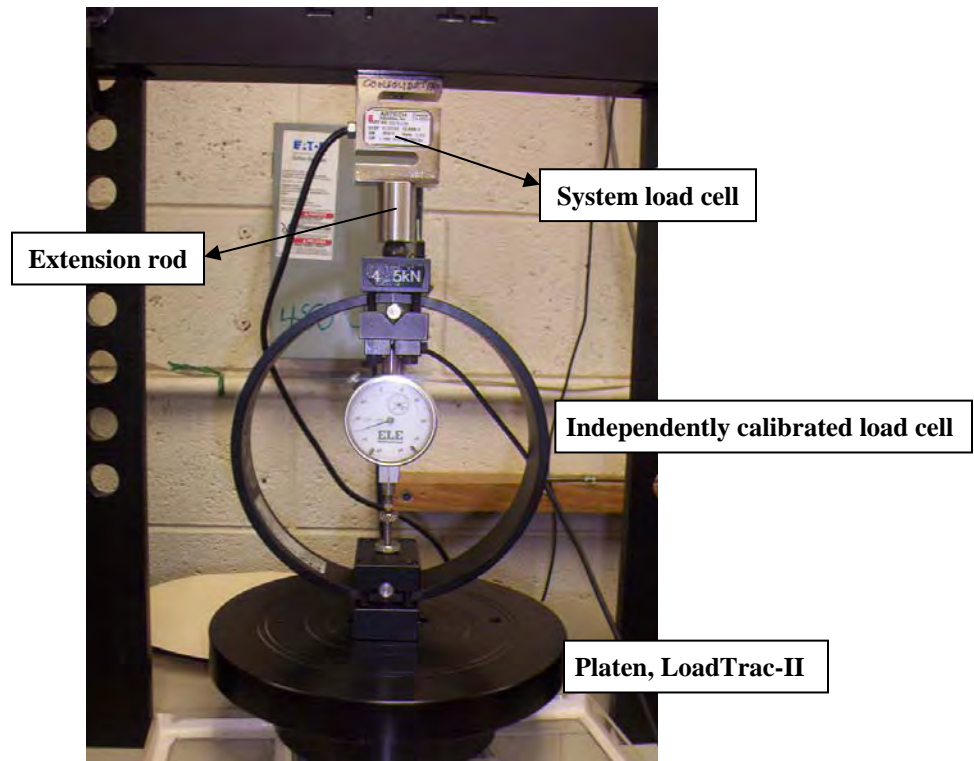


Figure A.6.1. Configuration used for the calibration of the system load cell.

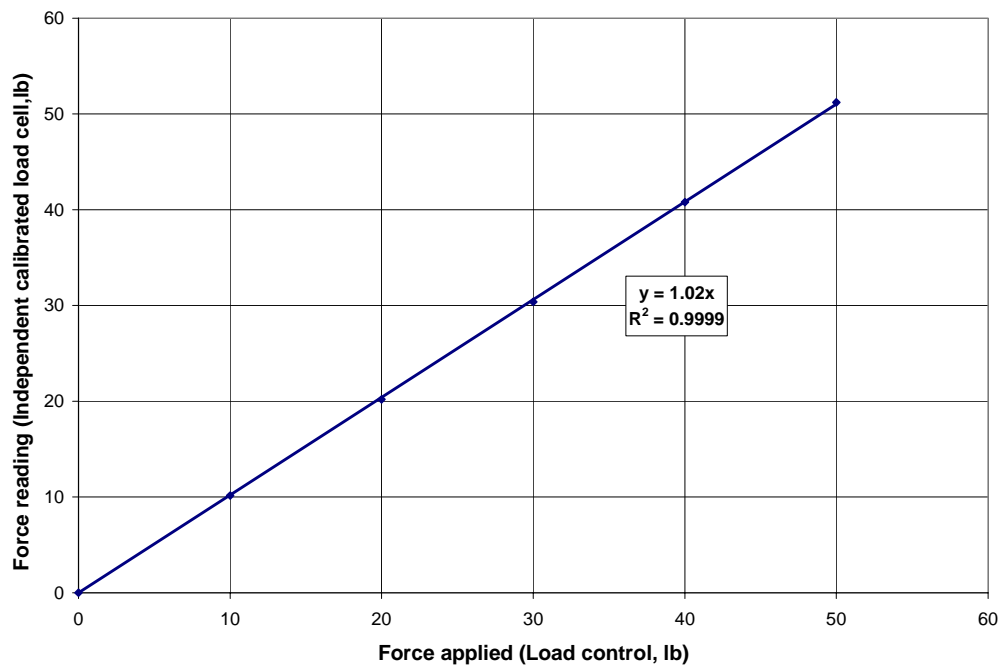


Figure A.6.2. Calibration line for the system load cell.

As may be noticed from Figure A.6.2, a correlation coefficient (R^2) of 0.999 was reached, which indicated that the calibration factors provided by Geocomp worked fine for the force transducer.

Pressure Transducer:

For the calibration of the system pore pressure transducers an independently calibrated pressure gage was used. Both flow pumps (FlowTrac/Cell and Sample) were connected in a closed system, using a tubing from each output valve to the independent pressure gage, as shown in Figure A.6.3. A series of pressure values was then put on the system, using the Cell Pressure Control window in the “Triaxial” software. The flow pump of the FlowTrac/Cell increased the pressure in the output line until the reading in the transducer matches (as per previous Geocomp calibration) the pressure value entered. As part of the system, the sample pressure transducer and the independent pressure gage reached the same pressure than the cell pressure transducer. The reading in the sample pressure transducer was checked in the System Monitor window of the “Triaxial” software and in the pressure gage. The pressure values applied to the system were used to produce the calibration lines shown in Figure A.6.4 and Figure A.6.5 for the cell and sample pressure transducer, respectively.

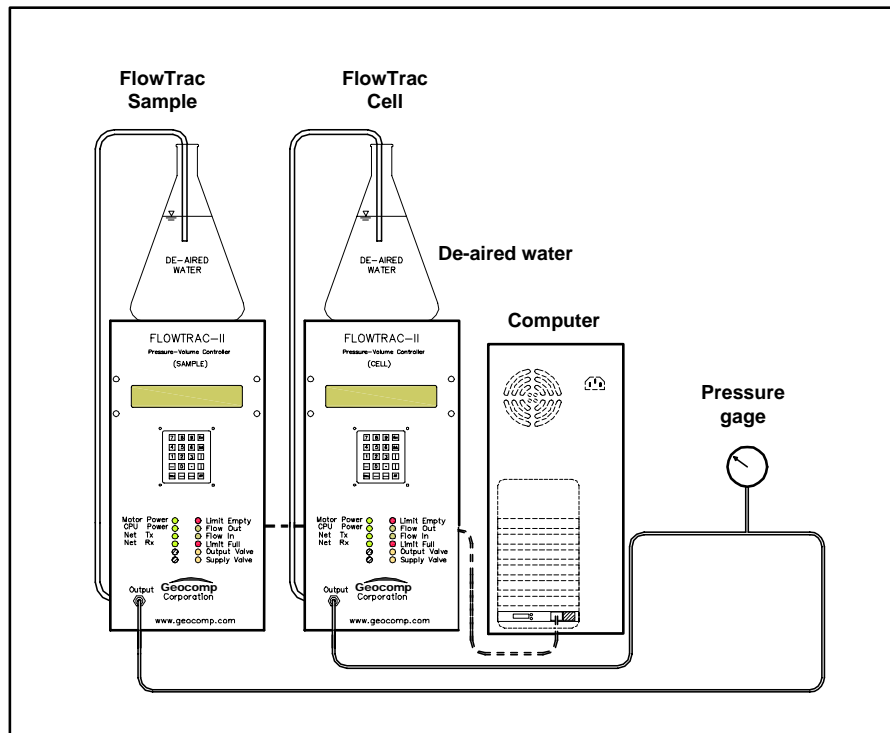


Figure A.6.3. Configuration used for the calibration of the sample pressure transducer. From Geocomp (2006).

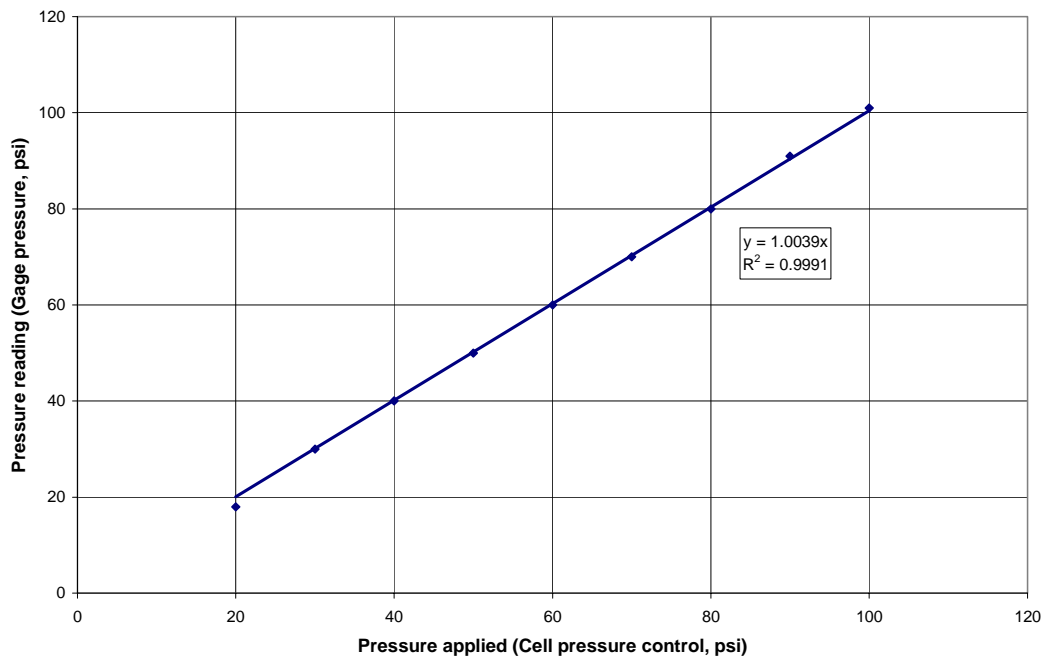


Figure A.6.4. Calibration line for the cell pressure transducers.

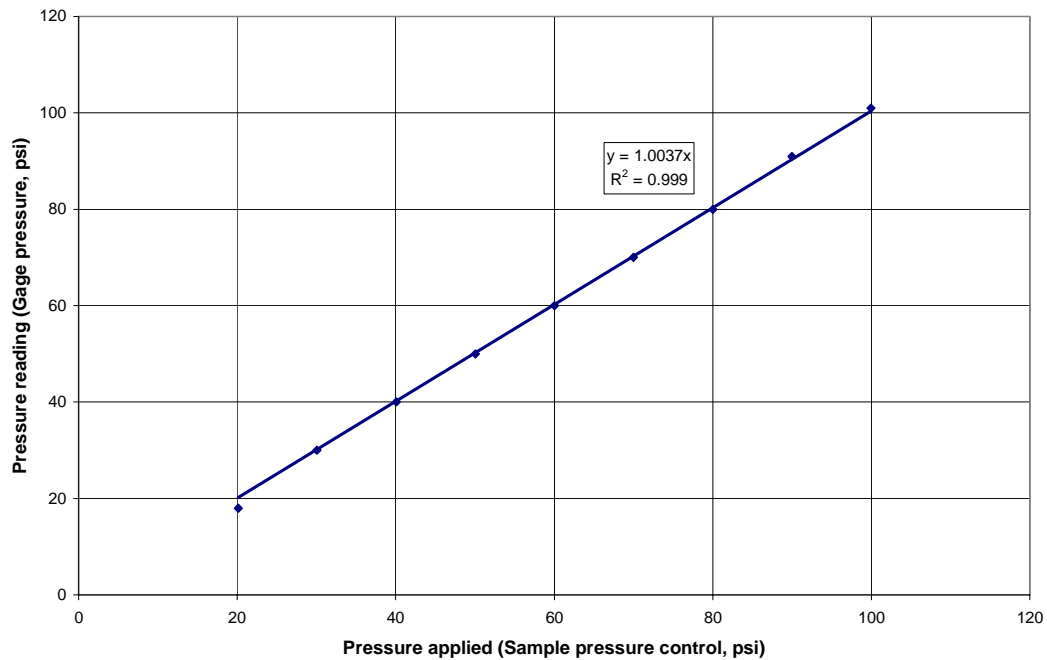


Figure A.6.5. Calibration line for the sample pressure transducers.

As may be noticed from Figure A.6.4 and Figure A.6.5, a correlation coefficient (R^2) of 0.999 was reached for each transducer, which indicated that the calibration factors provided by Geocomp worked fine for the cell and sample pressure transducers.

RC Equipment Calibration

Two important properties of the RC device are required to reduce the data: the mass moment of inertia of the RC driving system (I_0), and the equipment-generated damping ratio (D_{eq}). These parameters were obtained by means of calibration tests described below.

Determination of I_0 :

The RC system was operated using two calibration specimens:

- Aluminum calibration specimens: Made of 6061-T6 aluminum with a mass density of 2.70 g/cm³, 12.55 mm diameter, and 101.50 mm height. The mass moment of inertia of the calibration specimen is 82.41 kg-mm² (I_{cal}).
- Aluminum calibration specimen with added mass: this configuration consisted of using the above calibration specimen with an added metal mass of mass density 2.64 g/cm³ and 76.2 mm in diameter. The additional mass moment of inertia of the added mass is 163.09 kg-mm² (I_{mass}).

The inertia of the driving system (I_0) can be calculated using the following equation (GCTS 2004):

$$I_0 = \frac{(I_{cal} + I_{mass})\omega_2^2 - I_{cal}\omega_1^2}{\omega_1^2 - \omega_2^2} \quad (\text{A.6.1})$$

Where:

$$I_{cal} = 82.41 \text{ kg-mm}^2.$$

$$I_{mass} = 163.09 \text{ kg-mm}^2.$$

ω_1 = resonant frequency with calibration specimen (from RC calibration test, see Figure A.6.6)

ω_2 = resonant frequency with calibration specimen + added mass (from RC calibration test, see Figure A.6.7)

Using Equation (A.6. 1), the inertia of the drive system was computed as 723.8 kg-mm². If we include the additional mass of the specimen top cap, the total mass moment of inertia of the drive system (including the cap) was 827 kg-mm².

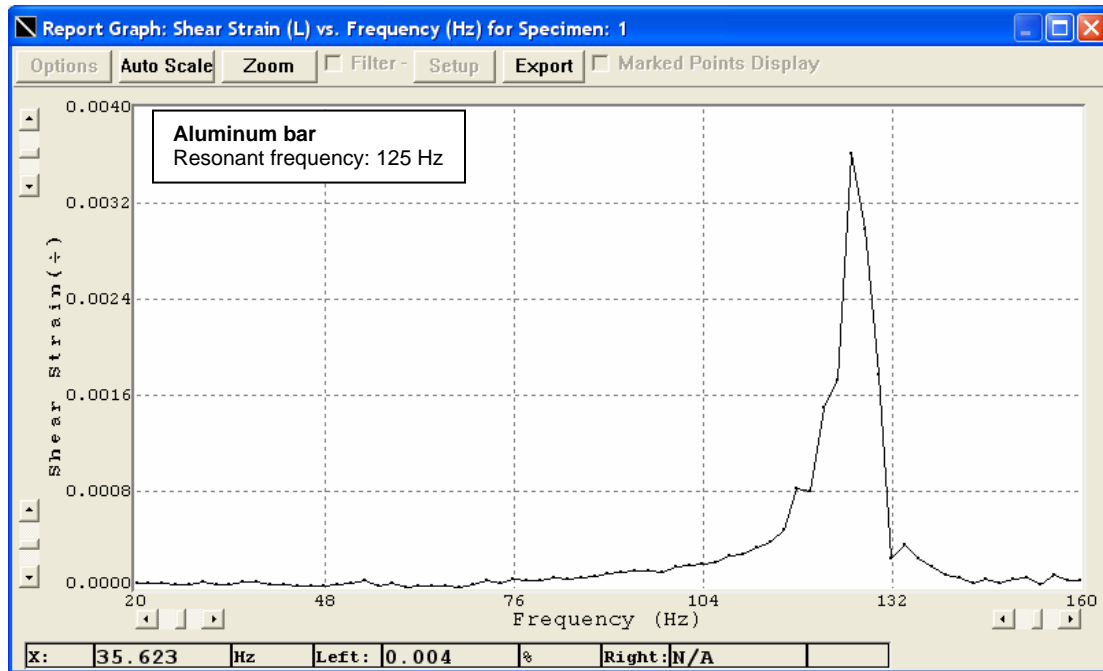


Figure A.6.6. Response curve for calibration test. Aluminum bar without the added mass.

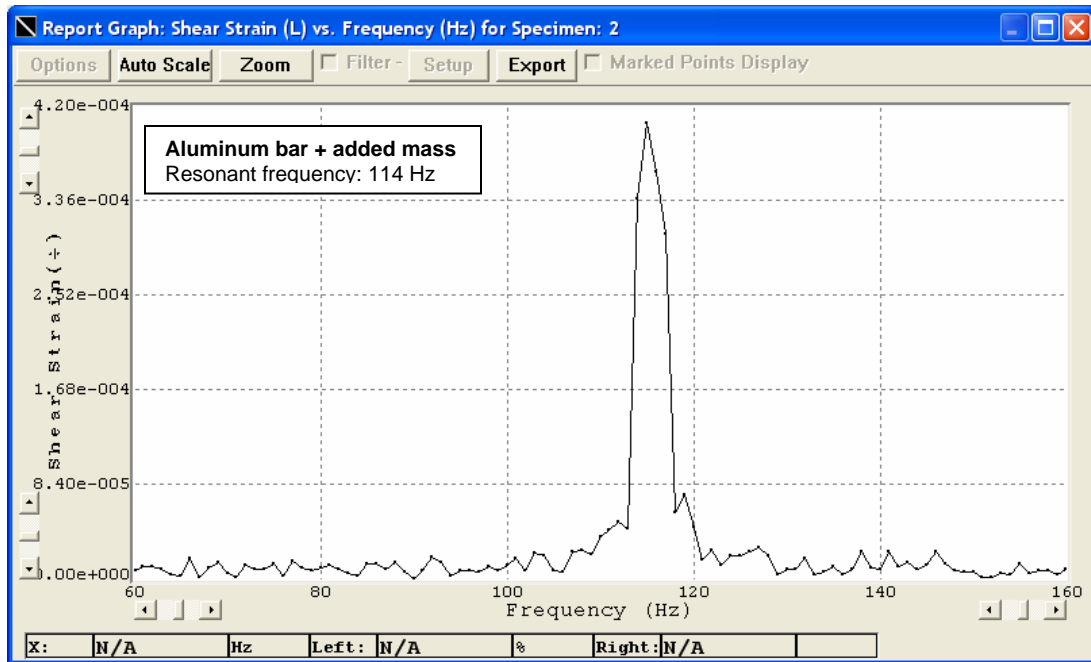


Figure A.6.7. Response curve for calibration test. Aluminum bar with the added mass.

Determination of D_{eq} :

The equipment-generated damping ratio was obtained using the results of the calibration tests, used to determine (I_0). (D_{eq}) was calculated using the free vibration decay method. For the calibration tests performed without the added mass, an average equipment damping ratio of 0.21% was obtained. For the calibration tests with the added mass, an average equipment damping ratio of 0.22% was obtained. Therefore an equipment-generated damping ratio value of 0.22% was selected for this study. A typical free vibration decay curve of the RC system obtained from a calibration test using the aluminum bar is shown in Figure A.6.8.

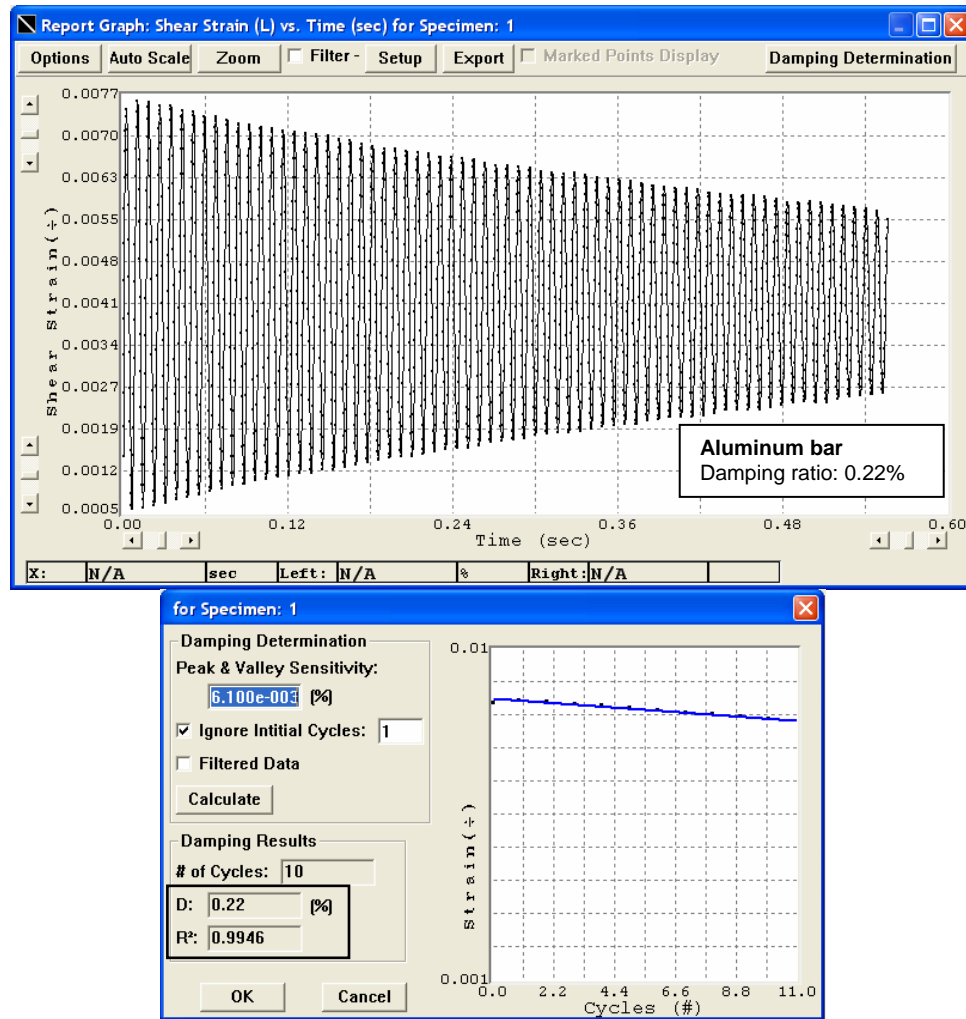


Figure A.6.8. Damping ratio calculation. Calibration test, aluminum bar.

Calibration of displacement sensors:

A micrometer was used for the calibration of the displacement sensors (proximitors) of the RC system. The proximitor was screwed on a leveled surface right in front to the magnet, which was screwed to a movable base that moves with a micrometer. The calibration setup used to calibrate the proximitors is shown in Figure A.6.9. The calibration include moving the magneto towards and away the proximitor. The readings

of the proximator obtained with the CATS software were compared to the micrometer readings. The calibration plots obtained for both proximators are shown in Figure A.6.10 and Figure A.6.11.

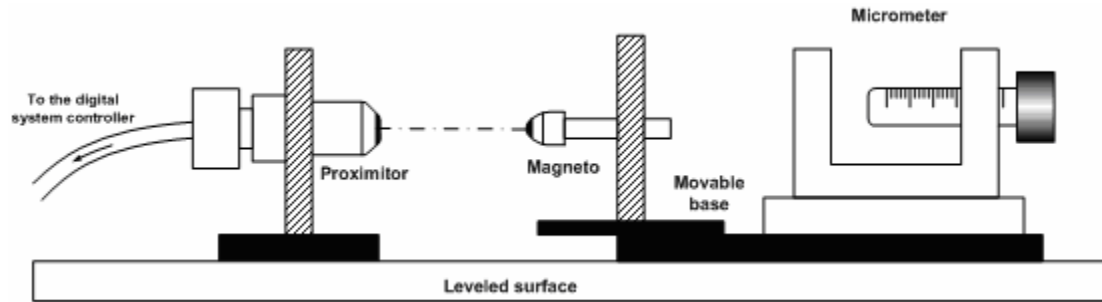


Figure A.6.9. Configuration used for the calibration of the RC displacement sensors.

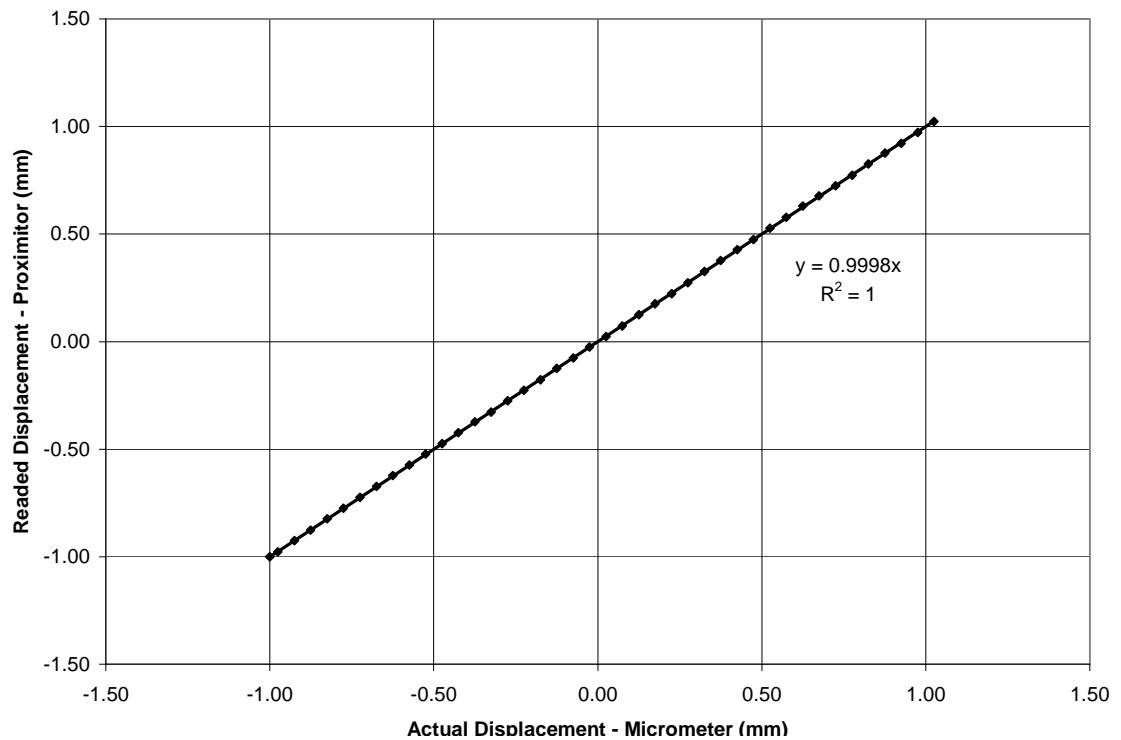


Figure A.6.10. Calibration line for the proximator # 1.

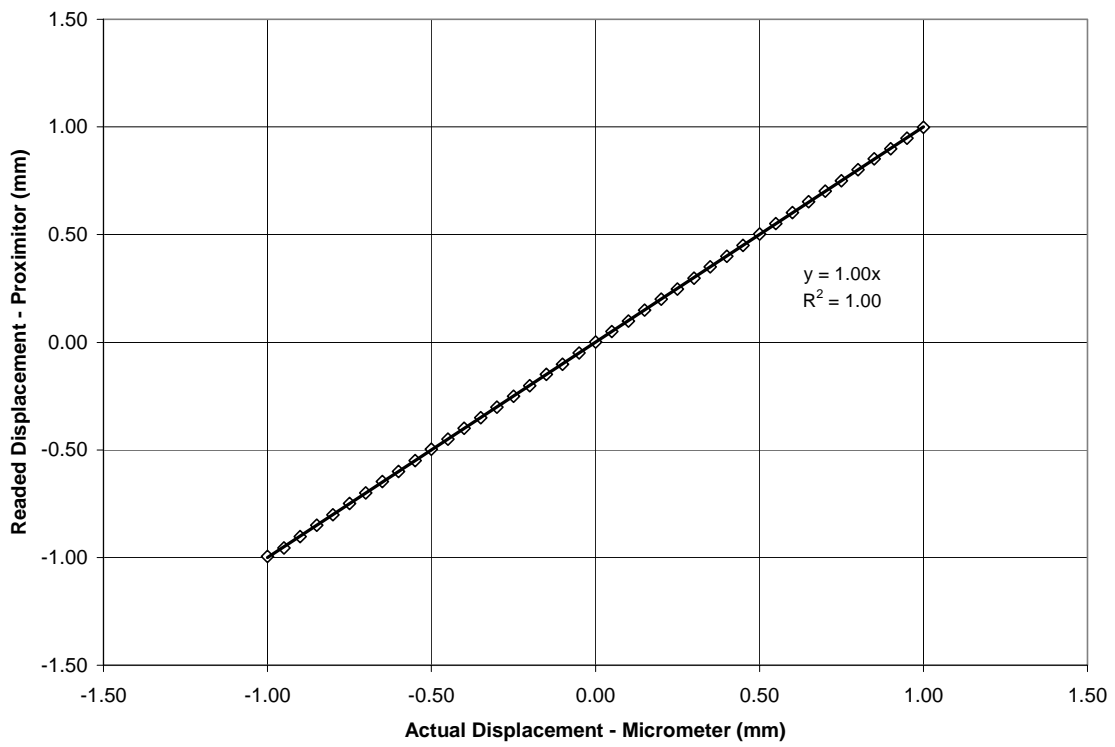


Figure A.6.11. Calibration line for the proximator # 2.

As observed, excellent correlation ($R^2=1.00$) was achieved for both proximators. This indicated that the calibration factors provided by GCTS worked fine for the displacement sensors.